Femtosecond pulse propagation in air towards Filamentation Nonlinear Optics

A Thesis submitted to

University of Hyderabad

In partial fulfilment of the award of the degree of

Doctor of Philosophy

in **Physics**

by

Samuel Anurag Nalam

(14ACPA06)

हैदराबाद विश्वविद्यालय
University of Hyderabad

प्रतिष्ठित संस्थान
INSTITUTION OF EMINENCE
राष्ट्रीय अपेक्षाएँ, वैश्विक मानक
National Needs, Global Standards

Under the supervision of

Dr. P. Prem Kiran

Advanced Centre for Research in High Energy Materials **(ACRHEM)**
School of Physics, University of Hyderabad
Hyderabad 500046, Telangana, India
August, 2021

Dedicated to my

Mother and Father

Declaration

I, **Samuel Anurag Nalam**, hereby declare that this thesis entitled **"Femtosecond pulse propagation in air towards Filamentation Nonlinear Optics"** has been submitted by me under the guidance and supervision of **Dr. P. Prem Kiran**, Associate Professor in School of Physics, Associate faculty in ACRHEM, University of Hyderabad, Hyderabad, India, as per the Ph.D. ordinances of the University, is a bonafide research work. I also declare that no part of this thesis has been submitted previously in part or full to this University or any other University for the award of any degree or diploma.

(Samuel Anurag Nalam)
Reg. No: 14ACPA06

P. Prem Kiran

Dr. P. Prem Kiran
Thesis Supervisor,
ACRHEM,
School of Physics,
University of Hyderabad.

Dr. P. Prem Kiran
Associate Professor
School of Physics
University of Hyderabad
Hyderabad-500 046. (TS) INDIA

Dr. P. Prem Kiran
Associate Professor
Tel.: +91-40-23138842
Fax: +91-40-23012800
E-mail: prem@uohyd.ac.in
premkiranuoh@gmail.com

ACRHEM, School of Physics
University of Hyderabad,
Prof. C. R. Rao Road,
Gachibowli,
Hyderabad – 500 046,
Telangana, India.

Certificate

This is to certify that the thesis entitled **"Femtosecond pulse propagation in air towards Filamentation Nonlinear Optics"** being submitted to the University of Hyderabad by **Samuel Anurag Nalam** bearing Reg. No. 14ACPA06 in partial fulfillment of the the requirements for the award of Doctor of Philosophy in Physics, is a *bonafide* work carried out by him under my supervision and guidance

The thesis has not been submitted previously in part or in full to any other University or Institution for the award of any degree or diploma.

P. Prem Kiran
Dr. P. Prem Kiran
(Supervisor)
Dr. P. Prem Kiran
Associate Professor
School of Physics
University of Hyderabad
Hyderabad-500 046. (TS) INDIA

Director
ACRHEM
Director
ACRHEM

Dean
School of Physics

संकाय अध्यक्ष / Dean
भौतिकी संकाय / School of Physics
हैदराबाद विश्वविद्यालय
UNIVERSITY OF HYDERABAD
हैदराबाद / HYDERABAD-500 046. भारत / INDIA.

CERTIFICATE

This is to certify that the thesis entitled **"Femtosecond pulse propagation in air towards Filamentation Nonlinear Optics"** submitted by **Samuel Anurag Nalam** bearing registration number **14ACPA06**in partial fulfillment of the requirements for award of **Doctor of Philosophy in physics at ACRHEM, School of physics, University of Hyderabad** is a bonafide work carried out by him under my supervision and guidance. This thesis is free from plagiarism and has not been submitted previously in part or in full to this or any other University or Institution for award of any degree or diploma.

Further, the student has the following publications before submission of the thesis for adjudication:

- **S. A. Nalam**, S. S. Harsha and P. P. Kiran, *Effect of Focusing element induced aberrations on filamentation and supercontinuum emission in ambient air*, Opt. Express 29, 14668-14681 (2021).
- **S. A. Nalam**, E. Manikanta, S. S. Harsha and P. P. Kiran, *Acoustic measurements on femtosecond laser induced filaments*, In: Singh K., Gupta A.K., Khare S., Dixit N., Pant K. (eds) ICOL-2019. Springer Proceedings in Physics, vol 258. Springer, Singapore. https://doi.org/10.1007/978-981-15-9259-1_93. (
- M. M. Neethish, V. V. Ravi Kanth Kumar, **S. A. Nalam**, S. S. Harsha, and P. P. Kiran, Supercontinuum generation from zinc borate glasses: bandgap versus rare-earth doping, Opt. Lett. 46, 1201-1204 (2021).
- R. Junjuri, **S. A. Nalam**, E. Manikanta, S. Sree Harsha, P. Prem Kiran, and Manoj Kumar Gundawar, *Spatio-temporal characterization of ablative Cu plasma produced by femtosecond filaments*, Opt. Express 29, 10395-10405 (2021).
- **S. A. Nalam**, E. Manikanta, S. S. Harsha and P. P. Kiran, *Filament Induced Acoustic Spectroscopy of aerosol clouds from Tryptophan*, (Manuscript under preparation to be submitted to JAP/JOSAB)

Also, made presentations in the following conferences:

- **S. A. Nalam**, S. S. Harsha and P. P. Kiran, *Femtosecond Filamentation for the detection of biological warfare agents (Riboflavin)*, 12th International High Energy Materials Conference & Exhibit, December 16th-18th, IITM Chennai, (2019). (POSTER)
- **S. A. Nalam**, S. S. Harsha and P. P. Kiran, *Influence of chirp and polarization on the third harmonic and supercontinuum generation dynamics during fs filamentationin air*, OSA Laser Congress, October 13th–16th, (2020). (POSTER)
- **S. A. Nalam**, S. S. Harsha and P. P. Kiran, *Spectral characterization of intense Femtosecond pulse propagation*, Ultrafast Science, October 22nd-24th, RRCAT, Indore (2018). (POSTER)
- **S. Anurag**, S. S. Harsha and P. P. Kiran, *Ultrafast Filamentation in Air: Application towards long distance remote sensing*, National Laser Symposium-27, December 3rd-6th, RRCAT, Indore, (2018). (POSTER)

The following courses have taken as the part of the course work:

Course No.	Course offered at	Title of the course	Credits	Pass/Fail
PY804	SoP	Advanced electromagnetic theory	4	Pass
PY803	SoP	Advanced Experimental techniques	4	Pass
PY801	SoP	Advanced Quantum Mechanics	4	Pass
PY801	ACRHEM	Research methodology	4	Pass

P. Prem Kiran

Supervisor,
Dr. P Prem Kiran,
Associate Professor,
ACRHEM, University of Hyderabad,
Hyderabad, India.

Dr. P. Prem Kiran
Associate Professor
School of Physics
University of Hyderabad
Hyderabad-500 046. (TS) INDIA

Director,
ACRHEM,
University of Hyderabad,
Hyderabad,
India.

Director
ACRHEM

Dean,
School of Physics,
University of Hyderabad,
Hyderabad,
India.

संकाय अध्यक्ष / Dean
भौतिकी संकाय / School of Physics
हैदराबाद विश्वविद्यालय
UNIVERSITY OF HYDERABAD
हैदराबाद / HYDERABAD-500 046. भारत / INDIA.

Acknowledgements

It is truly an honour that I can formally thank everyone who have been part of my PhD. My journey and growth during my PhD was more than just an academic accomplishment for which I have to thank the University of Hyderabad and my supervisor Dr. P. Prem Kiran for giving me the space to think openly. My supervisor Dr P Prem Kiran has allowed me to conduct myself and my research freely for only as long as I am being honest to the scientific temper and thought. This has not only encouraged me to open my mind to broad and various avenues of thought and research but also inculcated the belief that curiosity should be nurtured and not restricted. I will forever be grateful for the exposure that was given to me by Dr P Prem Kiran from when I was studying for my bachelor's degree and I first witnessed the femtosecond laser.

It was a great privilege to have had Prof Soma Venugopal Rao and Dr Manoj Kumar as the members of my doctoral committee, who have pushed me to work on my research abilities and build on my presentation skills. Discussions with my doctoral committee have formed the foundation of the thesis that I have presented. I have been enlightened about academic ethics and conduct from the faculty of ACRHEM and SoP who have taught me both in the classroom and by example.

My PhD work would not have been possible without the enthusiastic and motivating support of Dr Sree Harsha, who has not only assisted me but also my colleagues with unfailing excitement and passion. The innumerable things that I have learned from Dr Sree Harsha are secondary compared to the motivation that I have received from him.

I am very fortunate to have conducted my PhD research work in ACRHEM. The world class level facilities made new and exciting research possible. I thank my current director Dr. V Kameswara Rao and former director Dr. K. Venkateswara Rao for their continuous support and smooth functioning of ACRHEM. I am also thankful to the Dean, School of Physics (SoP), UoH for the academic support.

I enjoyed working with my seniors Dr. Nagaraju, Dr. Manikanta and Dr. Sai Shiva who were very encouraging during the course of my PhD and educated me on the academic difficulties of PhD. I have also had many learning experiences with my seniors Dr. Rajendhar Junjuri, Dr Abdul Kalam, Dr. Byram Chandu and Dr Ganesh Damerla. I will surely remember

the days and nights spent in the company of my friends and colleagues Yellaiah, Phanisree, Dr. Krishna Kanth, Dr. Bharathi, John, Linga, Naveen, Raghavendhar, Neethish, Dr. Archana, Dr Som Datta, Shashank, Arun, Deepanjan, Rajesh, Nagaraju, Jaganadh and Akash.

I am ever grateful for the friends that I have been blessed with, Sarayu, Sham, Somnath, Omkar, Rachna, Kranti, Ganesh, Ajay, Asith, Sion, Jagdeesh, Ranjan and many more who have become family during the course of my PhD. I am glad to have shared my apartment with really special and intriguing people, Dr Kesaban, Raja and Pratap (colleague as well) who witness and also share my unique experiences.

During my PhD I have played basketball and represented the University during which I have learnt great lessons in sportsmanship, hard work and teamwork and made a great many friends some of them being Karthik, Akhil and Manish. I was also part of JCM orchestra, a western classical music orchestra based from Hyderabad for whom I played the violin. I was able to learn and practice music because of this which greatly assisted me during my PhD. I would also like to thank the Students' Federation of India – HCU unit (SFI-HCU) for involving me in the activities and endeavours due to which I have met numerous people from different regional, cultural and academic backgrounds.

My PhD would not have been possible without the support, compassion and patience of my parents, Dr N Madhusudhana Rao and Dr N Amulya Rao. They have strengthened and nurtured me much before and during my Phd. My brother Paul Gaurav no matter where he is stationed at, has been a strong source of support and encouragement. I believe my family is my greatest strength and it is my biggest driving force to make them proud.

Table of Contents

7. APPLICATION OF FILAMENTS……………………………...162

List of Figures

List of Tables

This page was intentionally left blank

CHAPTER 1: Introduction

Abstract:

Intense Femtosecond pulse propagation in air leads to a highly dynamic phenomenon called filamentation. The thesis discusses filamentation in air and the various aspects of filamentation which arise from the long range highly intense propagation of femtosecond pulses. This chapter briefly discusses generation of intense femtosecond pulses and the nonlinear phenomenon that arise during the fs pulse propagation in a medium leading to the formation of filaments. The prolonged propagation arising due to the dynamic interplay between the third order material response to the electric field and the plasma build up is a home for many non-linear processes. The electromagnetic propagation equation was used to account for the multiple processes that arise during filament propagation such as multiphoton ionization, Kerr self-focusing, self-phase modulation, higher harmonic generation and absorption. Filamentation is a highly dynamic regime because of which simulation alone cannot help understand the processes in filamentation which can be modulated or enhanced. We have therefore attempted to empirically characterize filaments generated under different input laser properties and correlate them to the corresponding emissions from filaments. This chapter establishes the basis and motivation for the thesis which is to holistically characterize filamentation with a goal towards important applications such as remote sensing.

1.1. Laser background

For a large part of history, light has mostly been used to illuminate and observe. The discovery of the laser in 1961 was a landmark for the multidimensional explorations and applications that coherent light from the laser brought about [1].Presently, optical or laser based devices exist in almost every aspect of our domestic and industrial footprints [2,3]. Laser driven research has broken barriers in communication, micro-structuring, surgery, ultrafast studies and remote sensing to name a few [4-10]. Exciting discoveries such as that of the discovery of gravitational waves was made possible by a large but simple Michaelson interferometer and a highly stable monochromatic laser complimented by precise and sensitive optical elements and detectors (LIGO – Laser Interferometer Gravitational-Wave Observatory) [11].

While extending our imaging ability and dynamics studies to a molecular level, lasers are also able to sustain and deposit high powers [12-14]. Micro-structuring and remote sensing are some of the applications that have found great development with the arrival of high power lasers [15, 16]. Precise spatial and temporal energy localization are some of the key attributes that help in micro-structuring, whereas the ability to propagate large distance without dissipation and mode distortion facilitates remote sensing abilities when supported by quantitative and qualitative spectroscopic studies. The high power levels achieved here can be from continuous wave lasers or pulsed lasers, which vary in the mechanism of amplification. Pulsed lasers give us the ability to localize energy temporally which not only helps save energy while achieving high peak powers but also provides us with tools of ultrafast imaging and spectroscopy [17]. Although pulsed laser applications and research has gone a great distance, the development does not appear to saturate in the near future due to the ever growing need as well as the scope of these ultrafast lasers. In this thesis, we intend to expand our understanding of the propagation and sensing ability of an intense femtosecond laser particularly in ambient atmosphere where we observe the highly dynamic regime called filamentation. The peak power and short timescale characteristic of these pulses facilitates fascinating and unprecedented phenomena which are both enlightening and empowering.

1.2 Ultrafast lasers

The first breakthrough for pulsed laser generation came about in the form of Q-switching [18, 19]. One could generate pulses in the order of nanosecond timescales and deliver megawatt peak power. Q-switching of the laser is done by modulating the laser cavity losses as to suddenly 'switch' the quality factor or Q-factor for a sudden outburst of energy. We can produce intense pulses longer than 1ps using this technique. The discovery of mode-locking pushed timescales much lower beyond the picosecond timescales into the femtosecond regime [20]. The discovery of modelocking by locking all the multiple resonator cavity modes in phase to give an ultrashort pulse produces pulses in the order of femtosecond, which could be amplified using the chirped amplification technique thereby generating intense ultrashort pulses. It is accepted that these pulses which are less than one picosecond can be considered as ultrashort pulses enabling ultrafast phenomenon. Early femtosecond lasers were built using various dye solutions as an active gain medium. The broadband fluorescence (> 100nm) of the dyes when suitably excited and the tunability over a large bandwidth make them very attractive for building ultrafast lasers. But dye lasers present operational challenges associated with circulation of the dye (plumbing and cell maintenance) as well as the stability of the dye molecules (photo-bleaching) for long term operation [21]. This challenge was overcome through the discovery of Chirped Pulse Amplification and discovery of Ti:Sapphire as a gain medium. With CPA, the pulse is amplified after it is 'stretched' and then 'compressed' just before exit [22]. CPA has therefore given access to high power femtosecond laser pulses, which exist for short timescales (~fs) and carry much higher powers (~GW), by compressing energy of the order of mill joule to a few femtoseconds. The evolution of the laser is shown in the figure 1.1.

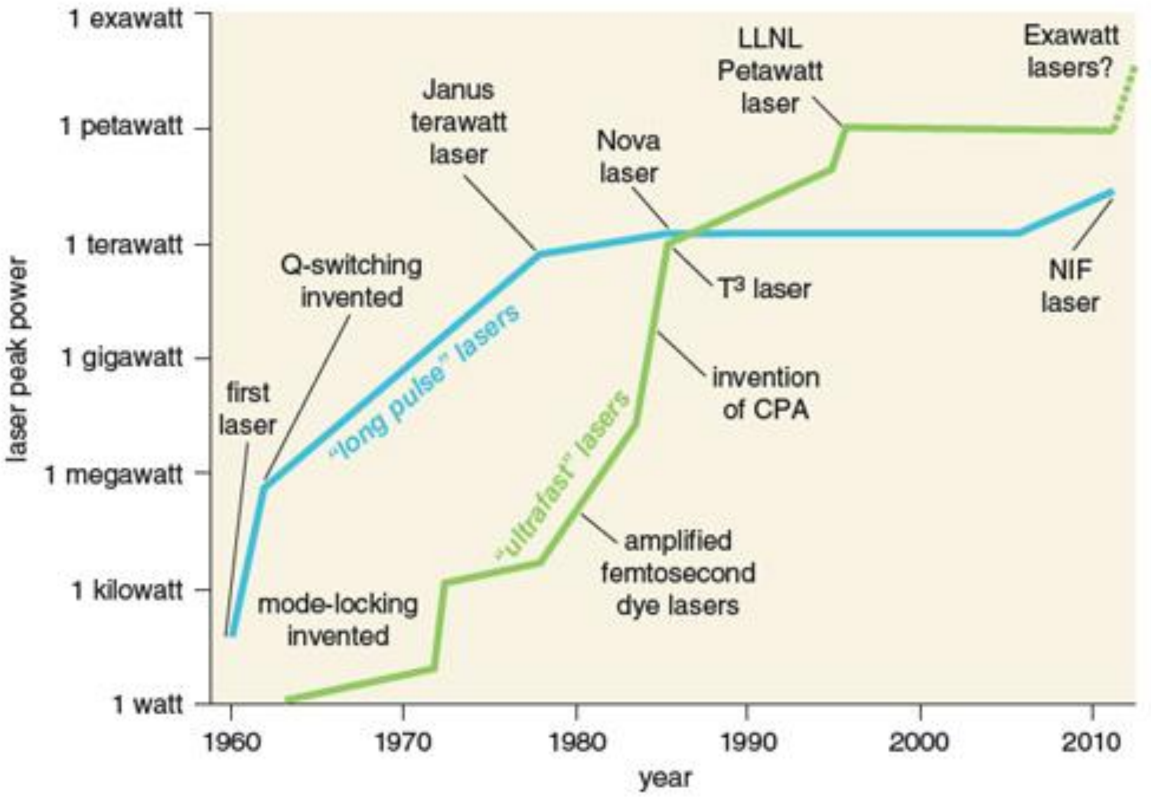

Figure 1.1: The evolution of pulsed laser and major landmarks in laser discovery (https://www.americanscientist.org/article/high-power-lasers).

Femtosecond pulses being the fastest man made event when they were first discovered, can assist studies of molecular dynamics and also inhibit chemical processes which occur in the tens to hundreds femtosecond scale. This low temporal extent of femtosecond lasers also assists in microscopic imaging and microfabrication. Multiphoton fluorescence studies which are made possible by ultrashort pulses also facilitate much smaller interaction zones [23]. As the temporal duration of the femtosecond pulses have large bandwidth due to the uncertainty principle which states that the spectral and temporal spreads are inversely related, a 100 fs pulse has a bandwidth of 10THz, there are much shorter ultrashort pulses (<2fs) whose bandwidth covers a whole octave because of which we call them white light lasers [24]. The concentration of mill joule energy into femtosecond timescales increases the peak power to the order of terawatts. Femtosecond lasers can now generate Petawatt (10^{15} W) powers and can achieve immense intensities (10^{20}W/cm^2) [25, 26]. In these regimes we are able to do ground breaking experiments which were not possible due to the lack of access to such high intensities. Some of the exciting works that are being done with these lasers are higher harmonic generation of pulses providing lasers in XUV and table top particle accelerators [27, 28]. We can therefore access extreme perturbations in laser matter interactions, the figure 1.2 shows the different regimes of interaction available due to intense ultrashort lasers.

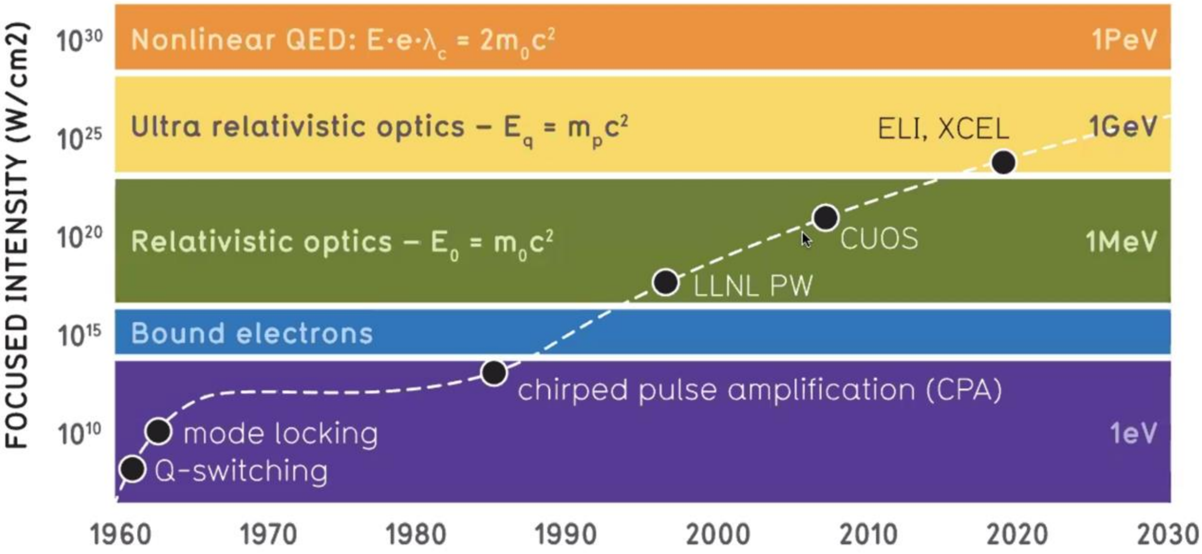

Figure 1.2: Different perturbative regimes accessed by intense ultrashort laser pulses according to the focused intensity that can be accessed [29].

Ultrafast lasers have found applications in a variety of interdisciplinary and fundamental endeavours. The ultrashort timescale, high degree of coherence and temporal repeatability of these lasers has helped characterize high speed electronic devices and build highly precise clocks [30]. The femtosecond scale time duration is used for ultrafast imaging of high speed events and in ultrafast chemistry for both observation and probing of many of the molecular level processes by using specially engineered pulse trains (double pulse or frequency modulation) [31, 32]. Laser plasma interaction is possible even in low density matter like air due to peak intensities exceeding ~10^{13}W/cm^2. Multiphoton ionization and tunnel ionization are the dominant plasma generating mechanisms in these time scales. The ability to propagate large distances has not only encouraged research towards application in free space communication but also in remote sensing as one can deposit a large amount of energy in the form of filamentation in a distant spot while at the same time create a broadband laser source that can excite a variety of atmospheric species [33]. Femtosecond lasers are also being applied in the medical field for multiple non-invasive diagnostics and surgery. Micromachining and microstructuring is looking towards femtosecond lasers due to the minimal heat deposition and micrometre level accuracy.

The laser used in our experiments compressed 2.5mJ of energy into ~50 fs, providing us with a ~50 GW peak power and peak intensity of ~10^{15}W/cm^2 in vacuum. At these intensities (TW/cm^2) accessed by our laser, perturbative nonlinear optics applies and the motions of bound electrons that mediate important laser–matter interactions are viewed as instantaneous. By scaling up the amplification techniques we can obtain petawatt range peak power lasers which provide even higher intensities (~10^{20}W/cm^2) where the electric field is more than the interatomic field in which case the instantaneous bound electron response does not apply, we observe high harmonic generation of XUV and X-Rays when propagated through inert gases. This coherent generation of low wavelength facilitates the white light laser and attosecond pulse generation [34].

1.3 Filamentation of laser pulses

The highly dynamic nature of intense ultrashort pulse propagation is due to multiple competing linear and non-linear light-matter interactions coming about under high intensity ranges of TW/cm^2 occurring in time scales of femtoseconds [35]. The non-intense regime of femtosecond pulse propagation alone undergoes many propagation effects like dispersion and diffraction which we consider as linear effects [36]. As we increase the energy of the pulse the electric field in the pulse becomes comparable to the interatomic electric field (~10^9 V/cm) because of which light matter interactions get perturbed much beyond the first order or linear terms. We can understand these perturbations by taking into account higher order terms of the non-linear material response to electric field relation,

$$P(E) = \epsilon_0(\chi^{(1)}E + \chi^{(2)}EE + \chi^{(3)}EEE \dots \dots) \tag{1.1}$$

One of the first nonlinear effect that comes into play is the Kerr self-focusing effect, a consequence of the third order nonlinearity in the polarization induced by an electric field which induces a refractive index proportional to the spatial and temporal intensity distribution of the pulse. As the pulse has Gaussian spatial intensity distribution, it induces a lens like effect which causes the beam to 'self-focus' leading to the collapse of the laser beam until plasma build up cancels the effect. We do not observe any non-linear effects due to the second order nonlinearity because air is a centrosymmetric homogenous medium and does not contain consistent molecular asymmetry to facilitate second order nonlinear effects. The Kerr self-focusing effect gets saturated with the onset of plasma which gets created because of the high density of photons creating a defocusing effect on the laser beam. The dynamic interplay between these competing nonlinear mechanisms forces the laser beam to be collimated in a thin channel of a few micrometer thickness. This highly intense confined propagation of the laser beam is called filamentation. The laser beam travels in this regime for distances far outlasting the Rayleigh range providing us with considerable medium and light interaction. This behaviour of the propagation provides us with a strong tool to efficiently probe various distant media and study them at different distances. Figure 1.3 shows the process of filamentation. The dotted line indicates the focusing profile under linear focusing.

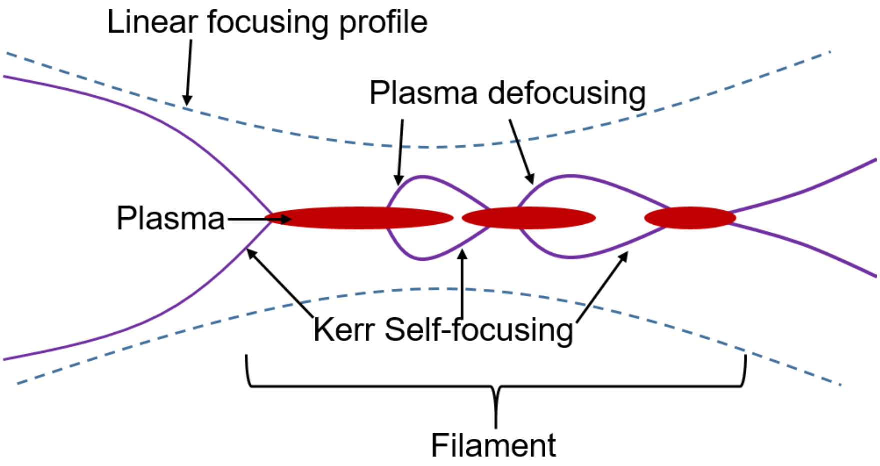

Figure 1.3: Kerr self-focusing and plasma defocusing leading to Filamentation.

The change in the refractive index from linear refractive index (n_0) due to the Kerr effect is given as a function of intensity (I) by the relation,

$$n = n_0 + n_2 I \tag{1.2}$$

The non-linear refractive index n_2 is calculated from the third order susceptibility ($\chi^{(3)}$) as,

$$n_2 = \frac{3}{4} n_0^2 \epsilon_0 c \chi^{(3)} \tag{1.3}$$

Where ϵ_0 is the permittivity of free space and c is the speed of light in vacuum. For a freely propagating pulse we can define the critical power (P_{cr}) at which the self-focusing effect exactly balances the diffraction effect, this is found by equating the diffraction length to distance at which beam diameter becomes 1/e times of initial pulse due to self-focusing. P_{cr} is therefore a quantity to characterize the non-linearity in the medium and minimum power for filamentation to overcome diffraction effects given by the relation,

$$P_{cr} = \frac{3.77\lambda^2}{8\pi n_0 n_2} \tag{1.4}$$

The self-focusing distance i.e. the distance at which a freely propagating beam collapses on itself was found analytically and can be given by the relation,

$$z_{sf} = \frac{0.367 k a_0^2}{\left(\left(\left({}^{P}/_{P_{cr}}\right)^{1/2} - 0.852\right)^2 - 0.0219\right)^{1/2}} \tag{1.5}$$

The plasma build up with increase in pulse intensity has an opposing effect to the pulse propagation and the plasma density influences the refractive index according to the equation

$$n(r,t) = n_0 - \frac{\rho(r,t)}{2\rho_c} \tag{1.6}$$

$\rho(r,t)$ defines the spatial and temporal plasma distribution and ρ_c is the critical density of the medium defined as the density where the plasma frequency is equal to the electromagnetic wave frequency given by,

$$\rho_c = \frac{m_e \omega_0^2}{4\pi e^2} \tag{1.7}$$

The plasma generation mechanism is predominantly by multiphoton Ionization in air because the mean collision time in air (300-800 fs) is much larger than the pulse duration for ionization mechanisms to be Inverse Brehmsstahlung ionization or Avalanche ionization. These two non-linear effects facilitate long range intense propagation of pulses over distances many orders larger than the Rayleigh range. This intense regime of propagation is home to numerous other non-linear processes like Self-phase modulation, conical emission, higher harmonic generation and mechanical wave generation (shockwaves) to name a few. Filamentation study therefore is capable of exploring a different paradigm of nonlinear optics which can be specialized to many other exciting directions in research.

1.4 Ultrashort pulses

The generation and application of ultrashort pulses requires knowledge of laser functioning and physics that governs the electromagnetic nature of femtosecond pulses. We first establish the physics that governs intense laser propagation and in the coming chapters discuss the laser operating mechanism. The physics is vital since the femtosecond pulse not only contains a broad spectral distribution subject to dispersion, but also propagates at an extremely high intensity inducing multiple non-linear phenomena [37]. Therefore in this section we incorporate an intense femtosecond pulse into the electromagnetic propagation equation in homogenous dielectric media derived from the Maxwell's equations [35]. This helps us understand the intense femtosecond pulse propagation and effect of linear and nonlinear matter interactions defined by the media and further attempt to incorporate such effects to simulate filamentation. The theory discussed describes in two steps: firstly, linear laser matter interactions and secondly, inclusion of higher order non-linear terms. These non-linear phenomena define the propagation dynamics of femtosecond pulses leading to filamentation and subsequent emissions.

1.4.1 Gaussian pulses

The simplest and ideal form of a Continuous wave laser is a monochromatic plane wave propagating in the z-direction. Its electric field will ideally have an infinite transverse spread. The electric field (*E*) of this laser in that case can be defined by the equation,

$$\vec{E} = \overrightarrow{E_o}\, exp(-\mathrm{i}(k.z - \omega_o t)) \tag{1.8}$$

Where E_0 is the Amplitude of the electric field which is constant in this case, k is the wave vector (scalar in this case), ω_0 is the radial frequency, z is the coordinate in the propagation direction. As we will mostly be working with the spatial and temporal intensity distribution of the pulse we will refer to the electric field amplitude E_o as E in the rest of this thesis. In physicality, a laser most commonly has a Gaussian spatial profile because it is an outcome of the lowest order mode in a waveguide. Therefore the electric field amplitude (E) will have a transverse spatial distribution can then be given by the equation,

$$E(r, z = 0) = E_o \exp\left(-\frac{r^2}{\omega_o^2} - \frac{ik_o r^2}{2f}\right) \tag{1.9}$$

Where, r is the transverse radial coordinate of the laser profile and f is the radius of curvature of the wavefront in case there is a lens at the outlet of the laser. This treatment of the laser will now undergo diffraction because the laser is now a monochromatic laser of multiple plane waves with slightly varying wave vectors. The propagation in a medium with non-negligible diffraction effects will cause the laser to diverge. A laser pulse being an electromagnetic pulse, can be mathematically represented as a Fourier integral of a superposition of a set of plane waves propagating in the z-direction in the form,

$$E(z, t) = \int_0^\infty E_0(\omega, t) \exp\big(i(\omega t - kz)\big)\, d\omega \tag{1.10}$$

$$k = \frac{\omega n(\omega)}{c} \tag{1.11}$$

This shifts the laser from a monochromatic regime to a broadband regime where linear and higher order dispersion effects influence the pulse propagation significantly. The linear and higher order dispersion effects are seen due to the frequency dependence of refractive index. The refractive index therefore can be represented with higher order contributions using the expansion.

$$\begin{aligned} n(\omega) = n(\omega_0) + \frac{dn}{d\omega}(\omega - \omega_0) + \frac{1}{2}\frac{d^2 n}{d\omega^2}(\omega - \omega_0)^2 \\ + \frac{1}{6}\frac{d^3 n}{d\omega^3}(\omega - \omega_0)^3 \ldots.. \end{aligned} \tag{1.12}$$

As one can see for a broadband pulse the refractive index is not constant because of which dispersion can't be neglected at least up to the second order ($d^2n/d\omega^2$). We can arrive at a constant time-bandwidth product for the pulsed laser depending on the temporal and spectral profile of the pulse which limits the minimum broadband range and pulse duration that can be achieved. The pulsed laser used in our experiment has a transform limited pulse width of ~50fs which corresponds to a frequency range of ~30nm. A pulsed laser seeded by modelocking has a secant hyperbolic temporal distribution which can be approximated to be a Gaussian pulse as their distributions are similar. This helps treat the femtosecond pulse as a Gaussian distribution both in space and in time. The combined equation for a propagating femtosecond pulse in time and space in vacuum can be given by,

$$E(r,t,z=0) = E_0 \exp\left(-\frac{r^2}{\omega_0^2} - \frac{ik_0 r^2}{2f} - (1+iC)\frac{t^2}{t_p^2}\right) \tag{1.13}$$

Where t_p is transform limited pulse duration and C is the Chirp parameter, which induces a quadratic phase in the pulse when it has a non-zero value. Chirp of the pulse will be discussed in more detail in the coming chapters (Chapter 3). The second order dispersion term (3rd term in equation 1.12) induces chirp in the pulse because of the quadratic phase that it induces into the frequency distribution of the pulse.

1.4.2 Ultrashort Propagation equation from Maxwell's equation

As the pulse undergoes many effects, simulation of such effects needs to account for all the factors that take part in intense pulse propagation. We can incorporate 1+1 dimensional simulation codes which are available to include dispersion, diffraction, self-focusing, ionization and absorption in the propagation of these pulses [35]. To understand pulse propagation one needs to first start with Maxwell's equations which define electromagnetic propagation in media. The Maxwell-Ampere and Maxwell-Faraday equation show that.

$$\nabla \times E = -\frac{\partial B}{\partial t} \tag{1.14}$$

$$\nabla \times B = \mu_0\left(J + \frac{\partial D}{\partial t}\right) \tag{1.15}$$

$$D(r,\omega,z) = \epsilon_0 \epsilon(\omega) E(r,\omega,z) + P(r,\omega,z) \tag{1.16}$$

The electric displacement *D* is substituted in the Maxwell-Ampere equation and is combined with Curl of the Maxwell-Faraday equation to give us the propagation equation which includes the nonlinear material response,

$$\nabla^2 E - \nabla(\nabla.\mathrm{E}) - \frac{1}{c^2}\frac{\partial^2}{\partial t^2}\int_{\infty}^{t}\epsilon(t-t')E(r,t',z)dt' \\ = \mu_0\left(\frac{\partial J}{\partial t} + \frac{\partial^2 P}{\partial t^2}\right) \tag{1.17}$$

Can be written in the frequency domain as,

$$\nabla^2 E - \nabla(\nabla.\mathrm{E}) + \frac{\omega^2 n^2(\omega)}{c^2}E = \mu_0(-i\omega J - \omega^2 P) \tag{1.18}$$

This equation treats both forward and backward propagating components and also resolves wavelength. However, simulation of this propagation equation requires large computation time and resources. We therefore simplify this equation for better computation without loss in integrity in the final solution. The above equation is first broken down by separating the transverse coordinates from the propagation coordinates which leads us to write,

$$\nabla^2 E = (\partial_z^2 + \nabla_\perp^2)E \tag{1.19}$$

As we consider the polarization and electric field to be perpendicular to the propagation direction the second term, $\nabla(\nabla.E)$ can be neglected for cases where the beam is not strongly focused. The propagation equation in the frequency domain now becomes.

$$(\partial_z^2 + \nabla_\perp^2)E(r,\omega,z) + k^2(\omega)E(r,\omega,z) = -\mu_0\omega^2 P(r,\omega,z) \tag{1.20}$$

The laser pulse can be considered to have a slow and fast varying component to the electric field which can then be broken down so that the propagation of the pulse can then be solved using only the slow varying component or envelope. The electric field can then be written as $E(r,t,z) = \hat{E}(r,t,z)\exp(ik_0 z - i\omega_0 t)$. The polarization can also be broken down into the slow and fast varying components in the same manner. $\hat{E}(r,t,z)$ is the slowly varying amplitude of the laser pulse. The polarization term *P* will account for the linear and non-linear material responses. On incorporating the Fourier counterpart of the Electric field distribution relation in the above equation gives,

$$\frac{\partial^2 \hat{E}}{\partial z^2} + 2i\frac{\omega}{v_g}\frac{\partial \hat{E}}{\partial z} = -\Delta_{\perp}\hat{E} - \left(k^2(\omega) - \frac{\omega^2}{v_g^2}\right)\hat{E} - \frac{\omega^2}{c^2}\frac{\hat{P}}{\epsilon_0} \tag{1.21}$$

This is a generalized exact equation defining the propagation of an electromagnetic pulse. We can neglect the second order term on the left hand side as it is negligible compared to the first order term. This approximation means that the amplitude is evolving slowly compared to the electric field oscillation.

$$|\partial_z^2 E| \ll 2\frac{\omega}{v_g}|\partial_z E| \tag{1.22}$$

The second term on the right hand side of the equation can be written as,

$$\left(k^2(\omega) - \left(\frac{\omega}{v_g}\right)^2\right) = 2\frac{\omega}{v_g}\left(k(\omega) - \frac{\omega}{v_g}\right) + \left(k(\omega) - \frac{\omega}{v_g}\right)^2 \tag{1.23}$$

By inserting this equation and neglecting second order terms, the equation in the frequency domain is.

$$\frac{\partial \hat{E}}{\partial z} = \frac{i}{2(\frac{\omega}{v_g})}\Delta_{\perp}\hat{E} + i\left(k(\omega) - \frac{\omega}{v_g}\right)\hat{E} + i\left(\frac{\omega}{c}\right)^2\left(\frac{1}{2(\frac{\omega}{v_g})}\right)\frac{\hat{P}}{\epsilon_0} \tag{1.24}$$

The second term on the Right hand side is dispersion relation accounting for all orders of dispersion above the first order of dispersion. This is the equation that can help simulate femtosecond pulse propagation even when the dispersion is taken up to the second order.. The above equation defines the linear propagation of a pulsed laser while including dispersion and diffraction. With the inclusion of non-linear contributions to polarization such as Kerr effect, plasma defocusing, multiphoton ionization and absorption, filamentation can be better understood using the above equation. These terms can be added into the polarization component of the above equations. The higher order medium response to the electric field is what causes many of the nonlinear processes that we observe at high intensity like second harmonic generation, sum/difference frequency generation, third harmonic generation, self-focusing and self-phase modulation. Inclusion of the above terms in the polarization term helps understand the influence of these terms. However, we do not observe second order material response to electric field in air because air is a homogenous centrosymmetric medium.

We therefore start observing higher order response from the third order at highly intense propagation in air. To show the inclusion of the higher order processes in pulse propagation we show Kerr self-focusing term which is due to the third order medium response to electric field

The Kerr Self-focusing term arises from the third order susceptibility to polarization which gives,

$$P \equiv \epsilon_0 \chi^{(3)} E^3 \tag{1.25}$$

The simple case of a nearly monochromatic light pulse gives rise to two terms in the polarization if E is taken as,

$$E = \frac{1}{2}\left[\hat{E} exp(ik_0 z - i\omega_0 t) + \hat{E}^* exp(-ik_0 z + i\omega_0 t)\right] \tag{1.26}$$

The E^3 term in the nonlinear polarization relation becomes,

$$E^3 = \frac{1}{8}\left[3\left|\hat{E}\right|^2 \hat{E} exp(ik_0 z - i\omega_0 t) + \hat{E}^3 \exp(i3k_0 z - i3\omega_0 t) + c.c\right] \tag{1.27}$$

The first term in this expansion contributes to Kerr Self focusing which will contribute to the polarization term in the following manner,

$$\hat{P} \equiv \frac{3}{4} \epsilon_0 \chi^{(3)} \left|\hat{E}\right|^2 \hat{E} \tag{1.28}$$

The third harmonic component at $3\omega_0$ is discarded to discretely include the non-linear terms separately. The inclusion of the third harmonic ($3\omega_0$) term will be discussed in detail in the coming chapters. When the Self focusing term alone is included in the propagation equation for a monochromatic wave, it will include only the diffraction term without dispersion (i), the propagation can be simulated using the equation,

$$\frac{\partial \hat{E}}{\partial z} = \frac{i}{2k_0} \Delta_\perp \hat{E} + i \frac{\omega_0}{c} n_2 I \hat{E} \tag{1.29}$$

This section describes all the factors that come into play during the process of filamentation such as self-focusing, plasma defocusing, dispersion, diffraction, ionization and absorption. As these processes compete in femtosecond time scales we first need know the different processes and then move onto understanding their dynamic behaviour.

Understanding and simulation of the pulse propagation through the non-linear Schrodinger equation approach shines ample light on the highly dynamic and unprecedented behaviour of filamentation [38, 40].

1.5 Motivation of the thesis

From the demonstration of long range propagation of fs pulses in atmosphere leading to filamentation by Braun et. al. in 1995 [39], the applications of femtosecond filaments have sky rocketed paving the way for accessing the novel regions which were inaccessible earlier. The filamentation termed as "collapsing light" or "light bullets" has opened up surrealistic advances associated with filamentation such as Filament induced Atmospheric monitoring [40], Filament assisted population inversion and lasing in air [42], Filament assisted precipitation[43], lightning discharge control [44] and attosecond pulse generation [45] to name a few. Filaments generated using a terawatt femtosecond laser launched into the atmosphere have demonstrated few kms of unperturbed propagation as shown in the figure 1.4. The cross section in the figure also shows the formation of multiple filaments that form over the distance of propagation. The high intensity provides an extremely efficient tool to probe and characterize the gaseous media via filament induced breakdown spectroscopy [46] or in ambient atmosphere [47]. The broadband Supercontinuum generated filamentation in a transparent dielectric media by SPM is an efficient tool and can be used as a broadband ultrashort source for transient Absorption spectroscopy studies used to study the electronic relaxation of excited states in molecular systems [32]. The filament propagating in air can also be a source in the RF and Terahertz frequency range where one can probe molecular vibrational and rotational states [48]. The oscillation of ions along the propagation of the filament produces a conical emission in the radio frequency range (MHz-GHz) as well [49-51]. Filamentation displays several fascinating phenomenon and can be an efficient tool in multiple exciting directions of fundamental and applied research.

One of the major challenges of fs filamentation physics is the precise characterization of filament itself in terms of its intensity and plasma density owing to high intensity and short temporal duration. Many efforts were made towards instantaneous characterization of filaments using optical techniques such as femtosecond time-resolved optical polarigraphy [52], ultrafast holography [53-56], and fluorescence imaging [57, 58] can capture individual pulse events at separated spatial locations over ranges much shorter than the length of a filament. Non-optical methods such a sonography [59, 60] and high-voltage discharge [61] can provide information over entire filament lengths but with spatial and temporal resolution inferior to optical methods.

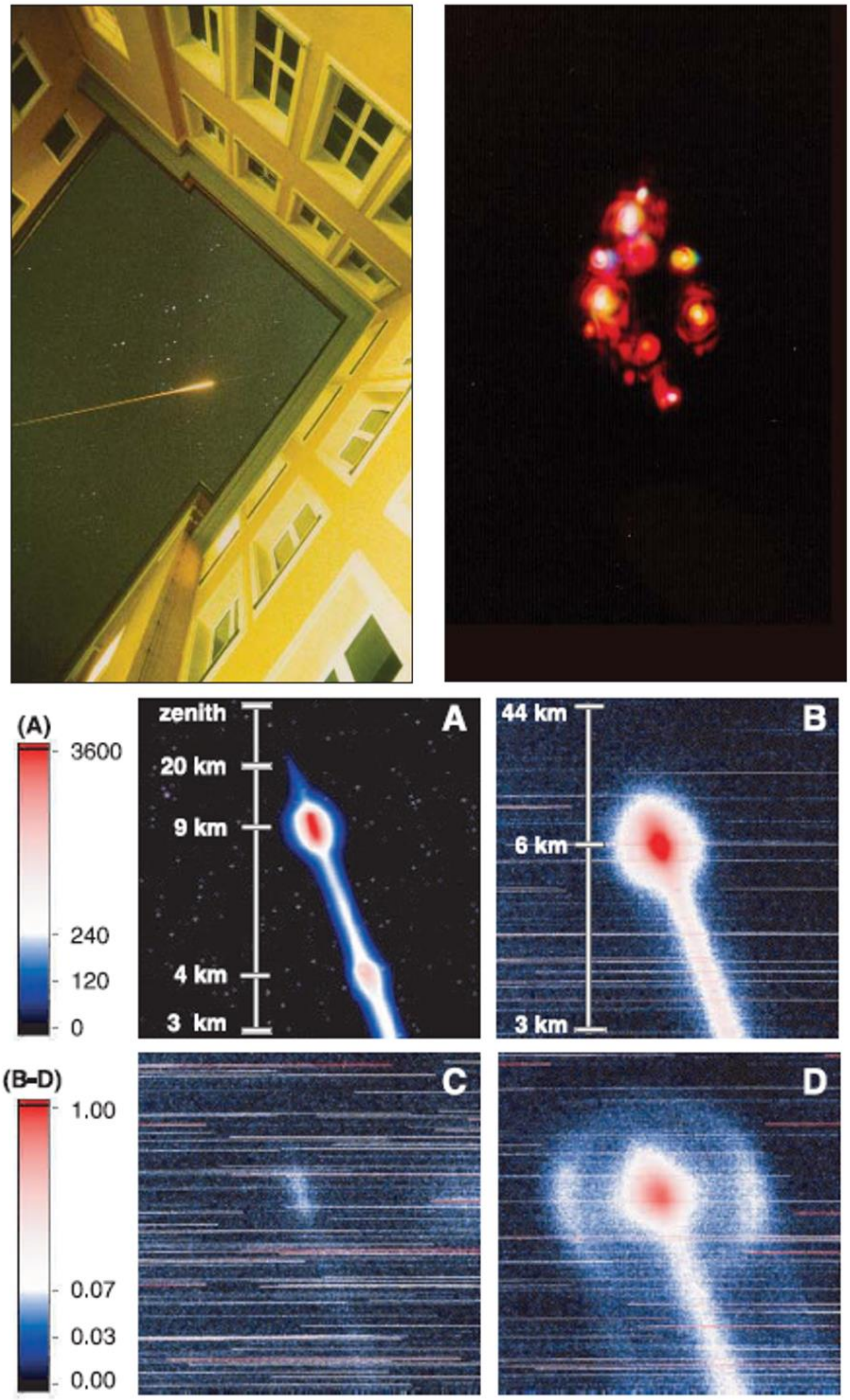

Figure 1.4: (top left) Filaments generated in atmosphere by propagating the terawatt laser into the sky; (top right) Multiple filament spots formed when observing the cross section of the beam after propagation [40]. White light filaments formed in air [62].

We have used both optical and non-optical characterization techniques to define and classify the various filaments generated according to the filament intensity, plasma density and spatial extent. The optical emissions from the interactions of intense femtosecond pulses with gaseous media and the mechanisms of emission have been vastly studied where these emissions in a controlled lab environment help one to characterize the intensity of the filament [63]. The non-optical methods include sonographic characterization of filaments. Using a holistic understanding of filaments generated under different input conditions (Polarization, power, focusing geometry, aberrations induced by the focusing optics, etc.), the emissions from a femtosecond filament such as the Supercontinuum, Third harmonic generation (THG), Radio frequency and acoustic emissions were studied and correlated. The thesis was largely aimed at the viability of filamentation for remote sensing and directed energy applications.

The thesis starts with a brief description of the underlying mechanisms of filamentation and the nonlinear processes associated with it. We then move on to discuss various characterization techniques (both optical and non-optical) and the instrumentation that were employed. The characterization was then applied to study filament behaviour under varying focusing element induced aberrations so that one can further identify other spatial-temporal distortions that influence filamentation [47]. Apart from the Supercontinuum that was generated from the filament, we also found the existence of coherent UV emission via the third harmonic generation of the fundamental frequency of the input laser. This UV emission was characterized by varying the input pulse characteristics such as power, polarization, chirp as well as focusing conditions [64]. The characteristic acoustic emission from the filaments was also found to have significant modulations when acoustic profiling of the filaments was done. These acoustic emissions were found to be an efficient tool in characterizing weak filaments which can otherwise be challenging to be characterized by optical techniques alone [60]. We have also demonstrated and reported the Radio frequency emissions from filaments which once characterized can provide remotely generated electromagnetic pulses and imaging techniques [62]. The thesis concludes by describing the future scope of filamentation in gaseous media and insightful experiments which need to be performed to further our understanding of intense laser matter interaction and advance the immeasurable application potential of femtosecond filamentation.

1.6 Organisation of the thesis

The generation, characterization and applications of femtosecond filamentation studied from different approaches is discussed. These characteristics were used to control and enhance the understanding into filament-matter interaction. The organization of the thesis is given below:

Chapter 1: Introduction

This chapter discusses the mechanism of filamentation in detail. Starting from the Maxwell's electromagnetic wave propagation equation, we explain the non-linear light-medium interaction of Gaussian light pulses in the femtosecond time scale up to peak powers of gigawatt. Evolution of filamentation studies such as critical power and estimation of self-focusing distance from CW to fs pulses was discussed. We then go on to discuss the non-linear processes that come about during highly intense regime of filamentation. We then discuss the motivation behind this thesis work and then go on to present the organization of the thesis.

Chapter 2: Details of experiment and calculations implemented

Femtosecond pulses were generated using a Ti: sapphire laser system (Libra, 4 W(max), M/s Coherent Co.) delivering ~ 50 fs at the repetition rate of 1 kHz and excitation wavelength centered at 800 nm. Different parts of the laser that helped us to generate and tailor the fs pulses are described in detail in this chapter. A single shot autocorrelator having a BBO crystal was used to produce the pulse intensity profile from which we estimate the pulse duration. Various diagnostic tools in the optical domain, acoustic domain and RF domain are presented. The optical emissions from the filament were collected using three different spectrometers according to the emission characteristics:

1) Kymera 328i spectrograph with an intensified 2D sCMOS detector (ISTARsCMOS-18U- E3, M/s. ANDOR) with a minimum gate width of 2ns.

2) Echelle spectrograph covers the spectral region of 220 – 880 nm with a resolution of 0.1 nm at 500 nm and is coupled to an ICCD (i-star DH334T-18U-E3, M/s. ANDOR) with a minimum gate width of 2ns;

3) USB-CCD spectrometer covering over 200 – 1100 nm (M/s. Ocean optics Maya)

The intensity of the filament and its electron density were estimated from the filament induced breakdown spectral (FIBS) emissions in the optical domain.

For the longitudinal imaging of the filaments we have used, 1) CCD cameras for smaller filaments, (SP620U, and Point grey GRAS20 from M/s. Ophir) and 2) a DSLR Nikon t4i camera for longer filaments.

Another challenge is to understand the longitudinal distribution of E-filed along the propagation of filament. To this effect we used an invasive technique, wherein the damage caused on the surface of a bulk Al plate is studied to estimate the longitudinal evolution of the E-field associated with a filament.

We have also analysed the acoustic emissions using calibrated microphone which has a frequency response over 20 Hz to 140 kHz (GRAS 40DP, sensitivity of 1 mV/Pa) and a dynamic range of 174 dB (re 20 μPa). The RF emissions were studied using co-axial antennas and RH-799 broadband Diamond antenna covering a broad spectral range from kHz to 2 GHz.

Chapter 3: Spectral Anatomy of fs filament and the associated super continuum emission: Effect of focusing optics and their aberrations

This chapter presents experimental results aimed at studying the effect of aberrations due to the focusing optics on laser filamentation in air and filamentation-assisted supercontinuum emission (SCE). The properties that were used to classify the filaments were intensity, electron density, spatial extent and supercontinuum generation. The studies were performed under four different configurations.

The existing literature shows that the focusing geometry and input power of the femtosecond pulses are most crucial to filament evolution. In the first configuration, we tried to establish the foundation of this thesis, by focusing fs pulses using different focusing conditions. We therefore classified the lenses firstly according to tight focusing and loose focusing regime of filamentation for the powers used in the experiments. The use of a combination of lenses to generate filamentation was also explored. Using two lenses f_1=-10cm, and f_2=15cm, we achieved the same effective focal length as that of a single lens.

In the second configuration, the effect of different focusing elements such as off-axis parabolic mirror (OAPM), Achromatic Doublet (AD), Plano-convex lens (PCX), Thin PCX, bi-convex lens (BCX) of same focal length on the filament and SCE were studied. The numerical aperture of the focusing optics was kept constant for all the optical elements to attribute difference in the filament properties to the optical element induced aberrations alone. The aberrations considered were Chromatic aberration, spherical aberration, first and second order dispersion [47].

In the third configuration, the filament behaviour was investigated under varying input pulse chirp. Chirping the input pulse not only broadens the pulse therefore reducing the peak power but also induces a quadratic phase with increasing or decreasing frequency according to the sign of chirp to the frequency distribution of the input pulse.

Apart from the above three modifications, asymmetry induced due to lens tilt also was found to drastically alter filament behaviour as we observe elongation of the filament, suppression of the supercontinuum generation and intensity.

Chapter 4: Filamentation Nonlinear Optics: Third Harmonic Generation from fs filamentation in air

The highly intense regime of filamentation is an outcome of non-linear perturbation of light-matter interaction, in which case we see the role of higher order terms in the material polarization leading to the generation of higher harmonics of fundamental frequency [36, 37, 64-69]. In the intensity regime of filamentation we induce higher order nonlinearity in the material response to electric field up to the third order nonlinearity.

The experiments were done to understand the process of THG from filamentation and methods to enhance its generation efficiency for sensing applications. We have therefore made a robust setup to systematically analyse the THG variations under two different focusing conditions which we have classified as loose and tight focusing. The THG was significantly modulated with input pulse properties (power, polarization, chirp, focal geometry and lens tilt). As the supercontinuum emission is also due to the third order nonlinearity, the third harmonic and supercontinuum emission were compared for the same input pulse variations [70].

The THG from filamentation can form the basis for a remote generated UV source which can be used as an efficient excitation tool for detection of many organic molecules, inorganic molecules, bio-aerosols etc, that absorb in the UV and fluoresce in the visible region.

In our demonstration, we have shown that by modulating the THG we can generate UV using an IR laser in a stand-off region of interest, this will provide a highly efficient tool to detect far off aerosol and atmospheric contents [30]. Thus filament induced THG overcomes the drawbacks faced by UV lasers and other light sources for remote sensing applications that get absorbed by atmospheric air.

Chapter 5: Evaluation of filament induced Acoustic emissions in air

In addition to the optical emissions and the THG, the plasma generated during the filamentation process generates shockwaves or acoustic waves into the ambient atmospheric air because of the creation of a steep temperature gradient between the filament region and surrounding ambient air. By varying the input power and the focusing geometry, filaments of different intensity can be generated and in turn acoustic waves of varying intensities. The analysis of the acoustic pulse profile and arrival time also shines more light on the filamentation dynamics. The arrival times are an additional indicator of free electron density in the filament [60, 69].

Chapter 6: Filament Induced eLectro Magnetic (FIeLM) emissions: L-band RF emissions from fs laser filaments

Electromagnetic emissions in the radio frequency range (~kHz-GHz) observed during laser matter interaction crudely said, is due to the movement of bulk charged particles or plasma (Cherenkov radiation). Discoveries such as that by Dahlbacka and Pearlman who reported RF emissions from laser plasma have suggested the use of laser generated RF as a viable RF source [71, 72]. Applying this, one can remotely generate radio sources which can penetrate the ground and be used as laser ground penetrating RADAR (LGPR) [40]. We have demonstrated RF emission from filaments generated using fs pulses in air. This work was done also to test the possibility of using acombination femtosecond pulse and nanosecond pulse for remotely generated RF sources [73].

Chapter 7: Application of fs filaments

The femtosecond laser pulse filamentation owing to the capability of longer propagation distances of up to few kms has become an extremely viable tool for remote sensing of far off atmospheric/gaseous regions. One of the major advantages of fs filamentation-matter interaction is the availability of residual fs pulses even after few km long propagation. However, the highly dynamic nature of filamentation brings about many challenges such as isolation and collection of the variety of emissions arising from the residual fs pulse and the filament induced plasma. To address this, FIBS as well as Two-photon fluorescence studies were performed with the aim of remote sensing of aerosol clouds.

Longitudinal E-field distribution in the filament is difficult to characterize due to the high intensity in the filament. To this effect the damage caused on the surface of Al is studied. The drilling time of the filament of an Al foil was found by collecting the front and back scattered signal from two different photodiodes. The studies were extended to the composite materials where the surface modification was studied by generating different filaments under different focusing conditions and placing the material at different positions along the filament and analysing the damage/breakdown of the materials [74].

A proof of concept study of Filament induced acoustic spectrosopy (FIAS) is performed using different concentrations of Tryptophan aerosol clouds. The temporal profile and frequency distribution of the acoustic pulse show significant variation with change in concentration of tryptophan particles in aerosol.

Chapter 8: Conclusions and future scope

This chapter summarizes the highlights of the work presented in the thesis and indicates the roadmap on taking the lab results to the field. Our demonstration of a remotely generated UV source from the third harmonic emission also can be tested on the field to detect organic species. The SCE from filaments is an excellent source for probing and imaging the spatio-temporal evolution of organic molecules, by enabling us temporal resolutions of a few fs over a large range of frequencies. Femtosecond pulses also being highly beneficial for probing fast processes which cannot be resolved using electronic instrumentation, increasing the resolution by at least 3 orders. Spatio-Temporal Evolution of Wavepackets (STEW) and transient event imaging of many underlying principles in materials science, chemistry, and biology can greatly aid our understanding of nature. These events require ultra-high temporal resolutions while doing real-time imaging. Pump-probe ultrafast imaging techniques require the scene to be repeatable. Therefore single-shot ultrafast imaging techniques have been developed to image non-repeatable transient events [76]. Other far reaching applications of filamentation which can be incorporated in our lab environment are discussed.

Filamentation is finding applications in multiple fields and the study of filamentation dynamics further provides us with a clear understanding of intense femtosecond pulse propagation and medium interaction. This thesis aims to create a holistic understanding of filament behaviour and the corresponding emissions to establish the foundation to apply and control femtosecond filamentation for remote sensing and directed energy applications.

References

1. T.H. Maiman, *Stimulated Optical radiation in Ruby*, Nature, **187**, 493-494 (1960).
2. *Celebrating 60 years of laser*, Commun Phys, **3**, 96 (2020).
3. W. Sibbett, A. A. Lagatsky, and C. T. A. Brown, *The development and application of femtosecond laser systems*, Opt. Exp **20**, 6989-7001 (2012).
4. Luc G. Legres, Christophe Chamot, Mariana Varna and Anne Janin, *The Laser Technology: New Trends in Biology and Medicine*, J. Mod Phys **5**, 267-279 (2014).
5. M. Toyoshima et al., *Ground-to-satellite laser communication experiments,* in IEEE Aerospace and Electronic Systems Magazine **23(8)**, 10-18 (2008).
6. R. Martínez Vázquez, G. Trotta, A. Volpe, G. Bernava, V. Basile, M. Paturzo, P. Ferraro, A. Ancona, I. Fassi, and R. Osellame, *Rapid Prototyping of Plastic Lab-on-a-Chip by Femtosecond Laser Micromachining and Removable Insert Microinjection Molding*, Micromachines, **8(11)**, 328 (2017).
7. X. Liu, D. Du and G. Mourou, *Laser ablation and micromachining with ultrashort laser pulses*, IEEE J. Quantum Electronics, **33(10)**, 1706-1716 (1997).
8. Jerome Lapointe, Yannick Ledemi, Sébastien Loranger, Victor Lambin Iezzi, Elton Soares de Lima Filho, Francois Parent, Steeve Morency, Younes Messaddeq, and Raman Kashyap, *Fabrication of ultrafast laser written low-loss waveguides in flexible As2S3 chalcogenide glass tape*, Opt. Lett. **41**, 203-206 (2016).
9. Kamil Stelmaszczyk and Philipp Rohwetter, *Long-distance remote laser-induced breakdown spectroscopy using filamentation in air*, Appl. Phys. Lett. 85, 3977 (2004).
10. R. Berera, R. Van Grondelle, and J. T. M. Kennis, *Ultrafast transient absorption spectroscopy: principles and application to photosynthetic systems*, Photosynth Res, **101**, 105–118 (2009).
11. A. Abramovici, W. E. Althouse, R. W. P. Drever, Y. Gürsel, S. Kawamura, F. J. Raab, D. Shoemaker, L. Sievers, R. E. Spero, K. S. Thorne, R. E. Vogt, R. Weiss, S. E. Whitcomb and M. E. Zucker, *LIGO: The laser interferometer gravitational-wave observatory*, Science, **256(5055)**, 325-333 (1992).
12. S. Ameer-Beg, W. Perrie, S. Rathbone, J. Wright, W. Weaver, and H. Champoux, *Femtosecond laser microstructuring of materials*, App. surface science **127**, 875-880 (1998).
13. W. J. Whitman, *The CO_2 laser*, Springer **53** (2013).
14. H. Wille, M. Rodríguez, J. Kasparian, D. Mondelain, J. Yu, A. Mysyrowicz, R. Sauerbrey, J-P. Wolf, and L. Woeste, *Teramobile: a mobile femtosecond-terawatt laser and detection system*, The European Physical Journal Applied Physics, **20(3),** 183-190 (2002).
15. M. Deubel, G. Freymann, M. Wegener, S. Pereira, K. Busch and C. M. Soukoulis, *Direct laser writing of three-dimensional photonic-crystal templates for telecommunications*, Nature Materials, **3**, 444–447 (2004).
16. G. Méjean, J. Kasparian, J. Yu, S. Frey, E. Salmon, and J-P. Wolf, *Remote detection and identification of biological aerosols using a femtosecond terawatt lidar system*, App. Phys. B, **78(5)**, 535-537 (2004).
17. Feng Liu, K. M. Yoo, and R. R. Alfano*, Ultrafast laser-pulse transmission and imaging through biological tissues*, Appl. Opt. **32**, 554-558 (1993).
18. T. J. Bridges and P. K. Cheo, P, *Spontaneous Self-Pulsing and Cavity Dumping in a Co2 Laser with Electro-Optic Q-Switching*, App. Phys. Letters, **14**, 262-264 (1969).

19. D. Maydan and R.B. Chesler, *Q-Switching and Cavity Dumping of Nd: Yalg Lasers*. J. App. Phys, **42,** 1031-1034 (1971).
20. A. Weiner, *Ultrafast Optics*, John Wiley & Sons, **72** (2011).
21. M. E. Fermann, A. Galvanauskas and G. Sucha (eds.), *Ultrafast lasers: technology and applications*, CRC Press, **80** (2002).
22. D. Strickland and G. Mourou, *Compression of amplified chirped optical pulses,* Optics Communications, **55(6)**, 447-449 (1985).
23. K. König, A. Ehlers, F. Stracke, and I. Riemann, *In vivo drug screening in human skin using femtosecond laser multiphoton tomography*, Skin Pharmacol Physiol, **19(2)**, 78-88 (2006).
24. N. Granzow, *Supercontinuum white light lasers: a review on technology and applications*, Photonics and Education in Measurement Science 2019, **11144**, 1114408 (2019).
25. M. D. Perry, D. Pennington, B. C. Stuart, G. Tietbohl, J. A. Britten, C. Brown, S. Herman, B. Golick, M. Kartz, J. Miller, H. T. Powell, M. Vergino, and V. Yanovsky, *Petawatt laser pulses*, Opt. Lett. **24**, 160-162 (1999).
26. X. Zeng, K. Zhou, Y. Zuo, Q. Zhu, J. Su, X. Wang, X. Wang, X. Huang, X. Jiang, D. Jiang, Yi Guo, N. Xie, S. Zhou, Z. Wu, J. Mu, H. Peng and F. Jing, *Multi-petawatt laser facility fully based on optical parametric chirped-pulse amplification,* Opt. Lett. **42**, 2014-2017 (2017).
27. J. Faure, Y. Glinec, A. Pukhov, S. Kiselev, S. Gordienko, E. Lefebvre, J-P. Rousseau, F. Burgy, and V. Malka, *A laser–plasma accelerator producing monoenergetic electron beams*, Nature **431(7008)**, 541-544 (2004).
28. J. J. Macklin, J. D. Kmetec, and C. L. Gordon III, *High-order harmonic generation using intense femtosecond pulses*, Phys. Rev. Letters **70(6)**, 766 (1993).
29. G. A. Mourou and V. Yanovsky, *Relativistic Optics: A Gateway to Attosecond Physics*, Optics & Photonics News, **15(5)**, 40-45 (2004)
30. S. T.Cundiff, and J. Ye, *Colloquium: Femtosecond optical frequency combs*, Rev. Mod. Phys.,**75(1)**, 325 (2003).
31. A. H. Zewail, *Femtochemistry: Atomic-scale dynamics of the chemical bond*, J. Phys Chem A, **104(24)**, 5660-5694 (2000).
32. R. Berera, R. Grondelle, and J. T. M. Kennis, *Ultrafast transient absorption spectroscopy: principles and application to photosynthetic systems*, Photosynth Res, **101**, 105–118 (2009).
33. H.L. Xu and S.L. Chin, *Femtosecond Laser Filamentation for Atmospheric Sensing*, Sensors, **11,** 32-53 (2011).
34. P. Agostini and L. F DiMauro, *The physics of attosecond light pulses*, Rep. Prog. Phys. **67**, 813 (2004).
35. A. Couairon, E. Brambilla, T. Corti, D. Majus, O. de J. Ramírez-Góngora, and Miroslav Kolesik, *Practitioner's guide to laser pulse propagation models and simulation*, Eur. Phys. J. Spec. Top. **199**, 5–76 (2011)
36. R. W. Boyd, *Nonlinear Optics*, Elsevier (2003).
37. S. L. Chin, *Femtosecond laser filamentation*, Elsevier (2009).
38. Y. R. Shen, *Self-focusing: Past and present*, Springer (2003).
39. A. Braun, *Self-channelling of high-peak-power femtosecond laser pulses in air*, Opt. Letters **20**, 73-75 (1995).
40. A. L. Gaeta, *Collapsing Light Really Shines*, Science **301**, 54 (2003).
41. A. Couairon and A. Mysrowicz, *Femtosecond filamentation in transparent media*, Phys. Rep. **441**, 47–189 (2007).
42. L Chin and H. Xu, *Tunnel ionization, population trapping, filamentation and applications*, J. Phys. B:At. Mol. Opt. Phys. **49**, 222003, (2016).
43. P. Rohwetter, J. Kasparian, Stelmaszczyk, Z. Hao, S. Henin, N. Lascoux, W. M. Nakaema, Y. Petit, M. Queißer, R. Salamé, E. Salmon, L. Wöste and K. J– P. Wolf, *Laser-induced water condensation in air*. Nature Photon, **4**, 451–456 (2010).
44. N. Khan, N. Mariun, I. Aris and J Yeak, *Laser-triggered lightning discharge*, New J. Phys., **4** 61 (2002)
45. P. M. Paul, E. S. Toma, P. Breger, G. Mullot, F. Augé, P. Balcou, H. G. Muller and P. Agostini, *Observation of a train of attosecond pulses from high harmonic generation*, Science, **292**, 1689 (2001)

46. R. Junjuri, S. A. Nalam, S. S. Harsha, P. P. Kiran and G. M. Kumar, *Spatio-temporal characterization of ablative Cu plasma produced by femtosecond Filaments,* Opt. Express 29, 10395-10405 (2021).
47. S. A. Nalam, S. Sree Harsha and P. P. Kiran, *Effect of Focusing element induced aberrations on filamentation and supercontinuum emission in ambient air,* Opt. Express 29, 14668-14681 (2021).
48. C. D'Amico, A. Houard, M. Franco, B. Prade, A. Mysyrowicz, A. Couairon, and V. T. Tikhonchuk, *Conical Forward THz Emission from Femtosecond-Laser-Beam Filamentation in Air,* Phys. Rev. Lett. **98**, 235002 (2007).
49. B. Forestier, A. Houard, M. Durand, Y.-B. André, B. Prade, J-Y. Dauvignac, F. Perret, C. Pichot, M. Pellet, A. Mysyrowicz, *Radiofrequency conical emission from femtosecond filaments in air*. Appl. Phys. Letters, **96 (14)**, 141111-141113, (2010).
50. L. Vinoth Kumar, E. Manikanta, Ch. Leela, and P. Prem Kiran, *Effect of laser intensity on radio frequency emissions from laser induced breakdown of atmospheric air*, J. Appl. Phys, **119**, 214904 (2016).
51. M. Richardson, M. Baudelet and T. Seiderman, *Fundamentals of filament interaction*, AFOSR/JTO MRI Annual Report (2016).
52. H. Kumagai, S-H. Cho, K. Ishikawa, K. Midorikawa, M. Fujimoto, S-I. Aoshima, and Y. Tsuchiya, *Observation of the complex propagation of a femtosecond laser pulse in a dispersive transparent bulk material*, J. Opt. Soc. Am. B **20**, 597-602 (2003).
53. S. Minardi, A. Gopal, A. Couairon, G. Tamoašuskas, R. Piskarskas, A. Dubietis, and P. Di Trapani, *Accurate retrieval of pulse-splitting dynamics of a femtosecond filament in water by time-resolved shadowgraphy*, Opt. Lett., **34**, 3020-3022 (2009)
54. S. Minardi, A. Gopal, M. Tatarakis, A. Couairon, G. Tamošauskas, R. Piskarskas, A. Dubietis, and P. D. Trapani, *Time-resolved refractive index and absorption mapping of light-plasma filaments in water*, Opt. Lett. **33**, 86-88 (2008).
55. D. G. Papazoglou and S. Tzortzakis, *In-line holography for the characterization of ultrafast laser filamentation in transparent media*, Appl. Phys. Lett., **93**, 041120 (2008).
56. M. Centurion, Y. Pu, and D. Psaltis, *Holographic capture of femtosecond pulse propagation*, J. Appl. Phys., **100**, 063104 (2006).
57. S. A. Hosseini, Q. Luo, B. Ferland,W. Liu, N. Ak¨ozbek, G. Roy, and S. L. Chin, *Long-range third-harmonic generation in air using ultrashort intense laser pulses*, Appl. Phys. B, **77**, 697 (2003).
58. A. Couairon, G. Méchain, S. Tzortzakis, M. Franco, B. Lamouroux, B. Prade, A. Mysyrowicz, *Propagation of twin laser pulses in air and concatenation of plasma strings produced by femtosecond infrared filaments, Optics Communications*, **225 (1–3)**, 177-192 (2003).
59. J. Yu, D. Mondelain, J. Kasparian, E. Salmon, S. Geffroy, C. Favre, V. Boutou, and J.–P. Wolf, *Sonographic probing of laser filaments in air*, Appl. Opt. 42, 7117-7120 (2003)
60. S. A. Nalam, E. Manikanta, S. S. Harsha and P. P. Kiran, *Acoustic measurements on femtosecond laser induced filaments*, In: Singh K., Gupta A.K., Khare S., Dixit N., Pant K. (eds) ICOL-2019. Springer Proceedings in Physics, vol 258. Springer, Singapore. https://doi.org/10.1007/978-981-15-9259-1_93.
61. S. Eisenmann, A. Pukhov, and A. Zigler, *Fine Structure of a Laser-Plasma Filament in Air*, Phys. Rev. Lett., **98**, 155002 (2007).
62. J. Kasparian, M. Rodríguez, G. Méjean, J. Yu, E. Salmon, H. Wille, R. Bourayou, S. Frey, Y. B. Andre, A. Mysyrowicz, R. Sauerbrey, J. P. Wolf and L Wöste, *White-light filaments for atmospheric analysis*, Science, **301(5629)** 61-64 (2003).
63. S. Xu, X. Sun, B. Zeng, W. Chu, J. Zhao, W. Liu, Y. Cheng, Z. Xu, and S. L. Chin, *Simple method of measuring laser peak intensity inside femtosecond laser filament in air*, Opt. Express, **20**, 299-307 (2012).
64. S. A. Nalam, S. S. Harsha and P. P. Kiran, *A method for tailoring of ultrashort infrared laser pulses for precise generation and control of an ultraviolet source for spectroscopic sensing* Patent Applied (Dec 2020)
65. S. Suntsov, D. Abdollahpour, D. G. Papazoglou, and S. Tzortzakis, *Efficient third-harmonic generation through tailored IR femtosecond laser pulse filamentation in air*, Opt. Express, **17**, 3190 (2009).
66. S. Suntsov, D. Abdollahpour, D. G. Papazoglou, and S. Tzortzakis, *Filamentation produced third harmonic in air via plasma enhanced third-order susceptibility*, Phys. Rev. A **81**, 033817 (2010).

67. N. Aközbek, A. Iwasaki, A. Becker, M. Scalora, S. L. Chin, and C. M. Bowden, *Third-Harmonic Generation and Self-Channeling in Air Using High-Power Femtosecond Laser Pulses*, Phys. Rev. Lett. **89**, 143901, (2002).
68. N. Aközbek, A. Becker, M. Scalora, S. L. Chin, and C. M. Bowden, *Continuum generation of the third-harmonic pulse generated by an intense femtosecond IR laser pulse in air*. Appl Phys B, **77**, 177–183 (2003).
69. J. A. Bittencourt, *Fundamentals of Plasma Physics*, Springer (2004)
70. S. A. Nalam, S. S. Harsha and P. Prem Kiran, *Influence of chirp and polarization on the third harmonic and supercontinuum generation dynamics during fs filamentation in air*, OSA Laser Congress, 13 – 16 October (2020).
71. J. S. Pearlman and G. H. Dahlbacka, *Emission of rf radiation from laser-produced plasmas*, J. Appl. Phys. **49**, 457 (1978).
72. H. Nakajima, Y. Shimada, T. Somekawa, M. Fujita and K. A. Tanaka, *Nondestructive Sensor Using Microwaves From Laser Plasma by Subnanosecond Laser Pulses*, IEEE Geoscience and Remote Sensing Letters, **6(4)**, 718-722 (2009).
73. S. Varma, J. Spicer, B. Brawley, J. A. Miragliotta, *Plasma enhancement of femtosecond laser-induced electromagnetic pulses at metal and dielectric surfaces*, Optical Engineering, **53(5)**, 051515 (2014).
74. Naveen. K. P., S. A. Nalam, G. M. Kumar and P. P. Kiran, *Filament Induced Surface Modification of Composite Material*, 2017 IEEE Workshop on Recent Advances in Photonics (WRAP), Hyderabad, India, (2017).
75. S. Yeola, D. Kuk, and K-Y. Kim, *Single-shot ultrafast imaging via spatiotemporal division of femtosecond laser pulses*, J. Opt. Soc. Am. B 35, 2822-2827 (2018).
76. D. Patel, D. Jang, S. W. Hancock, H. M. Milchberg, and K-Y. Kim, *Simplified single-shot supercontinuum spectral interferometry*, Opt. Express **28**, 11023-11032 (2020).

This page was intentionally left blank

CHAPTER 2: Details of experiment and calculations implemented

Abstract:

Filaments generated from intense femtosecond pulses make invasive attempts of characterization futile, because of which we have used multiple techniques to characterize the filaments and correlated them. The femtosecond pulse was generated using an amplified Ti:Sapphire laser system which produces femtosecond pulses with peak power of the order of tens of gigawatts. The primary amplification technique used in this laser is the chirped pulse amplification which helps produce intense ultrashort pulses. The femtosecond pulse was characterized using a single shot autocorrelator and the variation in the pulse width and pulse profile with chirp (Positive or negative chirp was induced by varying grating separation in the output grating compressor). Filaments were first studied using spectroscopic techniques which help estimate the on axis intensity and electron density. Spectral studies were also done to study the filament interaction with aerosols and other solid materials. As this spectroscopic study requires different forms of spectral data acquistions we have used 3 different spectrometers for the experiments done according to the suitability. Spatial extents of the various filaments were recorded using different cameras according to the dimensions of the filament and resolution required. Filaments were also characterized using the acoustic emissions which were recorded using a microphone with a broad frequency response coupled to an oscilloscope with a bandwidth capable of resolving the acoustic signal oscillations. RF emissions from the filament were also studied and their enhancement was primarily studied using antennas coupled to a spectrum analyser or an oscilloscope.

2.1 Introduction

When the femtosecond pulse propagates in any medium, the input energy of the femtosecond pulse is distributed and dissipated between numerous absorption and nonlinear processes and inherent pulse energy is transformed into different forms of optical emissions (FIBS, SCG), terahertz emission, RF emissions and mechanical emissions (shockwaves and acoustic waves) [1]. The partition of energy between all of these mechanisms is partially understood. We intend to approach this study by studying the filament dynamics, in relation to the effect of change in input laser pulse properties on filamentation and then correlate these to the subsequent emission characteristics. Filamentation occurs at a time scale of femtoseconds during which the input pulse spectrum can change from tens of nanometres to a whole octave. The high intensity ionizes the medium of propagation creating a quasi-static plasma even in air whose characterization alone can provide ample information on filament propagation dynamics and associated electromagnetic emissions. The filament emissions correlated to the filament structure (obtained from imaging the filament) and the FIBS atomic emission spectrum acquired along the propagation of the filament can give us a holistic picture of the many mechanisms at play during intense femtosecond propagation. Other than optical emissions spanning from UV to IR, filamentation has also shown to generate mechanical waves or acoustic emissions. This is because of the steep temperature gradient that exists between the filament region and the ambient air. These acoustic emissions were studied using microphones and analysed according to the temporal profile, which also provides the frequency distribution of the acoustic pulse. Acoustic characterization show a close relation to the plasma characteristics of the filament like giving insight into multiple filamentation. Bulk movement of plasma in the filament generates electromagnetic pulses in the radio frequency range which were characterized using antennas coupled to a spectrum analyser. The coherent conical emissions like the supercontinuum generation and Third harmonic generation can be a viable spectroscopic source for probing remote regions and materials characterizations. Techniques for enhancement and modulation of these emissions were also studied and characterized.

In this chapter, the various experimental excitation sources, optical layouts and diagnostic tools used for generation and characterisation of filaments are briefly described. The spectroscopic techniques used to estimate filament intensity and electron density is also elaborated.

2.2 Amplified Ultrafast Ti: Sapphire laser system

We have used a class IV amplified Ti:Sapphire laser system, which operates at a central wavelength of 800nm and delivers femtosecond pulses of ~45fs pulse duration, and average power up to 4W (4mJ per pulse) at 1kHz repetition rate. The amplification of the modelocked fs pulse train is done using a regenerative amplifier using the chirped pulse amplification technique which provides intense femtosecond pulses [2]. The one box amplified laser system Coherent Libra optical bench consists of four individual modules (i) Coherent Vitesse seed laser (oscillator) (ii) Regenerative amplifier (iii) Coherent Evolution-25 pump laser (for regenerative amplification) and (iv) The compressor and stretcher modules [3]. Figure 2.1 shows the top view of the Libra optical bench. Ocean optics Maya 2000 spectrometer was used to measure the spectrum which shows a central wavelength of ~ 797 nm with a 25nm bandwidth. We have also characterized the pulse using a single shot autocorrelation which provides the temporal profile of the pulse using field autocorrelation. Further details will be given in the coming sections.

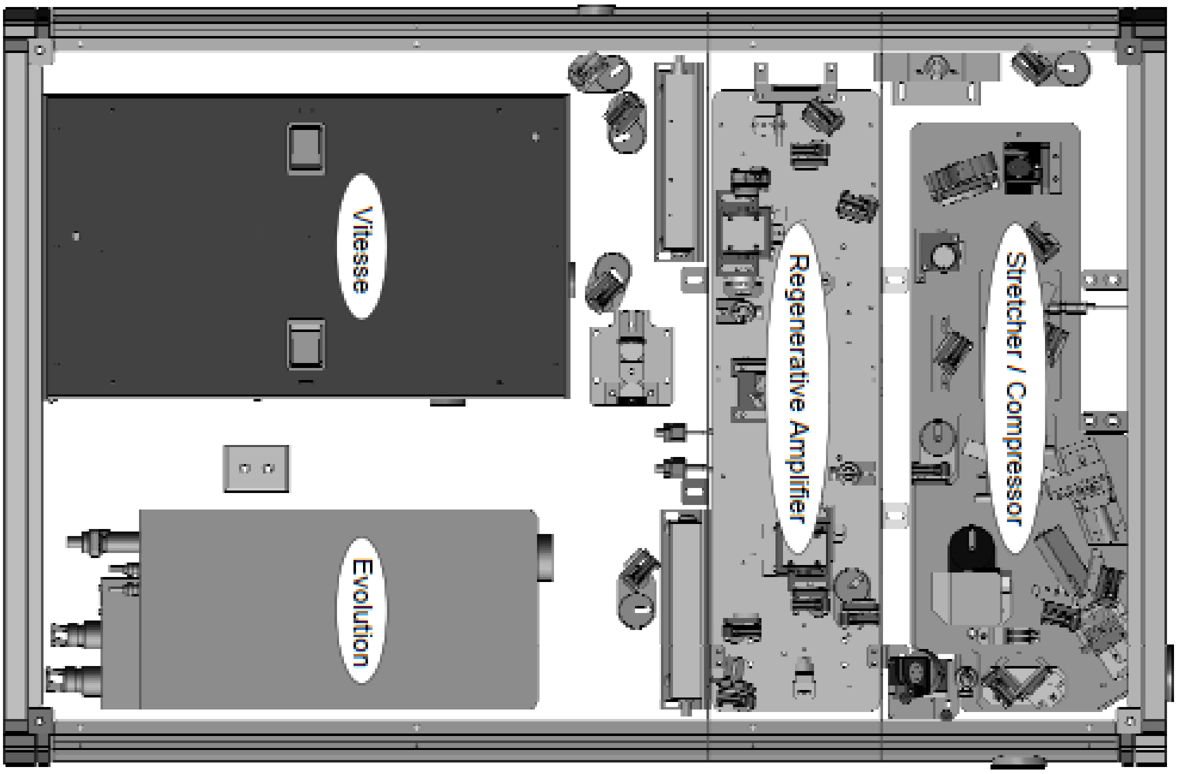

Figure 2.1: Top view of the layout of the Libra system.

The Vitesse laser is the seed laser used in the system. It is a compact Verdi (CW DPSS pump laser) pumped ultrafast laser which produces sub-100fs Gaussian pulses at an output average power of ~300mW at 80MHz repetition rate with a bandwidth of 30nm. The Vitesse laser comprises (1) A sealed Verdi laser head (2) Sealed Verdi pumped Ultrafast (VPUF) laser and (3) Power track mirror. To ensure most efficient performance the Verdi laser head and VPUF are sealed. Figure 2.2 shows the layout of the Vitesse laser.

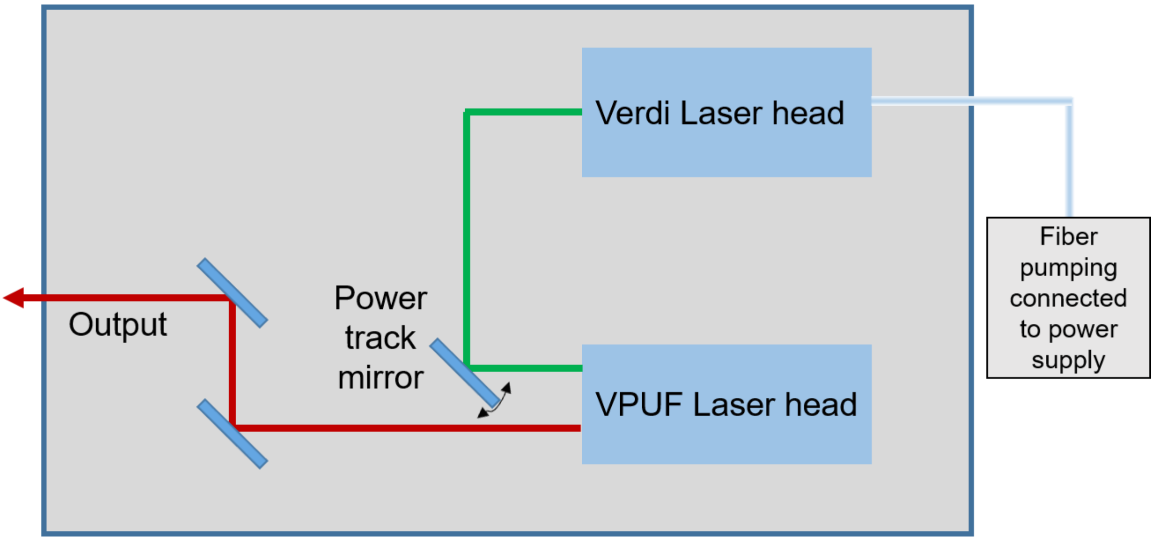

Figure 2.2: Layout of the Vitesse laser consisting of the Verdi laser and VPUF laser unit.

The Verdi laser pumps the VPUF to generate the ultrashort pulses. The active medium in the Verdi (Vanadate Nd:YVO_4) is first pumped using an array of diode lasers whose output at 808nm is carried to the Verdi laser head using an umbilical. The Verdi laser produces continuous laser light at 1064nm with and average power of 2W. The output from the Verdi laser head is frequency doubled to 532nm using a temperature tuned LBO (Lithium Triborate, LiB_3O_5) crystal and used to pump the VPUF by directing the Verdi Laser output using a piezo driven mirror. The VPUF consists of a Ti:Sapphire crystal and negative dispersion mirrors. Multiple reflections from the negative dispersion mirrors correct for dispersion and produce sub-100fs pulses. The cavity is passively mode-locked through Kerr-Lens mode locking whose initiation gets triggered by an automatic starter [4]. From this we get ultrashort pulses with low noise and a large bandwidth, having an average power of 300mW and repetition rate of 80MHz. The figure 2.3 shows the internal schematics of the Verdi and VPUF unit.

To pump the amplifier module the Evolution laser is used, with an active medium Nd:YLF (Nd:YLiF$_4$, yttrium lithium fluoride). It is pumped using AlGaAs (Aluminium Gallium Arsenide) laser diodes. The output is frequency doubled wavelength of 527nm with a 1kHz repetition rate. The thermal losses are reduced because of the narrow bandwidth of the diode lasers which also simultaneously allows efficient pumping with maximum light in the absorption band. Natural birefringence, long upper state life time (470 μs) and low thermal sensing enable Nd:YLF in achieving high powers. The pulse generation is through acousto-optic Q-switching [5-9]. An LBO crystal is used to frequency double the output by operating

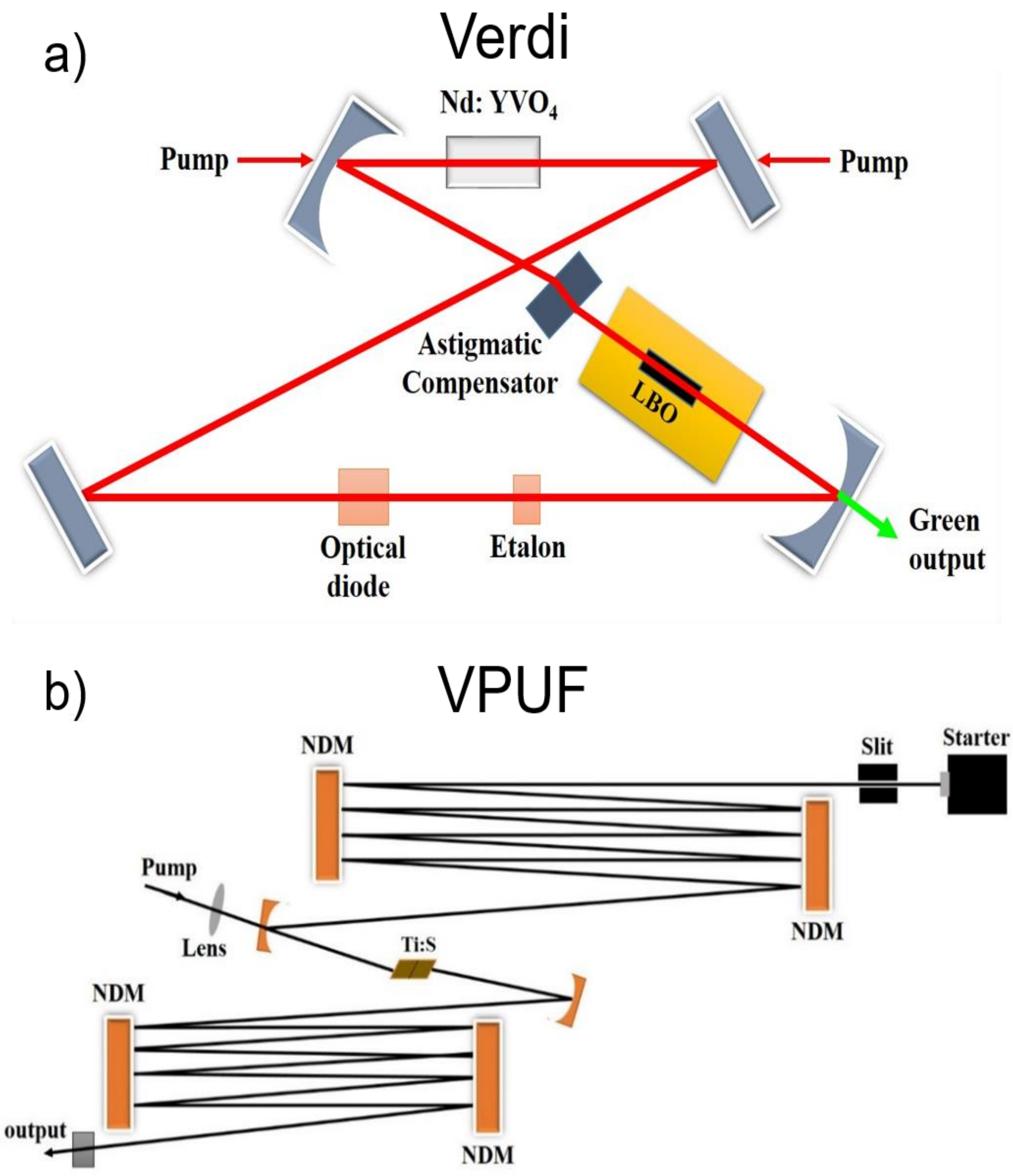

Figure 2.3: a) Schematic of the Verdi unit; b) Schematic of the VPUF unit.

at non-critical phase matching conditions. The LBO should therefore be maintained at a particular temperature to ensure optimal frequency doubling. Figure 2.4 shows the schematic along with the different components of the evolution laser.

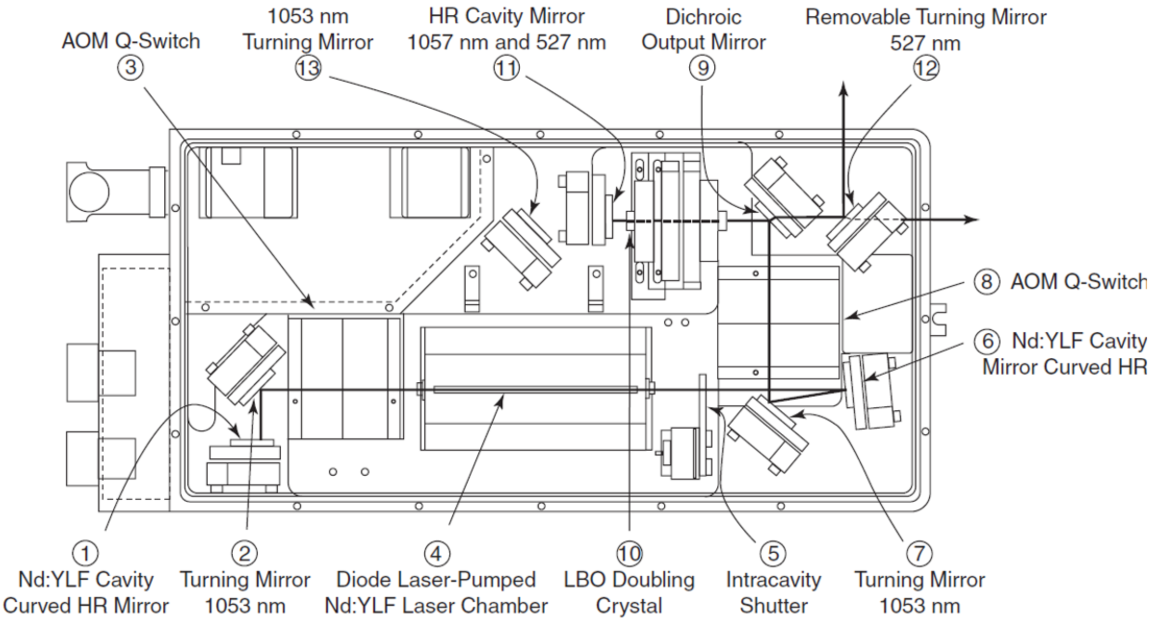

Figure 2.4: layout and components of the evolution laser.

The next component in the laser system is the Regenerative amplifier which is based on the Legend EliteTM platform (M/s Coherent, USA). It was designed to be compact and has an active cooling system of the enclosed module. The amplifier design provides excellent stability and has reduced susceptibility to environmental factors. The synchronization of the seed laser and the pump is done using the Pockels cells connected to Signal Delay generator (SDG) which is part of the amplifier system [9, 10]. The seed pulses are stretched before entering the amplifier and compressed after amplification using grating arrangements which stretch and compress the pulse according to the frequency components.

The maximum power a seed femtosecond pulse can be amplified up to is limited by the material threshold of the components being used in the amplification process, because of which we were not able to generate high power ultrashort lasers until the discovery of the Chirped Pulse Amplification (CPA) technique [11]. In this technique the pulse is 'stretched' using a grating pair, by inducing a quadratic phase to the frequency components of the pulse thereby chirping the pulse. The pulse now has a time duration og ~200ps. This pulse can easily be amplified to have powers high enough avoiding material breakdown when 'compressed' right before the exit of the laser using another grating pair called the compressor. The stretcher and compressor were integrated into a single box in the regenerative amplifier module [12-14]. Figure 2.5 shows the layout of the Regenerative amplifier and the stretcher-compressor module. Table 2.1 describes all the parts in the schematic.

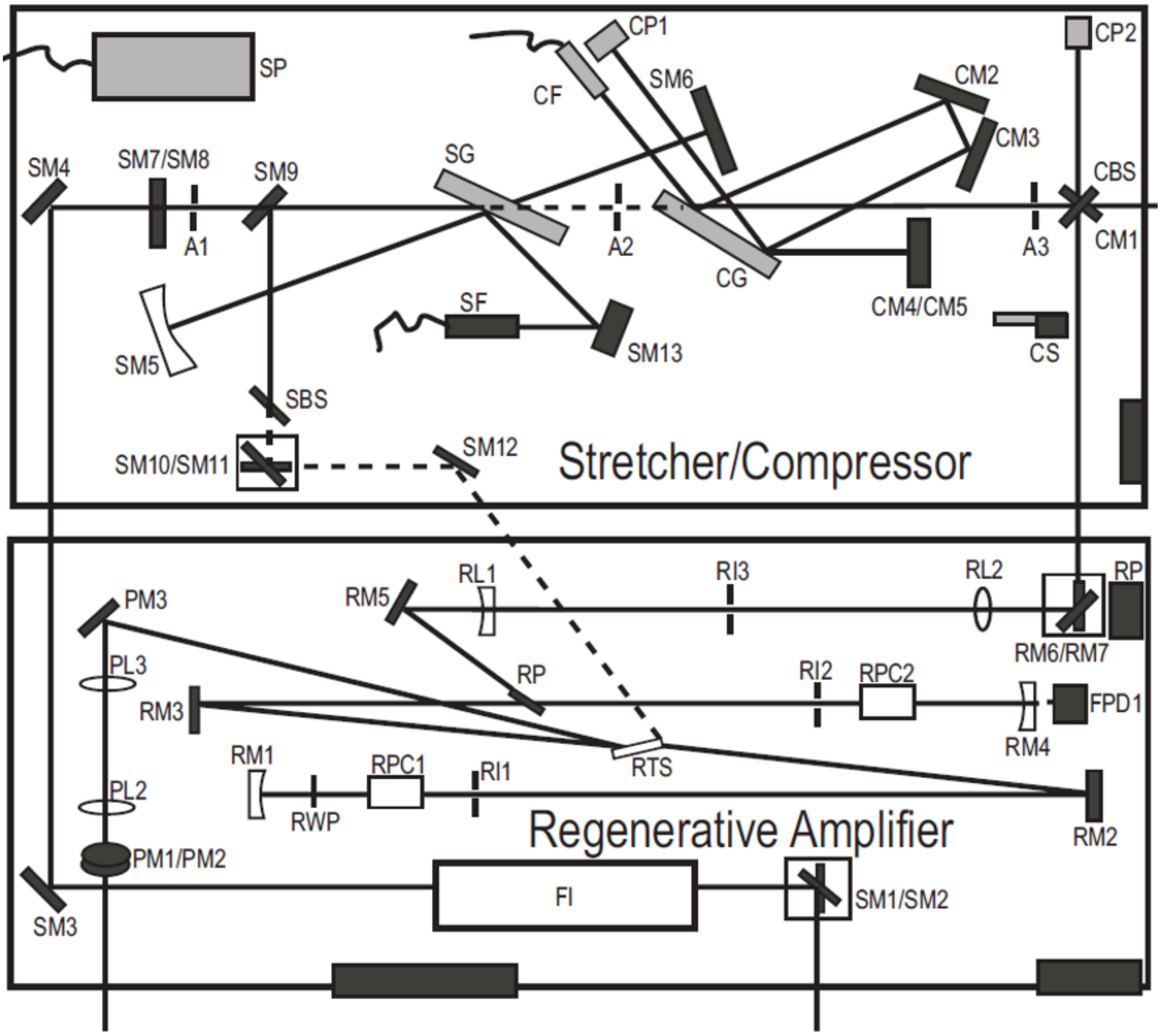

Figure 2.5: Layout of the Regenerative amplifier and stretcher/compressor of the laser amplifier. The components are given in detail in table 2.1.

Power modulation of the input pulse was done using a combination of a Half-wave plate and a polarizer. The half wave plate rotates the polarization direction of the input pulse by twice the angle between the input polarization direction and the optic axis. The polarizer which is set to give maximum transmission for the polarization direction at laser output separates the laser pulse after the half wave plate according to the angle between the polarizer axis and pulse polarization direction. This was found to efficiently and conveniently change the power of the input pulse. We have also used beam splitters to do power variation but found that it raises many alignment difficulties although there is negligible pulse alterations.

Table 2.1: components of the Amplifier system as shown in figure 2.5.

Compressor Optics	**Regen Optics**	**Stretcher Optics**
Compressor shutter (CS)	Regen Ti:Sapphire crystal (RTS)	Seed routing mirror (SM1-SM4)
Routing mirror (CM1)	Cavity end mirrors (RM1, RM4)	Faraday isolator (F1)
Compressor grating (CG)	Cavity folding mirrors (RM2, RM3)	Stretcher grating (SG)
Horizontal retro reflector (CM2/CM3)	Alignment iris (RI1-RI3)	Spherical gold mirror (SM5)
Vertical retro reflector (CM5/CM5)	Pockels cell (RPC1, RPC2)	Flat folding mirror (SM6)
Beamsplitter (CBS)	¼-wave plate (RWP)	Stretcher retro reflector (SM7/SM8)
Fiber optic input (CF)	Polarizer (RP)	Seed routing mirror (SM9-SM12)
Spectrometer (SP)	Regen routing mirrors (RM5-RM7)	2nd order routing mirror (SM13)
Alignment apertures (A1-A3)	Regen telescope lenses (RL1, RL2)	Fiber optic input (SF)
Pump beam optics (PM1-3)	Photodiodes (RP, FPD1,CP1, CP2)	Beamsplitter (SBS)

2.3 Single Shot Autocorrelator

Femtosecond pulses being one of the shortest events generated by man, pose the challenge of being difficult to characterize. The best response time that can be achieved using photodiodes is in the order of picoseconds. This led us to explore self-referencing of the pulses where the ultrashort pulse is used to measure itself. This is done by autocorrelation of the ultrashort pulses [15, 16]. There are two types of autocorrelation namely intensity autocorrelation and field autocorrelation. The intensity autocorrelation can be done using a Michaelson interferometer and the fourier transform of the output autocorrelation is the spectrum of the input pulse. This does not provide phase information, but only profile information. Whereas, field autocorrelation requires the use of a non-linear crystal like a second harmonic or third harmonic crystal and higher intensity in the pulse to facilitate second or third harmonic generation, but provides complete information of the pulse including spectral phase when the output autocorrelation is analysed in a spectrometer. We do an intensity autocorrelation on a second harmonic crystal in the Single Shot Autocorrelator. The SSA can be externally triggered and internally triggered at 100Hz. The advantage of the single shot autocorrelator is that the delay between the two identical pulses is induced while varying along the SHG crystal because of non-collinear interaction of the identical beams, providing an autocorrelation plot in a single shot. Spectral analysis of the intensity auto-correlated signal would provide information of the spectral phase. The schematic of the single shot autocorrelator is shown in the figure 2.6.

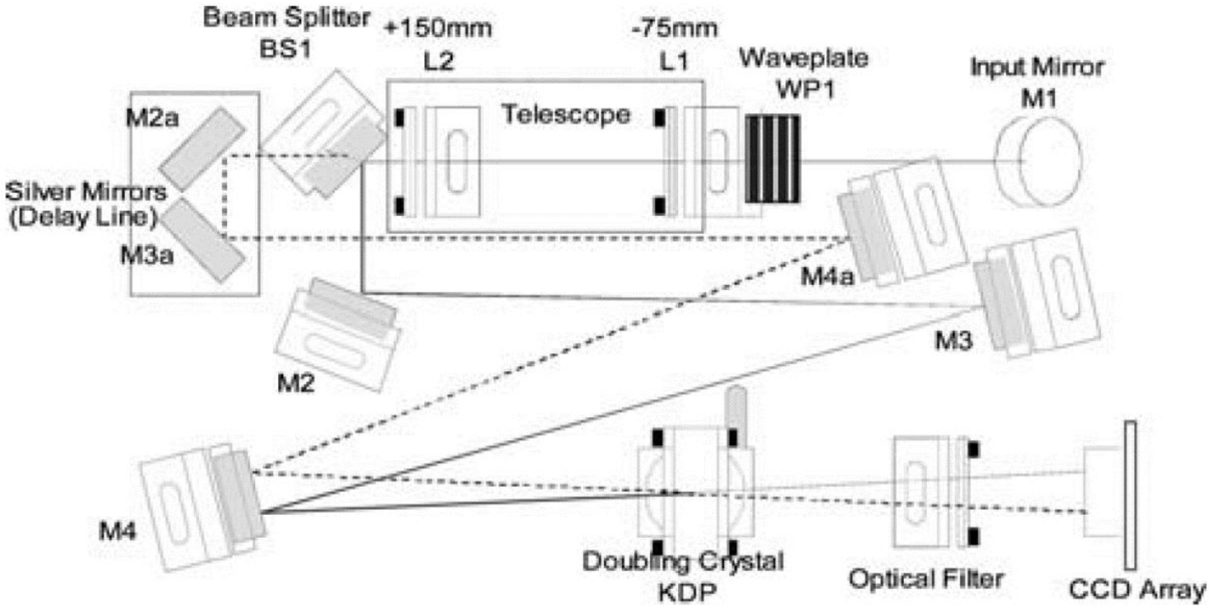

Figure 2.6: Optical design of the Single shot autocorrelator.

The sensor being used is a single array CCD whose output is connected to the oscilloscope, the autocorrelation signal is shown in the figure 2.7. As the CCD sensor is a single array sensor, the signal is sampled out from the end of the array in the form of a time signal. The sensor therefore gets refreshed every 10ms. The figure shows the autocorrelation signal induced by different delays induced by the delay stage. The autocorrelation plots are shown with change in the delay in micrometres. The baseline of this signal will be in the order of milliseconds, this needs to be calibrated into femtosecond scale by varying the delay between the identical beams, which causes a shift in the peak of the autocorrelation plot. Using this we can estimate the proportionality factor to translate the observed profile to the original autocorrelation profile in the femtosecond scale.

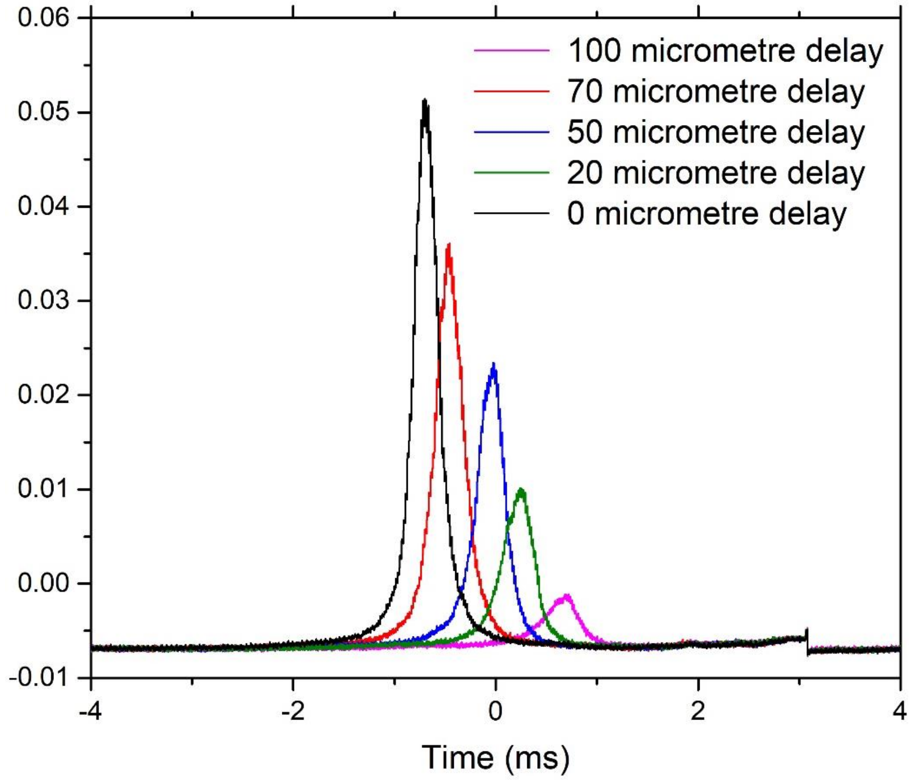

Figure 2.7: Autocorrelation plots for varying positions of the delay stage relative to the zero delay position.

The calculation of pulse duration from the autocorrelation plot is as below. Shift in the peak is taken as t_0 in ms, delay in stage movement is taken as x in mm, measured pulse duration from oscilloscope τ_0 in ms. Therefore, we can write,

$$Optical\ path\ length\ (mm) = 2x \tag{2.1}$$

$$Optical\ path\ delay\ induced\ (s) = \frac{2x}{3 \times 10^{12}} \tag{2.2}$$

$$Calibration\ to\ find\ proportionality\ constant\ (C)(s/ms) = \frac{\frac{2x}{3 \times 10^{12}}}{t_0(ms)} \tag{2.3}$$

$$Pulse\ duration\ (s) = \tau_0(ms) \times C \tag{2.4}$$

The true pulse duration is found by dividing the autocorrelated pulse duration by √2 for Gaussian pulses.We have therefore estimated the pulse duration of the transform limited pulse to be 60fs.

The fs regenerative amplifier comprises of a stretcher and compressor grating setup which helps us to stretch and compress the oscillator pulses pre and post amplification of the pulse using the CPA technique. Optimal separation between the compressor gratings provides us with a transform limited pulse, deviation from this separation induces chirp into the pulse due to GVD that is induced as a consequence of increase or decrease in grating separation. This separation is adjusted using a module provided with the laser. The module however does not give a quantized value of separation or chirp induced but increases or decreases the separation in quantized steps. We have therefore used the SSA to characterize the output pulse to estimate the chirp carried by the output pulse from the regenerative amplifier. SSA does not provide the sign of chirp but we can identify it by noting the direction of movement of the compressor gratings. Figure 2.8 show the different autocorrelation profiles from the SSA with steps of compressor grating separation. Pulse durations were estimated from the profiles and the chirp was estimated using the relation,

$$C = \sqrt{1 + \frac{\tau_0^2}{\tau_{in}^2}} \tag{2.5}$$

The Chirp was estimated and the figure 2.9 shows the induced chirp and pulse duration with compressor grating separation steps. This correlated information of the compressor steps to the induced chirp and pulse duration can now be exploited to study influence of pulse profile.

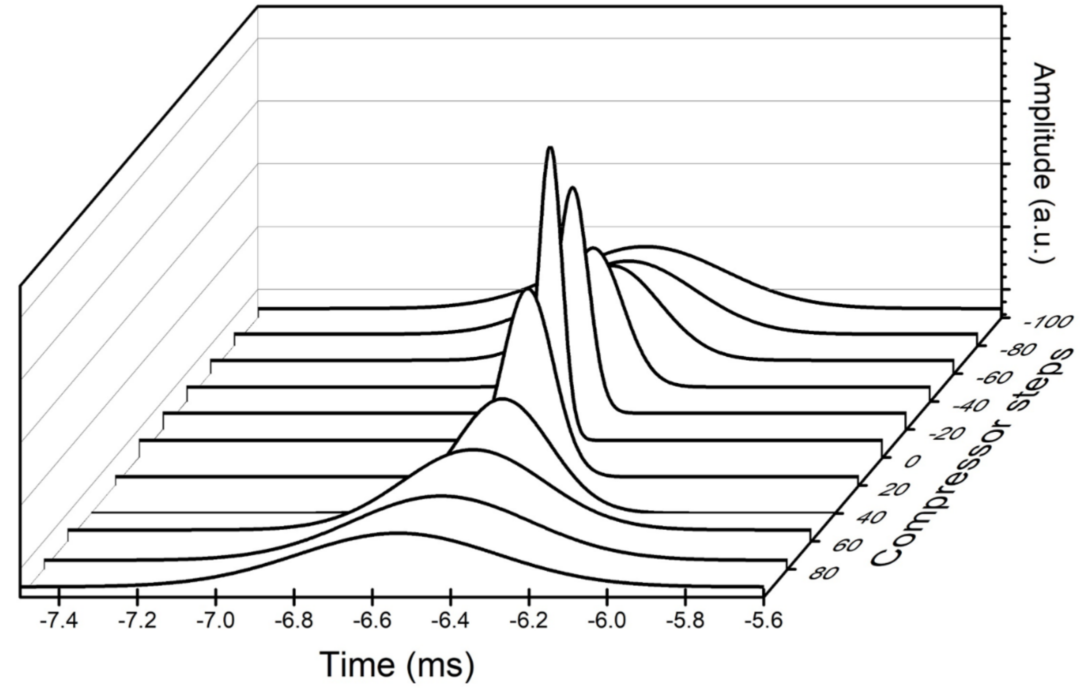

Figure 2.8: Autocorrelation plots for varying steps of the compressor grating separation.

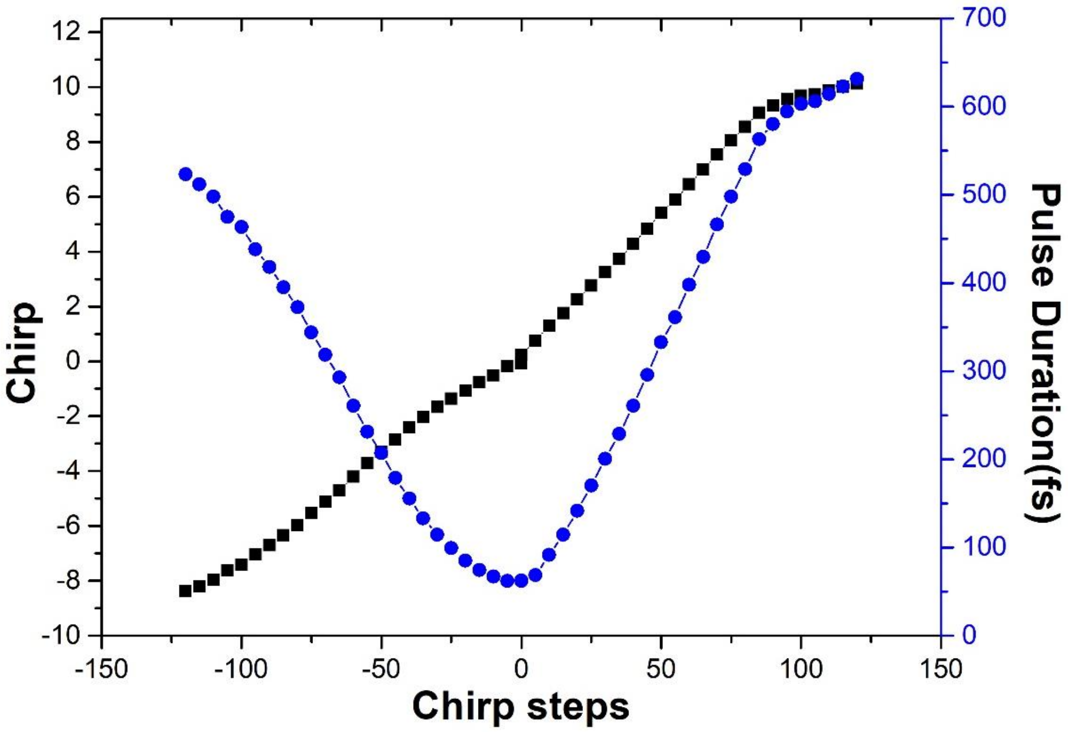

Figure 2.9: Chirp and pulse duration according to the steps of the compressor grating separation.

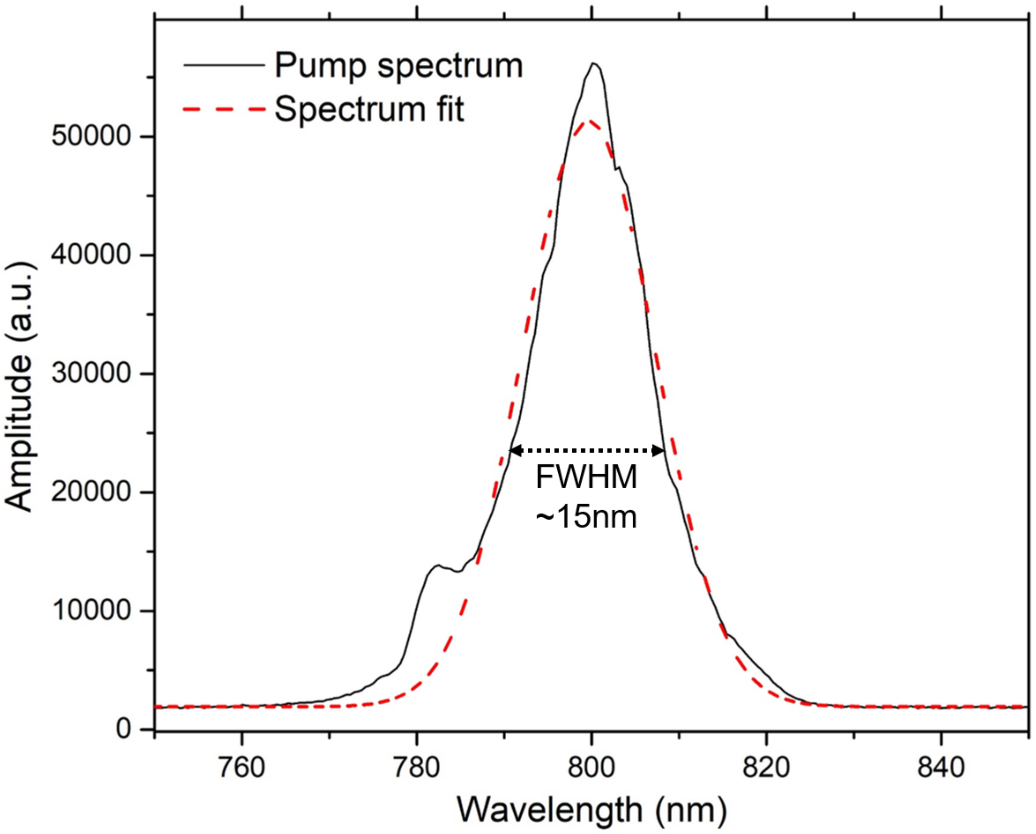

Figure 2.10: Spectrum of the laser output.

Figure 2.10 shows the laser pulse spectrum having a FWHM of 15nm (gives pulse duration of 60fs from the time bandwidth product). Characterization of the pulse with compressor grating separation and estimation of the induced chirp were used in the later works to study effects of changes in pulse profile on filamentation and the subsequent emissions from the filament.

2.4 Spectrometers

A large part of filament characterization was done by studying the optical emissions from filaments. These include transverse fluorescence emissions, FIBS, supercontinuum and higher harmonic generation. Several attributes of spectrometers need to be considered such as dynamic range, acquisition time, repetition rate, trigger and resolution according to the requirement or experiment being conducted. We have therefore used different spectrometers according to the experiment being performed and the region of the spectrum being acquired and the spectral resolution required. The spectrometers used were:

2.4.1 Maya 2000 (Ocean Optics)

This is a hand held USB spectrometer which can be coupled with an optical fibre. The sensor used in this spectrometer is a single array CCD. We used this spectrometer to characterize the supercontinuum and Third harmonic generation from the filament [17,18]. As the pulse post filamentation containing SCG, THG and pump pulse is intense enough to ignore background noise, we use this spectrometer for fast acquisition of these emissions. These components of the pulse post filamentation were separated from the pump using an external grating with 600 l/mm (This was done to isolate the pump at 800nm to avoid saturation of the spectrometer). The diffracted SCG is shined onto a Teflon sheet and the scattered light is collected so as to clearly identify the blue end of the spectrum. The 1st order of the diffracted THG is collected using a fiber coupled UV-NIR light collector MEOPT-0007 coupled to the Maya 2000. Figure 2.11 shows the Maya 2000 spectrometer that was used and a typical FIBS spectrum from air collected by it. The FIBS spectrum shown here shows the highlights the prominent peaks of oxygen and nitrogen which comprise most of the atmospheric composition [16]. This spectrum was acquired by collecting the transverse emitted FIBS signal using the optical fibre placed closely to the filament in the perpendicular direction.

Figure 2.101: Image of the Maya 2000 spectrometer used.

The Maya 2000 spectrometer was used to collect and characterize the third harmonic UV (THG) and supercontinuum broadband (SCG) emissions from the filament as shown in the figure 2.10. The multiple spectral component of the pulse post filamentation were first separated using a grating thereby primarily isolating the spectral components from the pump wavelength. Using the collection optics and fibre with the Maya helps provide a sturdy experimental setup which can characterize the forward propagating coherent emissions from the filament.

Figure 2.12 shows the schematic of the setup. The SCG was shined onto a Teflon sheet and the scattered signal was collected using a fibre head. This was done because the broad diffracted spectrum of the SCG cannot be completely collected, and usage of lenses will impose wavelength dependant absorption. Moreover, focusing the supercontinuum onto a focal spot would possibly damage the instrumentation. The fibre was therefore positioned so as to get the best signal to identify the blue end of the supercontinuum spectrum, which depends on the plasma, intensity and length of the filament. The THG was obtained by collecting the first order diffraction of the THG using the collection optics MEOPT-0007 coupled to the Maya 2000 using a spectrometer.

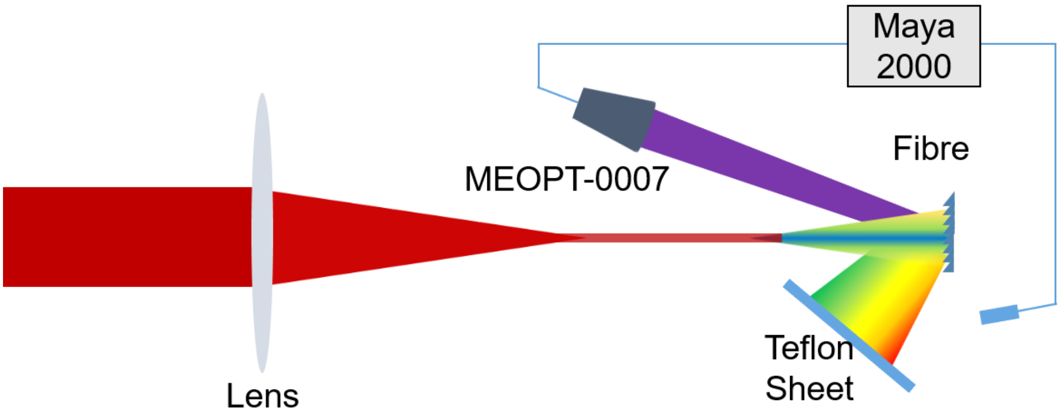

Figure 2.112: Schematic for acquisition of SCG and THG. MEOPT-0007- Collection optics. Light is diffracted of grating, scattered SCG from Teflon sheet is analysed to find blue end of spectrum and collection optics is used to collect the THG.

2.4.2 Mechelle spectrograph equipped with ICCD

Another spectrograph used for FIBS measurements was the ANDOR Mechelle spectrograph (ME-5000) which is based on the echelle grating setup which employs a gratingprism combination aligned perpendicular to each other to give high resolution in one acquistion over a broad range of wavelength (200nm-900nm) [19]. It was equipped with the iStar ICCD (DH334T-18U-E3) whose intensifier can be triggered at 1kHz. However, since the sensor is a CCD, the refresh time is high because of which the high repetition rate acquisitions are accumulated on the CCD sensor. Echelle spectrographs are rugged and can be utilized in field applications especially because they don't have any moving parts. The spectrometer was calibrated using two lamps calibrated viz. Mercury –Argon lamp for wavelength calibration and DH-3 lamp (Deuterium-Halogen lamp) for intensity calibration. The Mechelle spectrograph was used primarily for FIBS studies of solids because of the high temporal resolution (Through delaying the intensifier triggering with minimum window of 1.5 ns) and high SNR which can be obtained from a single shot of laser matter interaction. Although the CCD sensor has a good quantum efficiency, it has a slow refresh time (1Hz) making this spectrometer unsuitable for fast repetition rate acquisitions. Figure 2.13 shows the setup used for all the FIBS studied on solids.

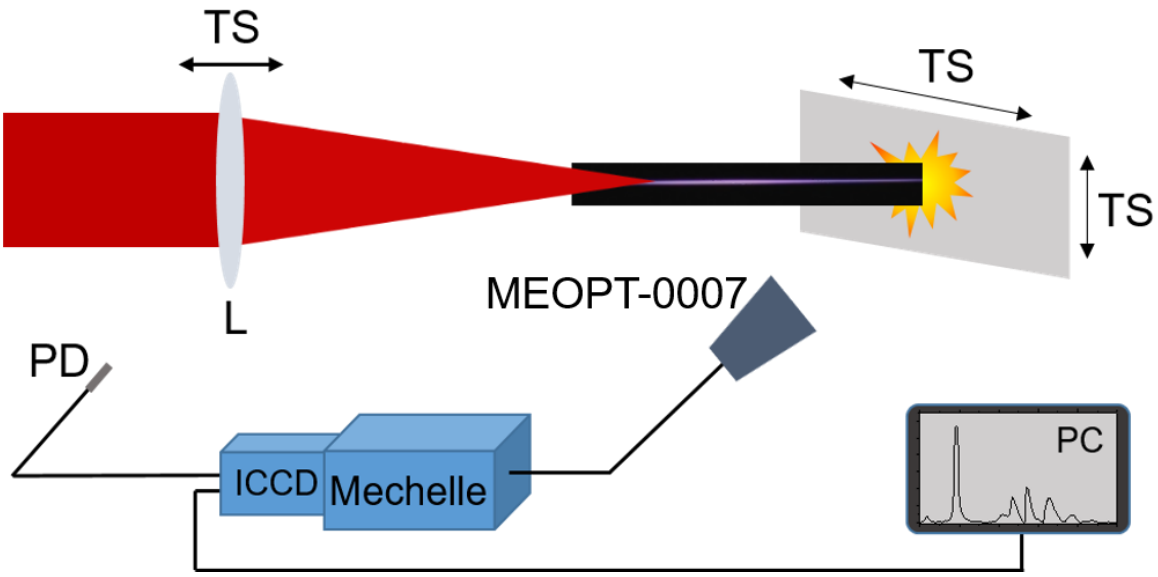

Figure 2.123: Schematic for LIBS acquisition using Mechelle spectrograph and collection optics MEOPT-0007. PD-photodiode; TS- translational stage; L-lens.

2.4.3 Kymera 328i

The spectrograph used for the collected FIBS signal was Kymera 328i, coupled with an intensified Andor sCMOS camera. It provides very high resolution over a broad frequency range by having a long through put and interchangeable gratings. The iSCMOS camera also provides good temporal resolution (2 ns) offered by the intensifier of the camera. The main advantage with this spectrograph with iSCMOS is the high frame rate which can keep up with 1kHz frame rate of the femtosecond laser. It is therefore possible to acquire spectrum from each pulse separately by gating the intensifier in iSCMOS. The spectrometer also is coupled with an InGaAs detector which has a wavelength acceptance range from 800nm -2000nm. The Kymera 328i is therefore capable of performing studies in the near IR region as well when the InGaAs detector is complimented by the grating with 300 lines per mm and blazed at 1000nm. Figure 2.14 shows image of Kymera328i coupled to an imaging lens, where one can image the filament onto the slit of the spectrograph to provide a spatial reconstruction of the spectrum along the filament.

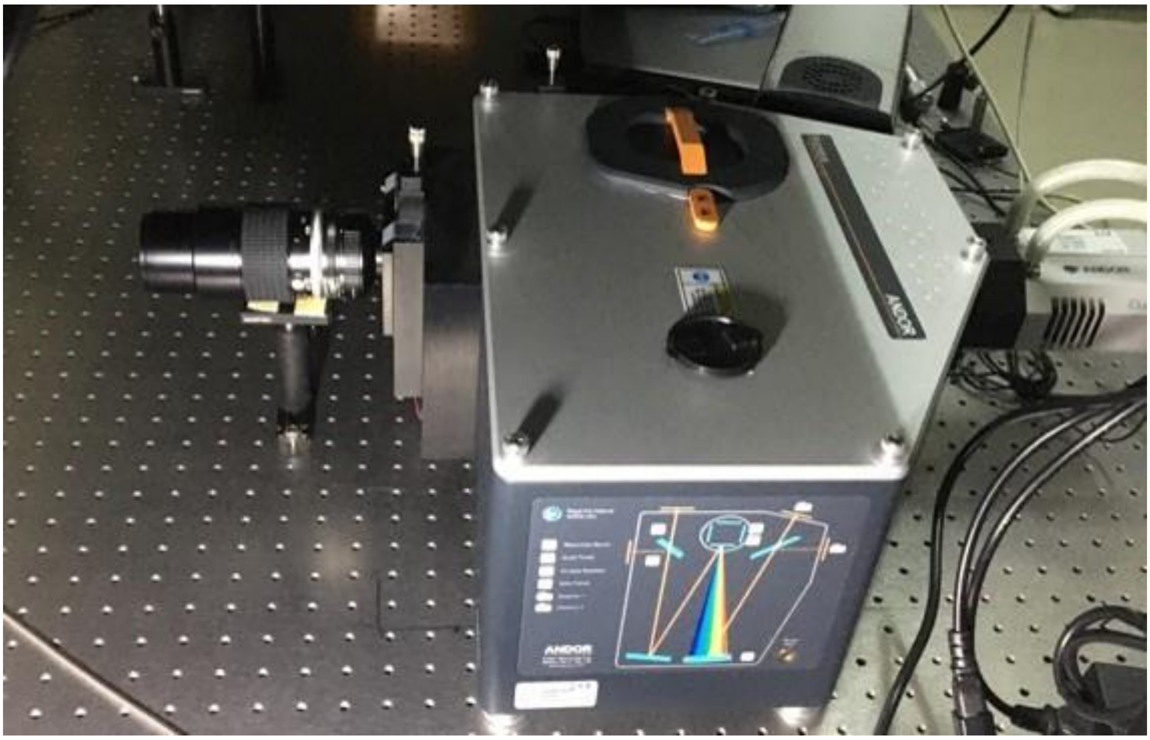

Figure 2.134: Kymera 328i coupled with an imaging lens.

The resolution depends on the grating being used because the grating used influences the diffraction angle. We have used a 600 lines/mm grating blazed at 750nm to collect spectrum in the range of 750-900 nm and a 1200 lines/mm grating blazed at 300nm to collect spectrum in the range of 320-400. For the low wavelength range the camera sensor covers ~25nm and for the high wavelength range the camera sensor covers ~50nm. Wavelength calibration was done using a mercury Argon lamp and intensity calibration was done using a Deuterium-Halogen lamp whose source spectrum was provided with the source. Figure 2.15 shows the main peaks from the background corrected spectrum obtained from the Mercury Argon lamp. The spectrograph was calibrated using this signal by matching the observed signal to the lines provided by the manufacturer of the Hg-Ar source. The resolution was also optimized and the best resolution was achieved when using the 600 lines/mm grating was 0.5nm and the best resolution obtained with the 1200 lines/mm grating was 0.2 nm.

The intensity calibration which was done using a source signal from a Deuterium Halogen lamp needed to be calibrated with each grating to calculate the correction factor that needs to be imposed on the raw spectrum. The formula shows the calculation of the correction factor.

$$Correction\ factor\ (CF) = \frac{Source\ signal}{Reference\ signal - Background} \tag{2.6}$$

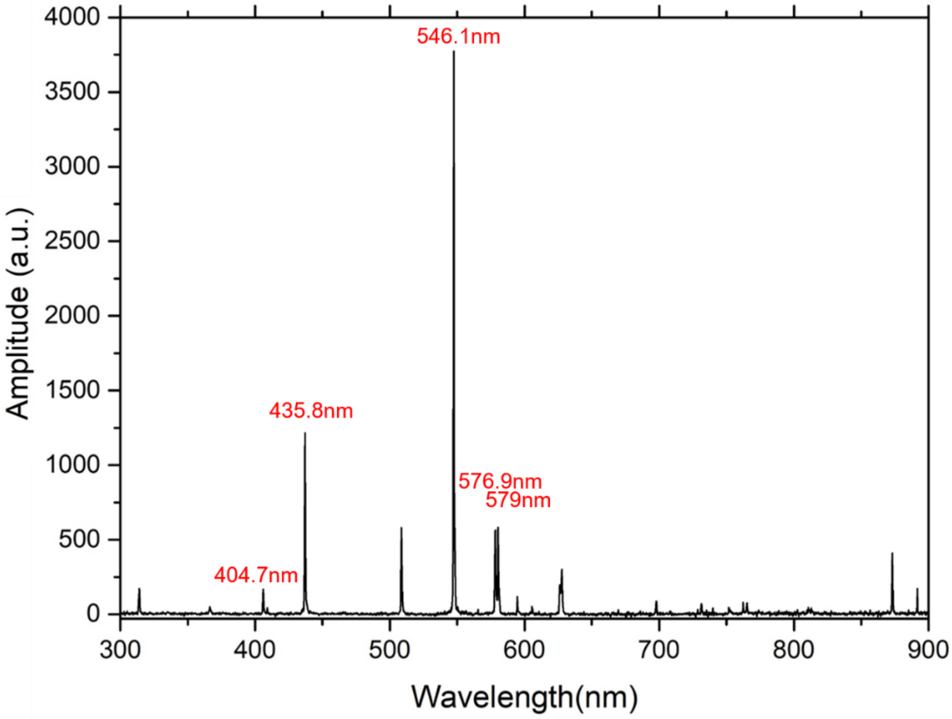

Figure 2.145: Spectrum acquired from Mercury Argon lamp after background correction.

$$Corrected\ signal = (Live\ signal - Background) * CF \tag{2.7}$$

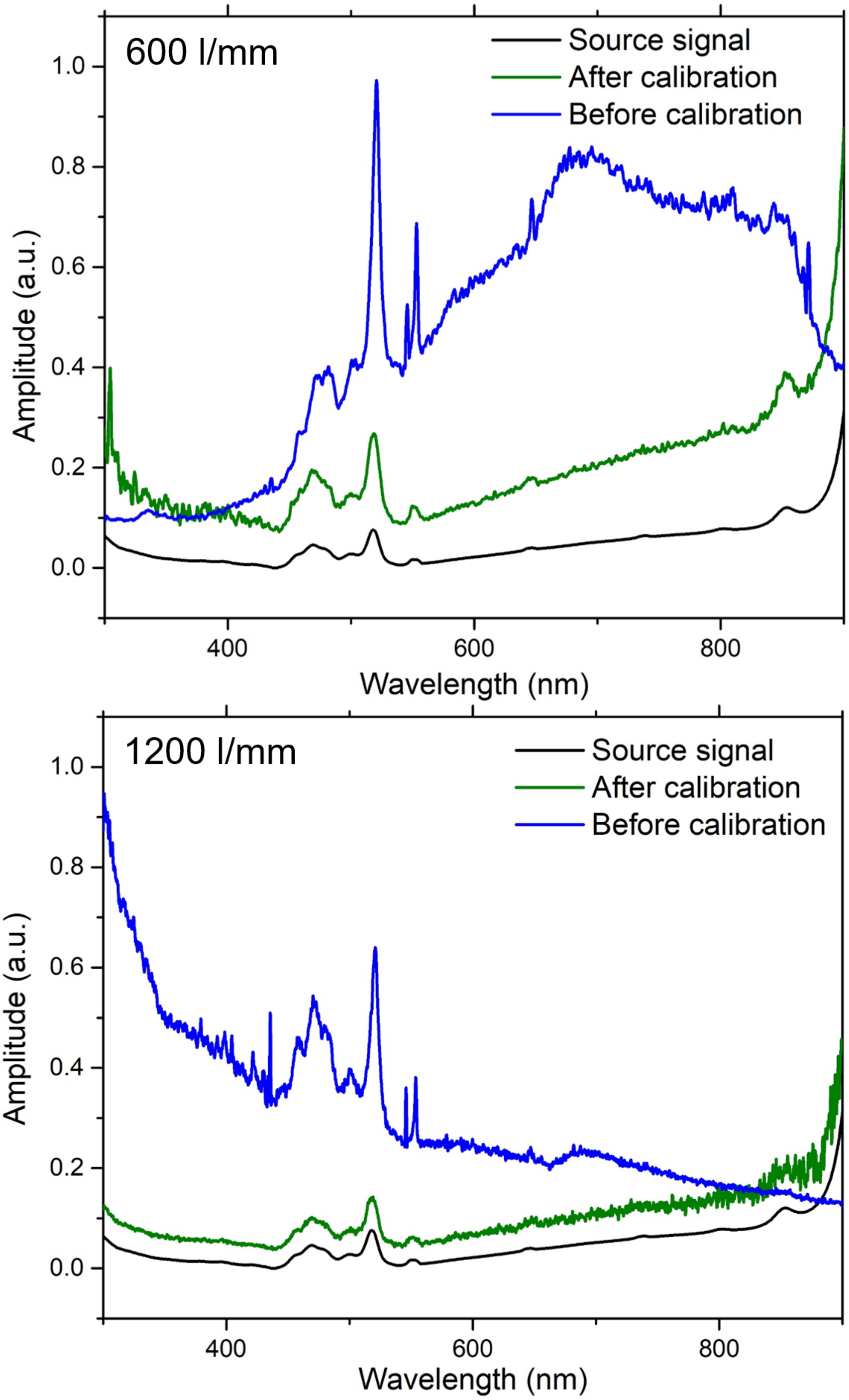

Figure 2.156: Spectra acquired from the deuterium halogen lamp before and after calibration when using two different gratings namely, 600l/mm (top) and 1200l/mm (bottom). Source signal is that provided by the manufacturer of the lamp.

Source signal is the spectrum provided by the manufacturer of the lamp, reference signal is the lamp spectrum observed by the spectrograph sensor, background is the background noise that needs to be first subtracted from any signal acquired by the spectrograph and live signal is the raw spectrum from any acquisition. We estimate the correction factor which is a function of the wavelength which as shown in the equation needs to be multiplied to the live signal. Figure 2.16 shows the spectrum of the calibration lamp acquired by the spectrograph using the 1200l/mm and 600l/mm grating. The 1200l/mm grating which is blazed at 300nm shows higher response to lower wavelengths whereas the grating with 600l/mm blazed at 750nm shows higher response at higher wavelengths.

2.5 Imaging of a femtosecond filament

Filamentation is a process which does not involve complete breakdown of the material i.e. although there is ionization, it is much less denser than the critical plasma density thereby facilitating free flow of the laser, because of which the plasma formed by femtosecond filamentation is a quasistatic plasma. However, since the whole process of filamentation occurs in the time scale of a few picoseconds the filament appears static, considering that the resolution of the best cameras is in the range of nanoseconds. Keeping this in mind imaging of the filaments was done using different cameras, with CCD and CMOS sensors. The CCD cameras used were (i) Spiricon SP620U and (ii) Point gray GRAS 20. The CMOS camera used was the Nikon t4i DSLR camera.

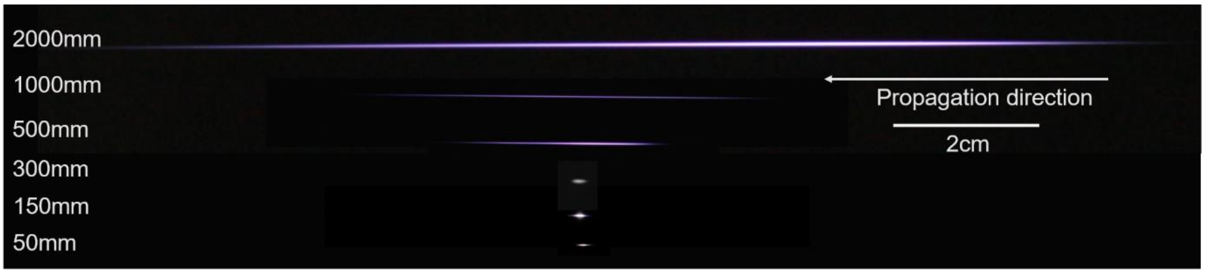

Figure 2.167: Images of the filaments imaged using the DSLR Nikon t4i camera. Exposure and gain was adjusted to capture complete spatial extent of the filaments generated using the lens with focal length=50mm, 150mm, 300mm, 500mm, 1000mm and 2000mm.

The cameras were chosen according to the spatial extent of the filament and the intensity of the optical transverse emissions from the filament. The CCD camera was used to image small filaments whose spatial structure needs to be resolved clearly. Whereas the CMOS camera was used to image long filaments extending more than a 5cm. Another advantage of CMOS camera is long exposure of about 30s which can help capture weak filaments which extend to more than 1m. Figure 2.17 shows images of filaments taken with the DSLR camera with change in brightness and spatial extent over 2 orders when focal length varies from 150mm to 2000mm.

Using the DSLR camera gives information on the spatial extent of the filament, helping study long and weak filaments as well. As the sensor of this camera is a CMOS sensor we do not have the high quantum efficiency nor dynamic range provided by the CCD sensor. Moreover, the lens design for the DSLR camera does not provide good enough resolution to study short or tightly focused filaments. We have used the CCD camera to therefore image tightly focused filaments (f/#<15). Figure 2.18 shows comparison of filaments taken with DSLR and CCD cameras.

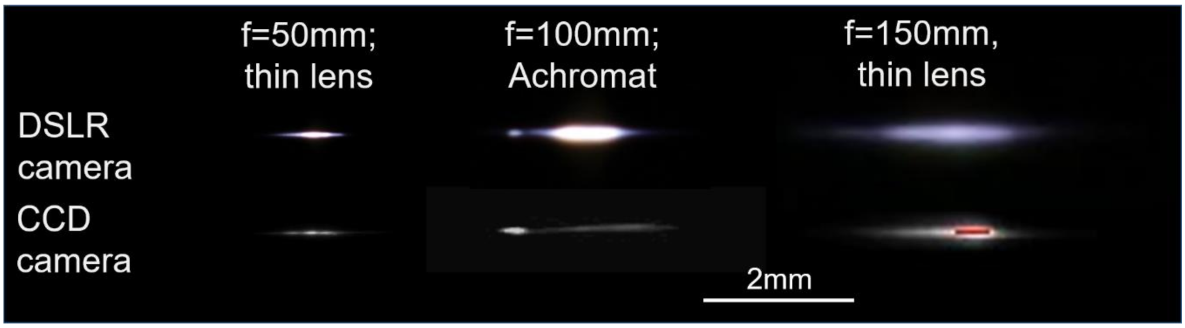

Figure 2.178: Images of filaments generated under tight focusing imaged using CCD and DSLR cameras.

2.6 Microphones for acoustic characterization

Plasma build up from the filament creates a steep temperature gradient with the atmosphere which leads to the creation of mechanical or acoustic waves which are studied using microphones [20-22]. We have used a calibrated microphone with a frequency response spanning a broad range from 20Hz to 140kHz (GRAS 40DP, sensitivity of 1mV/Pa) along with a 174 dB (re 20 μPa) dynamic range. A preamplifier is connected to the microphone before sending the signal to the oscilloscope (details of the oscilloscopes used are in the next section). The displacement of the diaphragm of the microphone because of the pressure wave created at the interface of the plasma and the surrounding atmosphere. This produces the electric analog signal comprising of positive and negative peaks indicating the pressure variation over the existing ambient pressure. The difference between the amplitudes of the negative and positive variations in the signal is taken as the peak to peak over pressure of the acoustic wave. The microphone used was an omnidirectional condenser microphone. The microphone is triggered using a photodiode placed near the experimental setup. A typical acoustic signal is as shown in the figure 2.19. One can find the peak to peak over pressure, arrival time and pulse burst time. The ratio of compression to rarefaction also provides information of the plasma expansion and redistribution processes.

The microphone shown in the figure 2.20 was calibrated using a pocket sized, calibrator which is battery operated (MODEL: G.R.A.S 42 AB) calibrator. It can produce a constant signal at 114dB re. 20μPa (equivalent to 10Pa) at 1kHz.

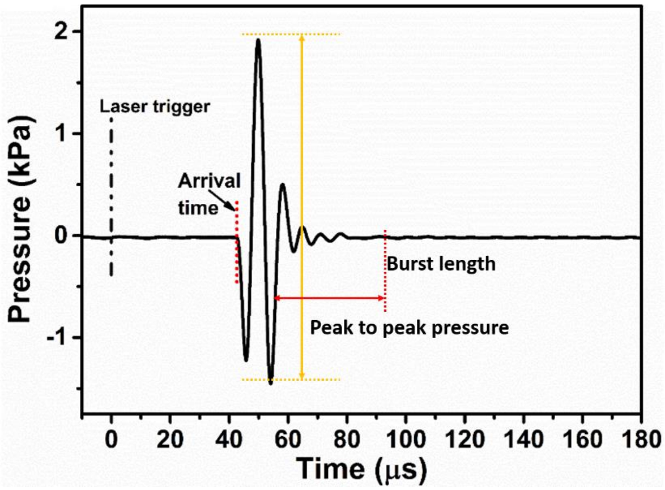

Figure 2.189: Typical acoustic signal showing the classification parameters.

Figure 2.20: Microphones used for the study.

The experiment was constructed so as to correlate the optical and acoustic emissions from the filament as shown in the figure 2.21. We have simultaneously obtained the optical and acoustic data The time domain signal was transformed into the fourier space using the fast fourier transform (FFT) thereby providing a frequency distribution of the acoustic signal.

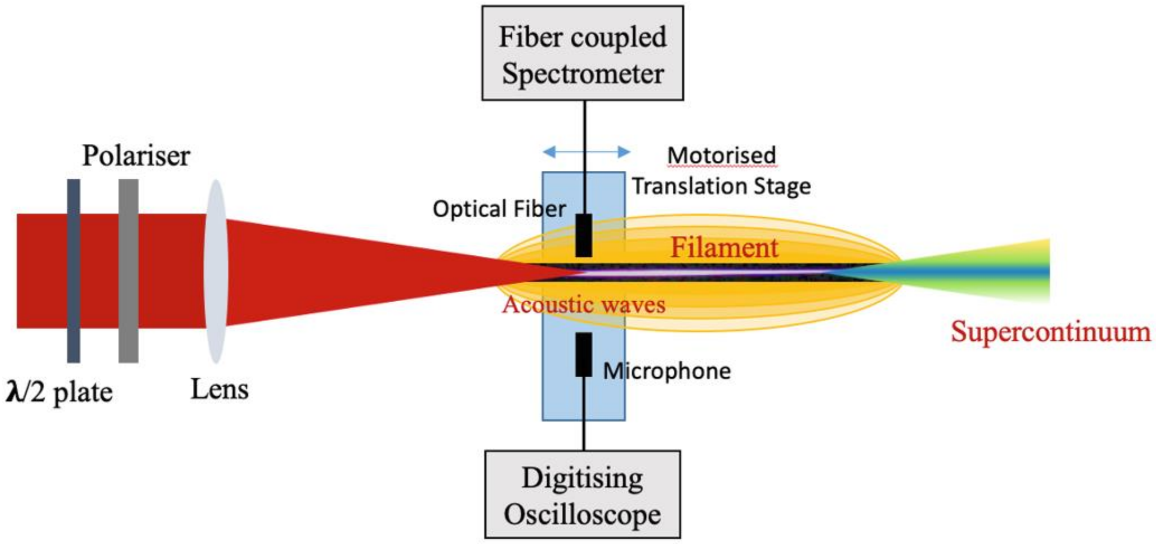

Figure 2.21: Experimental setup for acoustic signal collection.

Other than peak to peak over pressure and frequency domain analysis, the acoustic signal also gives information through the arrival time of the acoustic pulse as differences in arrival times indicate the existence of transient shock waves. The length of the acoustic pulse train also can be used to characterize the filament and subsequent plasma, like the existence of multiple filaments which cannot be found from optical characterization alone as will be shown in the coming chapters.

When Fourier transform was applied to the microphone signal, zero padding was done to the signal where a baseline signal is added to the signal even after the acoustic pulse relaxes. This is an analytical technique used to better resolve the existence of different frequency components in the acoustic spectrum (increase the frequency resolution of the FFT). Figure 2.22 compares zero padded and nonzero padded frequency distribution obtained from two acoustic signals obtained from filament interaction with aerosols made with varying quantities of tryptophan.

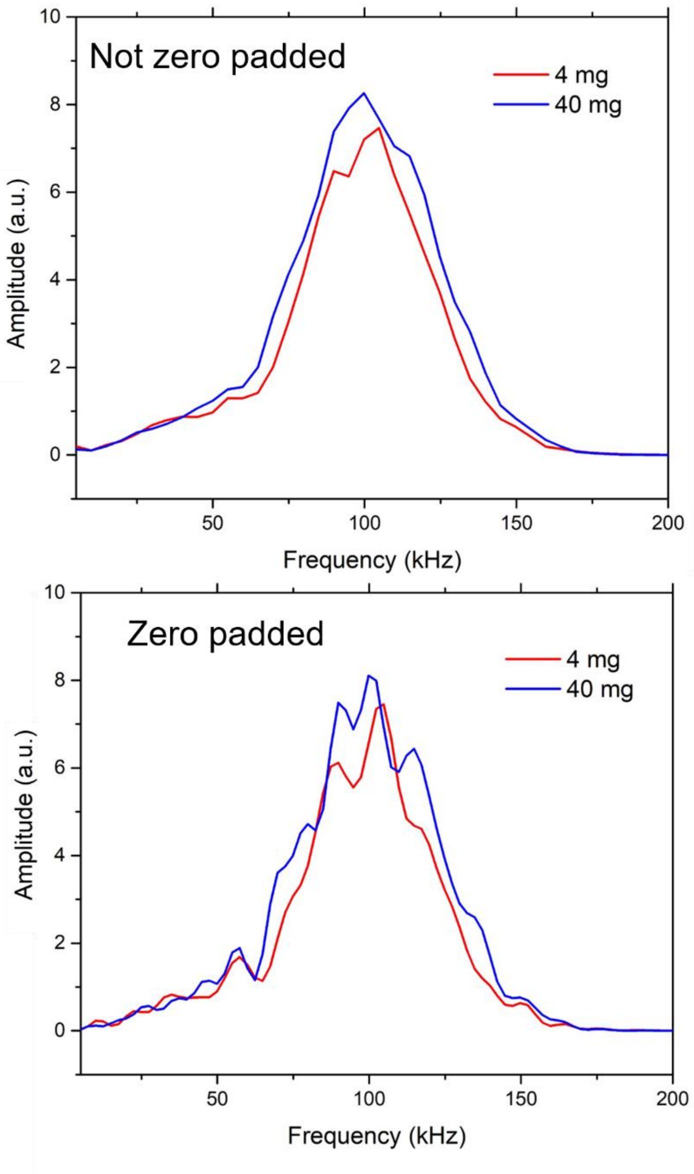

Figure 2.192: Frequency distribution obtained before zero-padding (top) and after zero-padding (bottom) to compare resolution.

2.7 RF characterization of femtosecond filament

Low frequency electromagnetic emissions which are part of the FIBS can be measured using antennas coupled to an oscilloscope. Low frequency RF emissions from laser matter interaction arise due to charge current and dipole oscillations [23-25]. The oscilloscope are both used according to frequency range and lifetime of the signal. We have also used 2 different oscilloscopes for the different experiments in this thesis, the details of the oscilloscope are given in Table 2.2.

Table 2.2: Detail of the oscilloscopes used.

Oscilloscope	Yokogawa DL1640L	Tektronix TDS5104B
Maximum Bandwidth	200MHz	1GHz
Channels	4	4
Sampling rate	200MS/s	5GSa/s

The frequency distribution of the particular electromagnetic signal is found by applying a fast Fourier transform of the time domain signal. Therefore the frequency response of such a setup can vary depending on the response of the detectors and instruments involved. When only considering the sampling rate of the oscilloscope available which can take up to 5 GSa/s the maximum frequency that can be resolved using this is <2GHz. Therefore we find that depending on the lifetime and frequency range of the electromagnetic pulse we need to choose the acquisition mechanism along with the appropriate antennas. As the frequency range being probed is in the range of 1-2 GHz we have made an antenna using a BNC cable and exposing 8mm of the inner wire. This is a dipole antenna which can be used in close proximity having bandwidth up to 4GHz. Translation of the near field dipole antenna along the filament shows RF having a conical distribution because signal is observed after translating beyond the filament. Figure 2.23 shows a typical RF signal transformed to the frequency domain obtained froma filament generated using a 500mm lens.

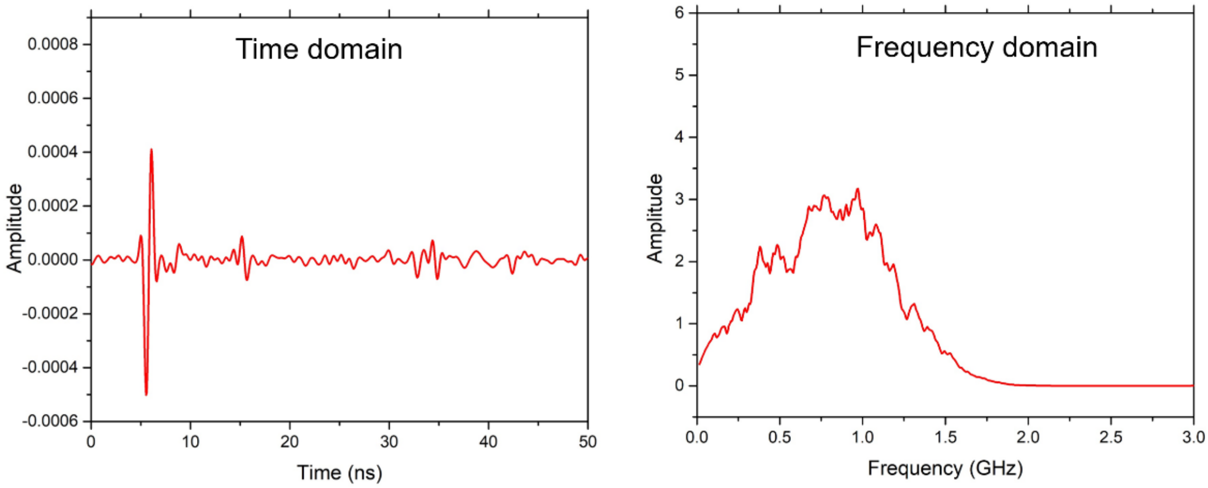

Figure 2.203: Typical RF signal from the filament and the corresponding frequency transform.

For the antenna we have used a whip antenna with a frequency range of 70-1000 MHz, whose radiation pattern is isotropic. The resonant frequency of this antenna is varied by changing the length of the antenna. This antenna can be operated using the oscilloscope or the spectrum analyser. We have also made an antenna using a coaxial cable whose reception of electromagnetic variations was demonstrated by cutting open the upper sheath of a BNC cable and exposing the inner cable to the electromagnetic radiation therefore making it a near field dipole antenna [26]. The variation in the electric field induces a current in the cable which is recorded on the oscilloscope. Figure 2.24 shows the image of the RF acquisition setup from filaments.

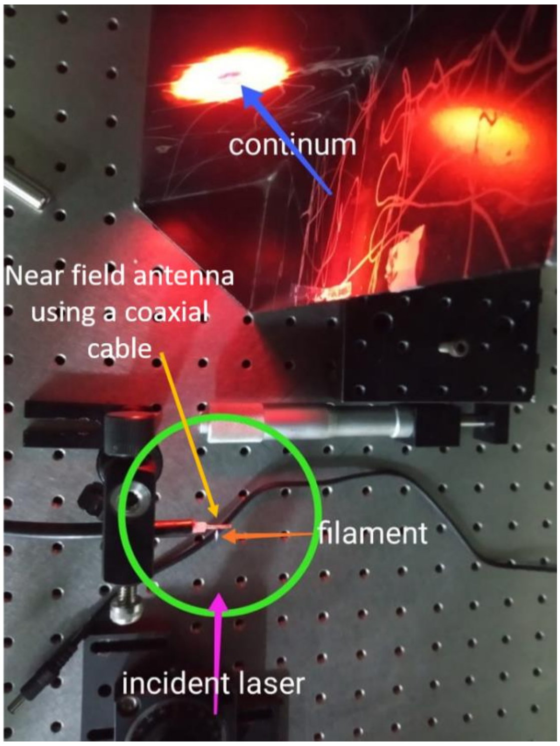

Figure 2.214: Image showing filament and positioning of the antenna beyond the spatial extent of the filament.

2.8 Intensity and electron density estimation from spectrum collected

Filament propagation being a highly intense phenomenon makes characterization using invasive techniques impossible. The transient nature which is 2 orders faster than the fastest photodiodes available also poses a challenge to appropriately reconstruct the spatial distribution of the filament and dynamics that exist. We have therefore used spectroscopic techniques to study the filament along the propagation distance we have primarily used the oxygen and nitrogen lines to estimate the intensity and plasma density in the filament in air. Figure 2.25 shows the setup to collect the transverse emitted FIBS from the filament in air.

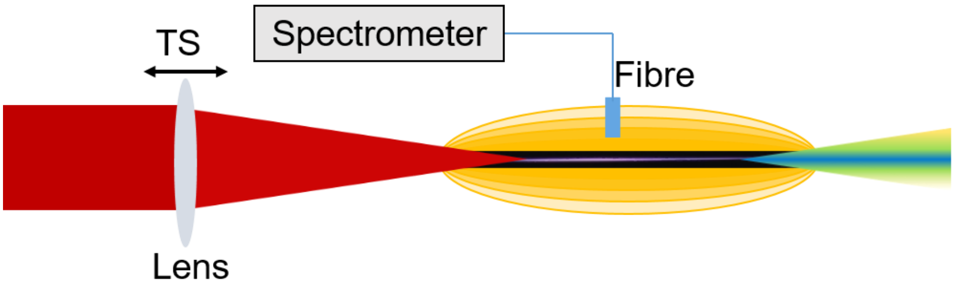

Figure 2.225: Schematic for collection of transverse emitted spectrum due to filament induced breakdown in the ambient atmosphere. TS-translational stage

The intensity of the filament in air was estimated using the ionized fluorescence lines of nitrogen and the electron density was estimated from the stark broadening. Oxygen spectral line at 845nm. Figure 2.26 shows a typical spectrum of FIBS in air along with the origin element of the lines taken using a Maya 2000 spectrometer.

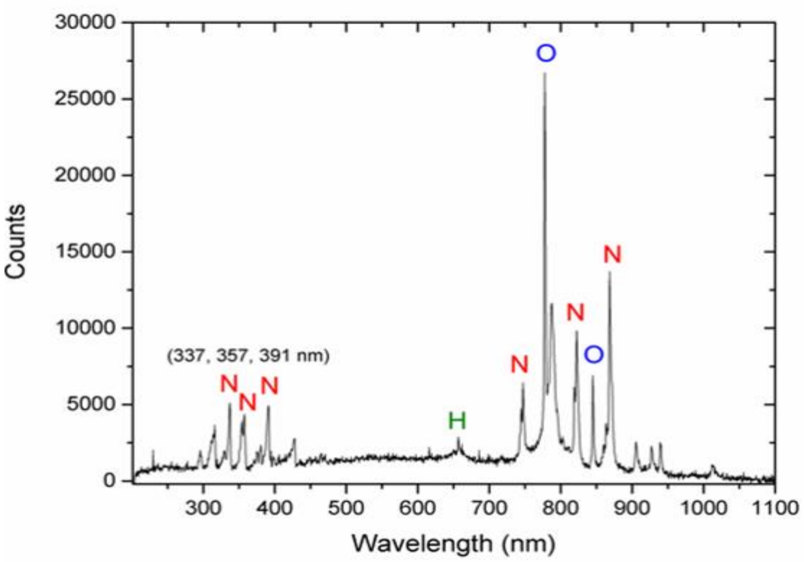

Figure 2.236: Typical FIBS signal in air showing the prominent nitrogen, oxygen and hydrogen.

2.8.1 Intensity estimation

The laser peak intensity is found by finding the ratio of the two fluorescence lines of Nitrogen at 391nm and 337nm [27]. The line centred at 391nm is the fluorescence transition of the Nitrogen ions ionized by direct ionization of inner valence electrons. Whereas, the intensity of the 337nm line is directly proportional to the total number of Nitrogen ions i.e. both species formed by direct ionization of inner valence electrons and normal ionization of least bound electron. The population of these ionized species is directly proportional to the intensity at different orders of non-linearity and proportionality, because of which the ratio of these lines can provide a direct correlation to intensity. The fluorescence line intensities can be understood to depend on the filament intensity according to relation,

$$S_{391} \propto N^{excited} = aI^{n1} \tag{2.8}$$

$$S_{337} \propto N^{total} = N^{excited} + N^{ground} = aI^{n1} + bI^{n2} \tag{2.9}$$

Where S_{337} and S_{391} are the intensity of the lines seen in the spectrum. I is the intensity of the light in the filament, a and b are the proportionality constants. The ratio R between these two lines can be found to be directly influenced by the intensity of the filament according to the relation.

$$R \propto \frac{1}{1 + \left(\frac{b}{a}\right)\left(\frac{n1}{n2}\right)^{3/2} I^{n2-n1}} \tag{2.10}$$

The relation between the ratio and peak intensity in the filament therefore takes the form,

$$I_0 = \beta\left(\frac{\alpha}{R-1}\right)^{m} \tag{2.11}$$

Where, α, β and m are constants which are found from experiment by Chin et.al. In their study this dependence was first verified by intensity estimation made from plasma channel dimensions and subsequent correlation to ratios estimated from different filaments generated under varying focusing conditions and input energies. As the ambient atmosphere, input laser characteristics and focusing conditions used in our experiment are in the same range we have used the constant values estimated by them as α=2.6, β=79 TW/cm^2 and m=-0.34. The intensities which were therefore measured along the propagation of the filaments generated using lenses with focal length at the same power are shown in figure 2.27.

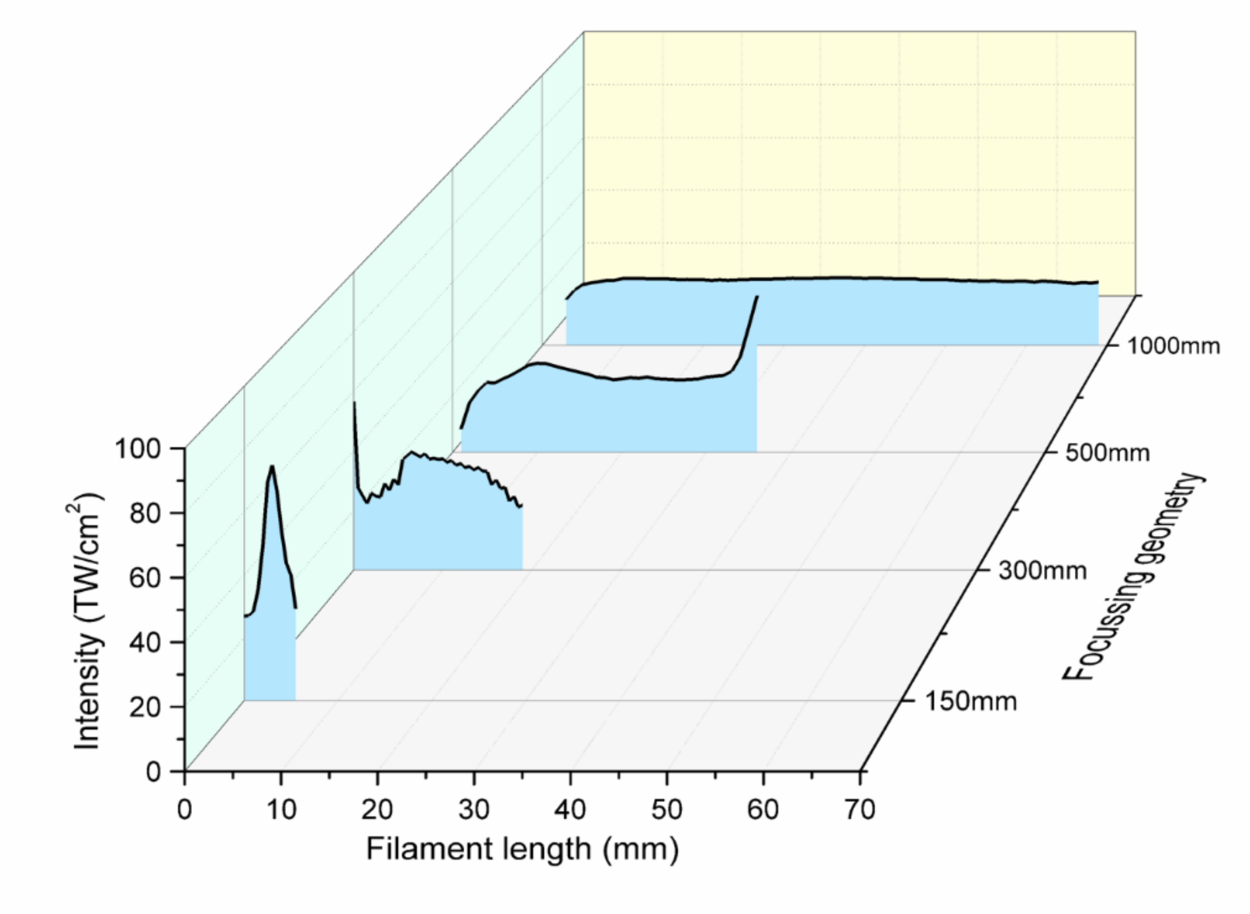

Figure 2.247: Intensity profile along the filament generated using lenses with varying focal lengths (f(mm)= 150, 300, 500 and 2000).

2.8.2 Electron density estimation

The electron density of the plasma can be estimated from the broadening of spectral lines primarily that of oxygen at 844.66 nm which is fitted to Lorentzian line shape. As the dominant line broadening mechanism is Stark broadening. The width of the emission line FWHM ($\Delta\lambda$) is therefore related to electron density (N_e) as,

$$N_e = \frac{\Delta\lambda}{2\omega} \times 10^{16} cm^{-3} \tag{2.12}$$

Where ω is the impact width. Its value at 844.66 nm line is 0.05140 nm [28]. The electron density that was estimated using this technique is shown in figure 2.28. The filaments were generated using three different lenses with focal length of 50mm, 150mm and 500mm.

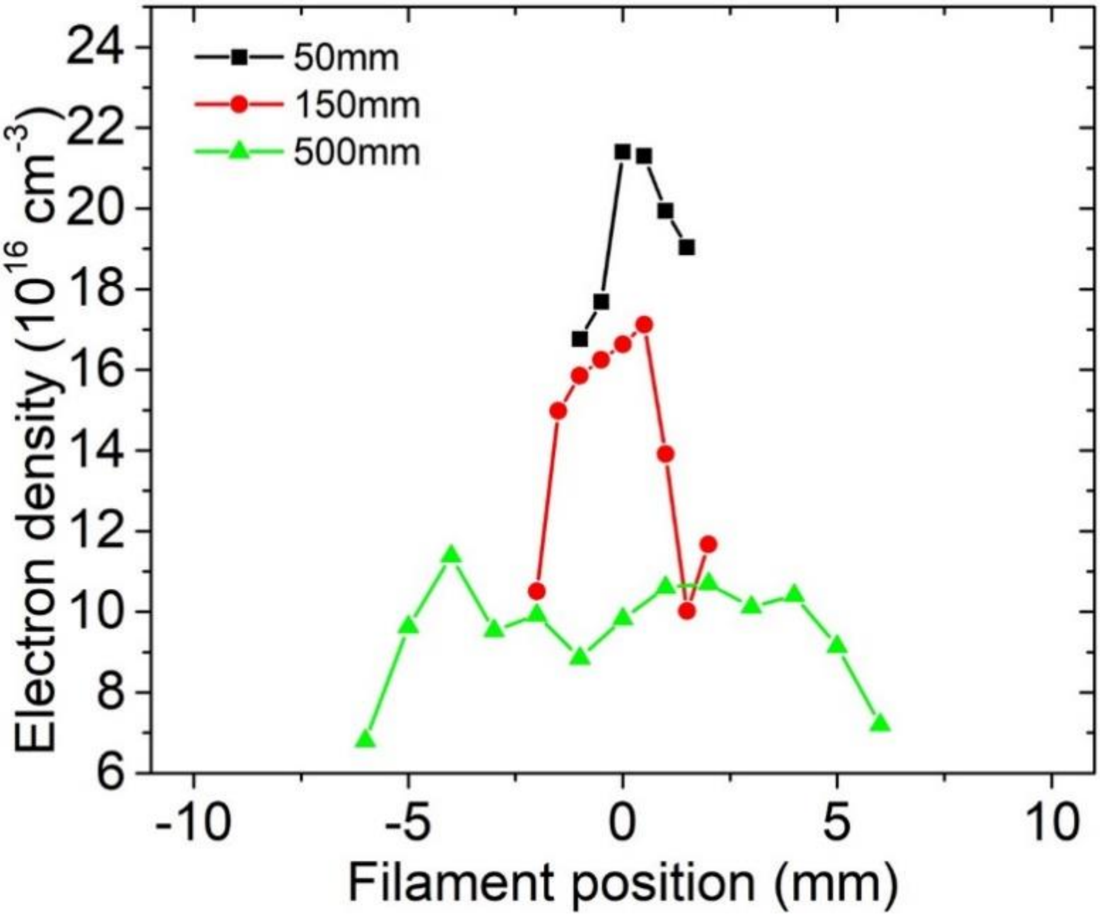

Figure 2.258: Electron density profile along the filament generated using lenses with varying focal lengths (f(mm)= 50, 150 and 500).

2.9 Summary

Filamentation being a highly dynamic phenomenon propagating at a very high intensity poses a challenge to characterize it. We have therefore used multiple characterization techniques involving spectroscopic analysis, acoustic & RF analysis and damage analysis along the filament generated under multiple varying input conditions like power, polarization, focusing conditions and aberrations. These were further correlated to the filament images to create a holistic understanding of the filaments. The emissions from filaments which can be used for the broad range of applications that filamentation can boost, such as third harmonic UV, Supercontinuum broadband, radio frequency and acoustic emissions were also systematically characterized. Intensity and electron density in the filament were estimated using spectroscopic techniques. Filamentation was first characterized holistically and the studies were extended to modulate and enhance the various emissions and characteristics of filamentation. Though the spectroscopic and imaging techniques give an insight into the filament propagation, they cannot explicitly give the details of the electric field.

References

1. A. Couairon and A. Mysrowicz, *Femtosecond filamentation in transparent media*, Phys. Rep. **441**, 47–189 (2007).
2. D. Strickland and G. Mourou, *Compression of amplified chirped optical pulses,* Optics Communications, **55(6)**, 447-449 (1985).
3. R. Paschotta, *Field Guide to Laser Pulse Generation*, SPIE press Bellingham, **14 (**2008).
4. T. Brabec, C. Spielmann, P. F. Curley, F. Krausz, *Kerr Lens Mode Locking*, Opt Letters, **17**, 1292-1294 (1992).
5. T. Bridges, P. Cheo, *Spontaneous Self-Pulsing and Cavity Dumping in a Co2 Laser with Electro-Optic Q-Switching*, App Phys Letters, **14**, 262-264 (1969).
6. D. Maydan, R. Chesler, *Q-Switching and Cavity Dumping of Nd: Yalg Lasers*. J. of App Phys, **42**, 1031-1034 (1971).
7. B. Denker, E. Shklovsky, *Handbook of Solid-State Lasers: Materials, Systems and Applications*, Elsevier (2013).
8. S. A. Hussain, *Discovery of Several New Families of Saturable Absorbers for Ultrashort Pulsed Laser Systems*, Scientific Reports, **9**, 1-9 (2019).
9. N. J. Berg, J. N. Lee, *Acousto-Optic Signal Processing: Theory and Implementation*, New York, Marcel Dekker, Inc. (Optical Engineering. Volume 2) (1983).
10. T. A. Maldonado, *Electro-Optic Modulators. Handbook of optics*, McGraw Hill (1995).
11. A. Weiner, *Ultrafast Optics*, John Wiley & Sons, **72**, (2011).
12. H. Fattahi, *Regenerative Amplifiers. In Third-Generation Femtosecond Technology*, Springer International Publishing: Cham, 73-86 (2016).
13. K. Wynne, G.D. Reid, R. M. Hochstrasser, *Regenerative Amplification of 30-Fs Pulses in Ti: Sapphire at 5 KHz*. Opt. letters **19**, 895-897 (1994).
14. J. Liu, G. Zhou, S. Pyo, *Parametric Gain of the Generation and the Amplification of Ultrashort Optical Pulses*, JOSA B **12**, 2274-2287 (1995).
15. M. Raghuramaiah, A. Sharma, P. Naik, P. Gupta, R. Ganeev, *A Second-Order Autocorrelator for Single-Shot Measurement of Femtosecond Laser Pulse Durations*, Sadhana, **26**, 603-611 (2001).
16. D. Rompotis, *A Single-Shot Nonlinear Autocorrelation Approach for Time-Resolved Physics in the Vacuum Ultraviolet Spectral Range*, (2016).
17. N. Aközbek, A. Becker, M. Scalora, S. L. Chin and C. M. Bowden, *Continuum generation of the third-harmonic pulse generated by an intense femtosecond IR laser pulse in air*. Appl Phys B, **77**, 177–183 (2003).
18. S. Skupin and L. Bergé, *Supercontinuum generation of ultrashort laser pulses in air at different central wavelengths*, Opt. comm., **280(1)** ,173-182 (2007).
19. M. Kotzagianni, S. Couris, *Femtosecond laser induced breakdown spectroscopy of air–methane mixtures*, Chem. Phys. Letters, **561–562**, 36-41 (2013).
20. J. Yu, D. Mondelain, J. Kasparian, E. Salmon, S. Geffroy, C. Favre, V. Boutou, and J.-P. Wolf, *Sonographic probing of laser filaments in air*, Appl. Opt. **42**, 7117-7120 (2003).
21. S. L. Chin, D. K. Evans, R. D. McAlpine, and W. N. Selander, *Single-pulse photoacoustic technique for measuring IR multiphoton absorption by polyatomic molecules*, Appl. Opt. **21**, 65-68 (1982).
22. E. Manikanta, L. Vinoth Kumar, P. Venkateshwarlu, C. Leela, and P. P. Kiran, *Effect of pulse duration on the acoustic frequency emissions during the laser-induced breakdown of atmospheric air*, Appl. Opt. **55**, 548-555 (2016).
23. B. Forestier, A. Houard, M. Durand, Y.-B. André, B. Prade, J-Y. Dauvignac, F. Perret, C. Pichot, M. Pellet, A. Mysyrowicz, *Radiofrequency conical emission from femtosecond filaments in air*. Appl. Phys. Letters, **96 (14)**, 141111-141113, (2010).

24. L. Vinoth Kumar, E. Manikanta, Ch. Leela, and P. P. Kiran, *Effect of laser intensity on radio frequency emissions from laser induced breakdown of atmospheric air*, J. Appl. Phys, **119**, 214904 (2016).
25. J. S. Pearlman and G. H. Dahlbacka, *Emission of rf radiation from laser-produced plasmas*, J. Appl. Phys. **49**, 457 (1978).
26. A. Proulx, A. Talebpour, S. Petit and S. L. Chin, *Fast pulsed electric field created from the self-generated filament of a femtosecond Ti: Sapphire laser pulse in air*, Opt. comm., **174(1-4)**, 305-309 (2000).
27. S. Xu, X. Sun, B. Zeng, W. Chu, J. Zhao, W. Liu, Y. Cheng, Z. Xu, and S. L. Chin, *Simple method of measuring laser peak intensity inside femtosecond laser filament in air*, Opt. Express, **20**, 299-307 (2012).
28. M. K. Gundawar, R. Junjuri, and A. K. Myakalwar, *Standoff Detection of Explosives at 1 m using Laser Induced Breakdown Spectroscopy*, Defence Science Journal **67**, 623-630 (2017).

This page was intentionally left blank

CHAPTER 3: Spectral Anatomy of fs filament and the associated super continuum emission: Effect of focusing optic aberrations.

Abstract:

As filamentation is a highly dynamic process which involves multiple competing processes, it was first studied under the variation of different pulse parameters. The filament thus generated was characterized using filament intensity, electron density, Supercontinuum generated and filament structure to directly correlate the effect of the pulse modifications. We have therefore classified our characterization into 4 configurations, each configuration inducing a distinct modulation while keeping other parameters constant. In the first configuration, pulse energy and focal geometry were varied. In the second configuration, influence of optical element aberration on filament behaviour was studied, keeping the focal geometry constant. In the third configuration, input pulse profile was modified by inducing chirp onto the pulse spectrum. In the fourth configuration, filamentation was studied when the focusing lens was tilted and cylindrical asymmetry was induced in the pulse front. These studies give a holistic picture of filament behaviour and the dominating mechanisms which govern the filamentation process.

3.1 Introduction

The femtosecond pulse undergoes many distortions during propagation in a medium, even when the pulse is not intense ($P<P_{cr}$) [11]. This is due to the short temporal duration and corresponding large bandwidth ($\Delta\lambda \sim 30$nm) in the pulse, which is subject to higher orders of dispersion. This dispersion induces varying phase to the frequency components of the femtosecond pulse, thereby changing the pulse profile. Inhomogeneous media also induce spatially varying modifications to the pulse. Other than these effects there are also aberrations induced by the optical elements being used [2]. As we move to higher intensities ($P>P_{cr}$) we find that non-linear effects such as intensity dependant refractive index, self-phase modulation, non-linear absorptions and higher harmonic generation also influence the spatio-temporal distribution of the femtosecond pulse [3, 38]. All the above mentioned distortions to femtosecond pulses have been characterized and one can simulate such effects on a femtosecond pulse [5]. The process of filamentation being highly dynamic, it is extremely sensitive to input pulse distortions because of which simulation of such effects on filamentation would be inconsistent and therefore unpredictable, demanding consistent empirical support [6]. To discretely characterize the direct effects of all the above effects on filamentation, we identify the spatio-temporal distortions such as medium propagation, external focusing, optical element aberrations and spatial asymmetry and correlate them to the corresponding filamentation observed by careful and systematic studies. Filamentation was characterized according to the visible spatial extent, FIBS, intensity, electron density and supercontinuum emission generated from the filament. These findings help establish the foundation for future studies in this thesis and provides a holistic understanding for femtosecond filament assisted application requirements.

The experiments done were done under four different configurations to establish the effect of all input pulse variations separately as listed below:

a) In the first configuration, fs pulses were focused using different focal geometries using lenses of different focal lengths. The first step was to separate tight focusing and loose focusing regimes of filamentation for the powers used in the experiments. This classification was made from the estimated peak intensity values and the spatial profile variation of the filaments with focusing length and power. A combination of two lenses (f_1=-10cm, and f_2=15cm) was used to generate filamentation and achieved the same effective focal length as that of a single lens. The filaments generated were compared with that generated using a single lens.

b) In the second configuration, the effect of different kinds of focusing elements such as off-axis parabolic mirror (OAPM), Achromatic Doublet (AD), Plano-convex lens (PCX), Thin PCX, bi-convex lens (BCX) of same focal length on the filament and SCE were studied. Aberrations induced of all the focusing elements were identified and they were classified and the corresponding generated filament characteristics were correlated.

c) In the third configuration, the filament behaviour was investigated under varying input pulse chirp [7]. Along with self-emission images and the associated supercontinuum emission we were able to further classify filament behaviour such as variation of onset and termination of filaments and increase/decrease of minimum wavelength of supercontinuum with chirp.

d) Apart from the above three distortions to femtosecond pulse, tilting of the lens also was found to drastically alter filament behaviour as we observe elongation of the filament along with suppression of the supercontinuum generation and intensity. We have therefore studied the filament under lens tilt thereby inducing spatial asymmetry during focusing in the 4th configuration.

3.2 Influence of Input power and focal geometry

Femtosecond pulses were focused using different focal geometries and input powers. The intensity of light was spectroscopically estimated along the filament from the filament induced breakdown spectrum as described in Chapter 2 [8]. The images of the filaments were taken using a Canon T4i camera to compare the wide range of spatial extents of the filaments (1mm - 1000mm generated in the lab). The ratio of the nitrogen lines at 391nm and 337nm and the intensity estimation are shown in the figure 3.1.

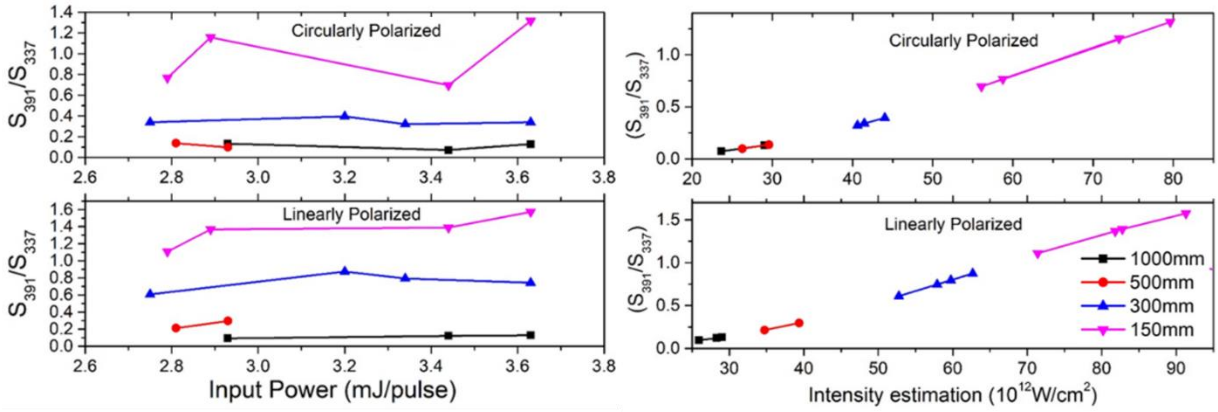

Figure 3.1: (Left) Ratio of ionized nitrogen fluorescence lines; (Right) Estimated intensity.

We have varied the energy of the fs laser pulse from 2.75 mJ to 3.6 mJ. The filaments were also generated using linearly and circularly polarized pulses. The peak intensity is higher for linearly polarized pulse generated filaments for all the focusing conditions and input powers [9]. The maximum peak intensity observed for filaments in our study was ~90 TW/cm^2, which was achieved for filaments generated with maximum available input energy of 3.6 mJ, using linearly polarized pulses and 150mm lens. The lowest intensity of 25 TW/cm^2 that could be estimated using spectroscopic techniques was that from the filament generated using a 1000 mm lens at a pulse energy of 2mJ. We find that the variation of filament peak intensity with input pulse energy in the range of energies used is more for shorter focal length lenses (ΔI_{fil} = 20TW/cm^2) as compared to longer focal length lenses (ΔI = 5 TW/cm^2). This indicates that intensity clamping occurs for higher focal length lenses at lower powers itself because of which one does not observe much variation in intensity for longer focal length lenses [10, 11]. Using the filament images and spectroscopic characterization, the first step was to classify the focusing conditions into tight focusing and loose focusing regimes of filamentation for the powers used in the experiments [12-13]. The images and intensity estimation from the spectra show a clear regime change in the filamentation process when focal length changes from 300mm to 500mm using the laser beam with beam width of 8mm. The major difference between the two focusing regimes is the evolution of the phase/pulse front. In the loose focusing regime the curvature of the phase front remains planar along the filament due to multiple cycles of Kerr self-focusing and plasma defocusing. While in the tight focusing regime, the phase front undergoes a Guoy phase shift after which the large divergence of the beam switches off the effects of Kerr Self-focusing and plasma defocusing. Supercontinuum emission generated from the filaments was also analysed and characterized using the minimum cut-off wavelength (λ_{min}) as a measure of the broadband emission, thereby quantifying the broadening towards the blue end of the spectrum. The variation in SCG with input pulse energy between filaments generated under tight focusing conditions (f=150mm) and loose focusing conditions (f=500mm) is shown in the figure 3.2. Spectrum was collected to obtain maximum of broadening towards the blue end of the spectrum. The shaded region shows bandwidth of the pump. In the loose focusing regime of filamentation, with the intensity of the filament clamped to ~10^{13} W/cm^2 displays a constant minimum cut-off wavelength (λ_{min}) of the SCE, while in the tight focusing conditions the intensity of the filament being and order of magnitude higher, i.e. ~ 10^{14} W/cm^2 has a continuously shifting minimum cut-off wavelength.

To generate filaments of at all desired distances, a combination of two lenses (f_1=-10cm, and f_2=15cm) was used to achieve the same effective focal length as that of a single lens some of which are not available in the lab. We were able to create filaments in a range of distances 0.3m-3.5m only limited by lab dimensions in the upper limit. The filament dimensions were modified by inducing chirp in the input pulse. Line profiles of the filaments generated by a single lens and that of the filaments generated using combination of lenses were compared. The filament intensity profile from the combination of lenses show a drop by ~50% in transverse visible emission when compared to that of filaments from single lenses, while the spatial extent was found to ~15% lesser. The findings from the lens combination study are given in more detail when the third configuration is discussed.

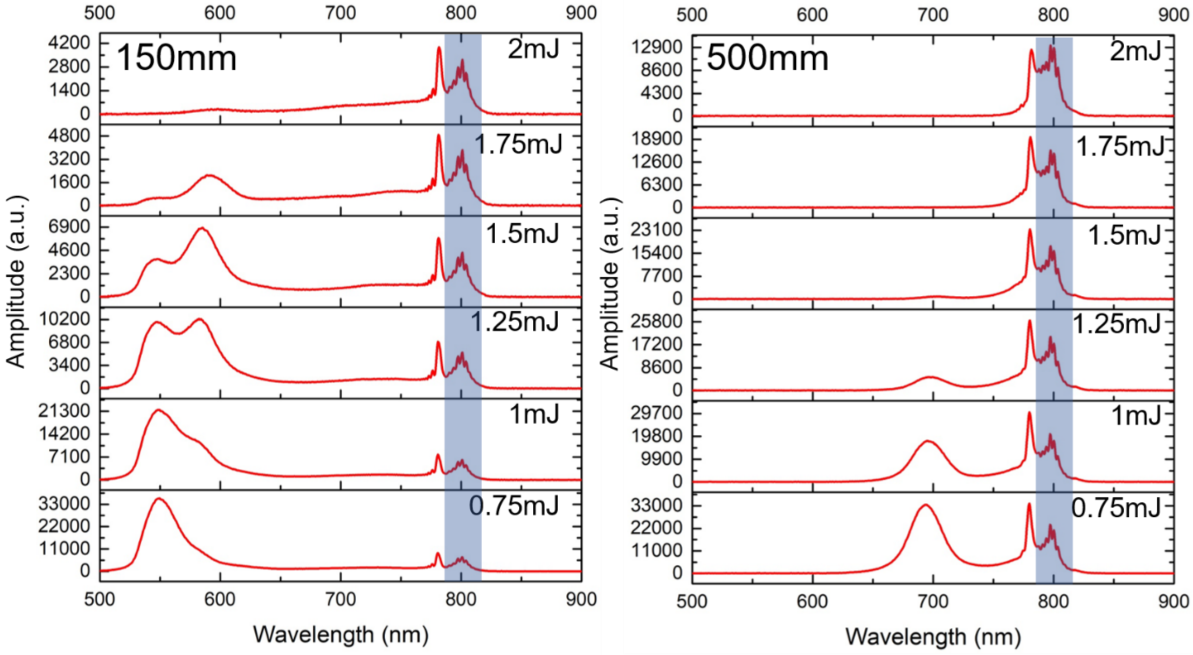

Figure 3.2: Comparison of SCG from filaments generated using lenses with focal length 150mm and 500mm over varying input energy. Shaded region shows the bandwidth of the pump pulse

3.3 Effect of Focusing element induced aberrations

Extensive work is being done to enhance and control various aspects of interaction of filamentation with the medium, done largely by tuning the intensity and collimating conditions of the lens of the input beam (discussed in the first chapter) [14]. Experiments in the laboratory have shown significant variations in filament characteristics like filament structure, intensity and supercontinuum emissions when generated under the same focusing geometry. This led us to design experiments so that one can identify other crucial input pulse characteristics other than intensity and beam curvature. Filamentation is a highly dynamic process with a number of competing non-linear processes which are highly sensitive spatio-temporal distortions in the beam profile, making simulation of filamentation under these input pulse distortions complicated and demands empirical support. The large spectral composition can be subject to linear and non-linear medium dispersion, reflecting in the spatio-temporal distribution of the pulse intensity [15, 16]. Knowing that the propagation and interaction of the femtosecond pulse with the medium in which it propagates, is highly sensitive to its temporal and spectral profile, the behaviour of tightly focused femtosecond pulses and subsequent filamentation was studied and characterized using different focusing elements, all having similar focal lengths so as to study the effect of focusing element induced aberrations on filamentaion. The filaments in this study were generated under tight focusing conditions. Filamentation under tight focusing conditions has shown to have contrasting emissions, intensity and dimensions as compared to that in loose focusing conditions, nevertheless the findings from the study can be extended to loose focusing conditions too. The experimental schematic is shown in figure 3.3.

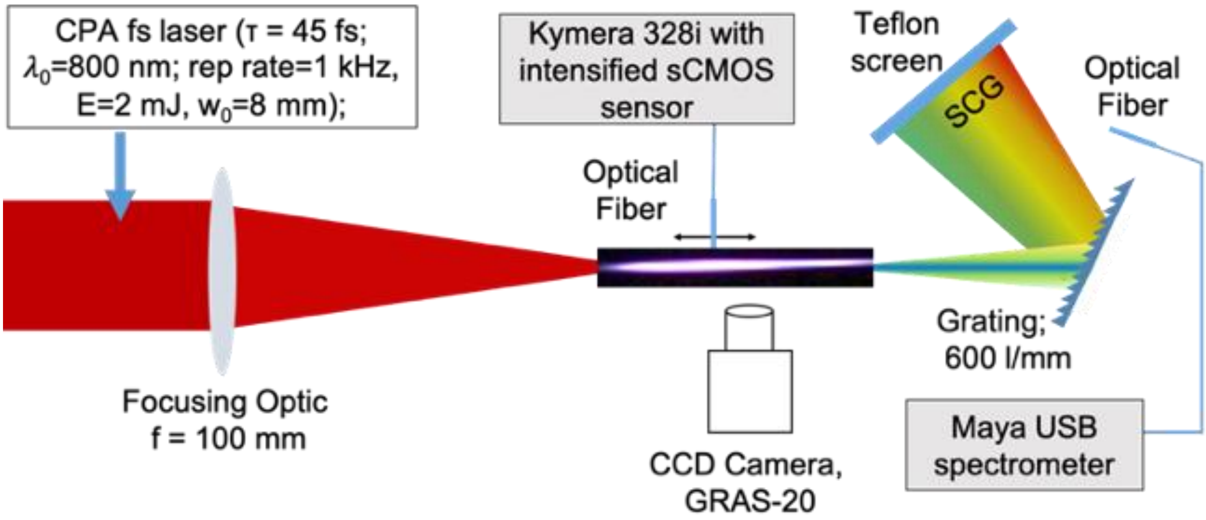

Figure 3.3: Experimental schematic. CCD camera to image the filament, Kymera 328i spectrometer used to analyae filament self-emission spectrum. Grating along with Maya 2000 spectrometer is used to analyse the SCG.

We have used different focusing optics with the same focal lengths, thereby keeping the focusing geometry constant. The input power of the pulse is also kept constant, thus narrowing the effects down to temporal and spectral aberrations. The spectral aberrations induced which were predominantly considered to be acting were first order and second order dispersion due to propagation through the lens medium. The first order dispersion causes a temporal shift in the pulse peak and therefore a delay between the pulse front and phase front, because of which we have an added curvature on the pulse front but not on the phase front (Pulse to phase front delay (PPD)). The second order dispersion or group velocity dispersion (GVD) induces Chirp in the pulse causing a broadening of the pulse. The group velocity dispersion is characteristic to the medium and the length of propagation in that medium. These temporal distortions caused due to dispersion vary radially along the radial position on the lens. The extent of Chirp or PPD induced due to the GVD and dispersion over the length of the propagation in the medium (*L(r)*) was calculated using equations (3.1), (3.2) and (3.3) as a function of the radial position on the lens. Another very critical aberration that needs to be considered is radially varying spherical aberration (SA). This arises due to lens design and influences the phase front. It is characterized by the longitudinal shift (LSA) of the rays from centre of the lens to the periphery of the lens at the focus. SA is defined according to the quality factor of the lens which is defined by the ratio of radii of curvature of the lens (R1, R2). The LSA of the Achromat doublet is 1mm, Bi-Convex lens is 1.7mm, Plano-Convex thick lens lens and thin lens are 1.2mm.

$$C(r) = \frac{2GVDL(r)}{\tau_0^2} \tag{3.1}$$

$$PPD(r) = \frac{L(r)}{v_g} \tag{3.2}$$

$$L(r) = 1 - \frac{r^2}{2}\left(\frac{1}{R_1} - \frac{1}{R_2}\right) \tag{3.3}$$

Chromatic shift in focus and increase in spot size were also estimated to be approximately ~77μm and ~0.5μm when the lens medium is fused silica having a focal length of 100mm. Although they are significant compared to Rayleigh range (~100μm) and spot size (~5μm) for a focused Gaussian beam, the spatial extent of the femtosecond filament is much larger than this to have a considerable effect in filamentation dynamics. As the input laser beam has most of its spatial extent close to the propagation axis we consider it largely paraxial, effect of aberrations due to marginal rays were considered to be negligible. We have discussed the influence of astigmatism on filamentation in the coming sections of this chapter separately. It should be noted that for the aberrations that have been mentioned the curvature of the beam discussed is the curvature of the pulse front. The curvature of the phase front is different from the pulse front. In the aberrations discussed, the spherical aberration acts on the phase front and the pulse front, but PPD acts only on the pulse front. Aberrations on phase front add to pulse front, but aberrations on pulse front do not add to phase front. This needs to be noted as dispersion and broadening of the pulse do not affect a monochromatic wave, but the aberrations such as spherical aberration or astigmatism will affect monochromatic waves as well.

Filamentation occurs as a result of a quasi-static interplay between plasma defocusing and Kerr Self focusing until the energy is lost in the numerous absorption and scattering processes. The pulse curvature is positive or negative in the filamentation regime depending on the dominating mechanisms i.e. Kerr Self focusing or plasma defocusing. The temporal distortions that come into play before onset of filamentation are dispersion and Group Velocity Dispersion (GDD) which can be understood as pulse front delay and pulse broadening. It was found that for the different focusing optics the filament structure and peak intensity vary distinctly, largely because the input spatial and temporal pulse properties are modified. These modifications to pulse curvature are understood at a point before filamentation begins and then correlated to the structure. The changes in the filament need to be methodically correlated to the aberrations induced by the lens.

Five different focusing elements were used in the study:

a) Off Axis Parabolic mirror (OAPM)

b) Dispersion corrected fs Thin lens

c) Thick BK-7 Bi-Convex lens

d) Thick BK-7 Plano-Convex lens

e) Achromat doublet.

These optics were chosen such that they had varying degrees of aberrations and varying degrees of group delay dispersion (GDD). The OAPM was the ideal focusing element with no apparent aberration, with only some possible degree of cylindrical asymmetry (arising only due to optic element alignment flaws) and no GDD. The thin lens was designed for femtosecond pulses with low group delay dispersion (GDD), because of which they have low overall GDD and PPD but is radially varying. The thick lens (Plano-convex and Bi-Convex lens) induce both radially varying and overall GDD and PPD degree of spherical and chromatic aberration as well as high GDD due to the thickness. It is to be noted that although the radii of curvature for the thick lens are different, the length of propagation in the lens according to the radial position are the same, because of which we find that the main difference between the two thick lens is the longitudinal spherical aberration (LSA). The Achromat doublet lens induces good amount of overall GDD and PPD. The radially varying aberrations in the Achromat while being minimal, once estimated show that they induce a curvature in the pulse front which is opposite that of the other optics. The estimated PPD and Chirp are shown in figure 3.4. The intensity of the light and electron density were estimated from the visible emission along the propagation of the filament.

The added curvature on the pulse front much before absorption processes start was simulated from the dimensions and material properties of the focusing element given in table 3.1.

Table 3.1: Optical properties of the different lenses (Source: SCHOTT optical glass data sheet) .

Optical element		**Thin lens**	**BCX**	**PCX**	**AD**
Medium		Fused Silica	BK-7	BK-7	N-LAK22; N-SF6HT
Refractive index		1.458	1.517	1.517	1.651; 1.805
Abbe Number		67.8	64.2	64.2	25.36; 55.89
First order dispersion ($dn/d\lambda$, μm^{-1})		-0.0352	-0.0418	-0.0418	-0.0601; -0.1587
Second order dispersion (k'', fs^2/mm)		57.540	70.372	70.372	106.53; 328.60
Lens dimensions (mm)	d	4.8	9.4	9.7	13.0; 2.0
	R_1	45.9	101.73	51.7	65.8; -56.0
	R_2	Inf	101.73	Inf	-56.0; -280.6

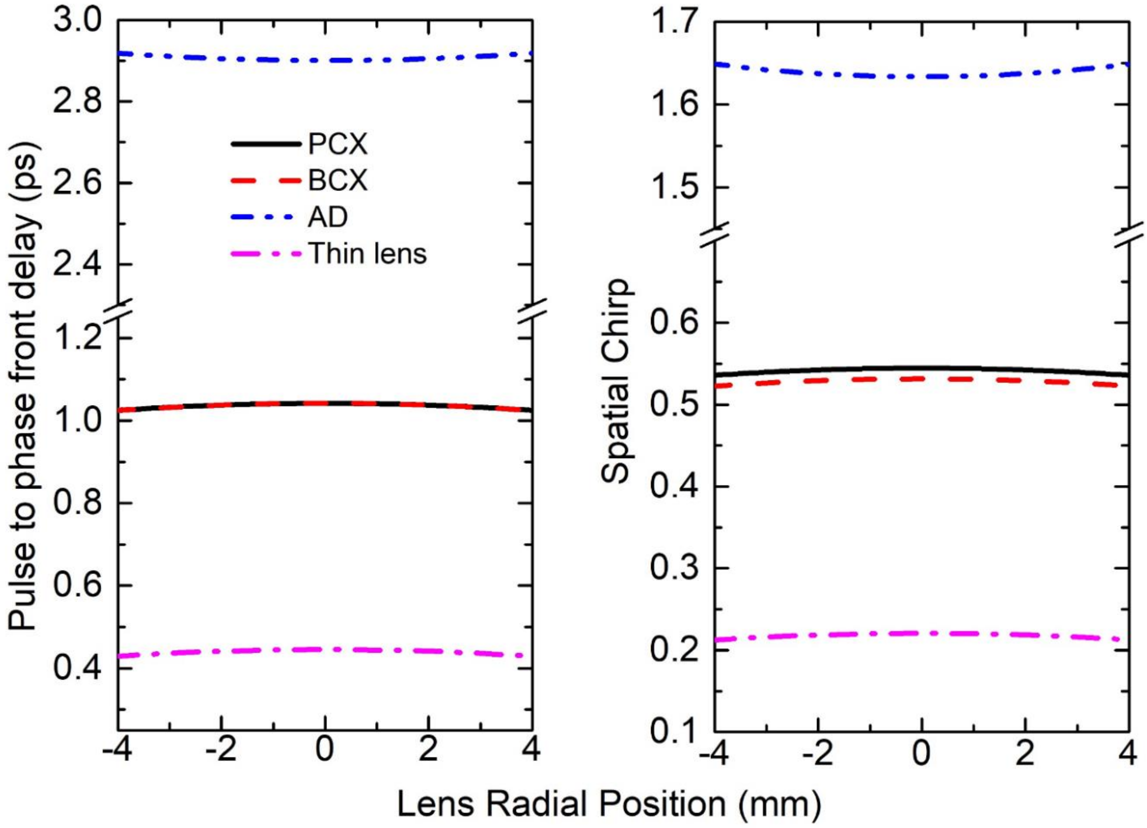

Figure 3.4: Estimated (a) Radially varying Pulse to Phase front delay and (b) the spatial chirp induced for different focusing elements.

We first characterize the different optics on the basis of the extent of the pulse curvature and aberration induced. In an Achromat doublet, the added curvature on the pulse front due to PPD is insignificant and opposite that of the other optics. Although the PPD and Chirp are maximum at the centre of the beam for this, it does not vary radially. The spherical aberrations induced due to this lens is also minimal (LSA~1mm) because of the dimensions of the lens. The only aberration to pulse front curvature is that added due to SA which is also imposed on the phase front, further getting minimized near the focus due to Kerr Self-focusing. The thin lens was found to have both spherical aberration (LSA~1.2mm) and radially varying PPD but low overall PPD. The thick lenses (PCX and BCX) also were found to have SA and both overall and radially varying PPD, LSA~1.2mm for PCX and LSA~1.7mm for BCX. In general applications PCX is more suitable for focusing a paraxial beam, whereas a BCX is optimal to collect light from a nearby point. These three lenses (thin lens, PCX and

BCX) induce an added pulse curvature due to the radially varying PPD. The main difference between the thick lenses and thin lenses is the PPD and Chirp induced at the centre of the beam. The PCX and BCX mainly differ in the extent of spherical aberration induced. The aberrations and their effects on the output pulse are summarized in table 3.2.

Table 3.2: Calculated Aberrations for the different focusing elements and their effects on the pulse.

Optical Element	AD	Thin lens	BCX	PCX
Thickness at the centre (mm)	15	4.8	9.4	9.7
Pulse to phase front delay (PPD) at centre of beam (fs)	2900	445	1041	1041
Radially varying pulse to phase delay	No	Yes	Yes	Yes
Longitudinal Spherical aberration[a] (mm)	1	1.2	1.7	1.2
Chirp at the center of the beam	1.6	0.22	0.53	0.54
Resultant Pulse width due to aberrations (fs)	160	47	58	58

The observations from the experiment are shown in figure 3.5. We find a large contrast in the filament structure from the multiple optical elements. The observable structural changes can be distinctly classified and described by,

a) Off Axis Parabolic mirror; the filament structure shows that the most intense part is at the end of the filament which has a length of ~3.5mm. The filament structure has a very characteristic shape with a tail (~3mm) and a bright end.

b) Achromat doublet, brightest part of the filament which was ~3mm in length, was found to be at the end. The intensity of the filament was found to be least among all the optics used in this case. The filament from the Achromat was also found to have the characteristic

c) Thin lens, most intense part is in the centre of the filament which was ~1mm long. The self-emission images indicate multiple filament formation which could be due to multiple breakdown or due to the dynamic interplay of Kerr self-focusing and plasma defocusing. The observable filament is narrower than the filaments from the thick lens but is thicker than the filaments observed from the Achromat doublet and OAPM.

d) Bi-Convex (BCX) and e) Plano-Convex (PCX) Thick lenses made of BK-7, the most intense part of the filament is at the centre of the filament which is ~1mm. Contrary to intuition considering the large amount of temporal and spatial aberrations, the filaments observed here were found to have the maximum light intensity among all the optics including the OAPM. The filaments are the widest for these lenses. The main difference between the PCX and BCX is the onset of filamentation, onset of filament from BCX was observed to overshoot other filaments by ~1cm.

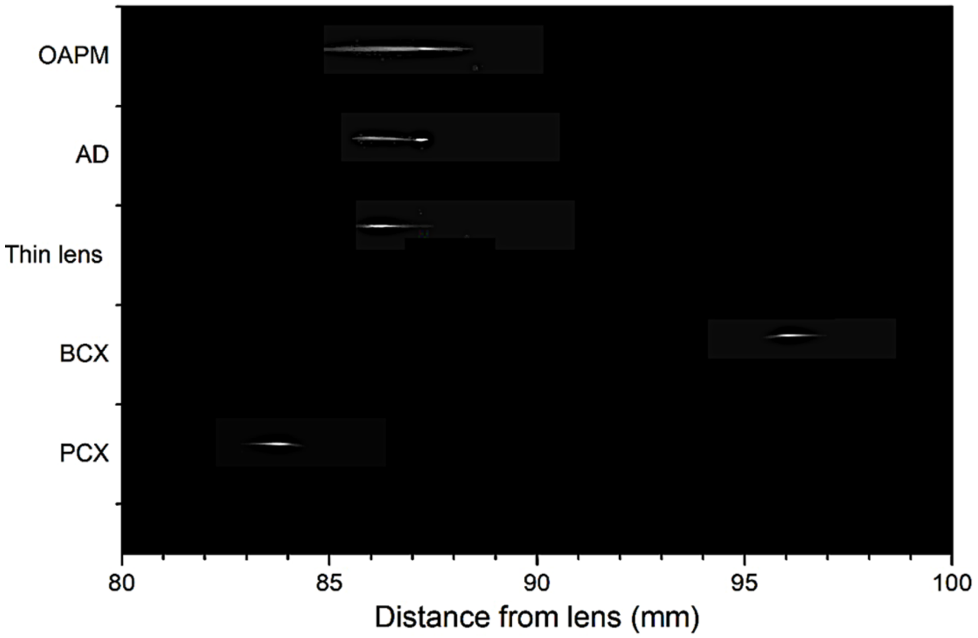

Figure 3.5: Filament images of the different focusing elements with distance from lens on the x-axis

The filament images show two contrasting filament shapes and dimensions, 1) filament with long tail and intense end, filament is ~3mm long, like the filaments generated from the OAPM and Achromat doublet, 2) Filament is 1mm long with most intense part at the centre, generated from the Thick lenses and thin lens. Taking into account the first type of filaments, the Achromat doublet lens has only SA and overall non-radially varying dispersion, but filament structure does not differ from filament from OAPM. The Achromat lens also induces

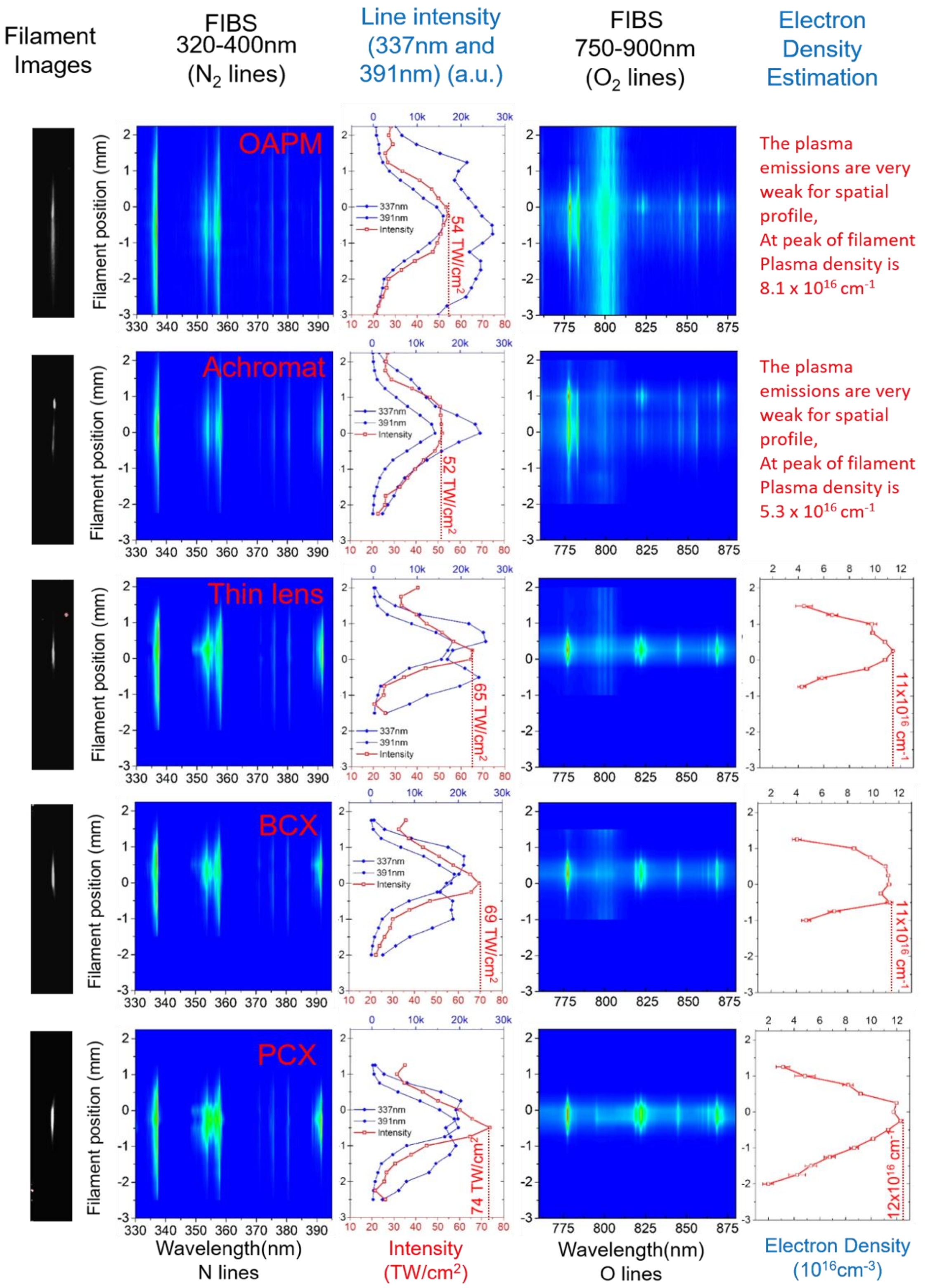

The plasma emissions are very weak for spatial profile,
At peak of filament Plasma density is 8.1×10^{16} cm^{-1}

The plasma emissions are very weak for spatial profile,
At peak of filament Plasma density is 5.3×10^{16} cm^{-1}

Figure 3.6: 1st Column: filament images; 2nd column: filament induced breakdown spectrum in air for Nitrogen lines (320nm-400nm); 3rd column: The filament intensity estimated from the nitrogen fluorescence lines at 337nm and 391nm; 4th column: filament induced breakdown spectrum in air for Oxygen lines (750nm-900nm); 5th column: Plasma density that was estimated from the stark broadening of the line at 845nm.

large overall Chirp and PPD, with minute radial variation with opposite curvature when compared to other transmitting optics.

When comparing the optics of the second type, with filaments of dimension ~1mm, the filament is restricted at 1mm length, this is due to the radially varying PPD which comes into play during propagation only at the intense regime of filamentation causing its early collapse, but does not affect the onset of filamentation. Onset of filament generated from the BCX (LSA~1.7mm) was found to overshoot that of the filament from thin lens and PCX (LSA~1.2mm) by 7mm (7 times filament length). This is because of the added curvature on the phase front and pulse front due to SA, which adds an opposing curvature to the curvature caused by Kerr self-focusing and radially varying PPD, thereby extending the onset of filamentation serving to show SA influence on filament onset and formation. The spherical aberration influences the onset of filamentation and radially varying PPD influences the collapse of filamentation.

Filament induced breakdown emissions from two spectral regions of 320 – 400 nm and 750 – 900 nm were mainly collected. The spectra shown are corrected for Bremsstrahlung background. These regions predominantly represent the emissions from N_2 and O_2 respectively, which are the major constituents of the molecular mixture of air. The ratio of the spectral emissions of N_2 over the 320 – 400 nm region helps us estimate the intensity of the filament [8]. Spectral lines of N_2 have more longitudinal extent than the visible images captured for all the focusing optics. The stark broadened line width of O_2 emission at 845 nm from the first ionized species of neutral oxygen molecule, is used to estimate the plasma electron density within the filament [17]. Figure 3.6 shows the filament induced self-emission in both the spectral regions and the corresponding intensity and electron density estimation.

The Supercontinuum generation is due to self-phase modulation which occurs due to the rate of change of refractive index of the medium causing a broadening in the pulse which is indirectly dependent on the Kerr effect and plasma build up. Self-steepening of the trailing part of the pulse causes the pulse to shorten leading to a broadening of the spectral distribution. The extent of broadening and the amount of Supercontinuum generated depends on the Intensity and the length of the filament. The broadening extent of the supercontinuum is therefore directly proportional to the peak intensity and the filament length, while the amount of supercontinuum generated depends on the length of the filament. The supercontinuum generation shows significant variation among the filaments from the different optical elements shown in figure 3.7.

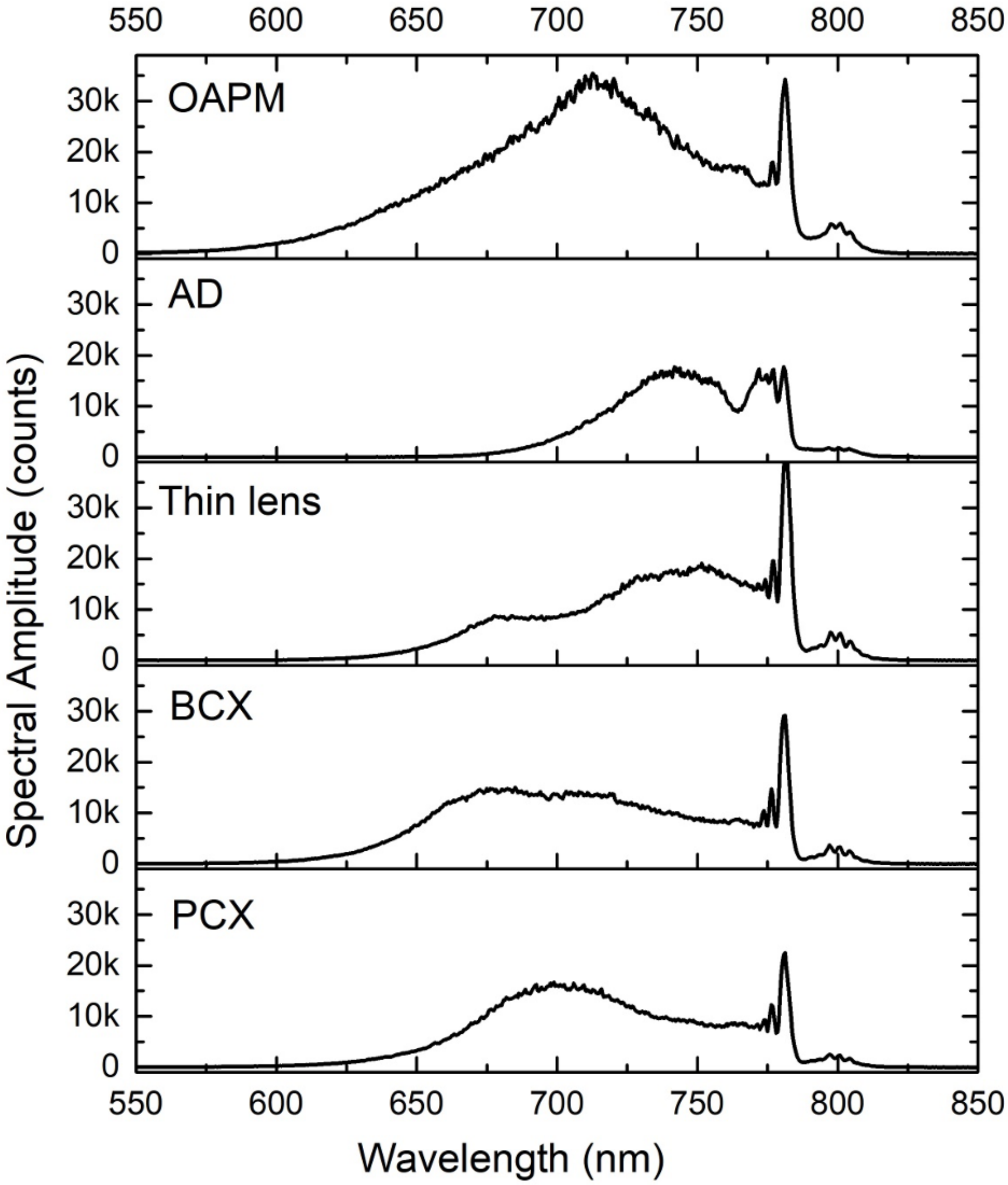

Figure 3.7: The SCG spectrum at zero chirp from the different focusing optics.

SCG for the transform limited pulse shows that the chirp induced by the elements reduces the SCG. As the achromat induces maximum chirp the extent of SCG characterized by the minimum wavelength is least here however since the spatial extent of this filament is more the Supercontinuum generated is higher than the other transmitting lenses. The other transmitting optical elements (thin lens, PCX and BCX) achieve higher filament intensity but smaller spatial extent due to early termination of filament caused by radially varying PPD. Moreover, the broadening into the higher frequencies also increases with increase in plasma density. Hence, we observe a larger broadening especially towards the higher frequencies when compared to Achromat, but lesser supercontinuum is generated because of small spatial extent. The Off-axis parabolic mirror generates maximum supercontinuum in terms of broadening extent and amount of generation as it does not induce any chirp and the filament does not terminate due to radially varying PPD.

Filament was generated using reflecting and transmitting optics. The filament generated under the focusing conditions of reflecting optics were found to contain the least number of aberrations, was compared to filaments generated WITH transmitting optics. The influence of different aberrations on the filament properties was explored under the same focal geometry. This has shown the large structural differences induced in the filament due to the lens composition and dimensions. It was observed that although the presence of media induces PPD and pulse broadening, it is the extent of the spatial variation of the PPD and overall chirp that influences the filament structure. Further we have found that the pulse to phase front delay plays a much larger role as compared to GDD as we have seen for filaments observed from lenses with (Thin lens) and without (Thick lens) dispersion correction. Although the GDD and dispersion induced by Achromat doublet is high, the filament behaviour in this case was found to resemble that of the OAPM, showing that there exists a significant but non-radially varying PPD, which is not critical for filament structure. We find that the presence of a radially varying PPD comes into play only at the filamentation regime restricting the filament length. The SA was also found to influence the onset of filamentation, because of the added curvature at centre of the lens. The spherical aberration and radially varying PPD together enable us to control the onset and collapse of filamentation. We have seen that the variation of input spatial (SA) and temporal aberrations (PPD) can affect a large extent of the filament characteristics like; 1) Filament length, as shown by radially varying PPD, 2) Onset of filamentation, as seen with variation of SA or chirp, 3) SCG, as it is an outcome of filament length and intensity, 4) Electron density, as seen for different extent of radially varying GDD. We have successfully correlated the various optical elements and aberrations to the filament characteristics. As seen above we have also enabled to a large extent appropriate usage of optical elements, for instance where we have counter intuitively shown that maximum confinement of energy was achieved with PCX at high chirp without loss in peak intensity.

3.4 Effect of Chirp of input pulse on filamentation

Intense femtosecond pulses are generated by compressing stretched and amplified pulses of ~2ps duration [7]. The 'compressing' of these pulses is done using a grating pair at the exit of the regenerative amplifier, which puts all the quadratic phase shifted frequency components of the stretched pulse in phase. As the optimum distance between a grating pair gives us a transform limited pulse, deviation from that separation therefore induces a quadratic phase in the frequency distribution of the pulse. We capitalize on the ability to vary this separation and quantify the modulations to the pulse profile (described in the 2nd chapter). The input pulse chirp was found to also demonstrate many observable changes in filamentation [18, 20]. As a chirped pulse has lower intensity it will have a longer self-focusing distance i.e. the onset of filamentation will increase. As air induces GVD it was proposed that a negatively chirped pulse (pre-compensated pulse) will compress close to a transform limited pulse after a particular distance of propagation in air [21, 22]. Chirped femtosecond pulses can alter filament behaviour significantly as also will be shown here and in the coming chapters. As chirping of femtosecond pulses causes a pulse broadening, positively and negatively chirped pulses of the same chirp value will have similar temporal profiles. We have understood that the changes in filamentation which are symmetric with positive and negative chirp variation are due to pulse broadening i.e. pulse duration changes and the changes that are not symmetric as those that depend on the sign of chirp or otherwise dependence on the leading and trailing frequencies.

According to our classification of tight and loose focusing conditions we have shown in the figure 3.8 the filament images with varying chirp. The filament generated from the 500mm focal length lens was found to vary quite symmetrically with chirp variation. The distance at which onset of filament occurred was found to increase with chirp, which is as expected as the increase in pulse duration causes a drop in peak intensity, causing an increase in self-focusing distance. The filament structure for those generated with the 150mm lens on the other hand has more complicated variations with change in chirp, in which we not only observe changes in transverse filament emissions, also indicating increase in spot size but also dramatic variations in filament onset and structure. One does not observe a large broadening towards the higher frequency side from Supercontinuum of loosely focused filaments, but the supercontinuum was found to be more prominent for positive chirp values as compared to negative chirp values. We have moved according to the number of steps of compressor grating separation, in the range of 60 steps (-30 to +30 steps) changes the chirp from -3 to +1.5 chirp. Beyond this range the intensity in the pulse falls due to increase in pulse duration because of which we do not observe an observable filament for the input powers available and used in the study.

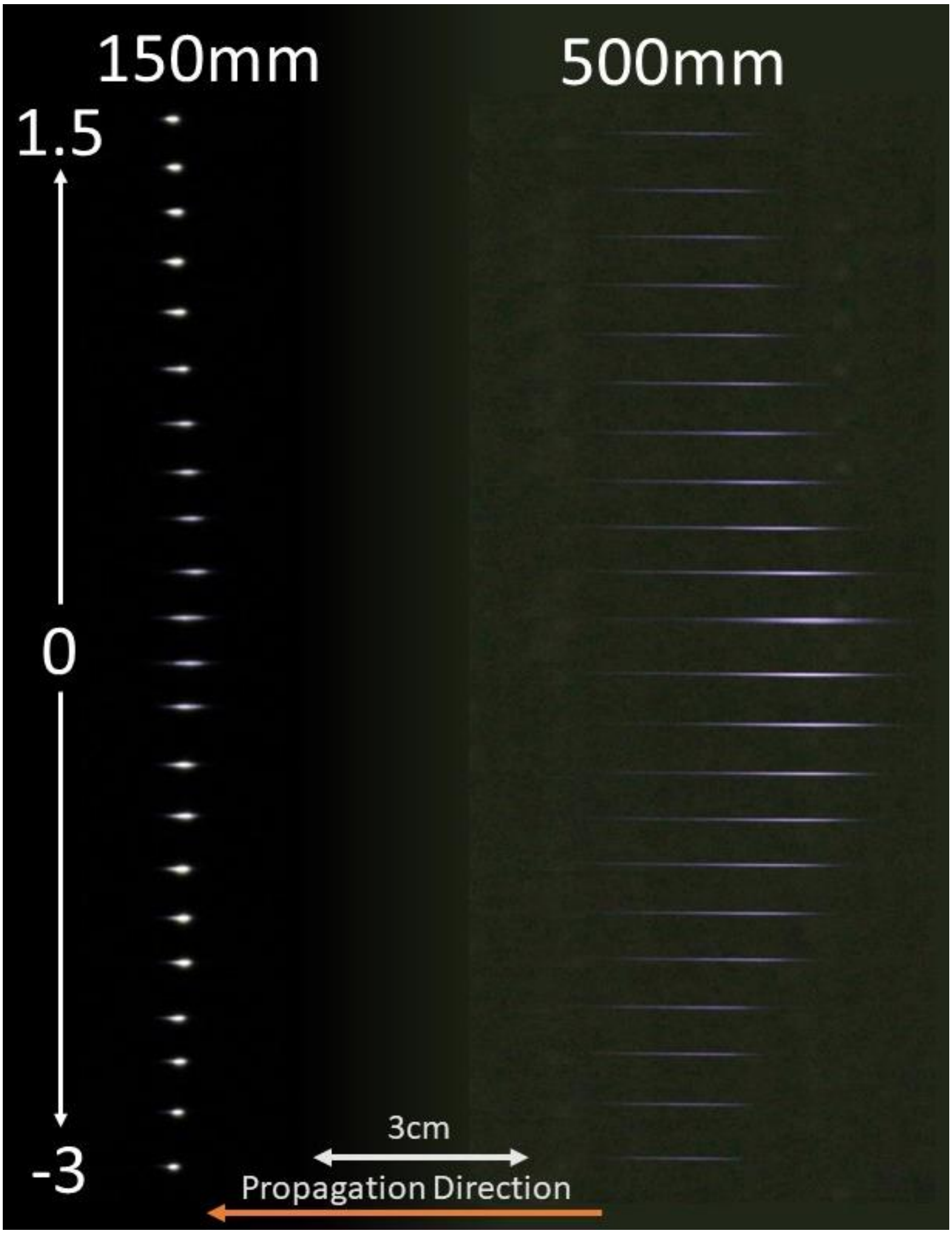

Figure 3.8: Filaments generated from 150mm and 500mm lenses while varying the chirp vertically.

The shortage of space and focusing optics to generate filaments under different focusing conditions has pushed us to use a combination of lenses to create the desired focusing geometry. Although this offers a range of tunable focusing geometries, the usage of two lenses induces larger losses and dispersion due to increased propagation in the lens medium. Lens combinations cause a much more gentler / slower focusing in comparison to single lens-slowly varying beam curvature. The difference in the filaments generated from a single lens and a combination of lenses was quantified in the first configuration described in this chapter. As we do not find drastic changes in filament properties other than reduced transverse emissions by ~50% and filament length by ~15%. The combination was used to create three different focusing geometries. The images of the filaments generated with chirp are shown in figure 3.9.

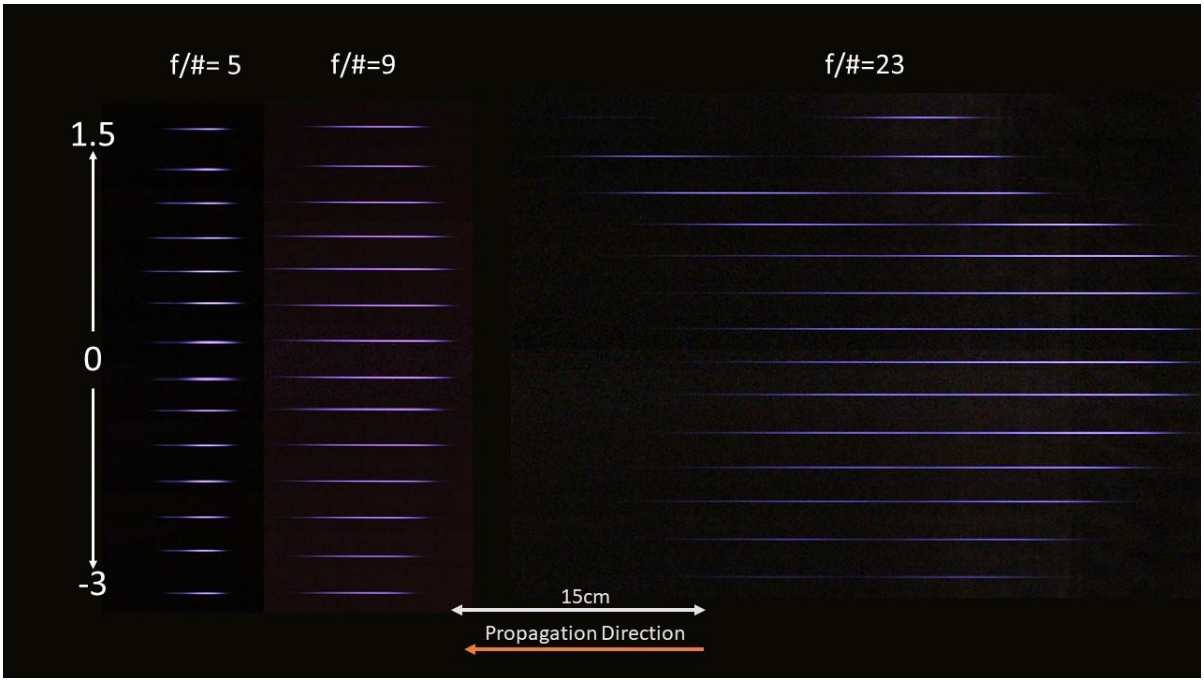

Figure 3.9: Filaments generated using a combination of two lenses (f_1=-100mm; f_2=150mm) at three different focusing geometries for various chirp values.

The long filaments that were generated using this setup using a chirped input pulse showed longitudinal double filamentation structure for both positive and negative chirp. As the plasma density is not high (~10^{15} cm^{-3}) for loosely focused filaments, the long propagation regime of ~0.5m causes self-compression of the stretched pulse, because of which we observe refocusing of the laser pulse to form a secondary collinear filament. The supercontinuum for the three different focusing elements with varying chirp is given in figure 3.10. The loose focusing regime was found to have large broadening towards IR as expected. This is due to drop in plasma density and long propagation regime.

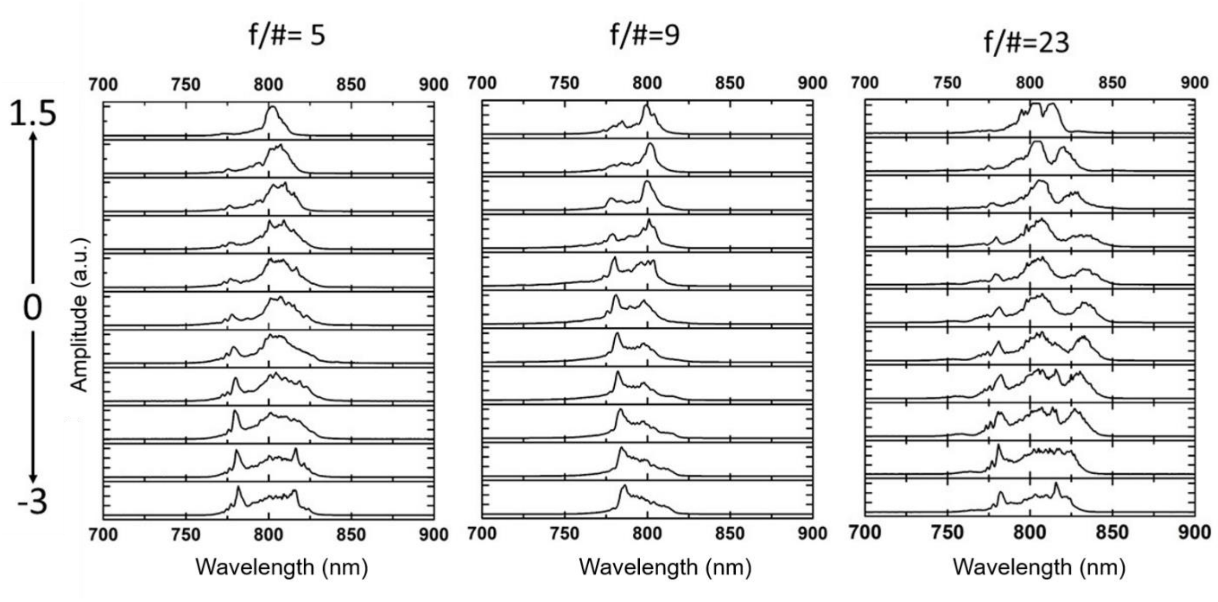

Figure 3.10: Supercontinuum spectrum from the filament generated for three different focusing geometries obtained using the lens combination.

Under tight focusing conditions as described earlier the filament variations are very drastic and prominent. We have therefore also studied the influence of aberrations induced by the optical elements on filamentation from chirped pulses. To do this study we have used the Filament images, Supercontinuum emission and self-emissions from the filament. The filament images and the corresponding supercontinuum spread are shown in the figure 3.11. We find that some of the optics generate bright filaments with chirp rather than with zero chirp, however spectral study at these regions does not show increase in light intensity. Filaments are bright at the optical wavelengths but not at UV wavelengths hence no enhancement in intensity. These bright filaments are caused as with increase in chirp the pulse duration increases, thereby approaching the average collision time of free electrons in air. The role of overall and radially varying GDD induced by the optics manifesting as pulse broadening can be observed in the chirp study.

The maximum SCG spread for an Achromat is observed at a significantly shifted value of Chirp ~2. The filament becomes almost invisible at this point, again showing that brightness of filament is not most intense part of filament. The maximum SCG spread is slightly shifted (Chirp value~1) for the thick lenses also. As the induced chirp by the element is positive and

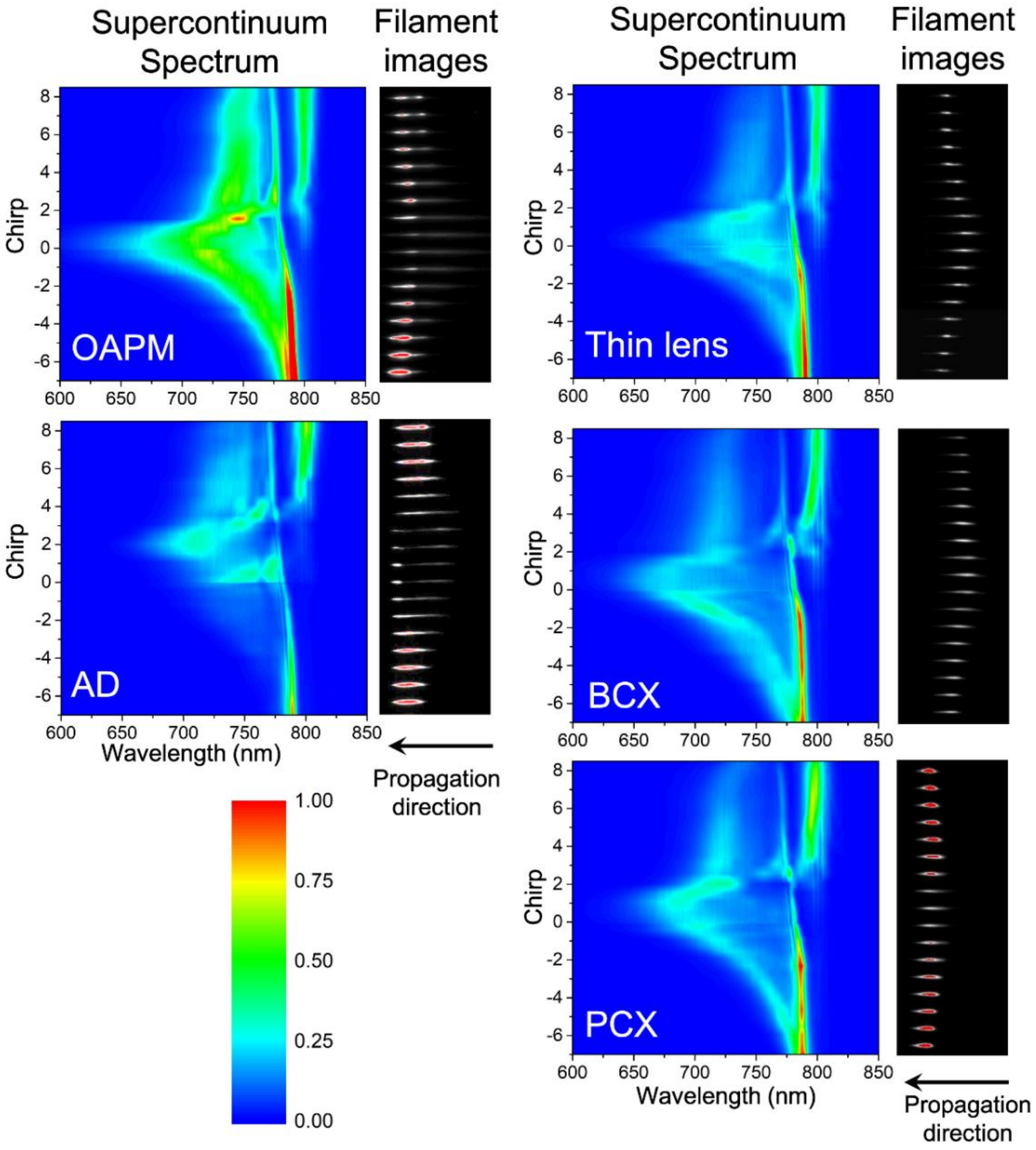

Figure 3.11: Supercontinuum spectrum and filament images as a function of input pulse chirp (spatial extent of each image window is 5.25mm).

the chirp value at the peak broadening extent is increasing with the increased chirp we can say that the increase in broadening extent at positive chirp is not because of compensation of induced chirp, but due to the overall PPD. When a chirped pulse experiences PPD the wavelength distribution of the input pulse shifts to the trailing wavelengths which will be lower wavelengths for positively chirped pulses and vice versa. Therefore for a positively chirped pulse we see an increase in broadening extent as chirp is increased till a particular value of chirp where it starts dropping again since the induced chirp also reduces the peak intensity of the pulse too. This is the positive chirp at which we get maximum Continuum broadening. This positive chirp value is directly proportional to the overall PPD induced as shown from the observations. The minimum wavelength found for the Supercontinuum generation from the different focusing elements with chirp is shown in the figure 3.12.

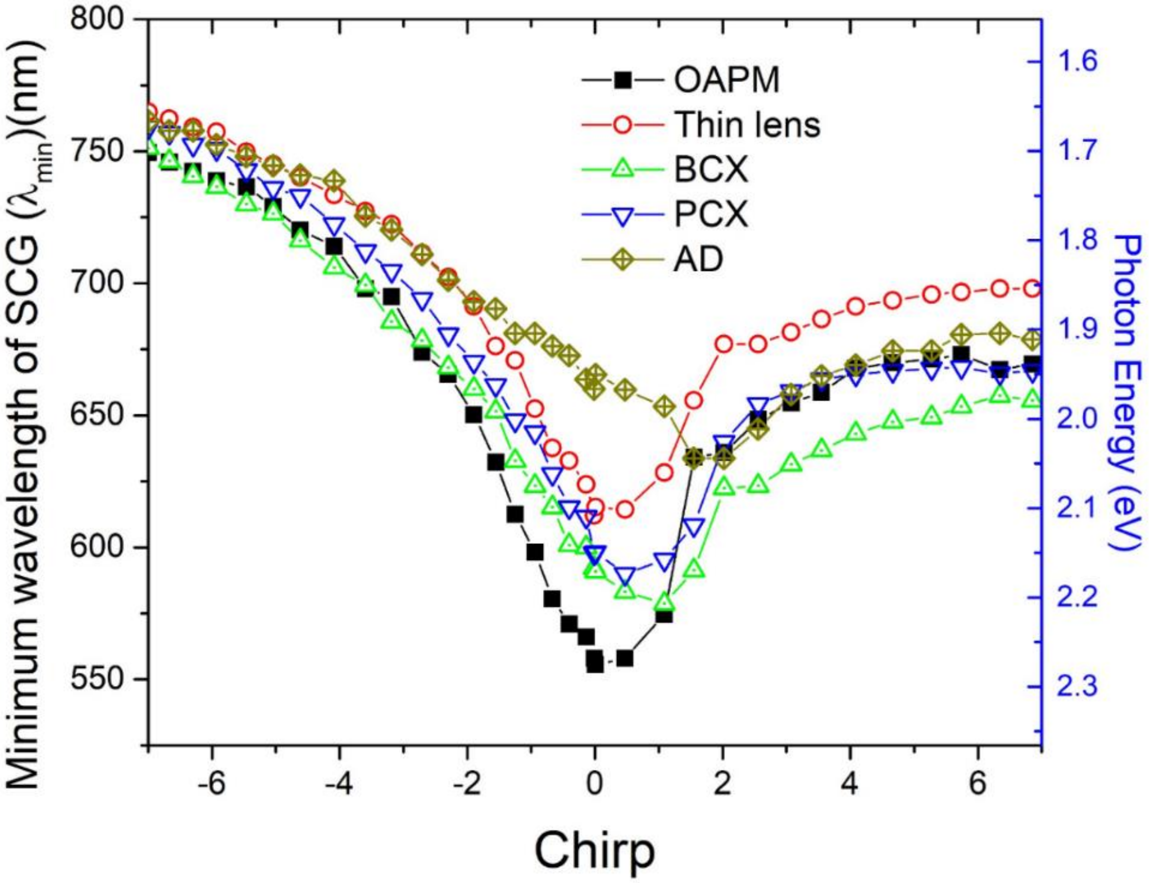

Figure 3.12: Variation of Minimum wavelength of SCG with chirp.

The chirp study of the lenses with filaments of length 1mm also show interesting results. Earlier study showed that the pulse curvature from PPD and SA define the filament structure, in this respect the PCX and thin lens have lesser SA compared to BCX, thereby influencing the onset of filamentation. Although the PCX is thicker and made of a different material when compared to the thin lens, the only difference that was established is the overall PPD, which does not influence the curvature of the pulse front. Filament from the thin lens undergoes minimal broadening. It is known that a chirped pulse undergoes larger pulse shift when propagating through a dispersive medium, therefore as the chirp is increased the radially varying PPD is much larger for chirped pulses for thick lenses, because of which the dominant aberration in a thin lens becomes SA with increase in chirp and the filament onset moves away from the lens, and also avoids collapse of filament at high chirp.

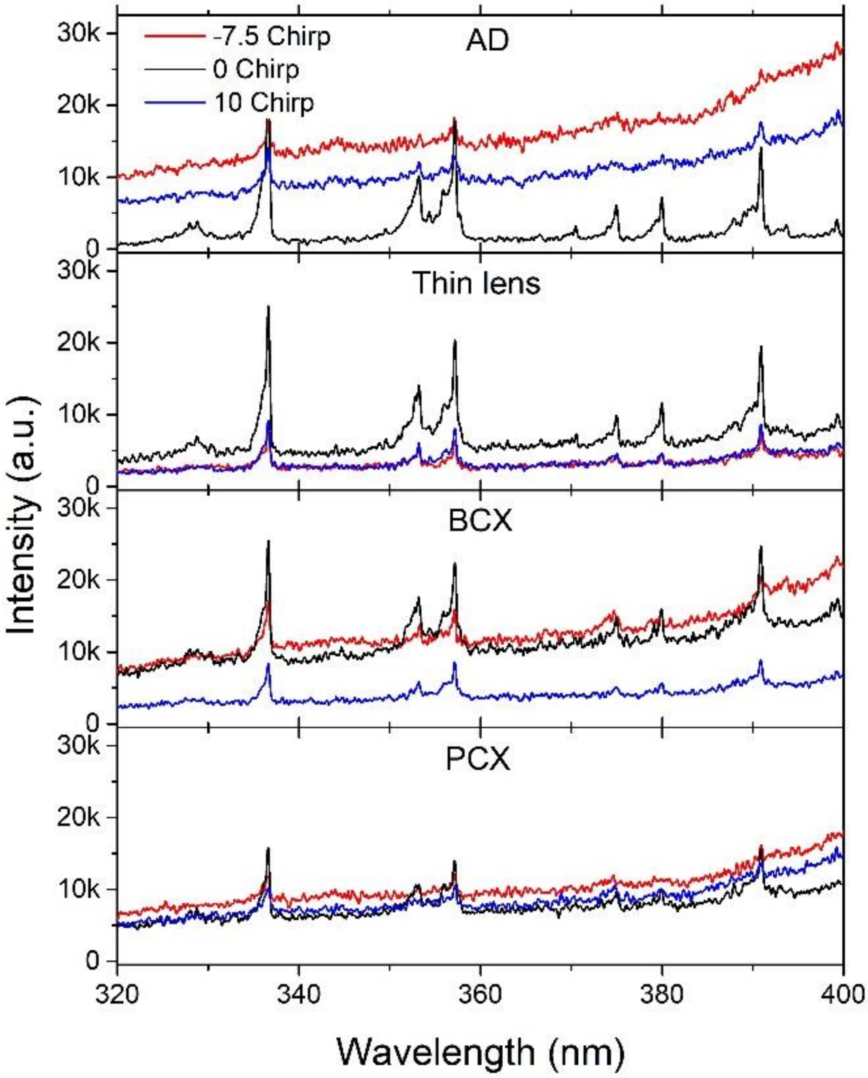

Figure 3.13: Filament self-emission spectrum in the range of 320nm-400nm for the different transmitting focusing elements at different chirp values.

The lens which have the dominant aberration as SA at high chirp i.e. thin lens and BCX do not see collapse of filament. Moreover, for PCX, with increase in chirp the dominating aberration is not only PPD but also radially varying GDD, with large pulse broadening at center of the beam, such that the pulse is shorter at the periphery of the beam than at the center. The spatial intensity profile of the beam is an accumulation of the input pulse front and the intensity reduction profile due to pulse broadening after propagating through the lens. This shifts the intensity of the pulse towards the edges of the beam, further enhancing the collapse of the filament. This is observed at large chirp for Achromat doublet lens too. The

BCX on the other hand also induces the same amount of GDD but we see that the filament behaviour with varying chirp is completely different from that of the PCX. This is because although the pulse is broadened, the induced SA which is much larger than PCX and Achromat doublet holds the peak intensity in the center of the beam making SA the dominating aberration. The images of the filaments from PCX and BCX over chirp show that they do not move in space, but the dominating mechanisms restricting their movements are different, for PCX it is the collapse of filamentation due to radially varying broadening and PPD, but for BCX it is SA. For the thin lens we find that at zero chirp the dominating mechanism is radially varying PPD but SA becomes more significant as we increase the chirp, which we can see as the filament moves forward with increasing chirp. The FIBS spectrum that is used to estimate the intensity is shown in the figure 3.13 and one can see the tail of the large continuum in the visible spectrum which is characteristic to some of the filaments at high chirp.

3.5 Filamentation under Lens tilt effect

For filament self-emission spectrum, it was observed that tilting of the lens used for the creation or localization of the filament doubled the signal to noise ratio of the back scattered fluorescence emissions during filament interaction with air [23]. The suppression of supercontinuum from filamentation because of lens tilt is one of the main reasons for this. The filament was also found to get elongated and eventually split into two filaments at a given lens tilt angle The effect of lens tilt was understood as a combination of two different planes of focusing namely, the sagittal and tangential focusing planes. Dergachev et al reported the filament elongation and splitting associated with supercontinuum suppression under loose focusing conditions [24]. Simulations incorporated a wavefront with cylindrical asymmetry undergoing propagation effects such as dispersion, Kerr-effect, multiphoton ionization, diffraction and plasma defocusing. They have used the same model as described above to explain filamentation under lens tilt. The difference in the two foci from the two focusing planes was estimated to be $\Delta f = f \sin\theta \tan\theta$ (f is focal length; θ is tilt angle). Saba Zafar et al have also shown the effect of astigmatism in filamentation in fused silica [25]. The conversion efficiency of supercontinuum was calculated with increase in lens tilt and they observed a sudden drop in conversion efficiency at 8^0 Lens tilt angle.

In our experiment we have primarily used the 150mm and 500mm lens to generate the filaments under astigmatism. We know that lens tilt induces some form of aberration in the wavefront. In the works detailed above, the aberration that was induced is that of astigmatism i.e. that caused due to difference in focus of the rays from sagittal and tangential plane of focusing. Although this treatment of lens tilt effect considers the tilted plane and non-tilted plane separately to explain the formation of two focii. This does not consider the tilt in the wavefront and assumes that rays coming from opposite sides of the rotational axis have the same focal length. We approach the lens tilt effect by considering the aberration as a comatic aberration where the lens tilt causes an elongation of the focus of the rays coming from the sagittal plane. As discussed earlier aberrations influence filamentation drastically. Lens tilt even at very small angles causes significant changes in filament structure because of the combination of the other aberrations with lens tilt especially in tight focusing geometry. To verify this we have imaged the filament while tilting the lens along the horizontal axis. The filament moves towards the lens with increase in lens tilt angle, but we find that the filament can be seen to split non-collinearly i.e. the filaments are forming from two different halves of the beam rather than two different planes of the beam. This is especially visible in tight focusing geometry.

Figure 3.14: Filaments generated using a 150mm lens under lens tilt.

We have also collected the transverse Filament induced breakdown spectrum along the filament. The SCG was also collected after separating it from the pump pulse using a grating. Figure 3.14 shows the filament images for a 150mm lens. In the tight focusing geometry we find that for small tilt angles the filament onset is before the 0^0 lens tilt filament and proceeds much beyond this filament. The images from figure 3.14 clearly show an asymmetry in the filament formation indicating that the two foci formed are not from the tangential and sagittal focus but from the two halves of the wavefront curvature. The filament therefore gets extended because different rays focus at different points according to the vertical position of the lens from which the rays are arriving. At a defined angle the wavefront splits creating two filaments. The images were taken again for the filaments generated by these lenses with smaller steps in angle variation. The images are shown in figure 3.15.

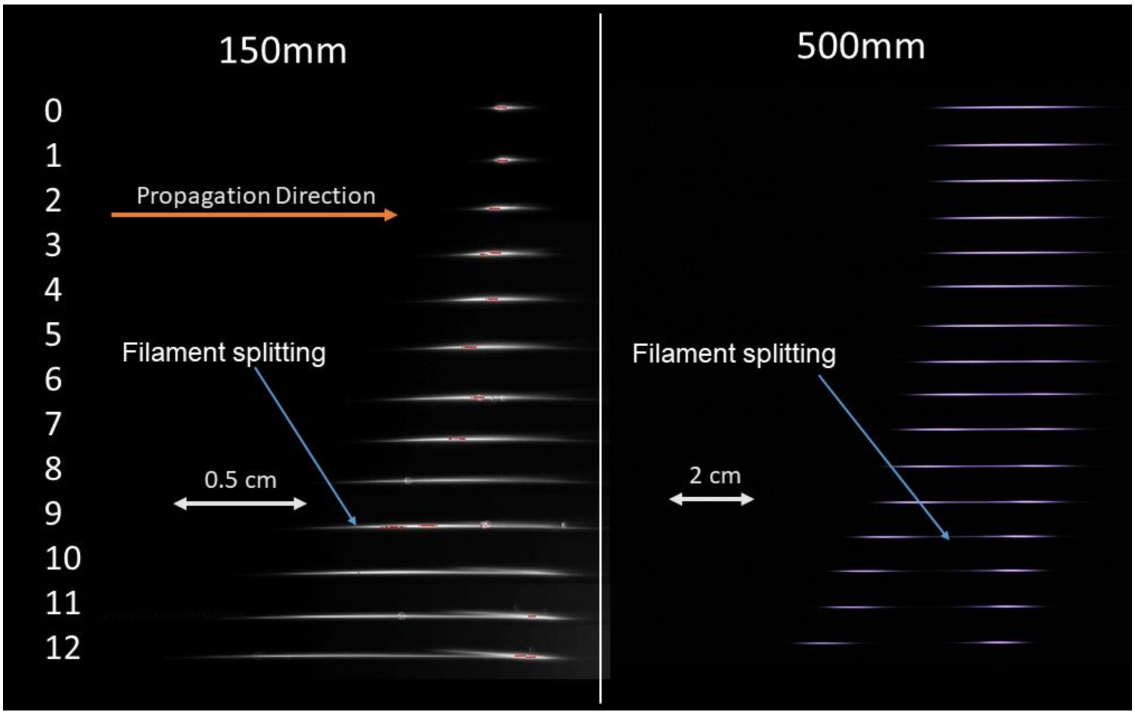

Figure 3.15: Images of filaments generated from 150 mm (left) and 500 mm (left) lens undergoing lens tilt from 0-12 degrees.

The FIBS was taken and the intensity of the filament was estimated along the propagation for the different angles of lens tilt. The FIBS signal is shown in figure 3.16.

The intensity estimation results are shown in figure 3.17. This spectrum collection was done with the tilt along the vertical axis. Spectrum collection with filament from 150mm lens was done up to 4mm because the instability in the wavefront causes loss of collinearity in the filament because of which there will be significant error in the spectrum collected. The filament generated from 500mm lens was found to be more collinear under lens tilt and we were able to acquire the FIBS signal and estimate intensity up to lens tilt of 12 degrees after which filament is not intense enough for us to acquire good signal to noise ratio from the FIBS signal.

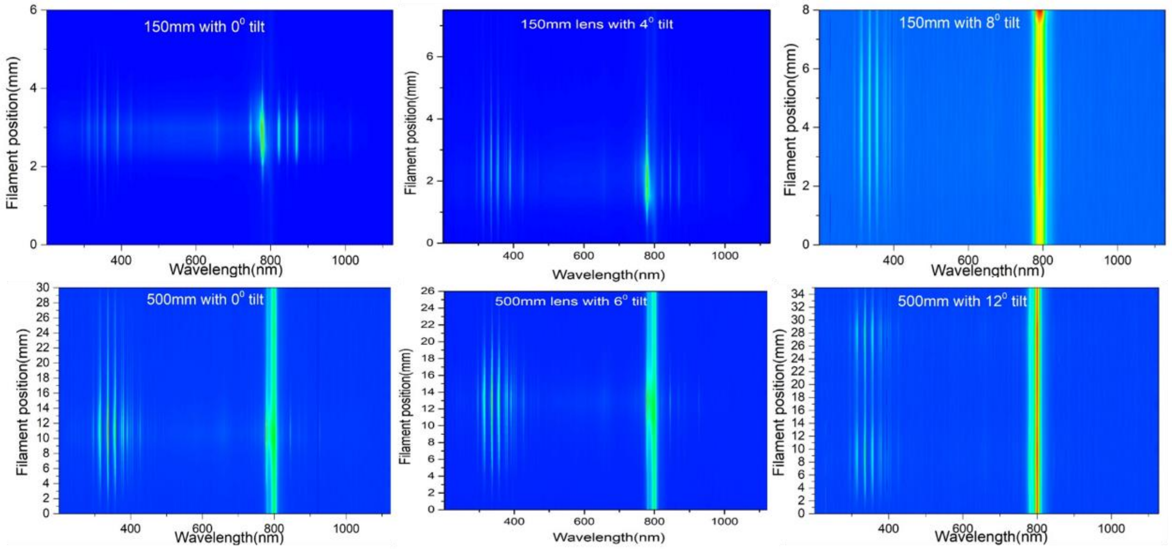

Figure 3.16: FIBS from the filaments generated from 150mm and 500mm at different lens tilt angles.

Filament intensity was found to drop by 50% for filaments generated from the 150mm lens, while the filament intensity could be estimated showed increase in filament length by at least 4 times.

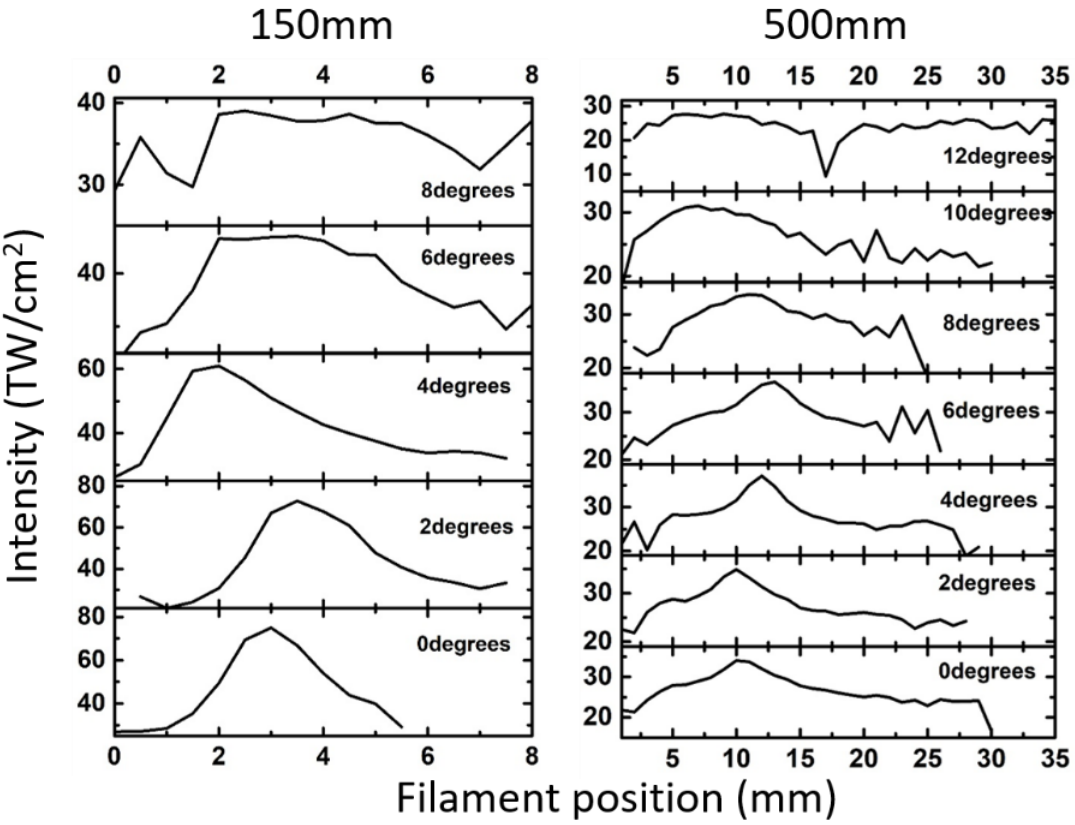

Figure 3.17: Intensity estimated for the filaments generated from 150mm and 500mm focal length lens.

The filaments generated with the 150mm lens showed large elongation of the filament to twice the length. We can also identify the splitting of the filament for large tilt angles (>10°). The images and longitudinal filament intensity estimation show that lens tilt effect of filamentation can be better addressed by considering the comatic aberration instead of astigmatic aberration.

The Supercontinuum generated from these two lenses was also collected and the change in SCG with tilt angle is shown in the contour plots in the figure 3.18.

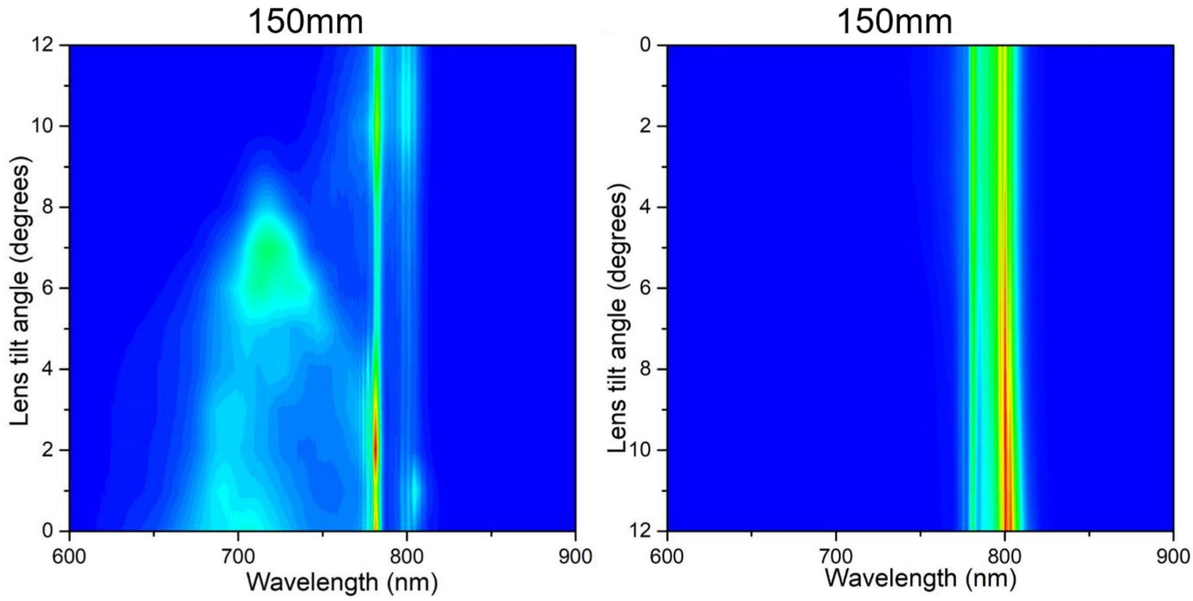

Figure 3.18: Supercontinuum collected from the filaments generated from the two lens (150mm and 500mm lens) undergoing lens tilt

We can see the suppression of supercontinuum at large tilt angles for the tight focusing geometry. However, there is a sudden increase in SCG generated from filament as the tilt increases from 6 ° - 8°. This is possibly due to re-interaction of the two separate filaments which does not occur under loose focusing conditions. Plasma build up is known to increase the blue frequency broadening in the pulse. Plasma build up and increase in plasma length due to filament interaction could be the main causes for increase in SCG generation at these angles. The elongation of the filament caused by lens tilt especially for loose focusing conditions can enhance filament emissions that depend on filament length. The filament from 500mm lens shows only spectral broadening but no supercontinuum generation.

3.6 Summary

Filament Characteristics and emissions need to be understood under the influence of the multiple effects and distortions that a femtosecond pulse undergoes. Keeping this in mind we have studied the filament characteristics and emissions under four different configurations to correlate input laser pulse modifications to filament behaviour. In the first configuration we have seen the effect of input pulse energy and focal length and identified loose and tight focused regimes of filamentation.

In the second configuration we have identified different aberrations that are induced by focusing elements on the input laser pulse and observed the corresponding filament structure, emissions, intensity and electron density. The study showed drastic changes in filament structure under the same focusing geometry, but varying aberrations. This study helped us choose the right optics according to the desired application and study using femtosecond pulses.

In the third configuration, the temporal profile of the pulse was modified by inducing a known amount of chirp to the frequency distribution in the pulse. Filament behaviour under varying pulse duration and chirp was also done under tight and loose focusing geometry. The filament onset, length and intensity can be tuned using this chirp tuning.

In the fourth configuration, the effect of lens tilt on filamentation was explored and the modifications in the wavefront due to tilting of lens was found to create elongation of the filament leading to filament splitting. Tilting of the lens under tight focusing geometries causes interaction of two filaments generated from the same lens in a particular range of angles, which causes a sudden plasma build up with increase in filament spatial extent. By using optimal lend tilt, Supercontinuum can be largely suppressed when fluorescence studies are to be done.

References

1. A. Weiner, *Ultrafast Optics*, John Wiley & Sons, **72**, (2011).
2. R. Kingslake and R B. Johnson, *Lens Design Fundmentals*, Elsevier (2010)
3. R. W. Boyd, *Nonlinear Optics*, Elsevier (2003).
4. Y. R. Shen, *Self-focusing: Past and present*, Springer (2003).
5. A. Couairon, E. Brambilla, T. Corti, D. Majus, O. de J. Ramírez-Góngora, and Miroslav Kolesik, *Practitioner's guide to laser pulse propagation models and simulation*, Eur. Phys. J. Spec. Top. **199**, 5–76 (2011)
6. A. Couairon and A. Mysrowicz, *Femtosecond filamentation in transparent media*, Phys. Rep., **441**, 47–189 (2007).

7. D. Strickland and G. Mourou, *Compression of amplified chirped optical pulses,* Opt. Commun. **55(6)**, 447-449 (1985).
8. S. Xu, X. Sun, B. Zeng, W. Chu, J. Zhao, W. Liu, Y. Cheng, Z. Xu, and S. L. Chin, *Simple method of measuring laser peak intensity inside femtosecond laser filament in air*, Opt. Express, **20**, 299-307 (2012).
9. Y. Shi, A. Chen, Y. Jiang, S. Li and M. Jin, *Influence of laser polarization on plasma fluorescence emission during the femtosecond filamentation in air*, Optics Communications, **367** 174-180 (2016).
10. A. Braun, *Self-channelling of high-peak-power femtosecond laser pulses in air*, Opt. Lett. **20**, 73-75 (1995).
11. W. Liu, S. Petit, A. Becker, N. Ak¨ozbek, C. M. Bowden, and S. L. Chin, *Intensity clamping of a femtosecond laser pulse in condensed matter*, Opt. Commun. **202**, 189–197 (2002).
12. P. P. Kiran, S. Bagchi, C.L. Arnold, S. Sivaram Krishnan, G. Ravindra Kumar, and A. Couairon, *Filamentation without intensity clamping*, Opt. Exp. **18**, 21504 (2010).
13. P. P. Kiran, S. Bagchi, S. Sivaram Krishnan, C.L. Arnold, G. Ravindra Kumar, and A. Couairon, *Focal dynamics of multiple filaments: Microscopic Imaging and Reconstruction*, Phys. Rev. A, **82**, 013805 (2010).
14. L. Bergé, S. Skupin, R. Nuter, J. Kasparian, and J-P. Wolf. *Ultrashort filaments of light in weakly ionized, optically transparent media*, Reports on progress in physics, **70(10)**, 1633 (2007).
15. A. L. Gaeta, *Collapsing Light Really Shines*, Science **301**, 54 (2003).
16. J. C. Wyant and K. Creath, *Basic wavefront aberration theory for optical metrology*, Applied optics and optical engineering, **11(2)** 28-39 (1992).
17. M. K. Gundawar, R. Junjuri, and A. K. Myakalwar, *Standoff Detection of Explosives at 1 m using Laser Induced Breakdown Spectroscopy*, Defence Science Journal **67**, 623-630 (2017).
18. J. Park, J-H Lee and C. H. Nam, *Laser chirp effect on femtosecond laser filamentation generated for pulse compression*, Opt. Exp. **16(7)**, 4465-4470 (2008).
19. R. Nuter, S. Skupin and L. Bergé, *Chirp-induced dynamics of femtosecond filaments in air*, Opt. lett. **30(8)**, 917-919 (2005).
20. A. Couairon, M. Franco, G. Méchain, T. Olivier, B. Prade and A. Mysyrowicz, *Femtosecond filamentation in air at low pressures: Part I: Theory and numerical simulations*, Opt. Comm. **259(1)**, 265-273 (2006).
21. O. Varela, B. Alonso, I. J. Sola, J. San Román, A. Zaïr, C. Méndez, and L. Roso, *Self-compression controlled by the chirp of the input pulse*, Opt. Lett. **35**, 3649-3651 (2010)
22. V. Shumakova, S. Ališauskas, P. Malevich, A. A. Voronin, A. V. Mitrofanov, D. A. Sidorov-Biryukov, A. M. Zheltikov, D. Kartashov, A. Baltuška, and A. Pugžlys, *Chirp-controlled filamentation and formation of light bullets in the mid-IR,* Opt. Lett. **44**, 2173-2176 (2019).
23. Y. Kamali, Q. Sun, J-F. Daigle, A. Azarm, J. Bernhardt and S. L. Chin, *Lens tilting effect on filamentation and filament-induced fluorescence*, Opt. Commun. **282(5)**, 950-954 (2009).
24. A. A. Dergachev, A AIonin, V. P. Kandidov, D. V. Mokrousova, L. V. Seleznev, D. V. Sinitsyn, E. S. Sunchugasheva, S. A. Shlenov, and A. P. Shustikova, *Plasma channels during filamentation of a femtosecond laser pulse with wavefront astigmatism in air*, Quantum Electronics **44(12)**, 1085 (2014).
25. Saba Zafar, Dongwei Li, Zuoqiang Hao, and Jingquan Lin, *Influences of astigmatic focusing geometry on femtosecond filamentation and supercontinuum generation in fused silica*, Optik **130**, 765-768 (2017).

This page was intentionally left blank

CHAPTER 4: Filamentation Nonlinear Optics: Third Harmonic Generation from fs filamentation in air.

Abstract:

One of the outcomes of the dynamic propagation regime of infrared femtosecond pulses is the UV generation due to third harmonic generation which gets amplified due to the cross phase modulation and plasma build up during filamentation. The Third harmonic which is isolated from the other spectral components (such as SCG) of the pulse after filamentation, using a grating was analysed using a spectrometer. As filamentation is highly susceptible to variation of input pulse conditions, the third harmonic as well can be modulated and enhanced by varying the input pulse conditions. We have therefore systematically observed and analysed third harmonic generation in UV with variation in input characteristics like input power, focal geometry, polarization, chirp and lens aberrations. As third order nonlinearity gives rise to both Third harmonic generation (THG) and Supercontinuum due to self-phase modulation a direct comparison of both THG and SCG was performed. Strong Enhancement of the third harmonic is observed when the input fs pulse has an elliptical polarization, which is reported for the first time. We also observe tuning of the third harmonic central wavelength with change in chirp of the input laser pulse and with tilt of the focusing element used to induce filamentation.

4.1 Third order non-linear effects

Filamentation is a playing ground for multiple higher order non-linear processes, which make it both sensitive to medium and input laser pulse parameters [1]. The high intensity confined within the filament, which is one of the root causes for such broad applications, enables higher order medium responses to electric field [2, 3]. In the intensity range used in our experiments we are able to go up to third order medium response in air [4]. Air being a centrosymmetric medium, it does not display second order nonlinearity in medium response

[36]. Although, SHG from gases was reported at intensities in the order of 10^{15}-10^{17} W/cm^2, we have not observed any predominant SHG owing to the intensity of the order of 10^{13}W/cm^2. The outcomes due to the third order non-linear medium response that are largely competing and interacting during filamentation are Self-focusing, Self-phase modulation and Third harmonic generation [5]. The interplay between Self-focusing along with the defocusing due to plasma generation is the foundation for the structure and behaviour of filamentation. Self-phase modulation is known to be an important tool for the generation of coherent broadband laser pulses with a spectral distribution of more than an octave called Supercontinuum Generation (SCG) [6]. Third harmonic generation produces light in the UV region when using a laser in the near infrared region [7, 8]. The third order susceptibility discussed also has other non-linear effects like cross-phase modulation between the fundamental and third harmonic generation (THG) which becomes a critical component especially during filamentation [9, 10]. We have observed enhancement and control of these processes with change in filamentation characteristics that has not been reported before by varying the input pulse characteristics. To further understand the underlying mechanisms for these enhancements, we holistically identify 3rd order non-linear processes and correlate them to understand and apply them in filamentation applications. This will help advance multiple remote sensing endeavours that utilize femtosecond pulses, providing an on demand, remotely generated coherent white light and UV source which can be used to probe and detect a broad range of molecular aerosols and suspended particles using UV excited fluorescence, FIBS of solid samples, etc [11].

We have not only shown enhancement of the above mentioned processes but also characterized their broad extent of variation with input pulse characteristics. These processes were also studied while rotating the focusing lens thereby also tilting the wavefront of the input pulse. The increase in SCG extent has been reported, the variation is not as distinct as for that observed from THG [12]. Here, SCG and THG are being correlated and studied because they are both an outcome of the 3rd order susceptibility of polarization. The observations as will be shown, not only display correlation but also provide insight into filament propagation and efficient THG and SCG generation. The first report of THG from filamentation and its generation mechanism by Akozbek et.al shows that THG becomes significant with the onset of filamentation as input power increases [7, 10]. The foremost restriction for Third harmonic generation is the Guoy phase shift before and after the focus leading to the destructive interference of the THG emission. With filamentation we see that as the power increases the symmetry of propagation before and after the focus is lost such that a large part of the THG is before the focus. Adding to that, multiple refocusing cycles while maintaining almost planar wavefront propagation make filamentation a good source of THG. THG from filamentation was further explored by interacting filaments [13, 14]. THG from interacting filaments also provides information of the transient processes in the filaments [15]. The interacting filaments enhance THG by increasing plasma density and thereby increasing asymmetry in the focusing region. Earlier studies have shown that the THG dependence on air pressure was found to be linear with increase in pressure, measured up to atmospheric pressure [16]. The THG dependence on pulse duration also found that for a given value of incident energy best THG generation does not necessarily occur at the transform limited pulse [17].

For any kind of higher harmonic generation it is required that the interaction be phase matched. THG from filamentation depends on the cross-phase modulation of medium refractive index along with plasma build-up effect on refractive index, enabling phase matching conditions between the third harmonic and the fundamental, therefore higher peak intensity of the pulse is detrimental for achieving best phase matching [2]. The peak intensity is inversely proportional to the pulse duration because of which we do not observe maximum THG for perfectly transform limited pulses. A part of this report further adds to this claim by exploring THG over varying pulse chirp, varying power and focal length. In these observations we find that correlation with SCG gives a complete picture of the dominating mechanisms which change with modifications in input pulse characteristics. Filament generated THG has been reported before, but only at purely linear or circular polarization. It is now known that circularly polarized light generates negligible THG because of lack of conservation of angular momentum. THG study with elliptical polarization shows interesting and unexpected results which should be inspected. This study consolidates also the third order effects and provides insight into the multiple competing mechanisms of filamentation. Introducing asymmetry in the wavefront by tilting the focusing lens also has drastic effects on filamentation and the subsequent third order processes that are observed [18-20]. Careful characterization was done of the variations in THG and SCG and were associated to filament characteristics during lens tilt.

4.2 Ultraviolet pulses from Third Harmonic generation from fs filamentation.

Two of the main restrictions for third harmonic generation from focused fs pulses [2] are:

1) Guoy phase shift before and after the focus leading to destructive interference between the third harmonic generated before and after the focus.
2) Dispersion, which causes the medium to have different refractive indices at different wavelengths, because of which we don't get efficient higher harmonic generation unless the wave vectors of the fundamental and harmonic are equal or phase matched.

Third harmonic generation from filamentation overcomes these challenges by firstly having a highly irregular plasma column and a regime of propagation which breaks the symmetry that causes destructive interference. Secondly, the plasma build up and cross phase modulation contribute to the refractive index making the wave vectors of the fundamental and third harmonic equal. This can be shown by first taking the input electric field to be,

$$E = \frac{1}{2}\left(\hat{E}_{\omega_o}\, exp\left(ik_{\omega_o}z - i\omega_o t\right) + \hat{E}_{3\omega_o}\, exp\left(ik_{3\omega_o}z - i3\omega_o t\right) + c.c\right) \quad (4.2.130)$$

Here, c.c implies complex conjugate. This understanding of the electric field indicates that we are taking two separate envelopes for the fundamental and third harmonic. This is under the assumption that the frequency distribution of these envelopes doesn't overlap. When this is substituted in the third order polarization relation,

$$P = \epsilon_o \chi^{(3)} E^3 \quad (4.2.2)$$

We get two different frequency components for the polarization part of the propagation equation. Therefore, the propagation equation described in the earlier chapters will now be a set of two coupled equations in the fundamental and third harmonic. Since we are observing THG in the filamentation regime, where there is intensity clamping, the wavefront can be taken to be planar or otherwise that there is no diffraction in the propagation [21]. For simplicity we are assuming that there is negligible group velocity dispersion and absorption due to multiphoton ionization, to analyse the contribution of plasma, self-phase modulation and cross phase modulation to refractive index which eventually converge to equal values for both the frequency components i.e fundamental and third harmonic. The earlier equation also assumes there is no phase difference between the two frequency components, we therefore add a phase difference components to the envelope such that we now write,

$$\hat{E}_{\omega,3\omega} = \left|\hat{E}_{\omega,3\omega}\right| exp\left(i\varphi_{\omega,3\omega}\right) \tag{4.2.3}$$

Substitution of this in the coupled equations and separating out the imaginary parts from the real, gives us four equations. It can be shown that the efficient phase matching is achieved when the phase difference between the two frequency components is 0 or π when we assume a planar wavefront and minimal losses due to absorption [37]. The envelope of the polarization which defines the refractive index of the fundamental and the third harmonic can be given by the relation,

$$\hat{P}_{\omega_o} = \epsilon_0 \chi^{(3)} \frac{3}{4}\left[\left(\left|\hat{E}_{\omega_o}\right|^2 + 2\left|\hat{E}_{3\omega_o}\right|^2\right)\hat{E}_{\omega_o} + \hat{E}^{*}_{\omega_o}{}^{2}\hat{E}_{3\omega_o}\right] - \frac{\omega_p^2}{c^2}\hat{E}_{\omega_o} \tag{4.2.4}$$

$$\hat{P}_{3\omega_o} = \epsilon_0 \chi^{(3)} \frac{3}{4}\left[\left(\left|\hat{E}_{3\omega_o}\right|^2 + 2\left|\hat{E}_{\omega_o}\right|^2\right)\hat{E}_{3\omega_o} + \frac{\hat{E}^{3}_{\omega_o}}{3}\right] - \frac{\omega_p^2}{c^2}\hat{E}_{3\omega_o} \tag{4.25}$$

These are the nonlinear contributions to refractive index due to third order processes (such as self-phase modulation and cross phase modulation) and plasma build up, at the two different frequency components which can be substituted in the wave equation described in the 1st chapter. The refractive index is directly related to the polarization term according to the relation,

$$n_{\omega,3\omega} = \sqrt{1 + \frac{\hat{P}_{\omega,3\omega}}{\hat{E}_{\omega,3\omega}}} \tag{4.26}$$

The multiple contributions to refractive index at the highly intense regime of filamentation therefore enable efficient phase matching of the fundamental and the third harmonic. Filamentation enables the wavefront within filament to have planar curvature for long distances at high intensities. It is also possible that the THG is generated at specific high intensity regions along the filament where the wavefront curvature stays almost parallel and phase matching is met. Although the THG is generated at the filament core it was shown that blocking the background reservoir of filamentation stops THG generation showing the continuous dynamic interaction with the background reservoir and plasma channel which keeps the wavefront parallel for long distance and enables efficient THG.

4.3 THG from filaments

Figure 4.1 shows the combined THG and SCG spectrum collected after diffraction from the grating. The spectra were taken so as to compare the SCG and THG to each other. The spectra shown in the figure is from a filament generated from a 500mm lens with linearly polarized pulses at an input pulse energy of 2mJ. The THG is characterized according to the peak wavelength and amplitude in the spectrum. The SCG is mainly characterized by the minimum wavelength of the spectrum. Although self-phase modulation causes broadening towards red side of the spectrum, we are only studying the broadening towards the blue side of the spectrum. The minimum wavelength therefore directly characterizes the enhancement of SCG.

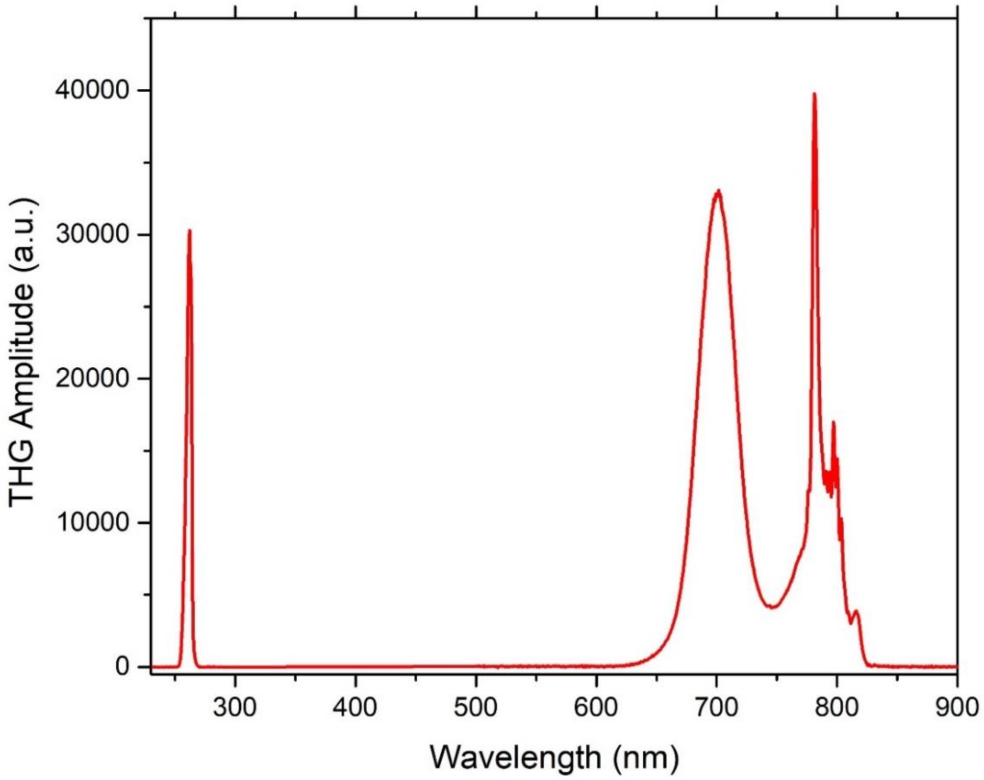

Figure 4.1: Combined spectrum THG and SCG acquired from the filament generated using a 500mm lens.

4.4 Control and optimization of THG

Linearly polarized laser pulses from a chirped pulse amplification (CPA) Ti: sapphire laser system (Libra, 4 W, M/s. Coherent Co.) delivering ~ 50 fs at the repetition rate of 1 kHz and excitation wavelength centred at 800 nm is used to generate filaments. We have varied the chirp of the pulse by changing the separation distance of the compressor gratings in the CPA system. The chirp induced was calculated by measuring the pulse duration using a single shot auto-correlator. The output pulse then passed through a combination of a half wave plate and a polarizer which allowed us to vary the input pulse energy, from 0.75 mJ to 2 mJ in steps of 0.25 mJ. The beam is then passed through a quarter wave plate to change the input polarization of the electric field from linear to circular, linear at 0° and circular at 45°, while all the points in between produce elliptically polarized light. A 500 mm and 150 mm lens are used to generate filaments in loose focusing conditions and tight focusing conditions respectively. The lens was placed on a rotating stage whose axis passed through the centre of the lens.

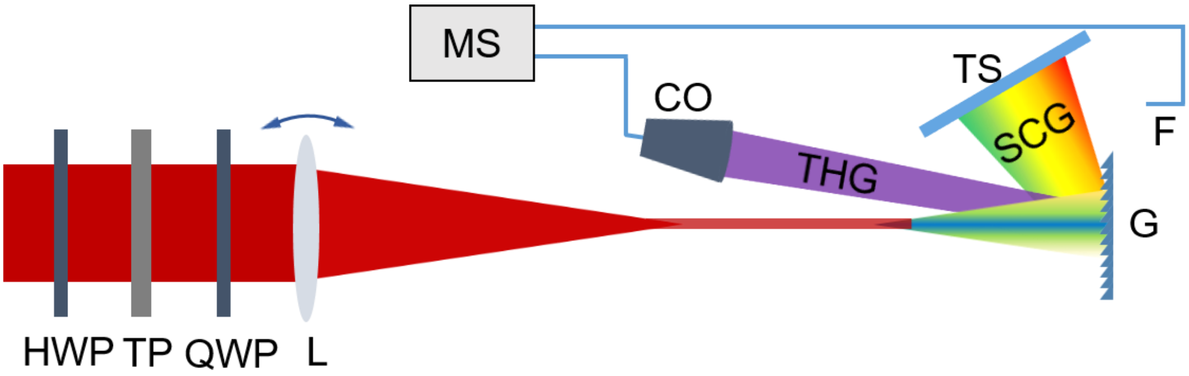

Figure 4.2: Experimental schematic for THG and SCG collection. Figure goes earlier and change position of THG. CO-Collection optics (MEOPT-0007), MS-Maya spectrometer, TS-Teflon sheet, G-Grating, F-Fiber, HWP-Half wave plate, QWP-Quarter wave plate, TP-Thin film polarizer, L-Lens

The conical output of SCG and THG in the forward direction was studied as a function of input pulse chirp and ellipticity of the polarization. As the forward emission component contains the pump at 800 nm, we have separated the SCG, THG and Pump signal by using a grating with 600 lines per mm. A handheld USB CCD spectrometer (Maya 2000, Ocean Optics) is used to collect both the SCG and THG with different collection mechanisms. To collect the THG a fibre coupled UV-NIR light collector MEOPT-0007 is used. The Supercontinuum being very broad has a wide spectral spread post grating, is scattered off a Teflon sheet and is coupled to the spectrometer via an optical fibre. The schematic of the experimental setup is shown in the figure 4.2.

4.4.1 Effect pulse energy and focusing geometry on THG from filaments

As it was discussed in the earlier chapters, focusing conditions play a large role in the filamentation dynamics. Higher numerical aperture leads to higher intensity but smaller spatial extent of the filament. According to the prominent difference that come up due to the focusing conditions we have classified the focusing conditions as loose and tight focusing [21, 22]. The SCG as discussed in the earlier chapters has larger broadening towards the blue end of the spectrum at all the available powers from the tightly focused filaments. It was therefore suggested that the intensity plays a crucial role in SCG, especially in this pulse energy regime. We have collected SCG and THG from the filaments at varying powers at two different focusing conditions classified as tight and loose focusing conditions, using lenses of focal lengths 150mm and 500mm respectively. The change in THG intensity with input pulse energy is shown in the figure 4.3.

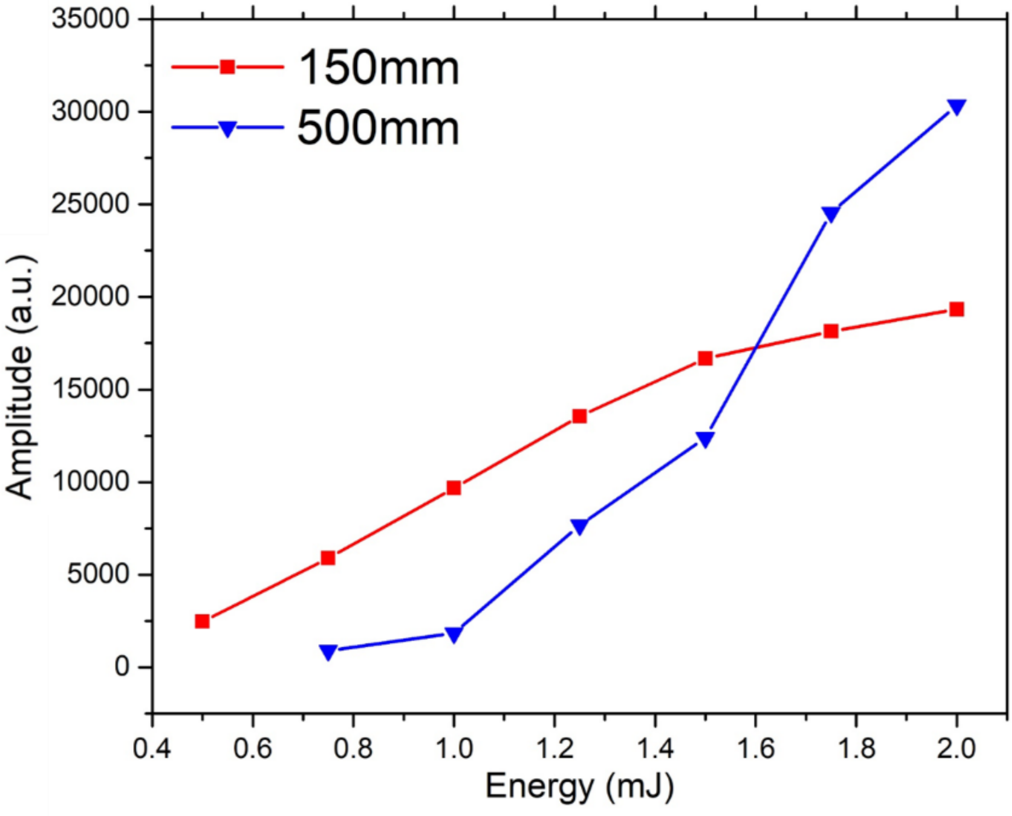

Figure 4.3: Change in THG intensity with increase in input pulse energy, from filaments generated using two different focal lengths, 150mm and 500mm.

At lower powers we observe that the THG generated is higher for tight focusing conditions, but with increase in power we find that there is a sudden increase in THG from the loosely focused filaments. The intensity of the THG appears to increase further beyond the input energy available to us for the filaments from loose focusing conditions whereas the intensity seems to be saturating at higher powers for the filaments from tight focusing conditions. Unlike what we observe from the SCG from filament which saturates for any filament beyond a certain input power, we find that the THG increases drastically beyond a certain power especially for the loosely focused filaments. THG is a process that is highly dependent on phase matching which means that THG is produced at specific points along the filament where there is optimal phase matching coming about due to plasma build up and cross phase modulation. This is not like the SCG where the generation does not require any phase matching and it occurs continuously over the propagation of the filament. Under loose focusing conditions we observe multiple refocusing cycles which can be resolved along the propagation of the filament. These refocusing cycles cause the phase matching conditions to occur multiple times over the propagation length. Increase in input pulse energy leads to an increase in the number of refocusing cycles in the filament generated under loose focusing conditions but not in that generated under tight focusing conditions because of the difference in input pulse front curvature. This is the main reason for the sudden increase in THG with increase in power in loose focusing geometry.

Figure 4.4 shows the spectrum of the THG that was observed under the two focusing conditions. We firstly observe a shift in the central wavelength towards higher frequencies of the THG from the loosely generated filament when compared to the tightly focused filaments. The peak shift is caused because the fundamental wavelength of the pump pulse shifts to the shorter wavelengths during propagation in the filament while also getting broadened due to self-phase modulation. We also find that the FWHM of the THG spectrum observed from the loosely focused filaments (6 nm) is broader than that observed from the tightly focused filaments (3.5 nm). This is because of the prolonged propagation of the generated THG in the filament which leads to the self and cross phase modulation of the THG which causes broadening in the THG.

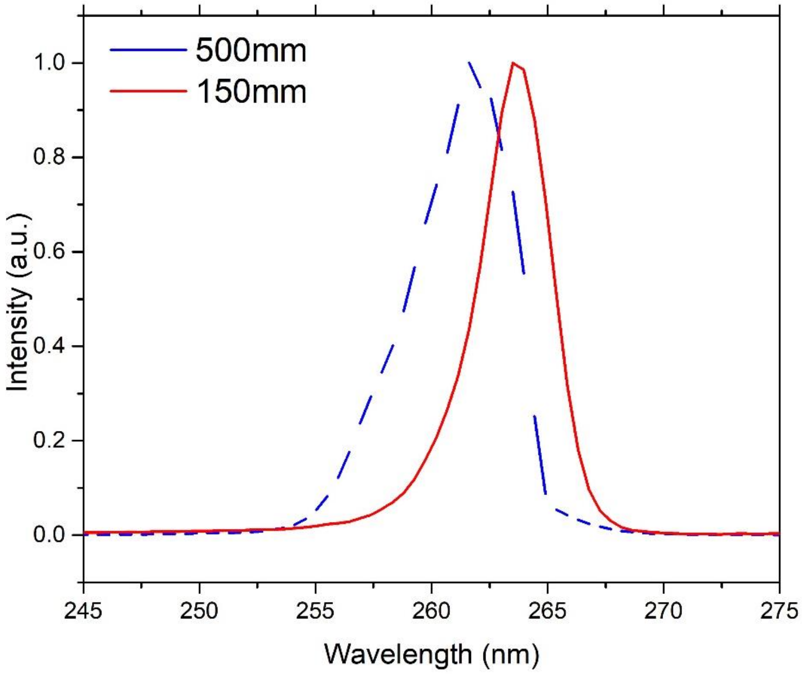

Figure 4.4: Normalized spectrum of THG from filament generated using 150mm and 500mm lens Instead of intensity use amplitude – change the y axis label

4.4.2 Effect of input polarization of fs pulses on THG from filaments

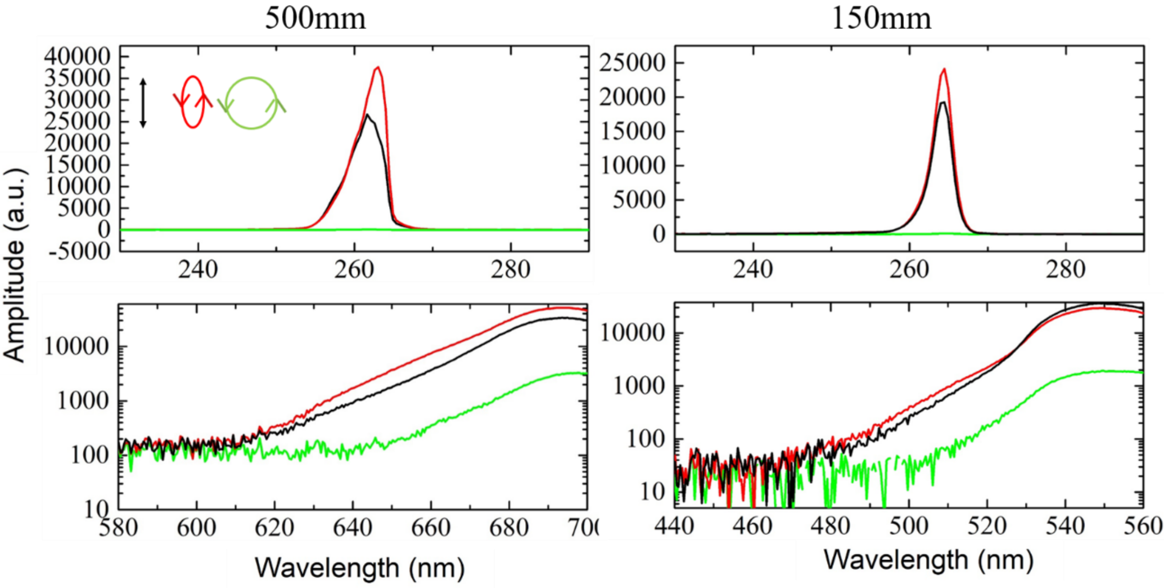

Figure 4.5: Shows the typical THG spectrum (top) and bluer part of the SCG spectrum (bottom) from the filaments generated using the 500mm (left) and 150mm (right) lens. The legend indicates ellipticity of the polarization.

Figure 4.5 shows the typical variation of the SCG and THG with polarization at an input pulse energy of 2mJ. The SCG extent is clearly higher for the filament from 150mm lens which extends up to 480nm as compared to the 500mm lens generated filament whose SCG extends up to 610nm. This is due to higher intensity in the 150mm generated filament estimated to be 80 TW/cm^2, whereas for filament from 500mm lens is 35 TW/cm^2 (estimated in earlier chapters). Although theory suggests that extent of SCG is directly proportional to both length of propagation and intensity, we find that Intensity of filament is more detrimental to SCG extent for this input pulse energy. However, at this pulse energy we also find that SCG increases for elliptically polarized light especially for the filament from 500mm lens. From the figure it can be seen that the THG is as expected for circularly polarized light where it is negligible when compared to linearly polarized, this is because of lack of angular momentum conservation for THG from circularly polarized light. The plots of THG from filaments of 150mm and 500mm lens clearly show increase in THG for elliptically polarized light. The increase in THG from filament of 500mm for elliptically polarized light when compared to linear polarized light is significantly higher than filament from 150mm lens. Closer look at the comparison of the THG spectrum from 500mm and 150mm also show that the THG spectrum is broader for the filament from 500mm. This is due to the self-phase modulation of the THG which propagates in the filamentation regime for a distance ~10 times longer than the filamentation regime of 150mm lens. The self-phase modulation term explicitly comes about as the first term in the equation 4.3. The increase in filamentation propagation regime for filament from 500mm is also the reason for larger THG increase at elliptically polarized light when compared to linearly polarized light especially at lower powers as will be shown. Therefore, for THG we find that length of propagation is the detrimental factor. The THG spectrum which was collected with change in quarter wave plate angle at 2mJ pulse energy is shown in the figure is shown in figure 4.6.

Yi Liu et al have shown that for optimal THG, increase in power increases the optimal focal length for THG, indicating that at a particular intensity, THG is maximum and once that intensity is achieved, length of propagation is the only deciding factor [14]. The observation of increase in THG at elliptical polarization is observed for the first time. As the increase in SCG extent with polarization has been earlier observed to increase at some degree of ellipticity, it was proposed that this is due to the rotational aspect of molecular susceptibility as this increase was not observed for mono atomic gases [12]. It can also suggest filament induced birefringence [23]. The extent of SCG was therefore first characterized according to the minimum wavelength and plotted with change in input power. Figure 4.7 shows the same from the filament generated from a 500mm lens.

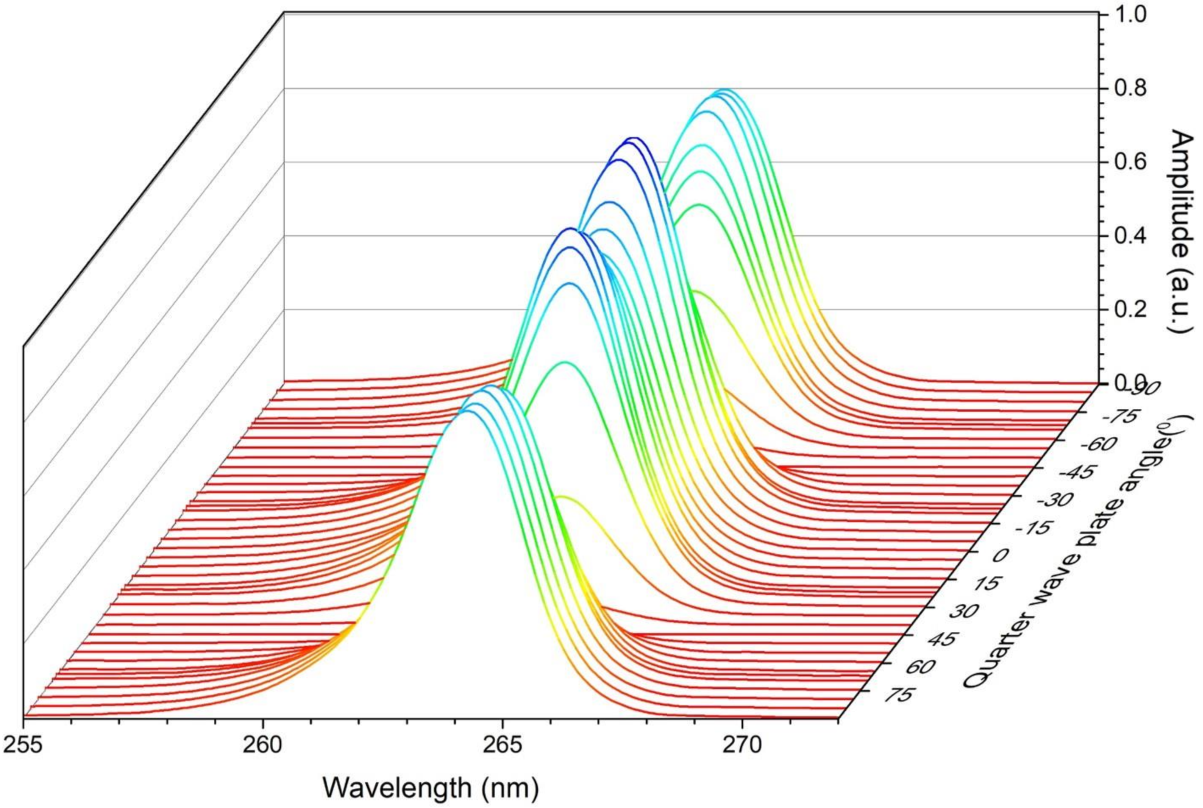

Figure 4.6: Shows the typical THG spectrum with change in quarter wave plate angle from a filament generated from 150mm lens and 2mJ pulse energy.

Simulation of THG with elliptically polarized pulses would require us to have four coupled equations making the simulation of THG difficult. The filament length also was found to vary with polarization and it was suggested that this was due to polarization dependent pulse shaping, which occurs due to the non-instantaneous dielectric response of the medium[24, 25]. We have therefore recorded the SCG and THG while changing the quarter wave plate angle over different input energies. The ellipticity of the input pulse is found from the quarter wave plate angle. The ellipticity therefore ranges from 0 to1, 0 being linearly polarized light, 1 being circularly polarized light and everything in between is elliptically polarized light.

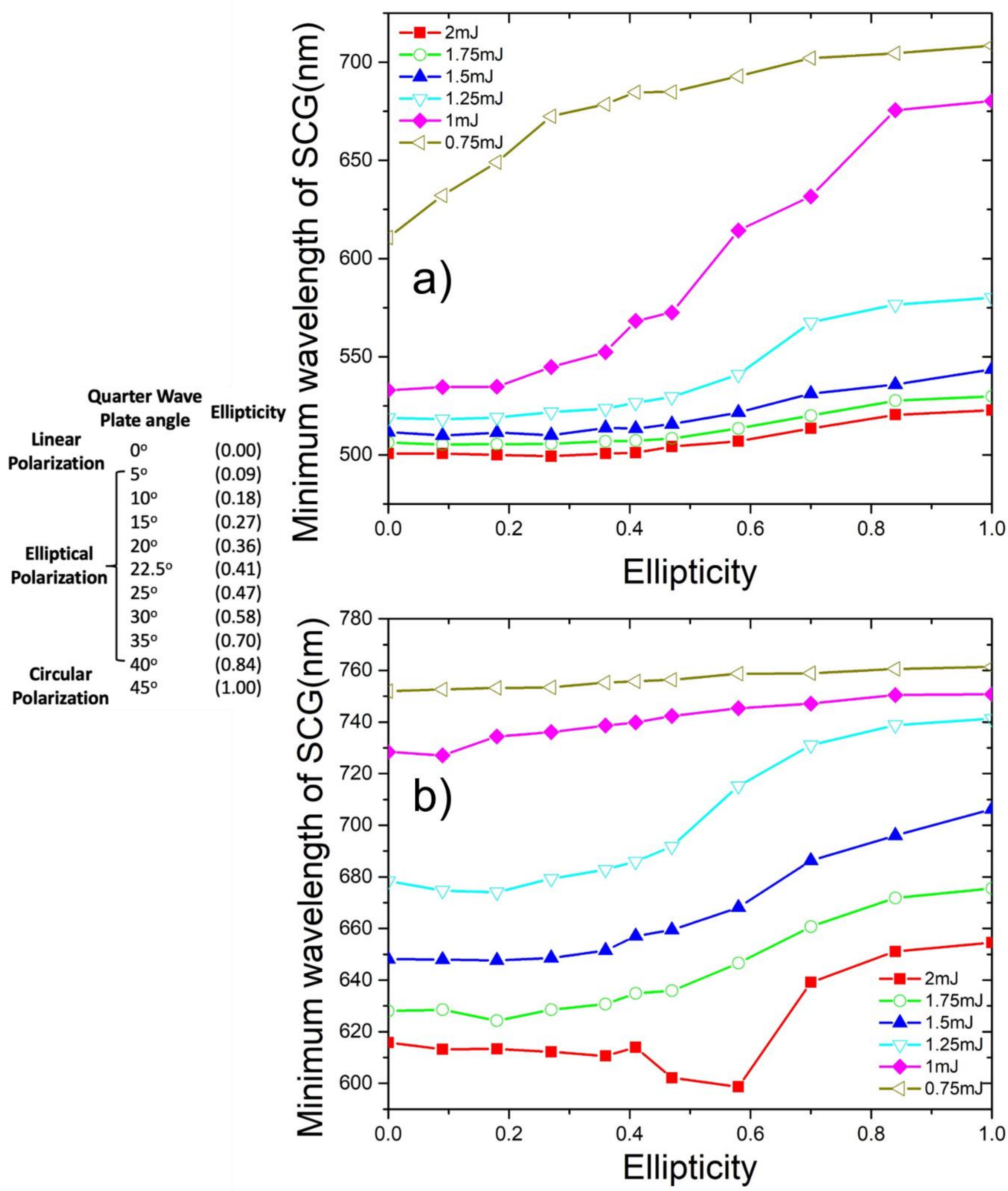

	Quarter Wave Plate angle	Ellipticity
Linear Polarization	0°	(0.00)
Elliptical Polarization	5°	(0.09)
	10°	(0.18)
	15°	(0.27)
	20°	(0.36)
	22.5°	(0.41)
	25°	(0.47)
	30°	(0.58)
	35°	(0.70)
	40°	(0.84)
Circular Polarization	45°	(1.00)

Figure 4.7: Minimum wavelength of SCG (λ_{min}) for filaments from (a) 150mm and (b) 500mm lens with change in ellipticity and pulse energy of input pulse.

The figure 4.8 shows the increase in THG at elliptically polarized input light for all powers for both lenses. Closer look shows large differences between THG between 150mm and 500mm lens. The THG has a very steady variation with a maximum at elliptically polarized light (at 22.5° and 67.5° quarter wave plate angle) at lower input powers of 500mm lens generated filament whereas 150mm lens generated filament THG doesn't vary as much. This variation in THG almost disappears for the 500mm lens generated filament when the SCG starts increasing with power, but after crossing 1.75 mJ pulse energy we see that THG variation

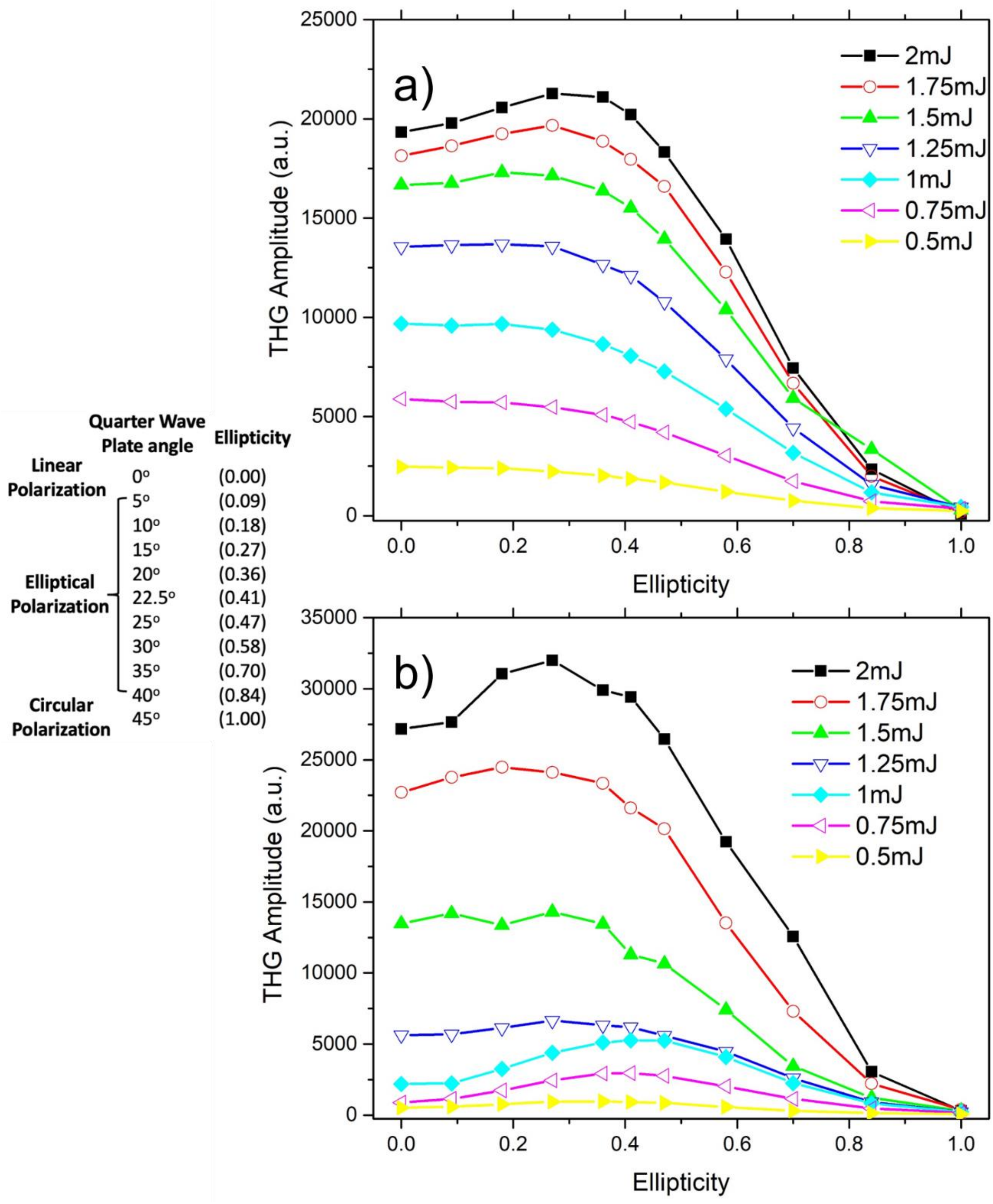

	Quarter Wave Plate angle	Ellipticity
Linear Polarization	0°	(0.00)
Elliptical Polarization	5°	(0.09)
	10°	(0.18)
	15°	(0.27)
	20°	(0.36)
	22.5°	(0.41)
	25°	(0.47)
	30°	(0.58)
	35°	(0.70)
	40°	(0.84)
Circular Polarization	45°	(1.00)

Figure 4.8: Plots showing variation of THG from filaments using (a) 150mm and (b)500mm lens with change in ellipticity and pulse energy of input pulse.

with input polarization increases at which power we also see an increase in SCG for elliptically polarized light in line with earlier cited report [12]. When observing the same for 150 mm lens generated filament we find that the variation of THG with polarization exists for all powers but is not as distinct as that for 500mm lens These observations show that the earlier discussed optimal intensity has been achieved by 150mm lens at lower pulse energy itself but not for 500mm lens where this intensity is achieved after crossing 1.75 mJ per pulse mark. It can also indicate an increase in the refocusing cycles when the energy increase from 1.25mJ to 1.75mJ per pulse. The drop in SCG extent at circular polarization is larger than that for linear polarization as the input power is reduced. This is due to the increase in critical power for circular polarization and reduction in plasma formation which is crucial for broadening of the blue end of the spectrum. The reduction in critical power also affects the propagation length and the peak intensity of the filament, thereby limiting the SCG. Circular polarized light continues to exhibit single filamentation at powers where linear polarization exhibits multiple filamentation [22]. The presence of multiple filaments especially in tight focusing regimes increases the amount of SCG but does not increase the extent of the SCG i.e. cutoff wavelength. Therefore we do not see equal drop in cut-off wavelength of SCG for linearly polarized light as that seen for circularly polarized light which drops steadily with power. The input power at which SCG from linearly polarized light shows a drop is where we see transition to single filamentation regime. The difference between SCG from circularly polarized light and linearly polarized light can give good insight into the presence of multiple filamentation or single filamentation. We do not observe the same behaviour for filament from 500mm lens as most of the intense filamentation regime is from a single filament, where the SCG from Circularly and linearly polarized light drop steadily with power.

4.4.3 Change in THG with Chirp of input fs pulse

The input pulse can be chirped by changing the separation between the compressor gratings, thereby inducing a group delay dispersion defined by the separation distance [26]. The fs pulse was characterized using a single shot autocorrelator and the induced group delay dispersion quantified by the chirp can be estimated [27-29].

Figure 4.9 shows the variation of THG and SCG extent with varying chirp and input power. Firstly, it can be seen that transform limited pulse with shortest pulse width or highest peak intensity does not produce best intensity indicating an intensity dependant phase matched

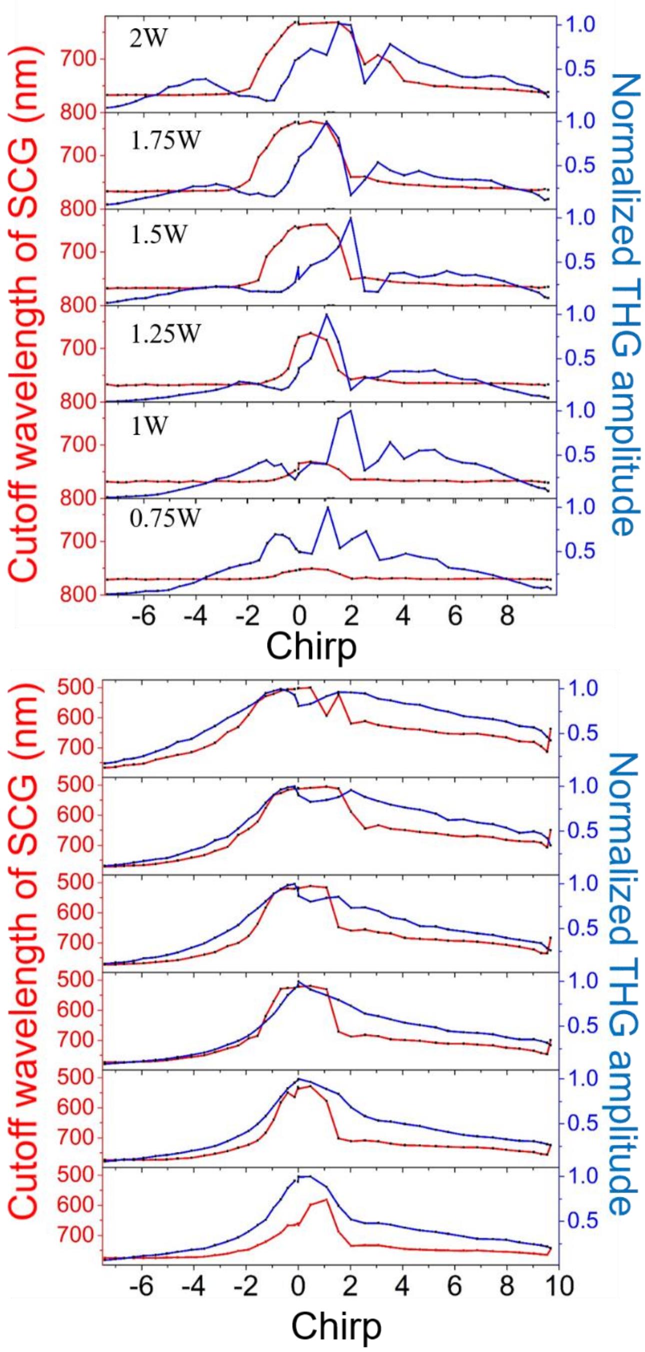

Figure 4.9: Plots showing THG and SCG extent with Chirp and power for 500mm lens (top) and 150mm lens (bottom) generated filament.

condition. Apart from that, we observe larger THG generation for positive chirp for 500mm lens generated filament which is not observed for 150mm lens. We also see that the chirp range for maximum SCG does not coincide with chirp range of maximum THG for 500mm lens generated filament which is not the case for filament from 150mm lens. The common observation between both the filaments is that THG increases once SCG declines for positive values of chirp for higher value of input pulse energy. This could indicate energy exchange between the two non-linear processes. Third harmonic that gets generated during filamentation experiences a refractive index close to that of the fundamental due to the contribution of plasma build up and cross phase modulation to the refractive index, enabling the third harmonic and fundamental to travel at the same velocity. The plasma density and refractive index changes which depend on intensity are therefore crucial for phase matching. This is the main reason for which we do not observe maximum THG for transform limited pulses. There are multiple ripples around the peak THG value for the filament from 500mm lens, which is clearly not observed for filament from 150mm. This is because of the multiple focusing and refocusing cycles that exist in the loose focusing regime, as the pulse energy reduces or the chirp increases the number of cycles reduces. In the range of chirp or input energy where the number of cycles is constant, there exists a defined intensity where there is optimal phase matching between the fundamental and third harmonic, at which intensity we see a maximum in THG for that particular number of focusing and refocusing cycles. Whereas in the case of filament from the 150mm lens where the number of refocusing cycles does not increase with power, the optimal THG for a given input laser energy is dependent only on the peak intensity which varies with chirp and input pulse energy. Therefore we clearly observe the ripples move towards the centre as input pulse energy is reduced. This is observed for lower input pulse energies as well. The SCG on the other hand does not require phase matching for efficient generation, only being influenced by the filament intensity and length. However, we find that THG which depends on phase matching inhibits SCG generation indirectly, this is observed with the sudden drop in SCG extent and subsequent rise in THG as can be seen from figure 4.10. It can also be seen that the positive chirp value at which chirp SCG drops is constant with drop in power whereas the negative chirp value at which SCG drops increases with increase in power. This could indicate the power exchange between THG and SCG. The exact reason for the increase in THG and drop in SCG is not theorized, but it could be due to the time dependent non-linear response of the medium which will encounter higher frequencies at the tail of the pulse with positively chirped pulses and lower frequencies at the tail with negatively chirped pulses. The sudden suppression of SCG with enhancement of THG as shown in figure 4.10 will enhance the signal to noise ratio of the signals. The intensity was estimated for the different filaments from varying input energies. The plots are given according to the estimated intensity.

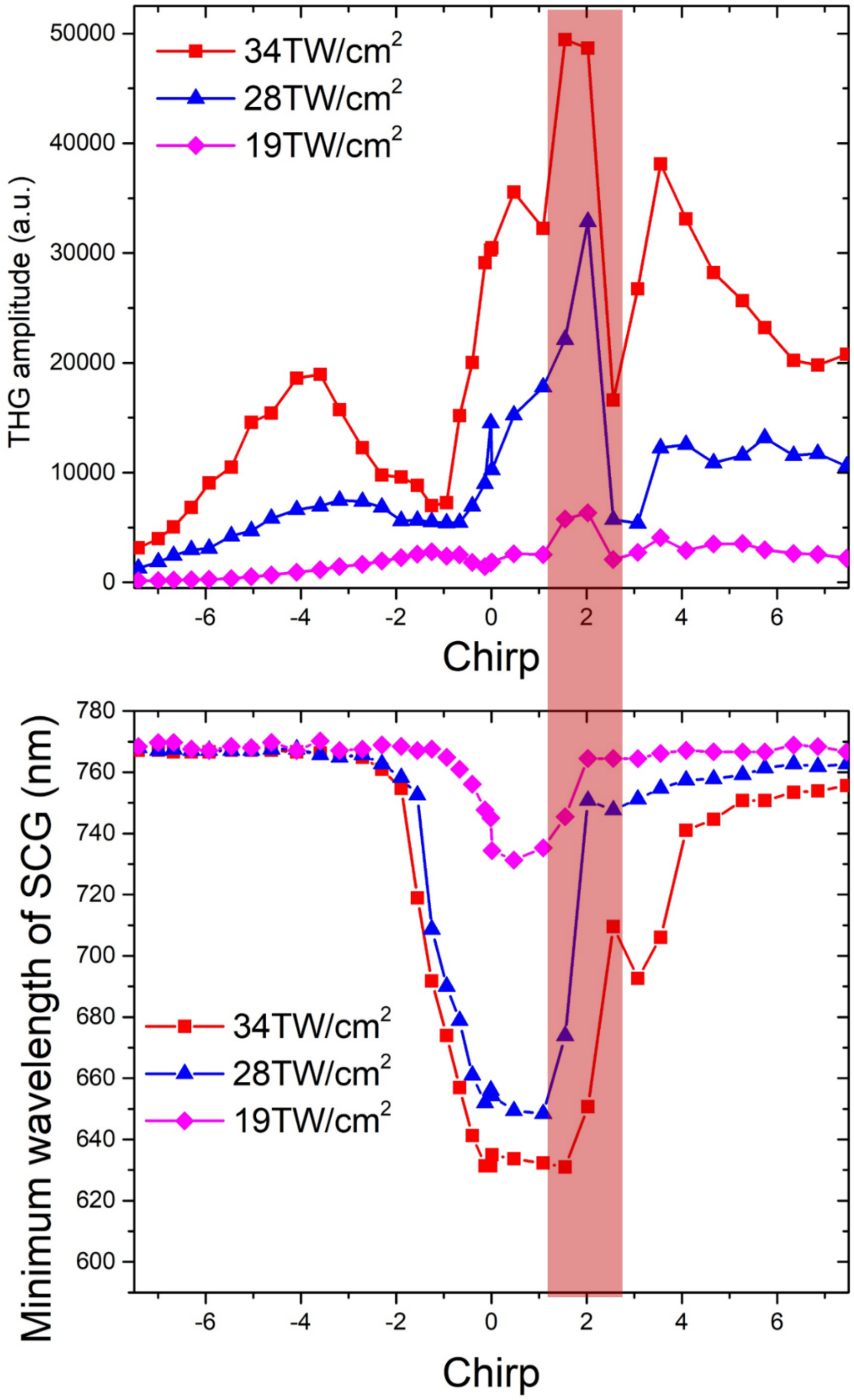

Figure 4.10: Combined spectrum and signal of THG and SCG. Shaded region shows enhancement of THG and suppression of SCG and for varying chirp.

Spectral analysis of the THG with chirp also shows variation of the central wavelength of THG with chirp value especially for tight focusing conditions. The central wavelength can be tuned within a range of 10nm with the input powers available to us. This is shown in figure 4.11 where we see the peak value of the spectrum and the central wavelength of the THG.

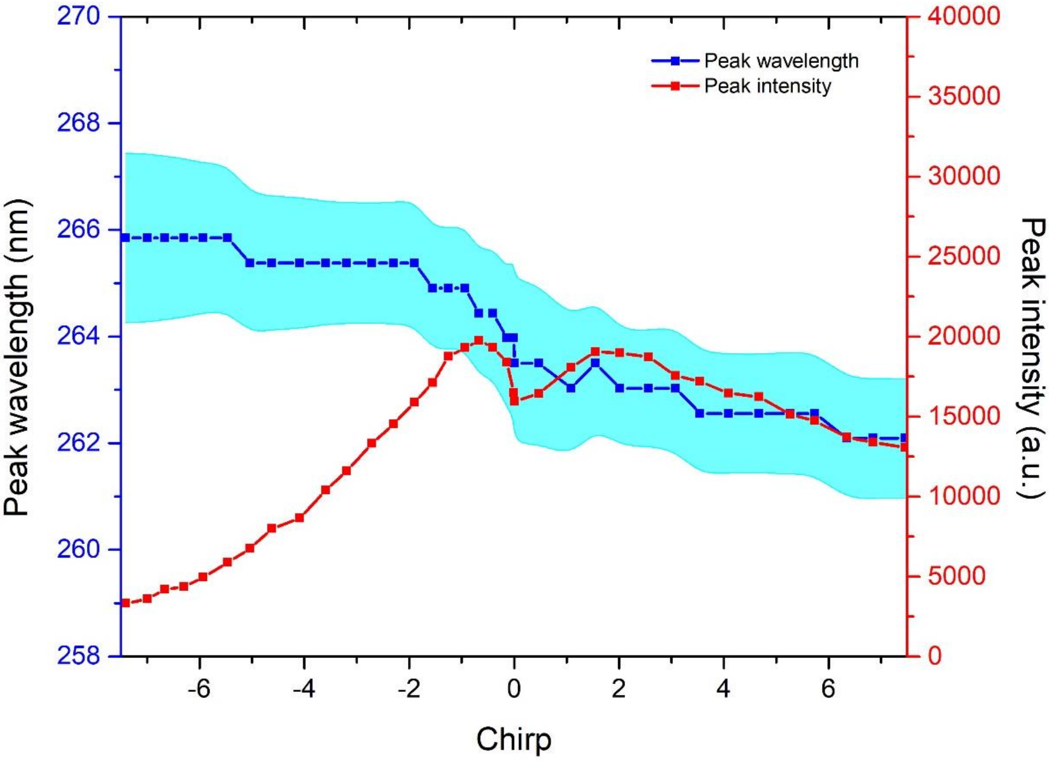

Figure 4.11: Spectrum of THG with chirp to show change in peak wavelength and intensity of THG. Shaded region shows the FWHM of THG.

4.4.4 Change in THG with Lens tilt

The effect of lens tilt on filamentation was discussed in third chapter where the filament was characterized according to the intensity, structure and supercontinuum generation. This was done under the two distinct focusing conditions which we have classified loose and tight focusing geometry. The filament intensity was estimated using the filament induced self-emission obtained along the filament propagation, where we can clearly identify the elongation of filament which eventually leads to formation of two filaments. The SCG drops for both focusing geometries with increase in tilt angle. However, a sudden increase in SCG is observed at a lens tilt angle of ~6^0.

Lens tilt effect on THG was therefore studied to explore the possibility of its enhancement as we observe some changes in SCG which is also a nonlinear process due to third order susceptibility. This was done also because literature has reported increase/enhancement of THG from interacting filaments. The efficiency of the THG was studied with interacting filaments by Hong Wu and group where background free THG was generated and enhanced by non-collinearly interacting the filaments [13]. As the interaction of filaments enhances the THG, study of THG enables time resolved information of the interaction of filaments and hence was used to study the plasma lifetimes according to the THG enhancements in different gases by Christof Jusko and group [15]. We have therefore exploited the effect of lens tilt which causes interaction of multiple filaments with a very simple mechanism to enhance THG.

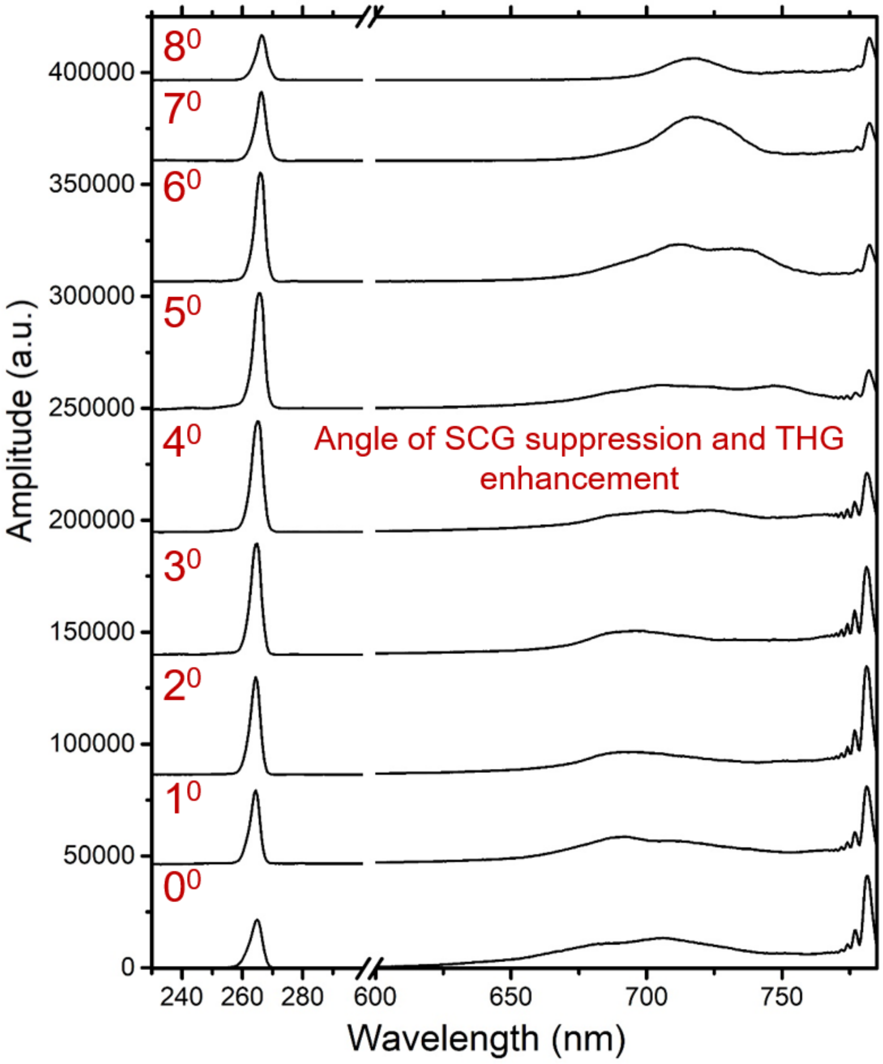

Figure 4.12: Shows suppression of SCG and enhancement of THG at an angle of 5^0 from a filament generated using a 500mm lens

The experiment was performed so as to collect the SCG and THG simultaneously from the filament. On doing so we can be sure that the input conditions do not vary. We can also identify the correlation between SCG and THG from this study. It was shown that we can suppress the SCG by inducing tilt in the lens. We were able to observe drastic enhancement in the THG at a characteristic angle of ~4^0 at which SCG gets suppressed as seen in figure 4.12. This sudden enhancement in the THG is due to interaction of multiple filaments formed due to asymmetry in the pulse front. We find that this enhancement is even more prominent under loose focusing conditions. THG observed from a filament generated from a 500mm lens with lens tilt is shown where we observe a 150% increase in THG intensity with change in tilt angle in the figure 4.13.

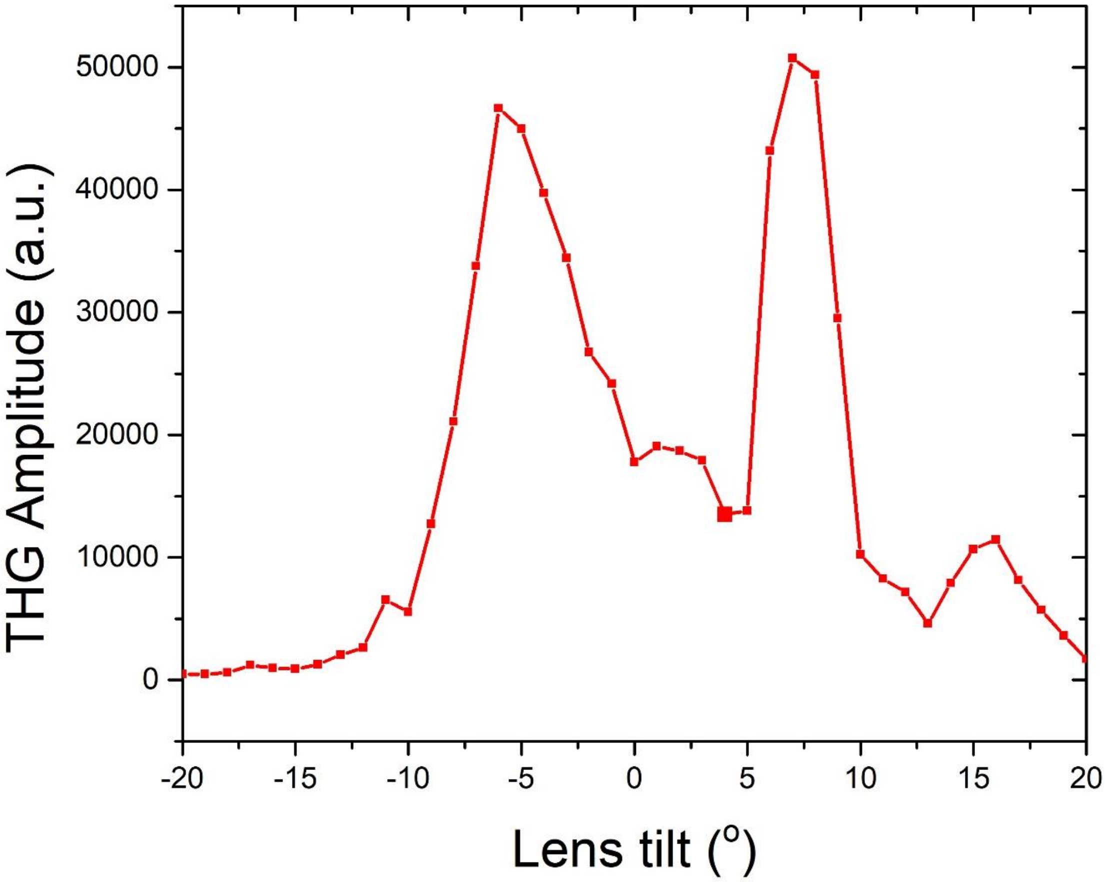

Figure 4.13: THG from filament from 500mm lens with lens tilt angle.

THG under lens tilt effect shows a drastic increase for the loosely focused filament when the lens is tilted at an angle of ~7^0. At this angle the supercontinuum is also suppressed and the only dominant emission is the THG. THG drops for both the focusing geometries with increase in lens tilt but has small increase at an angle of ~6^0 for the tightly focused filament but the loosely generated filament sees increase in THG by almost 3 times. Using a single lens we were able to interact two filaments and enhance THG. It can also be shown that frequency tuning is possible by tilting the lens as show in the figure 4.14.

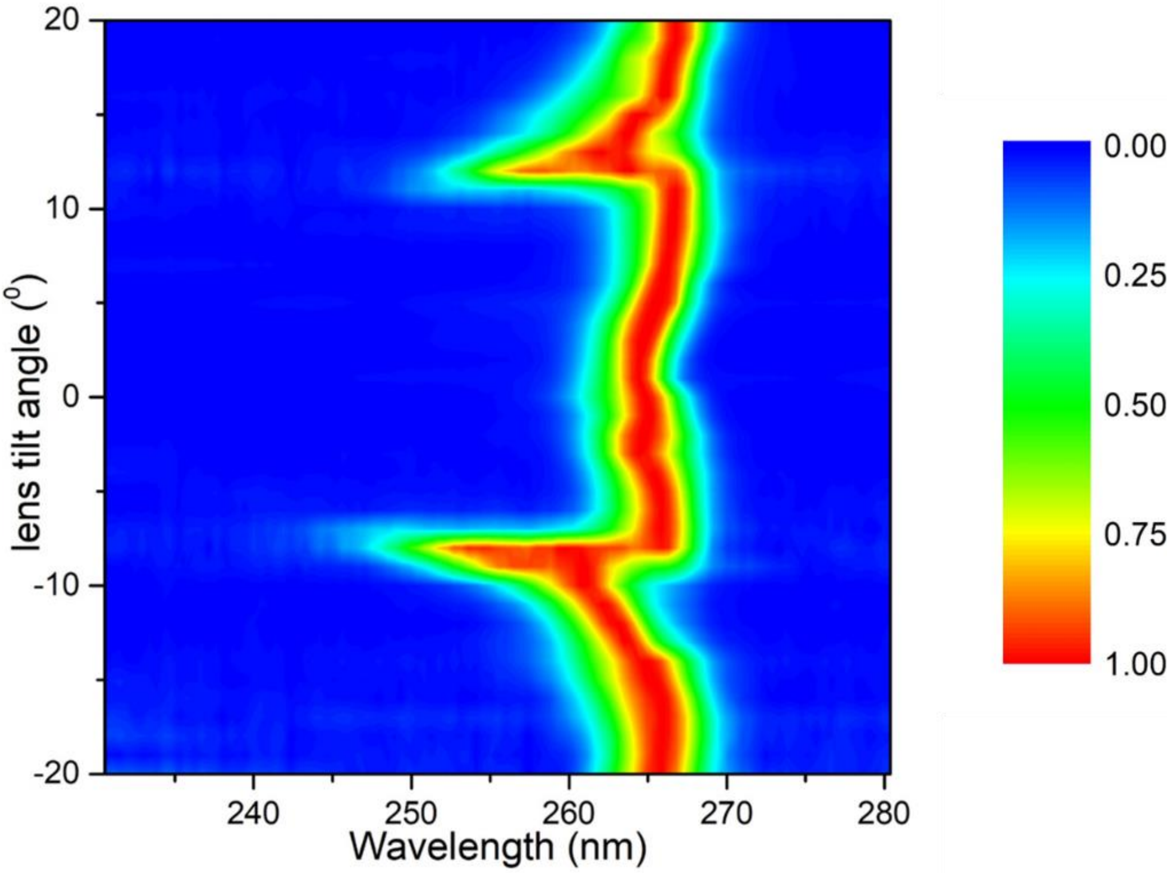

Figure 4.14: Spectrum of THG (normalised amplitude) with lens tilt angle to show change in central frequency of THG from filament generated using a 150mm lens.

4.5 Summary

We have systematically correlated the THG and SCG emission from filaments generated under different focusing conditions while varying power, Chirp and polarization. The results not only show large correlation but also provide insight into the various competing mechanisms during filamentation and provide knowledge of the filament structure. Change in the SCG and THG with input pulse properties indicates energy exchange between the underlying processes that facilitate these emissions like Third harmonic generation and self-phase modulation. This work not only shows the large susceptibility of filaments to the input pulse characteristics but also provides a strong tool for remote sensing and detection using Filament generated UV and Continuum for LIDAR applications. Moreover filamentation induced THG shows its sensitivity towards the phase matching conditions which exist in the highly dynamic filamentation process which are repeated from pulse to pulse and consequently SCG which although does not require phase matching is also found to be susceptible to input laser conditions.

References

1. A. Couairon and A. Mysrowicz, *Femtosecond filamentation in transparent media*, Phys. Rep. **441**, 47–189 (2007).
2. S. L. Chin, *Femtosecond laser filamentation*, Elsevier (2009).
3. A. Weiner, *Ultrafast Optics*, John Wiley & Sons, **72** (2011).
4. R. W. Boyd, *Nonlinear Optics*, Elsevier (2003).
5. A. Couairon, E. Brambilla, T. Corti, D. Majus, O. de J. Ramírez-Góngora, and Miroslav Kolesik, *Practitioner's guide to laser pulse propagation models and simulation*, Eur. Phys. J. Spec. Top. **199**, 5–76 (2011).
6. R. Alfano, *The Supercontinuum Laser Source*, Springer-Verlag New York (2016).
7. N. Aközbek, A. Iwasaki, A. Becker, M. Scalora, S. L. Chin, and C. M. Bowden, *Third-Harmonic Generation and Self-Channeling in Air Using High-Power Femtosecond Laser Pulses*, Phys. Rev. Lett. **89**, 143901, (2002).
8. S. Suntsov, D. Abdollahpour, D. G. Papazoglou, and S. Tzortzakis, *Efficient third-harmonic generation through tailored IR femtosecond laser pulse filamentation in air*, Opt. Express, **17**, 3190 (2009).
9. S. Suntsov, D. Abdollahpour, D. G. Papazoglou, and S. Tzortzakis, *Filamentation produced third harmonic in air via plasma enhanced third-order susceptibility*, Phys. Rev. A **81**, 033817 (2010).
10. N. Aközbek, A. Becker, M. Scalora, S. L. Chin, and C. M. Bowden, *Continuum generation of the third-harmonic pulse generated by an intense femtosecond IR laser pulse in air.* Appl Phys B, **77**, 177–183 (2003).
11. M. Durand, A. Houard, B. Prade, A. Mysyrowicz, A. Durécu, B. Moreau, D. Fleury, O. Vasseur, H. Borchert, K. Diener, R. Schmitt, F. Théberge, M. Chateauneuf, J-F. Daigle and J. Dubois, *Kilometer range filamentation*, Opt. Express **21**, 26836-26845 (2013).
12. S. Rostami, M. Chini, K. Lim, J. P. Palastro, M. Durand, J-C. Diels, L. Arissian, M. Baudelet and M. Richardson, *Dramatic enhancement of supercontinuum generation in elliptically-polarized laser filaments*, Scientific reports **6(1)**, 1-8 (2016).
13. H. Wu, T. Yang, Y. Wang and L. Ding, *Background-free third-order harmonic generation induced by dynamic gratings in dual filaments*, J. Opt. Soc. Am. B **26**, 645-649 (2009).
14. Y. Liu, M. Durand, A. Houard, B. Forestier, A. Couairon, and A. Mysyrowicz, *Efficient generation of third harmonic radiation in air filaments: A revisit*, Opt. Commun. **284(19)**, 4706-4713 (2011).
15. C. Jusko, A. Sridhar, E. Appi, L. Shi, U. Morgner and M. Kovacev, *Filamentation-assisted plasma lifetime measurements in atomic and molecular gases via third-harmonic enhancement*, J. Opt. Soc. Am. B **36**, 3505-3513 (2019)
16. Y Liu, C. Kou, A. Houard and A. Mysyrowicz, *Optimizing the third harmonic generated from air plasma filaments pumped by femtosecond laser pulses*, J. Opt. Soc. Am. B **36**, G13-G18 (2019).
17. R. A. Ganeev, M. Suzuki, M. Baba, H. Kuroda and I. A. Kulagin, *Third-harmonic generation in air by use of femtosecond radiation in tight-focusing conditions*, Appl. Opt. **45**, 748-755 (2006).
18. Y. Kamali, Q. Sun, J-F. Daigle, A. Azarm, J. Bernhardt and S. L. Chin, *Lens tilting effect on filamentation and filament-induced fluorescence*, Opt. Commun. **282(5)**, 950-954 (2009).

19. A. A. Dergachev, A. A. Ionin, V. P. Kandidov, D. V. Mokrousova, L. V. Seleznev, D. V. Sinitsyn, E. S. Sunchugasheva, S. A. Shlenov, and A. P. Shustikova, *Plasma channels during filamentation of a femtosecond laser pulse with wavefront astigmatism in air*, Quantum Electronics **44(12)**, 1085 (2014).
20. S. Zafar, D. Li, Z. Hao, and J. Lin, *Influences of astigmatic focusing geometry on femtosecond filamentation and supercontinuum generation in fused silica*, Optik **130**, 765-768 (2017).
21. P. P. Kiran, S. Bagchi, C.L. Arnold, S. Sivaram Krishnan, G. Ravindra Kumar, and A. Couairon, *Filamentation without intensity clamping*, Opt. Exp. **18**, 21504 (2010).
22. P. P. Kiran, S. Bagchi, S. Sivaram Krishnan, C.L. Arnold, G. Ravindra Kumar, and A. Couairon, *Focal dynamics of multiple filaments: Microscopic Imaging and Reconstruction*, Phys. Rev. A, **82**, 013805 (2010).
23. C. Marceau, S. Ramakrishna, S. Génier, T-J. Wang, Y. Chen, F. Théberge, M. Châteauneuf, J. Dubois, T. Seideman, and S. L. Chin, *Femtosecond filament induced birefringence in argon and in air: Ultrafast refractive index change*, Opt. Commun. **283(13)**, 2732-2736 (2010).
24. G. Z. Zhu, T-J. Wang, Y. Liu, N. Chen, H. Zhang, H. Sun, H. Guo, J. Zhang, X. Zhang, G. Li, C. Liu, Z. Zeng, J. Liu, S. Chin, R. Li and Z. Xu, *Polarization-dependent femtosecond laser filamentation in air*, Chinese Optics Letters **16** 073201 (2018).
25. Y. Shi, A. Chen, Y. Jiang, S. Li and M. Jin, *Influence of laser polarization on plasma fluorescence emission during the femtosecond filamentation in air*, Opt. Commun. **367** 174-180 (2016).
26. D. Strickland and G. Mourou, *Compression of amplified chirped optical pulses,* Optics Communications, **55(6)**, 447-449 (1985).
27. M. Raghuramaiah, A. Sharma, P. Naik, P. Gupta, R. Ganeev, *A Second-Order Autocorrelator for Single-Shot Measurement of Femtosecond Laser Pulse Durations*, Sadhana, **26**, 603-611 (2001).
28. J. Park, J-H. Lee and C. H. Nam, *Laser chirp effect on femtosecond laser filamentation generated for pulse compression*, Opt. Exp. **16(7)**, 4465-4470 (2008).
29. R. Nuter, S. Skupin and L. Bergé, *Chirp-induced dynamics of femtosecond filaments in air*, Opt. lett. **30(8)**, 917-919 (2005).

This page was intentionally left blank

CHAPTER 5: Evaluation of filament induced Acoustic emissions in air

Abstract:

Plasma build up along with Kerr self-focusing is the foundation for the prolonged propagation of femtosecond pulses through the process of filamentation. The spatial plasma distribution along the length of the filament is highly dependent on the properties of the input fs pulse, properties of medium as well as the focusing conditions. The plasma which forms, achieves equilibrium by energy dissipation through a number of processes. Other than optical emissions the energy gets dissipated in the form of mechanical waves as well in the form of shock waves which are initiated in the vicinity of the filament which very quickly decay into acoustic waves. In this chapter we present the work done on characterising these acoustic waves from filaments. The acoustic signals radiated along the length of the filament reflect the plasma dynamics within the filament. We find that acoustic characterization of filaments is a novel complimentary technique to optical characterisation methods, which help provide a complete understanding of the filament dynamics within a given medium. The large dynamic range (SNR) of microphones can detect acoustic signals from a range of filaments, especially weak filaments with weak optical emissions, which cannot be characterized by spectroscopic techniques alone. Acoustic profiling of the filaments is demonstrated to be a viable addition to femtosecond filament sensing providing filament information which cannot be otherwise obtained from the electromagnetic emissions.

5.1 Filament induced hydrodynamics of plasma and acoustic emissions

Laser matter interactions involve deposition of a large amount of optical energy in a very short timescale [39-3]. The various processes that unfold such as plasma formation, medium breakdown and nonlinear mechanisms, lead to a variety of electromagnetic emissions some of which have been discussed in earlier chapters [4-8]. This chapter focuses on the mechanical emissions that arise from laser matter interactions, and explore acoustic and shockwave emissions that arise from femtosecond filament generated in air. The creation of a plasma when a laser pulse with sufficient irradiance interacts with the medium is the main reason for the generation of mechanical waves in matter [9, 10]. Unlike the case of picosecond and nanosecond laser pulses, where the dominating ionization mechanisms are inverse bremsstrahlung ionization and avalanche ionization, the ionization mechanism during a femtosecond pulse interaction with air is multiphoton ionization (MPI) [11, 12]. This ionization that occurs due to intensities of 10^{13} W/cm^2 at femtosecond time scales, also causes negligible heating, because of which the acoustic emissions from intense femtosecond pulse interaction with air become a direct indicator of the plasma density. The large amount of energy which gets deposited in the medium along with subsequent formation of plasma, is dissipated into multiple energy dissipation pathways, giving rise to electromagnetic emissions (optical, UV, RF, THz. etc) which were analysed and studied using spectrometers/spectrum analysers and acoustic emissions which are studied using microphones [13]. This is illustrated in figure 5.1. Filamentation is a long range propagation regime of intense femtosecond pulses where the plasma formed is not dense enough to cause complete breakdown because of which the long plasma channel has a very characteristic spatial profile which gets reflected on the acoustic emission properties via the dissipation of plasma density.

As these acoustic emissions can be remotely generated, they can be put to use towards sensing of remote regions to detect particle sizes and concentration. Hyun Jin and group have shown that one can distinguish particle sizes lower than 50nm and particle concentrations as low as ppt using a nanosecond laser by analysing the number and magnitude of shock waves created in an aqueous solution of the particles [14]. It was suggested that the magnitude and number of shockwaves is proportional to the average particle size and concentration. Although, the visible part of the filament is where the plasma and the most intense region of propagation exists, this region has continuous energy exchange with the background reservoir surrounding the plasma column, which can be seen when filamentation is terminated when the background surrounding reservoir is blocked using a pinhole. Therefore, during filamentation, even though the presence of large particles or droplets in the atmosphere result in random sudden changes in medium which in turn cause a localised breakdown, the propagation of the fs pulse continues unperturbed[15]. This enables the ability to propagate and transmit fs laser pulses over large distances with the use of filamentation (with pulse pre-compensation to account for dispersion accrued). This allows us to create remote localised acoustic sources. Acoustic characterization and sensing is also beneficial and effective because the acoustic systems are rugged, easy to use complimented with a large dynamic range.

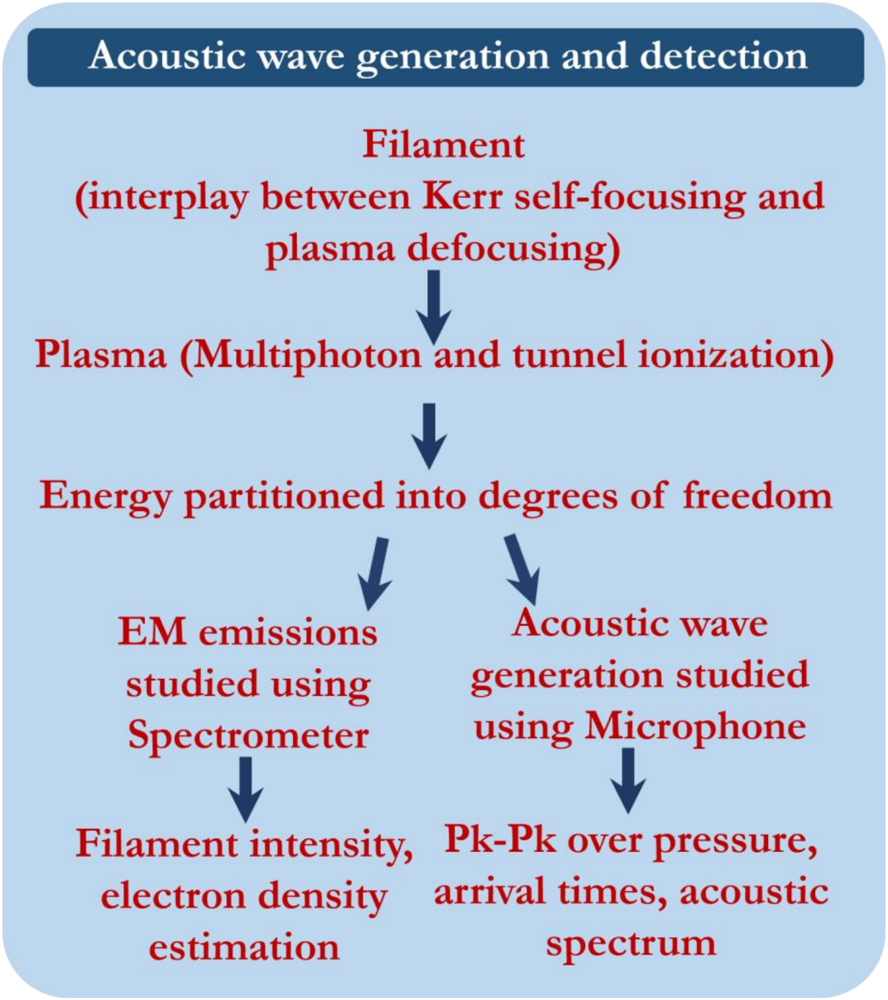

Figure 5.1: Schematic showing the generation of acoustic waves from filamentation.

In this chapter we have first correlated the filament characteristics to the corresponding acoustic emission profile along the spatial extent of the filament. The spatial acoustic profile was obtained by scanning the microphone along the filament. Electron density and intensity along the filament which were estimated from filament self-emission, were correlated with the acoustic data. After characterization of the acoustic emissions with respect to the spatial filament electron density, we find that acoustic emission from the filament can be used to characterise filament properties such low plasma density filaments or multiple filaments which conventional optical/spectroscopic methods cannot detect. Moreover, the high dynamic range of 3 orders can be used to characterize a broad variety of filament formation.

5.2 Acoustic characterization of fs filaments

The experimental setup used to for acoustic diagnostics of the filament is illustrated in figure 5.2. The microphone used for the experiments was a GRAS 40DP, with a sensitivity of 1mV/Pa and frequency response from 20Hz to 140kHz. The static pressure of atmospheric pressure at 10^5 Pa is taken as zero (reference) on the y-axis, therefore giving a flat curve when there is no acoustic source. The oscilloscope used for the acquisition is triggered using a laser triggered photodiode, and only the window of the first acoustic peak is taken to avoid the reflected components [16]. Once the signal is acquired in the time domain, we obtain the various parameters used to analyse the acoustic pulse namely, arrival time (A_t), peak to peak over pressure (P_k), pulse burst time (W_t), decay time (D_t) and ratio of compression to rarefaction. The spectrum of the acoustic pulse is then obtained using a fast fourier transform (FFT) of the temporal pulse to get the frequency content of the pulse. The frequency distribution provides information of the existence of distinct oscillations in the plasma. This cannot be extracted from analysis of the pulse profile in the time domain alone.

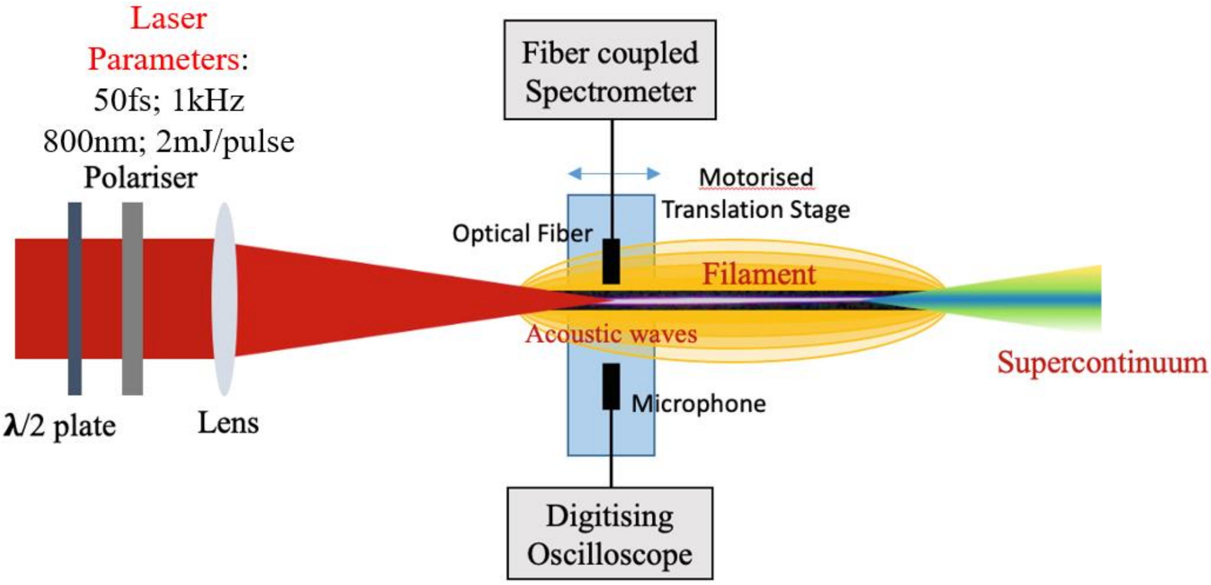

Figure 5.2: Experiment schematic for acoustic characterization of filaments.

The acoustic pulse which was collected is shown in the figure 5.3a. The acoustic profile can provide ample information regarding the dynamics of the generated plasma. We can do this because of the high repeatability of the plasma dynamics and subsequent acoustic pulse from filamentation triggered by the fs laser pulse. We can therefore characterize the acoustic pulse according to the arrival time, amplitude of the peak to peak overpressure and pulse duration/burst time. We can also characterize the pulse according to the ratio of compression to rarefaction. Figure 5.3b also shows the corresponding frequency spectrum of the acoustic pulse which was obtained by FFT. The shown acoustic pulse has a uniform profile which is further supported from the frequency distribution which shows a broad frequency distribution centred around 110 kHz having a FWHM of ~ 45 kHz.

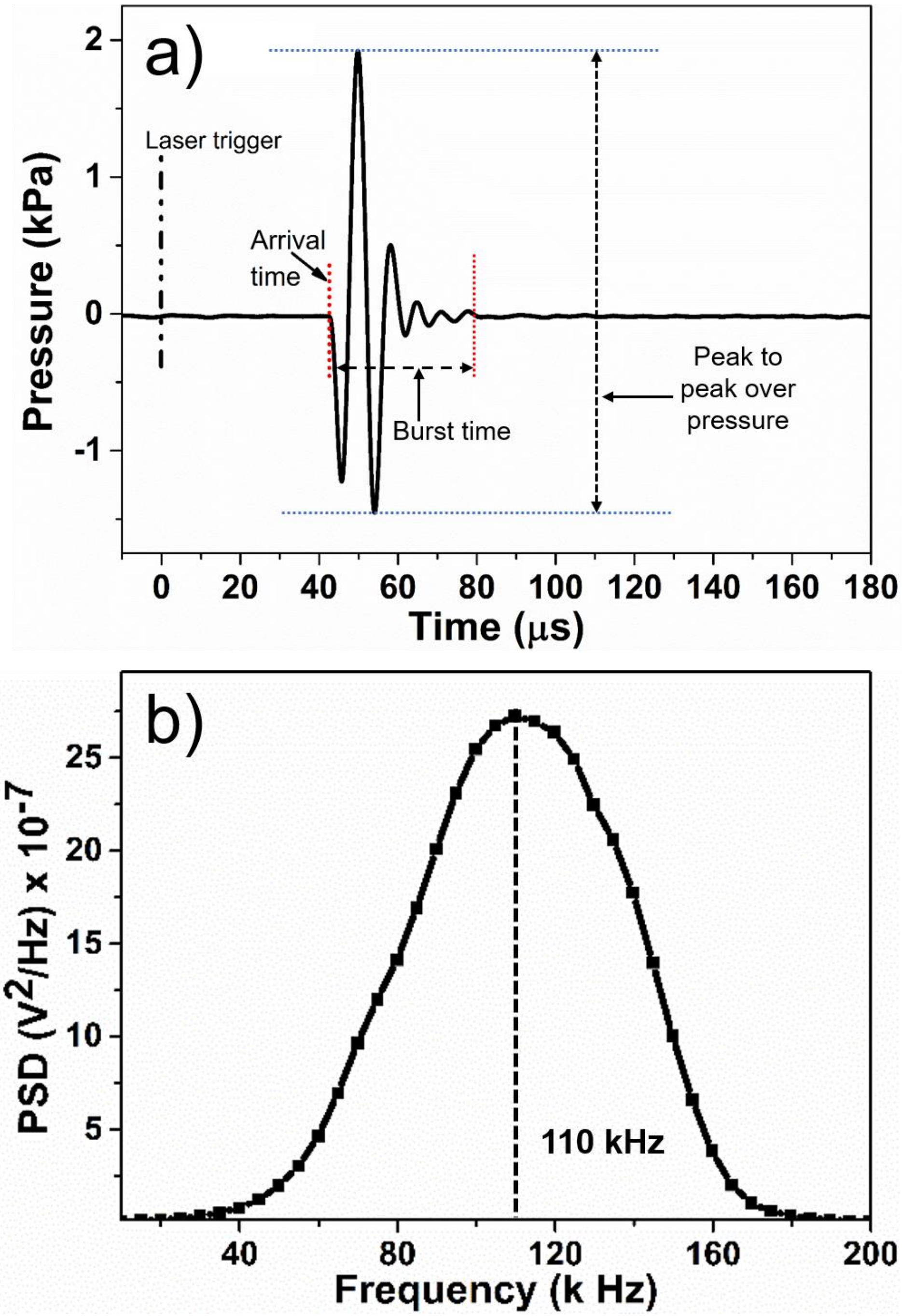

Figure 5.3: Time domain and frequency domain signal from the filament generated using a 150mm lens.

The acoustic pulse was acquired along the length of the filament thereby establishing the spatial acoustic profile of the filament. Figure 5.4 shows the variation of peak to peak over pressure along the filament with the optical image of the filament generated using a 150mm lens superimposed. We find that the microphones provide a spatial resolution of 2 mm and we can map the spatial extent of the filament even beyond the visible portion of the filament as shown in figure 5.4.

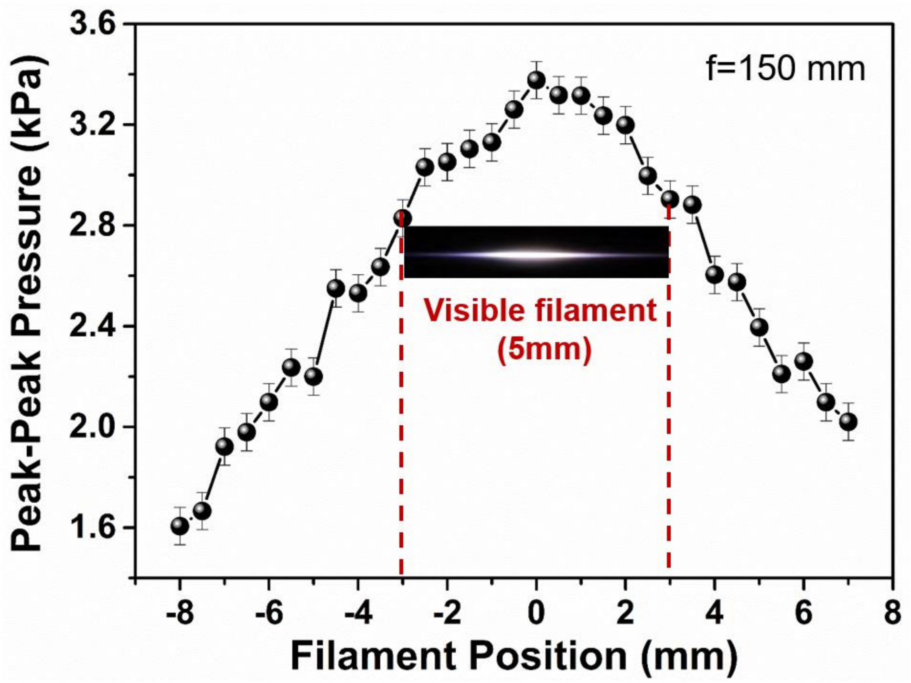

Figure 5.4: Peak to peak over pressure profile along the filament generated from a 150mm lens.

Filaments were generated with the 150mm lens under varying input pulse energies ranging from 0.25 mJ to 2.3 mJ per pulse. This was done to observe the effect of the change in plasma electron density on the acoustic emissions from the filament. As the filament is generated from a 150mm tightly focused laser pulse, the spatial extent of the filament is small (3 mm). We know that the peak intensity increases with pulse energy. This was shown in chapter 3 where the intensity of the filament increases up to the maximum pulse energy available at 3.6 mJ per pulse. Filament generated from a 150mm lens also has negligible shift in onset of filament with change in input pulse energy. Figure 5.5 shows the peak to peak over pressure observed with change in input pulse energy.

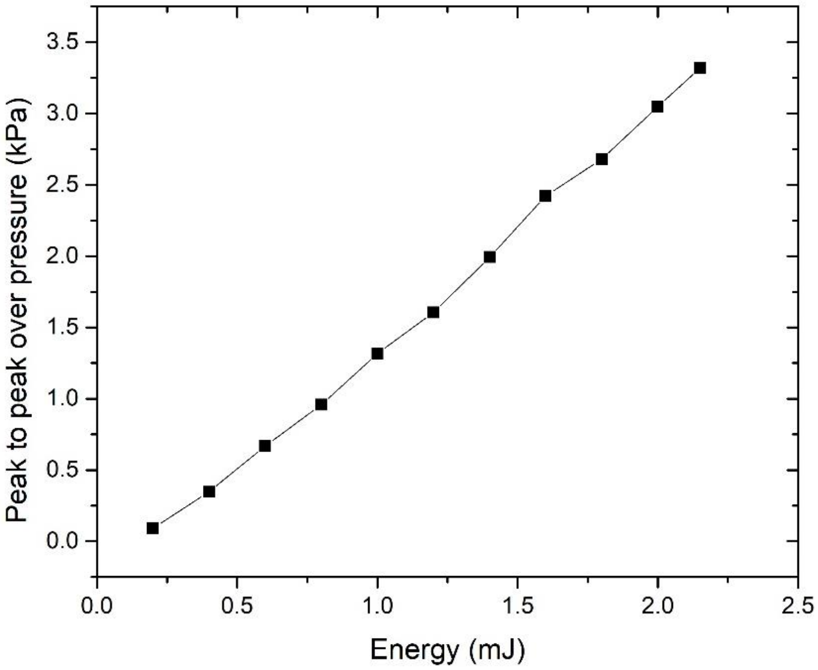

Figure 5.5: Change in peak to peak over pressure with input pulse energy from a filament generated using a 150mm lens in air.

We measured the arrival time along with the burst length of the acoustic pulse with change in input pulse energy for the filament generated with the 150mm lens, shown in the figure 5.6. We observe a decrease in arrival time of the acoustic pulse with increase in pulse energy. This happens because more intense plasmas with high electron densities emit acoustic waves at higher velocities. The arrival times can therefore be seen to be inversely proportional to the plasma density.

In figure 5.7 we compare the spatial variation of peak to peak over pressures measured for filaments generated from 500mm and 2000mm lens. The relative magnitude of the over pressures for the 2 cases as can be seen in the figure reflect the electron density estimation along the filament generated using a 500mm lens. It should also be noted that the filament generated from the 2000 mm couldn't be characterized by spectroscopically as the filament self-emission signal is too weak. In such cases the acoustic characterization can be very good tool to give an estimate of extent of filament and distribution of electron density as the acoustic profile of the 2000mm lens is well mapped. Filament images show that the filament generated from 500mm and 2000mm have a visible spatial extent of 3cm and 15cm respectively. It can be seen that acoustic signal exists beyond the visible extent and optical characterization extent.

We can identify the existence of filaments by simultaneously analysing the arrival times and acoustic pulse profile. Change in the acoustic peak to peak over pressure can be systematically correlated to other characterization techniques (using self-emission spectra or damage analysis) and calibrated to estimate electron density in the filament.

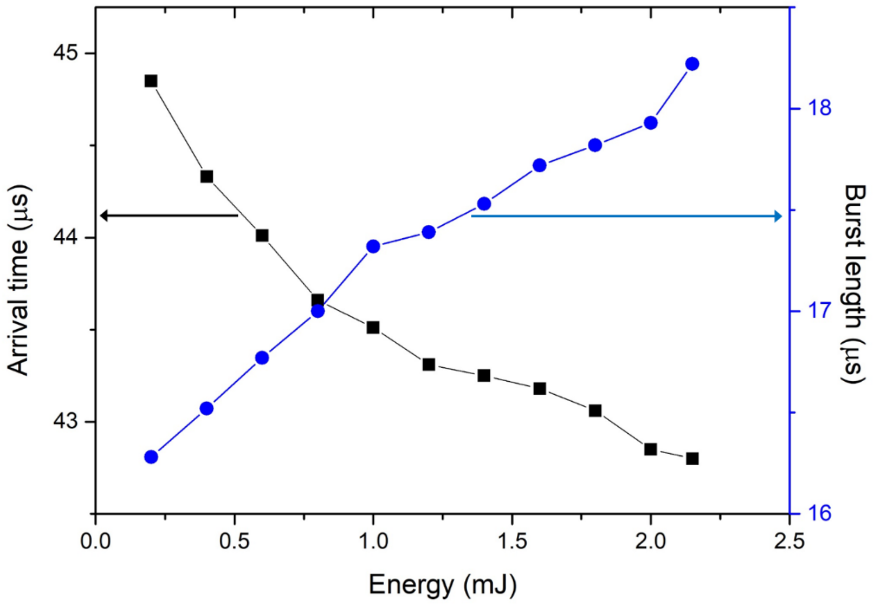

Figure 5.6: Arrival times and burst time of acoustic pulses with change in pulse energy from a filament generated using a 150mm lens.

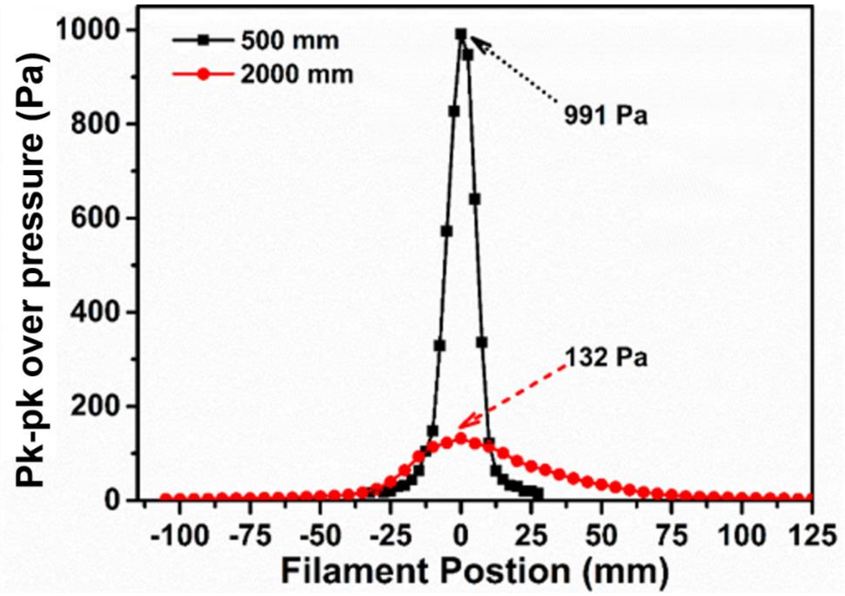

Figure 5.7: Magnitude of peak to peak over pressures along filaments generated from 500mm and 2000mm lenses.

5.3 Spatial characterisation of acoustic emissions from filaments generated with different focal geometry

Acoustic emissions along the filaments generated using different lenses was measured by translating the microphone along the length of the filament. The arrival times and the peak pressures vary along the filament indicating varying electron densities and filament intensities. The filaments which were classified as loose and tightly focused filaments were taken to be the primary classification for this study of focal geometry on filament induced acoustics as well.

The microphone used has a spatial resolution of 2mm, because of which short filaments cannot be well resolved. It can be seen that the microphone picks acoustic signals from regions where filament does not emit in the visible region. The acoustic profile of the filaments generated from the lens having focal length 150mm and 300mm which correspond to tight focusing conditions and 500mm and 2000mm which correspond to loose focusing conditions are shown in the figure 5.8.

It can be seen from the plots that the arrival time of the pulse increases when the microphone goes beyond the visible spatial extent of the filament for tightly focused (f=150mm and 300mm) but the profile of the pulse does not. Acoustic studies done on laser matter interaction of nanosecond and picosecond pulses have shown that the arrival time is inversely proportional to the electron density and peak to peak over pressure is directly proportional to the electron density [6, 17]. We will find from acoustic studies of filamentation that arrival times and burst time of the pulse also reflect the plasma dynamics in the filament. During filamentation, the initial wavefront before the onset of filamentation is crucial to the subsequent dynamics. These dynamics define the existence of intensity clamping and plasma generation in the filament. As the filament from the 150mm lens is very small due to the large curvature in the initial wavefront, we find that the filament cannot be resolved beyond the spatial extent of the microphone. Increase in focal length increases the radius of curvature of the wavefront because of which we increase in the filament generated from the 300mm lens where we observe an minimal change in arrival time (<2µs) for a region (~20mm) of the spatial acoustic profile of the filament [18-20]. When observing the acoustic profile of the filament from 500mm lens, along with drop in magnitude, we find drastic changes in pulse profile and burst length especially at the peripheries with negligible changes in the arrival time.

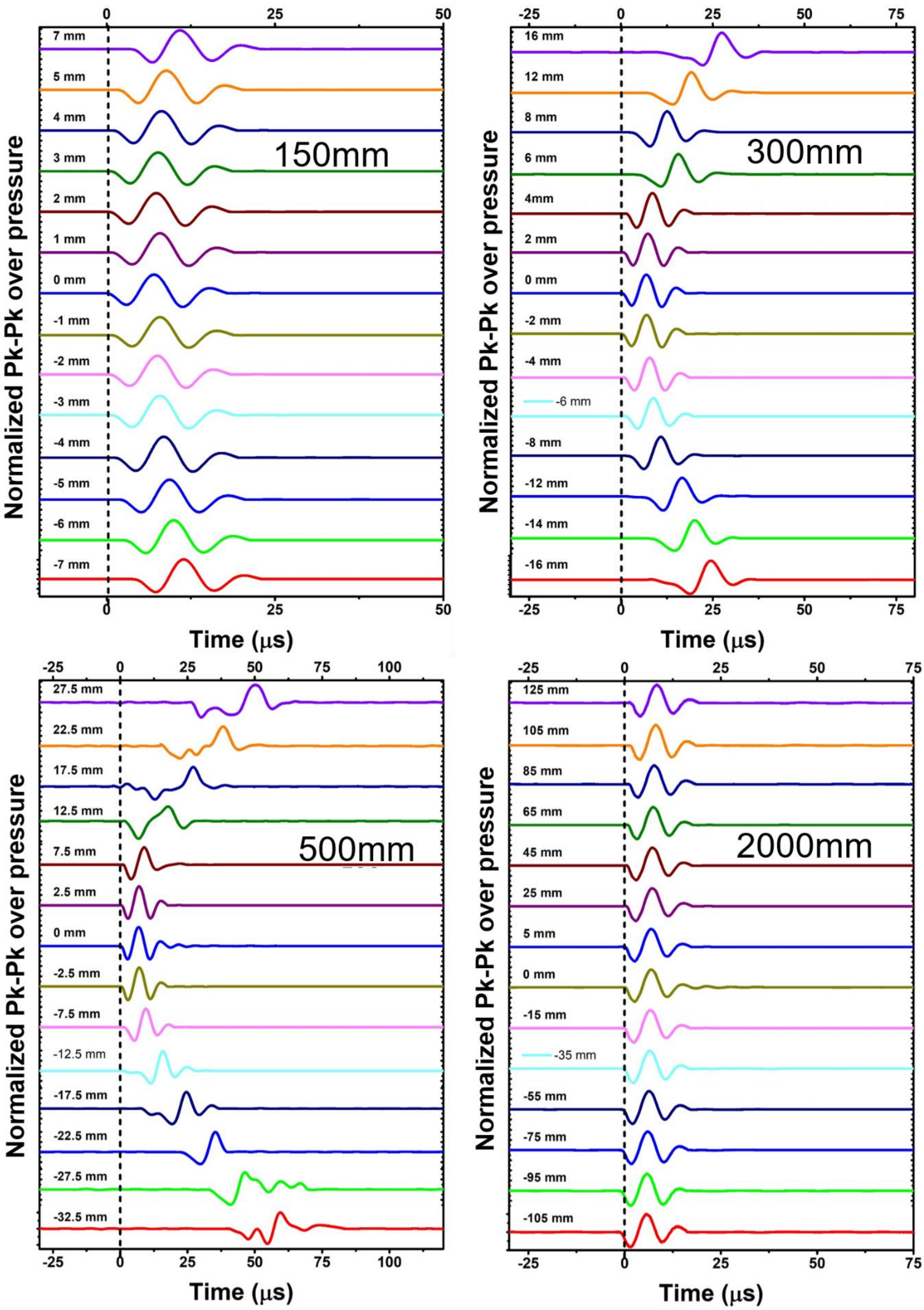

Figure 5.8: Acoustic profiles of filaments generated using lenses with; (top) tight focusing conditions (focal length (mm) =150 and 300) and (below) loose focusing conditions (focal length (mm) =500 and 2000).

To further understand this, the estimated electron density and intensity of the filament which influence the acoustic emission are shown in the figure 5.9.

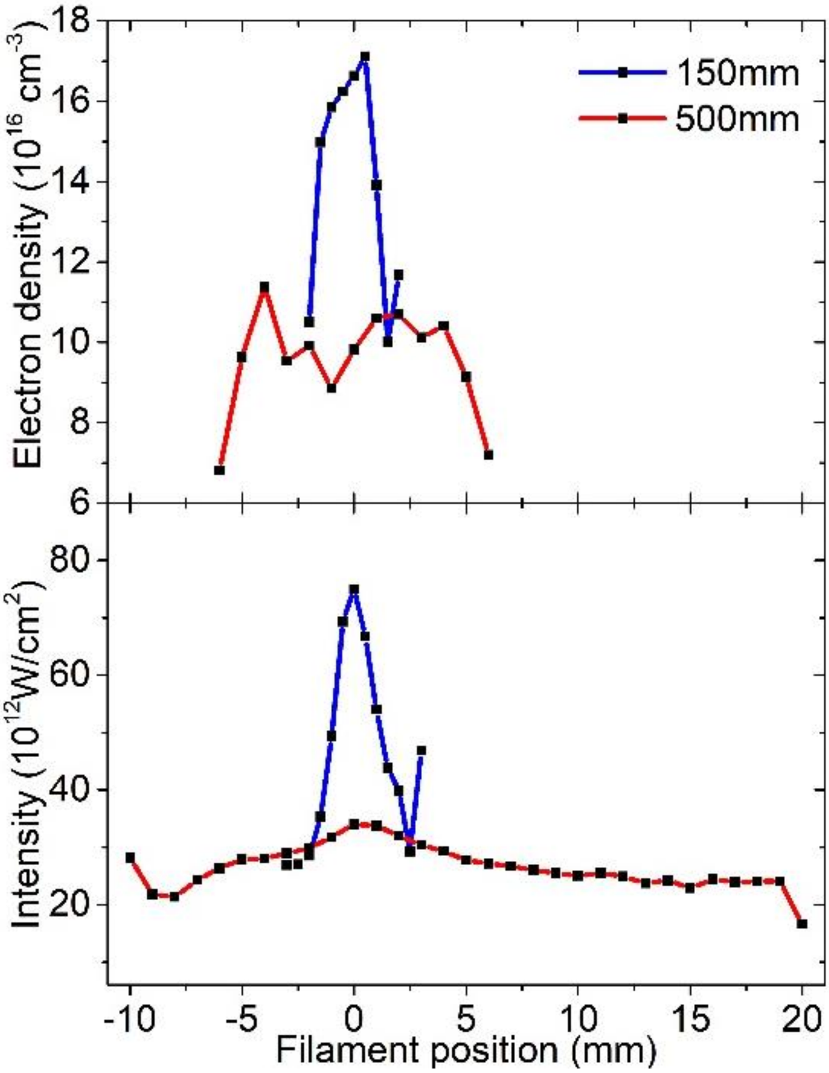

Figure 5.9: Electron density and intensity profile alone filaments generated using 150mm and 500mm lenses.

The filament generated from the 500mm lens could be spectroscopically characterized up to a spatial extent of 30mm, but the acoustic profiles show that the spatial extent of the filament is ~50mm. Moreover, we also observe a drastic change in the pulse profile and burst length at the peripheries of the filament. It is hypothesised that this is due to the existence of multiple weak filaments which propagate collinearly before and after the regime of single filamentation [19]. The multiple filaments have their own corresponding acoustic signals which interfere and modify the observed acoustic pulse. We know there exist multiple filamentation even in tightly focused filament but the tight packing and negligible differences between electron densities of the filaments causes the temporal profile to be highly uniform which is further supported when the ourier transform is taken to make the frequency distribution [20]. The electron density and intensity plots estimated from the filament induced self-emission spectrum of the filament generated using the 500mm lens do not show occurrence of dynamic changes at the peripheries of the filament which are revealed in the acoustic signal profile of the filament.

The acoustic emission from the filament generated using the 2000m lens on the other hand shows a highly uniform profile along the filament whose arrival time and pulse profile do not vary over a distance of ~25cm while the visible extent is ~15cm. The wavefront that leads to the filament generated using the 2000mm lens has a large radius of curvature because of which the filament observed has a uniform plasma density over a long distance. As this filament is not visibly bright, spectroscopic or optical characterization is a challenge. This experiment shows the ability of acoustic profiling of filaments to detect weak filaments which can be further characterized. This can be done when the acoustic signals are calibrated with respect to known electron densities according to the distance from detector to source of signal. The filament generated from the 2000mm lens has a characteristic cylindrical acoustic emission profile which only varies in amplitude along the filament but has a constant arrival time. There is also minimal variation in acoustic profile as it will be further justified from the frequency distribution of the emissions obtained from the Fourier transform of the input pulse.

The change in arrival time and pulse width/burst lengths for the different focusing conditions are shown in the figure 5.10. We can see that the curve of the burst time and arrival time have same profile all along the profile of the filament generated by the 150mm lens, even beyond the filament extent. There is a minor deviation between the profiles of the two curves showing arrival times and burst length at the peripheries of the filament generated using the 300mm lens. This deviation between the curves becomes significant from the filament generated from the 500mm filament. We attribute this is to the existence of multiple filaments at the peripheries of the filament whose acoustic signals interfere and produce increased burst times. This can be emphasized further when one does a frequency transform and observe the spectral components in these positions along the filament. The burst time and arrival time plots observed for the acoustic pulses from filament generated using the 2000mm lens shows uniform distribution of electron density and uniform acoustic emissions along the length of the filament

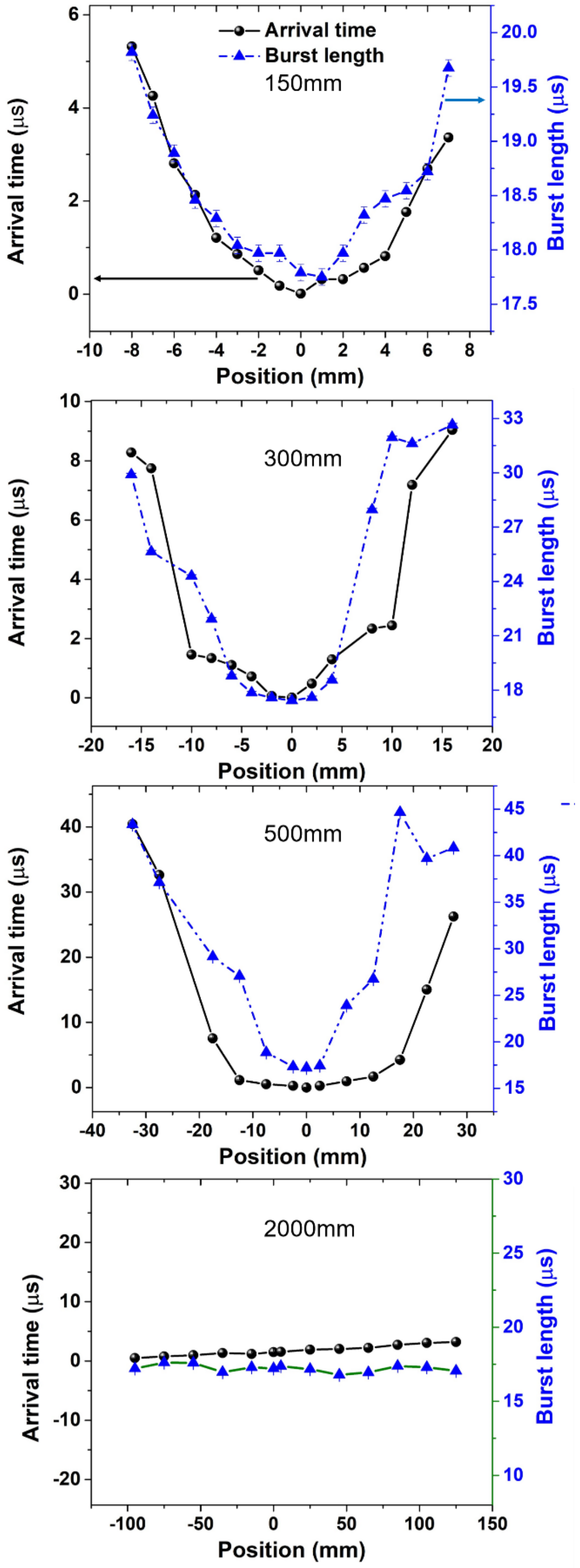

Figure 5.10: Arrival times and pulse widths/burst times of the acoustic pulses along the filament generated from 150mm, 300mm, 500mm and 2000mm lenses.

The filament from 2000mm has a highly uniform spatial profile only showing drop in the magnitude along the filament while the pulse profile and arrival time remain constant. The curves are therefore parallel to each other and the x-axis which is the position along the filament. This uniform acoustic profile exists much beyond the visible filament while having a cylindrical emission profile. This also indicates the significance of the input pulse front curvature which leads to filamentation and the subsequent dynamics. We observe a transition from tight focusing conditions to loose focusing conditions, along with filament behaviour during this transition using a simple and effective method.

5.4 Frequency spectrum of the acoustic pulse: Spatial variation along the filament

The acoustic pulses were further transformed to the frequency domain by fast Fourier transform. Acoustic pulses being transient signals (<20μs) have a broad frequency distribution. The acoustic pulses were first zero padded before doing the Fourier transform to increase the resolution of the Fourier distribution. The frequency distribution at the most intense part of the filament for all the lenses used is shown in the figure 5.11.

Frequency analysis of the signals shows that although the electron densities vary, the peak frequency at the most part of the filament remains constant at 100-110kHz even when the electron density reduces by ~5 times when filament generation varies from 150mm to 2000mm focal length. This is unlike acoustic generation from laser matter interaction of longer pulses in the picosecond or nanosecond regime where we observe, drop in central frequency of the frequency distribution with increase in pulse energy. This observation in the case of longer laser pulses is due to the correlation of plasma width to the central peak frequency of the plasma which forms due to inverse Brehmsstrahlung ionization or avalanche ionization. In the longer pulse regime the time scale of the laser and laser energy determines the energy redistribution leading to acoustic pulse generation in air, where the average collision time in air is ~400fs. This can be further emphasised when comparing acoustic emissions from nanosecond and picosecond pulses in air, the central peak frequency for ns pulses (30mJ , 7ns) is ~70kHz and the central peak frequency for ps pulses (30mJ, 30 ps) is ~100kHz [6]. The increased lifetime and dimension of plasma leads to the acoustic emission dropping in peak central frequency. In the case of femtosecond pulses the lifetime of the plasma does not depend on the laser as the laser pulse is much shorter than the plasma lifetime and energy redistribution processes. Therefore, we do not observe a large shift in the frequencies between filaments formed in air with varying electron densities.

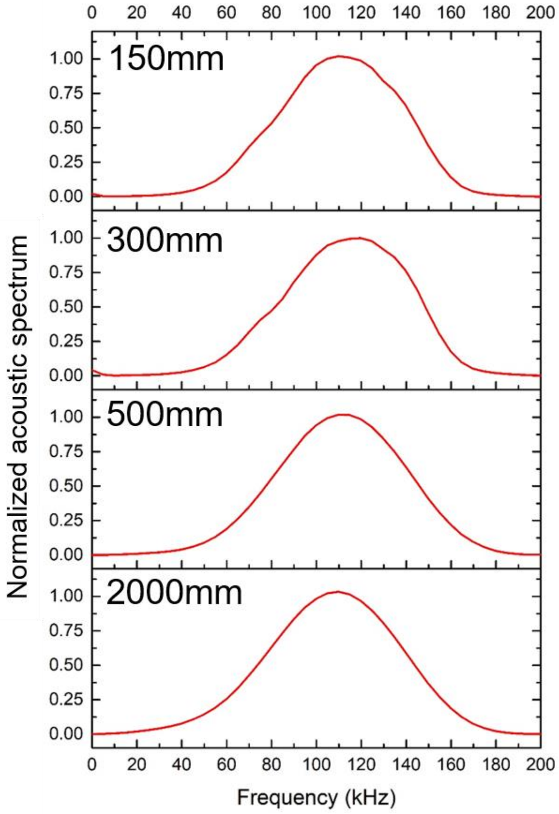

Figure 5.11: Frequency distribution at most intense region of filaments generated from the different lenses (f(mm)=150, 300, 500 and 2000).

The central frequency of all the filaments at the most intense region is found to be the same and is centered around 100-110kHz. We also characterised the spatial variation of the frequency content of the acoustic pulses along the length of the filament for all the filaments from various lenses. The figure 5.12 shows contour plot of the normalized frequency distribution along the length of the filament for the tight focusing regime of filaments generated using lens of focal length 150mm and 300mm. It can be seen that the central frequency starts reducing once the microphone crosses the spatial extent of the filament which is as expected. The acoustic frequency distribution profile along the filament generated from 150mm lens is smooth as we do not have the spatial resolution because the filament length is comparable to the diameter of the microphone diaphragm (~1/8inch). The acoustic frequency distribution profile for the filament generated from the 300mm lens although largely uniform, shows existence of minimal irregularities at the periphery of the filament which can indicate interference of multiple acoustic signals from multiple filaments.

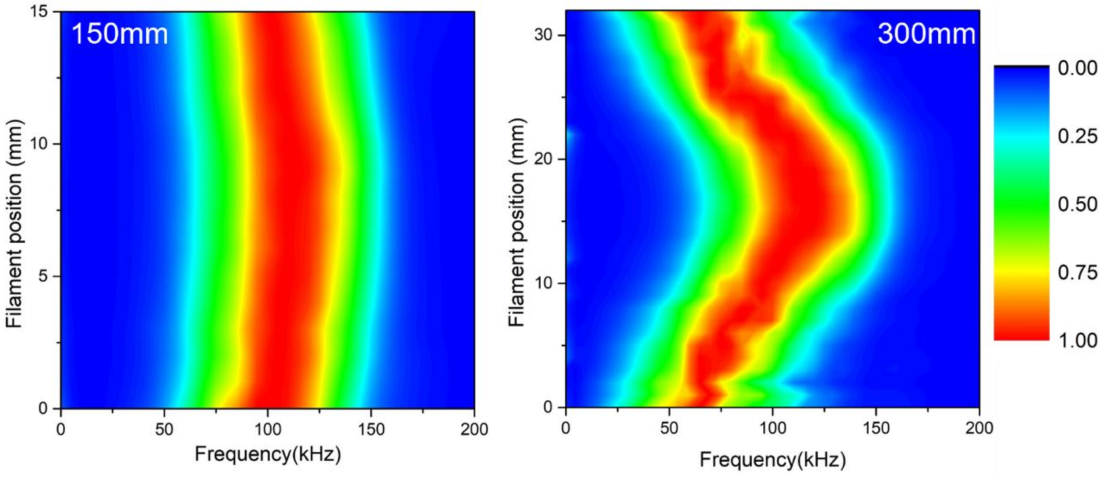

Figure 5.12: Central frequency of acoustic signal along the filament from filaments generated from lens having focal length of (left) 150mm and (right) 300mm.

The figure 5.13 shows contour plot of the normalized frequency distribution along the filament for the loose focusing regime of filaments generated using lens of focal length 500mm and 2000mm lens. The acoustic frequency distribution profile for these filaments show large differences especially when studying the periphery of the filament. The frequency distribution at the peripheries of the filament generated using the 500mm lens clearly shows the existence of multiple frequency components. The filament generated from 2000mm lens on the other hand displays a uniform emission at a single frequency all along the filament.

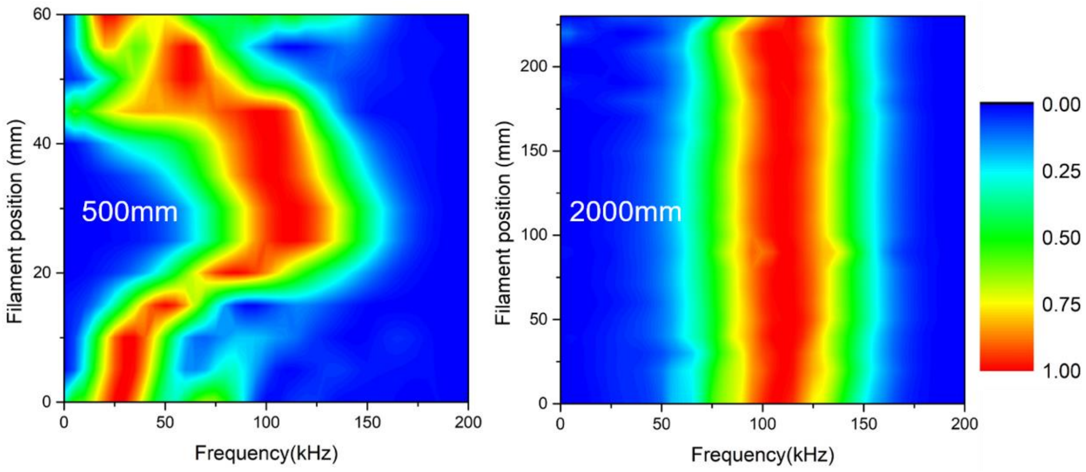

Figure 5.13: Central frequency of acoustic signal along the filament from filaments generated from lens having focal length of (left) 500mm and (right) 2000mm.

Figure 5.14 shows profiles at the central and peripheral positions to better illustrate the existence of multiple frequencies from the acoustic profile obtained from the filament generated using a 500mm lens. Multiple filamentation occurs for filaments generated using the 150 mm and 300mm focal length also, but they are tightly packed and therefore cannot be resolved, especially for filament generated using the 150mm lens. The filament from the 300 mm lens shows slight evidence of multiple filamentation but it becomes more evident in the filament from the 500 mm lens as the filaments separate out better. Other than just showing existence of weak filaments we can observe significant characteristic changes in the acoustic pulse profile (due to addition of individual acoustic pulses from multiple sources) and frequency distribution from the acoustic signal obtained from the tail and front of the filament generated from 500mm lens. Figure 5.14 shows the acoustic pulse profile and frequency distribution at the points at the filament position where multiple frequency components are observed. A complex shape obtained due to coalescing of individual acoustic emissions from multiple filaments in turn leads to a frequency spectrum with multiple frequency peaks.

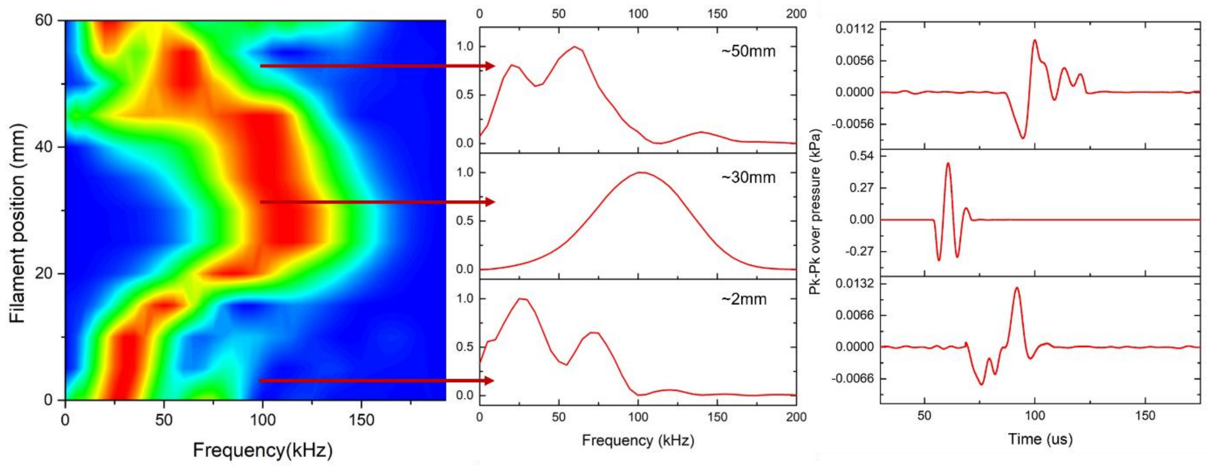

Figure 5.14: Acoustic signal frequency distribution at different positions along the filament generated by the 500mm lens.

This is the region of weak filaments which are propagating separately before and after coalescing into a single filament. The acoustic signal due to the interference of the acoustic pulses from multiple filaments is the cause for the increase in the pulse width and the existence of multiple frequencies at the peripheries of the filament generated from the 500mm lens as shown in the figure 5.14. Acoustic profiling can therefore in principle be used to identify weak filaments and also identify other properties of filaments such as multiple filamentation which conventional optical characterization techniques don't provide unless we use high resolution imaging of the filament. Therefore spatial acoustic profiling of a filament can provide a holistic picture of the different kinds of filaments that can be generated.

5.5 Spatial characterisation of acoustic pulses from filaments generated from a single lens and a lens combination (telescope)

The filaments were generated under the same focusing conditions using a lens combination and the acoustic profiles were compared. As we have observed contrasting acoustic emission profiles generated from the 500m and 2000mm lens, we have generated filaments under these same focusing conditions. Acoustic signals from filaments generated under an effective focal length of 500mm are shown in the figure 5.15. This was done to not only test the existence of similar acoustic pulse instabilities for common focusing geometry, but also develop an effective variable focal length mechanism.

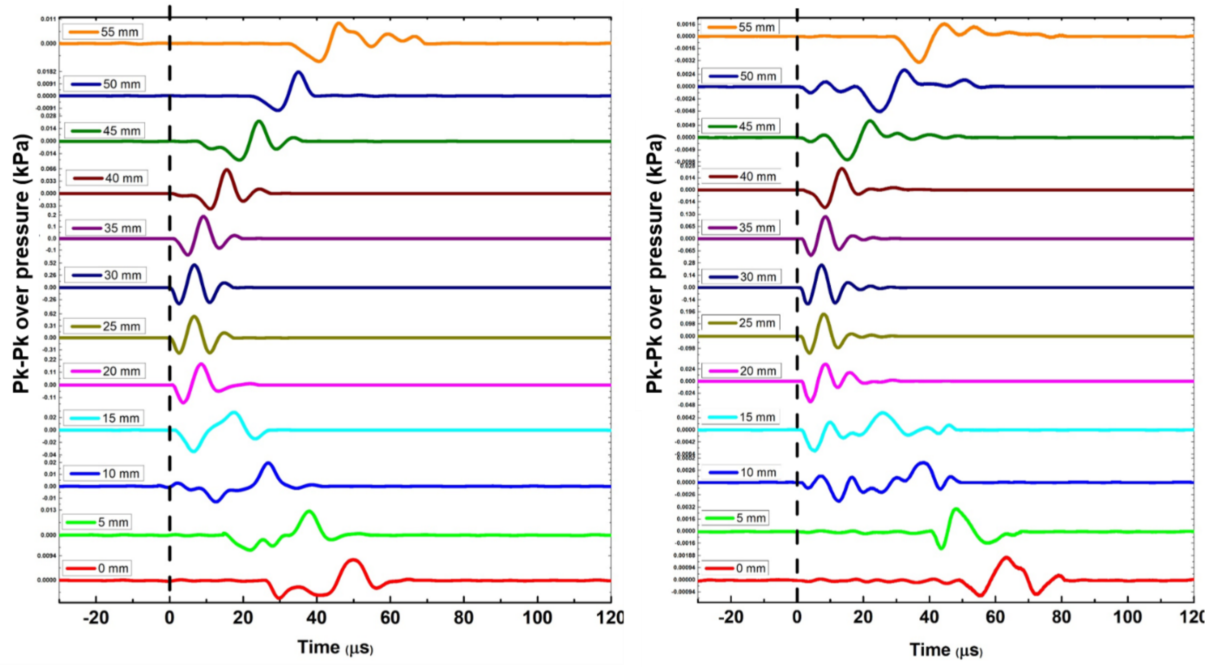

Figure 5.15: Acoustic pulses along the filaments generated using a single lens and a combination of lenses with f_{eff}=500mm.

We observe the similar behaviour between both the filaments along with the change in pulse profile at the peripheries of the filament. We observe a drop in the amplitude of the peak to peak over pressure by ~50% from the filament generated using the combination of lens. This is because of the increased dispersion and scattering that occurs due to the propagation of the pulse through two lenses instead of one lens which reduces the input pulse intensity. The instability in the acoustic profile is more emphasized from the filament from the combination of lenses. The instability exists for longer distance before the onset of the uniform acoustic pulse profile and also begins earlier after the uniform acoustic pulse profile for the filament generated from the combination of lenses. We observe this because of the increased number of spatial instabilities and aberrations arising due to propagation through two lenses in the case of the filament generated from a combination of lenses. These observations become more emphasized when noting the frequency distribution comparison of the acoustic profile from filament generated under the two focusing mechanisms shown in the figure 5.16. The frequency distribution shows common central frequency at 110 kHz at the most intense part of the filament, but the number of frequency components that arise from the peripheries of the filament generated using the combination of lenses are more.

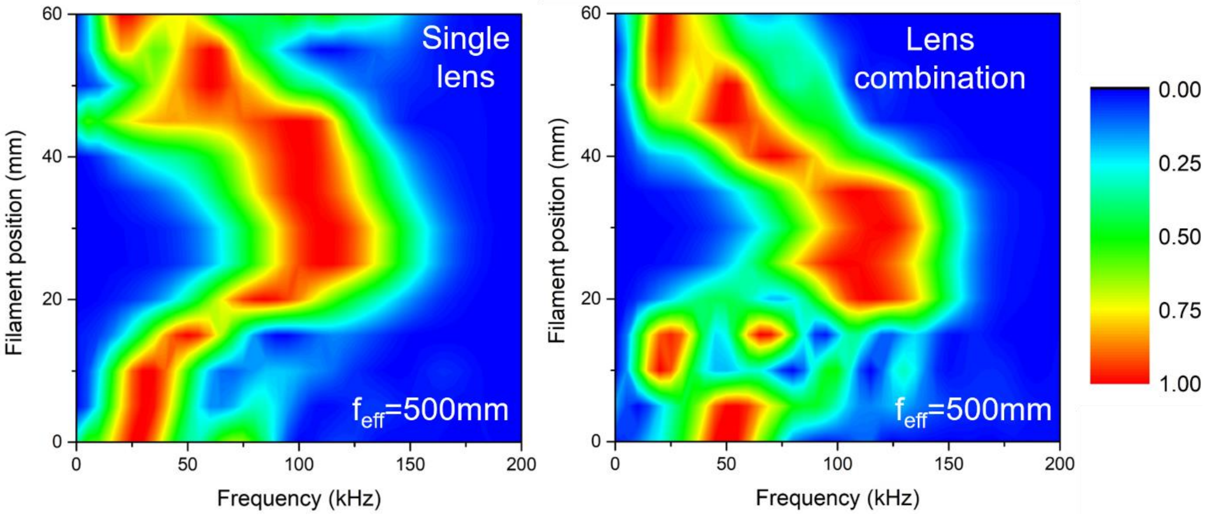

Figure 5.16: frequency distribution of acoustic pulses from filaments generated using a single lens and a combination of lenses with f_{eff}=500mm.

Filaments were generated using the combination of lenses with an effective focal length (f_{eff}) of 2000mm using a single lens and a combination of lenses. The observed acoustic pulses with propagation are compared as shown in figure 5.17.

The filaments generated have the same acoustic profile along the filament, with a drop in the amplitude of the peak to peak over pressure by ~80%. The difference in amplitude reflects the electron density difference between the filaments generated from the two focusing mechanisms. This drop is much larger than that was observed from filaments generated under an effective focal length of 500mm. The frequency distribution of the acoustic signals along the filaments generated plotted in figure show that other than drop in the amplitude of the peak to peak over pressure, there is no significant contrast between the filaments generated with this effective focal length.

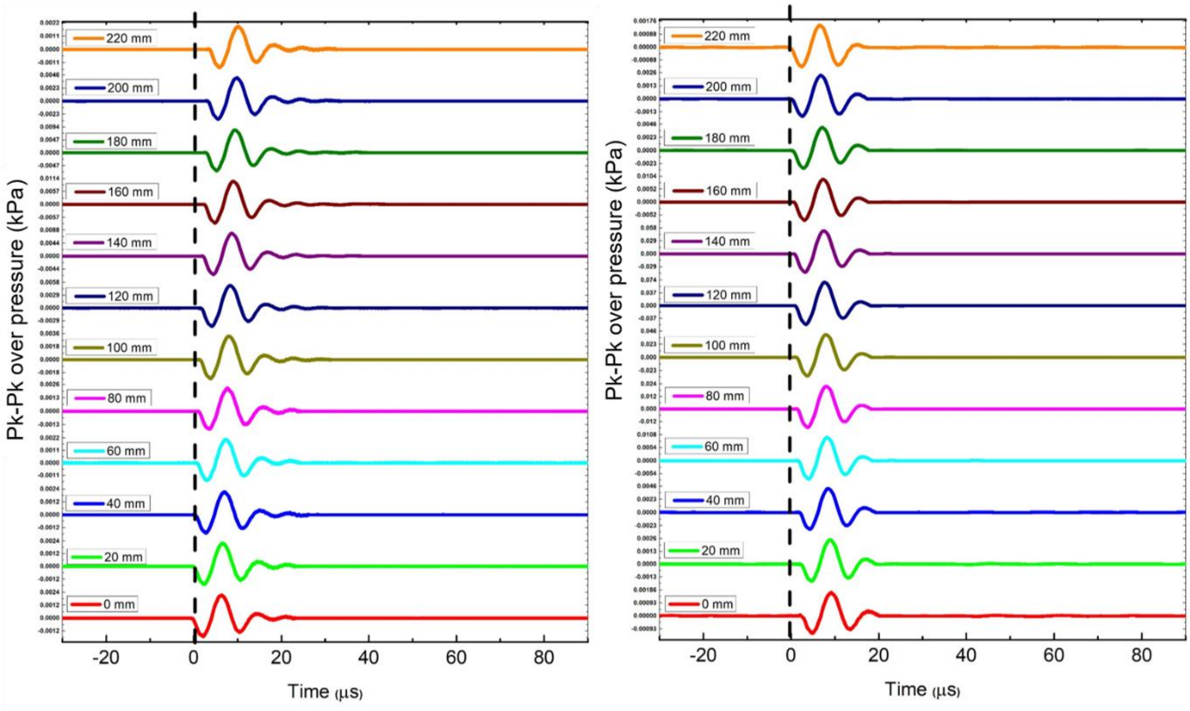

Figure 5.17: Acoustic pulses along the filaments generated using a single lens and a combination of lenses with f_{eff}=2000mm.

We observe a constant peak frequency at 110 kHz which stays constant all along the propagation of the filament for both focusing mechanisms as seen from the figure. This shows that filaments generated using a lens combination have the same properties as those generated from a single lens, except for a drop in intensity. Clear correlation between acoustic signal properties such as peak to peak over pressures and arrival times can help identify and distinguish weak filaments which cannot be characterized spectroscopically.

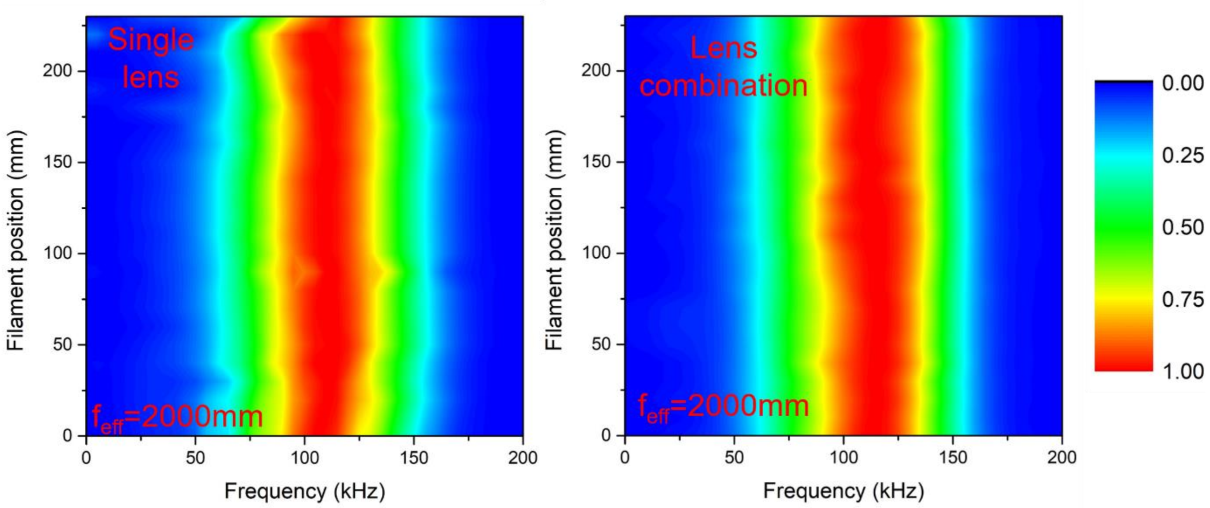

Figure 5.18: frequency distribution of acoustic pulses from filaments generated using a single lens and a combination of lenses with f_{eff}=2000mm.

5.6 Effect of aberrations and pulse chirp on Filament induced acoustic emissions

The third chapter of this thesis highlights the effects of optical element induced aberrations on filamentation. The various filament characteristics such as SCG, intensity and electron density were correlated to the aberrations estimated from the different optical elements used under common tight focusing conditions. We have extended this study to do an acoustic analysis of the filaments generated under the tight focusing conditions, a regime where optical element induced aberrations are crucial in filamentation. The acoustic signal was collected with change in chirp as well, by changing the separation between the gratings of the laser amplifier [21]. This was done because we observe many changes in filamentation dynamics with chirp. The study was performed only under tight focusing geometry (f/#<10) because the onset distance of filament generated under loose focusing conditions changes with change in chirp demanding full acoustic profiling with chirp [22-26]. In the study, a variety of lens were used, the results show the variation of acoustic peak to peak over pressures obtained from a GVD corrected thin lens, thick lens and achromatic doublet. The thin lens was made to have low GVD for use with femtosecond pulses which have a broad frequency distribution. The thick lens induces a good amount of GVD and pulse delay which varies radially along the transverse profile of the beam, inducing the most number of aberrations. The achromatic doublet on the other hand also induces a large amount of dispersion due to the thickness but this lens is designed to not have a radially varying component of dispersion or pulse delay. As can be seen in the figure 5.19, with change in chirp, we find that filaments from both the thick and thin lens show maximum peak to peak over pressure at zero chirp. As seen we do not observe large contrast between thick lenses and GVD corrected thin lenses, other than a difference in the peak to peak to peak acoustic pressure. It was shown in the third chapter that the existence of a radially varying phase in the pulse front is a crucial factor for filament characteristics. Therefore, although we see that the thick lens has a much higher overall GVD as compared to the thin lens, the added curvature in the pulse front is the same for both the lenses. The third chapter also discusses filamentation generated from an achromatic doublet lens lens which does not have a radially varying phase in the pulse front but has a large overall GVD. Because of the overall first order and second order dispersion that gets induced in the pulse that propagates through the achromat we find improved filament characteristics for chirped pulses rather than unchirped transform limited pulses.

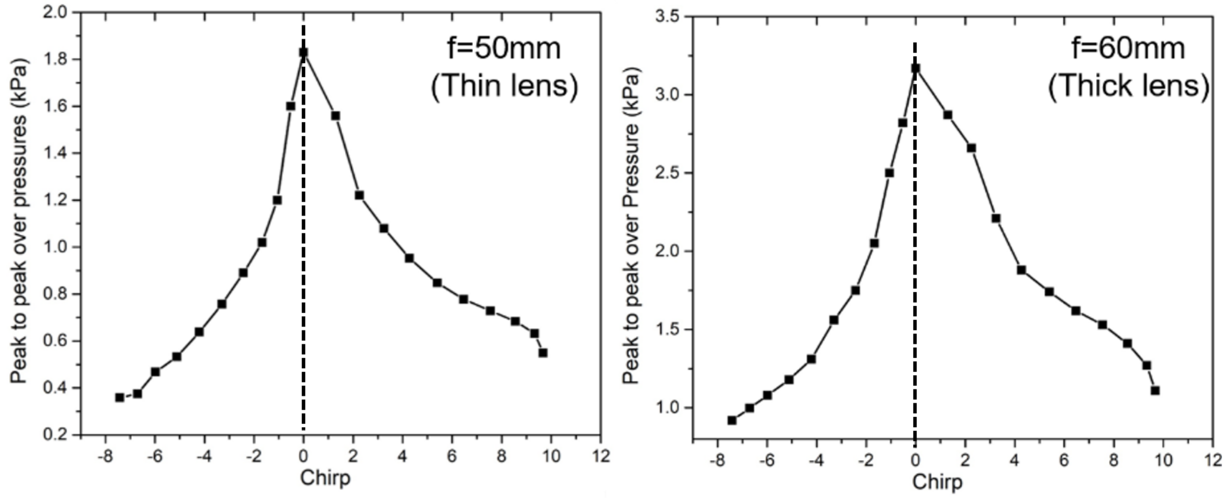

Figure 5.19: Peak to peak over pressures from filaments generated using a thin lens with focal length 50mm (left) and thick lens with focal length of 60mm (right) with change in chirp.

The filament from the achromatic doublet on the other hand has maximum peak to peak over pressure at positive chirp as can be seen in the figure 5.20. As detailed in earlier chapters, at this chirp we also observe increase in supercontinuum generation at the same chirp value of ~2 for the filament from the achromatic doublet.

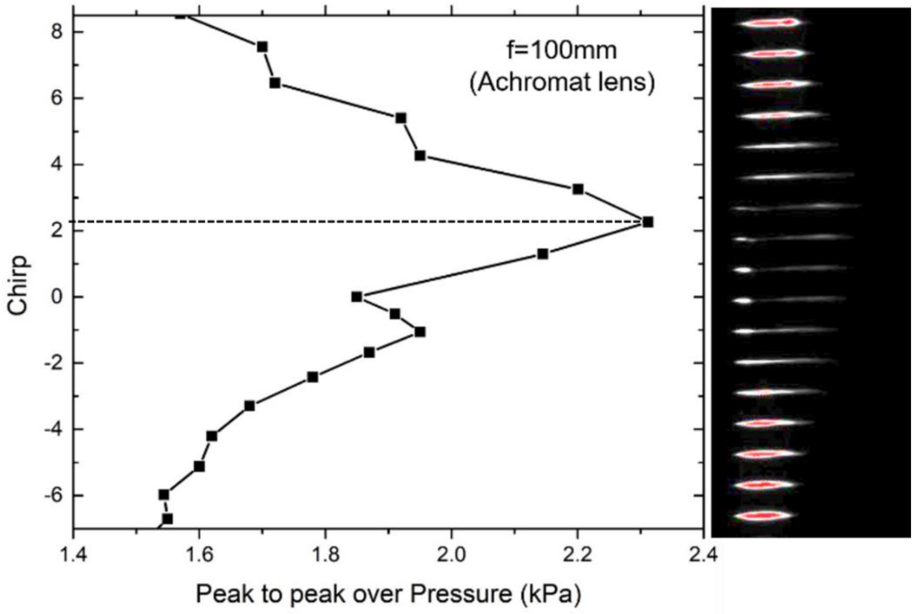

Figure 5.20: Peak to peak over pressures with varying chirp and corresponding filament images from filaments generated using an achromat doublet lens with focal length of 100mm.

It was suggested that the increase in supercontinuum at positive chirp is due to shift in the central wavelength towards higher frequencies. The positive chirp combined with the considerable amount of first order dispersion which induces pulse to phase front delay causes the peak to shift towards the higher frequencies. It can also be seen that acoustic peak to peak over pressure increases for negative chirp as well, this is due to compensation of GVD induced by the achromatic doublet that occurs by inducing negative chirp thereby increasing the intensity of the pulse. When observing filament images from achromatic doublet it can be seen that the filament disappears at positive chirp of 2 and reappears at higher chirp along with a corresponding large continuum which can be shown from the FIBS spectrum from chapter 3. The existence of a broader supercontinuum and higher magnitude of peak to peak over pressure at 2 chirp indicate larger electron density compared to zero chirp although the plasma is not visible.

5.7 Summary

Femtosecond filamentation causes the generation of acoustic waves from the filament due to plasma that expand into ambient atmosphere which launch acoustic waves propagating with varying parameters such as peak-peak overpressures, burst length, arrival time, frequency distribution. In this chapter the non-optical characterization of fs filaments in atmosphere is presented. Filament characteristics such as the intensity and electron density were correlated to the acoustic emission profile along the filament. We find that the plasma density is proportional to peak to peak overpressures associated to the observed acoustic signals. Acoustic profiling of filaments can therefore probe the plasma dynamics existing inside a filament. The Fourier transform of the acoustic signals was done to provide the frequency distribution of the acoustic pulse as well. We have found that acoustic profiling of plasma density in the filament is more sensitive than optical techniques, especially when we observe weak filaments whose optical emissions cannot be collected and also because it has a dynamic range of three orders. The temporal pulse length along with the spectral decomposition of the pulse shows the development and termination of multiple filamentation in the filament. The longitudinal acoustic emission profile was also able to distinguish single and multiple filamentation, such that we can also identify the exact region of multiple filament coalescence into a single filament. To further explore the extent of acoustic characterization of filaments, filaments with varying aberrations were compared. The acoustic characterization of filament from an achromat doublet lens with varying chirp was done and it can be seen that plasma and intensity trends observed using spectroscopic trends are reproduced in the acoustic signals observed. The studies were extended towards sensing of molecular aerosols by using acoustic data from filament aerosol interaction. The detailed results are presented in Chapter 7.

References

1. A. Braun, *Self-channelling of high-peak-power femtosecond laser pulses in air*, Opt. Letters **20**, 73-75 (1995).
2. A. L. Gaeta, *Collapsing Light Really Shines*, Science **301**, 54 (2003).
3. A. Couairon and A. Mysrowicz, *Femtosecond filamentation in transparent media*, Phys. Rep. **441**, 47–189 (2007).
4. J. Yu, D. Mondelain, J. Kasparian, E. Salmon, S. Geffroy, C. Favre, V. Boutou, and J.-P. Wolf, *Sonographic probing of laser filaments in air*, Appl. Opt. **42**, 7117-7120 (2003).
5. S. L. Chin, D. K. Evans, R. D. McAlpine, and W. N. Selander, *Single-pulse photoacoustic technique for measuring IR multiphoton absorption by polyatomic molecules*, Appl. Opt. **21**, 65-68 (1982).
6. E. Manikanta, L. Vinoth Kumar, P. Venkateshwarlu, C. Leela, and P. P. Kiran, *Effect of pulse duration on the acoustic frequency emissions during the laser-induced breakdown of atmospheric air*, Appl. Opt. **55**, 548-555 (2016).
7. B. Forestier, A. Houard, M. Durand, Y.-B. André, B. Prade, J-Y. Dauvignac, F. Perret, C. Pichot, M. Pellet, A. Mysyrowicz, *Radiofrequency conical emission from femtosecond filaments in air*. Appl. Phys. Letters, **96 (14)**, 141111-141113, (2010).

8. C. D'Amico, A. Houard, M. Franco, B. Prade, A. Mysyrowicz, A. Couairon, and V. T. Tikhonchuk, *Conical Forward THz Emission from Femtosecond-Laser-Beam Filamentation in Air,* Phys. Rev. Lett. **98**, 235002 (2007).
9. V. Jukna, A. Jarnac, C. Milián, Y. Brelet, J. Carbonnel, Y-B. André, R. Guillermin, J-P. Sessarego, D. Fattaccioli, A. Mysyrowicz, A. Couairon, and A. Houard, *Underwater acoustic wave generation by filamentation of terawatt ultrashort laser pulses*, Physical Review E, **93(6)** 063106 (2016).
10. S. Conesa, S. Palanco, and J. J. Laserna, *Acoustic and optical emission during laser-induced plasma formation*, Spectrochimica Acta Part B: Atomic Spectroscopy, **59(9)**, 1395-1401 (2004).
11. S. L. Chin, *Multiphoton Ionization of Gases*, Elsevier (2012).
12. B. A. Tozer, *Theory of the ionization of gases by laser beams*, Physical Review, **137(6A)**, A1665 (1965).
13. J. K. Wahlstrand, N. Jhajj, E. W. Rosenthal, S. Zahedpour, and H. M. Milchberg, *Direct imaging of the acoustic waves generated by femtosecond filaments in air*, Opt. Lett. **39**, 1290-1293 (2014).
14. H. Jin, J-W. Kim, Ji-A. Son and J-G. Choi, *An acoustic based, laser induced breakdown method for determining the sizes and concentrations of nanoparticles*, Physical Chemistry Chemical Physics, **12(20)**, 5199-5202 (2010).
15. P. Sprangle, J. R. Penano, and B. Hafizi, *Propagation of intense short laser pulses in the atmosphere*, Phys. Rev. E, **66(4)**, 046418 (2002).
16. N. B. Zorov, A. A. Gorbatenko, T. A. Labutin and A. M. Popov, *A review of normalization techniques in analytical atomic spectrometry with laser sampling: From single to multivariate correction*, Spectrochimica Acta Part B: Atomic Spectroscopy, **65(8)**, 642-657 (2010).
17. J. R. Freeman, S. S. Harilal, P. K. Diwakar, B. Verhoff and A. Hassanein, *Comparison of optical emission from nanosecond and femtosecond laser produced plasma in atmosphere and vacuum conditions*, Spectrochimica Acta Part B: Atomic Spectroscopy **87**, 43-50 (2013).
18. W. Liu, S. Petit, A. Becker, N. Ak¨ozbek, C. M. Bowden, and S. L. Chin, *Intensity clamping of a femtosecond laser pulse in condensed matter*, Opt. Commun. **202**, 189–197 (2002).
19. P. P. Kiran, S. Bagchi, C.L. Arnold, S. S. Krishnan, G. Ravindra Kumar, and A. Couairon, *Filamentation without intensity clamping*, Opt. Exp. **18**, 21504 (2010).
20. P. P. Kiran, S. Bagchi, S. Sivaram Krishnan, C.L. Arnold, G. Ravindra Kumar, and A. Couairon, *Focal dynamics of multiple filaments: Microscopic Imaging and Reconstruction*, Phys. Rev. A, **82**, 013805 (2010).
21. D. Strickland and G. Mourou, *Compression of amplified chirped optical pulses,* Opt. Commun. **55(6)**, 447-449 (1985).
22. J. Park, J-h. Lee and C. Hee Nam, *Laser chirp effect on femtosecond laser filamentation generated for pulse compression*, Opt. Exp. **16(7)**, 4465-4470 (2008).
23. R. N., S. Skupin and L. Bergé, *Chirp-induced dynamics of femtosecond filaments in air*, Opt. lett. **30(8)**, 917-919 (2005).
24. A. Couairon, M. Franco, G. Méchain, Thomas Olivier, Bernard Prade and André Mysyrowicz, *Femtosecond filamentation in air at low pressures: Part I: Theory and numerical simulations*, Opt. Comm. **259(1)**, 265-273 (2006).
25. O. Varela, B. Alonso, I. J. Sola, J. San Román, A. Zaïr, C. Méndez, and L. Roso, *Self-compression controlled by the chirp of the input pulse*, Opt. Lett. **35**, 3649-3651 (2010)
26. V. Shumakova, S. Ališauskas, P. Malevich, A. A. Voronin, A. V. Mitrofanov, D. A. Sidorov-Biryukov, A. M. Zheltikov, D. Kartashov, A. Baltuška, and A. Pugžlys, *Chirp-controlled filamentation and formation of light bullets in the mid-IR,* Opt. Lett. **44**, 2173-2176 (2019).

This page was intentionally left blank

CHAPTER 6: Filament Induced eLectro Magnetic (FIeLM) emissions: L-band RF emissions from fs laser filaments

Abstract:

Emissions in the radio frequency region from laser matter interaction due to bulk charge oscillations and currents, provides a highly promising technique for characterization of materials and remote generation of electromagnetic RF pulses. Although one can generate a plasma in a remote region using femtosecond pulses, the highly transient nature was thought to not produce ion movement which generates RF. We have shown generation and detection of RF from femtosecond filamentation which is highly directional and dependant on the plasma dynamics. Time domain signals were collected using a dipole antenna, which were transformed to the frequency domain using Fourier transform. To correlate the RF generated to the plasma dynamics, we have first observed the influence of focal geometry on the RF emission, which was extended to the study with change in polarization showing highly contrasting results when compared to other emissions from filamentation. RF emissions were also studied under the influence of lens tilt which, not only enhances the RF signal but also cleans the pulse profile as can be seen from the signal and the frequency distribution.

6.1. Electromagnetic pulses from laser matter interaction

Femtosecond filament which is the outcome of the interplay between Kerr self-focusing and plasma defocusing generates a quasistatc plasma column along its highly intense propagation regime [1]. The coexistence of the laser pulse and plasma column in the filament creates charge separation and current flow which causes emissions in the lower frequency range in the electromagnetic spectrum along with that generated in the visible frequency range [2]. This transient electromagnetic pulse is characteristic to the plasma generated and therefore also the input fs pulse. Plasma properties such as temperature and density define the various emissions that arise during recombination and plasma evolution which tends to equilibrium after the laser pulse has passed [3-5]. These emissions can be both mechanical and electromagnetic emissions. As discussed in the earlier chapter mechanical emissions give rise to shockwaves or acoustic emissions, arising due to steep pressure and temperature gradient that exists between the plasma and the surrounding atmosphere [6, 7]. The electromagnetic emissions arising from molecular transitions have been extensively studied in the earlier chapters. These emissions lie in the visible and near visible spectral range.

We also observe electromagnetic emissions in the THz and radio frequency range from the filament, a range of frequencies in which very few sources are available [8, 9]. The THz emission which is due to electron current created by the pondermotive force increases by an order when propagating 2 color filaments made from the fundamental and second harmonic [10, 11]. Intense laser matter interaction has also shown low frequency emissions in the radio and microwave frequency range. RF emissions from nanosecond and picosecond laser matter interactions arise also due to charge acceleration by the laser. Ionization mechanisms are also largely avalanche ionization and inverse Bremsstrahlung ionization for laser matter interaction in that pulse duration [12]. The plasma generation in the case of femtosecond filaments in air is largely multiphoton ionization and there is negligible heating because of which multiple discrete electric moments can be detected [13]. Emissions in the RF range from femtosecond filaments are mainly due to charge separation along the filament and pondermotive force that accelerates lighter ions comparted to heavier ions [14]. RF from Filament interaction with solid targets is much more intense and it was found that RF emissions from any material is element specific thereby provides another characterization technique using laser matter interactions [15]. The ability to create a filament in at remote distances provides us with a unique tool to generate RF in a desired region [16]. The plasma generated from a filament was also shown to be applicable as an antenna [17].

The very first observations of RF emissions from laser generated plasma by Pearlmann and Dahlbacka was observed by irradiating thick and thin films targets with 50ps pulses centred at 1.06μm, where a broad range of RF emissions were detected ranging from 1 to 300MHz [18]. It was suggested that the mechanism of emission was due to macroscopic charge oscillations as the frequencies were much below the plasma frequency of the medium [19]. Microwave emissions were also observed using high energy nanosecond pulses produced using a CO_2 laser and it was hypothesised as due to ion-acoustic instabilities arising from propagation of supra thermal electrons from the light induced breakdown [20]. Sub-terahertz radiation was observed from filaments generated using the Teramobile. It was suggested that electrons left in the trailing plasma channel oscillate at the plasma frequency to produce this radiation [19]. We find that RF emissions from laser matter interactions cover a broad range of frequencies where conventional RF sources cannot emit.

Ground penetrating radar (GPR) which is used to detect subsurface objects is limited by the requirement of a broad range of emitters and antennas [21]. The emissions in the RF range arising from the laser induced breakdown can be used towards laser driven ground penetrating radar (LGPR), as they can be a replacement of the conventional ground penetrating radar which requires a broad range of antennas and long acquisition time especially to probe remote regions [22]. The broad emission from filaments along with the ability to be generated from a remote location make Femtosecond filament induced LGPR a highly promising prospect for future detection technologies. The ability to remotely generate an electromagnetic pulse in the RF range also provides us with countermeasure tools where one can disable electronic equipment with electromagnetic pulses generated near the target threats [23]. The combination of a femtosecond and a nanosecond pulse shows increase in RF by an order when the femtosecond pulse precedes the nanosecond [24].

Although ns and ps pulses demonstrate RF emissions owing to the long pulse duration (compared to fs) which heats and accelerates the electrons, fs pulse generated RF emissions have not been deeply explored mainly because the plasma is not dense and also because the pulse duration was thought to be too short to induce bulk charge movement or charge flow which causes RF emissions [25]. Moreover, the highly transient nature of fs laser generated plasma especially in air makes RF acquisition using spectral analysers a challenge. The ability of femtosecond lasers in the infrared region to propagate long distances in atmosphere provides us with a great remote generation tool, if one can generate RF using femtosecond filaments. However, the efficiency of conversion of input femtosecond pulse energy which forms the filament in air to RF is in the order of 10^{-8}[4]. The aim of this work is to detect and enhance the RF from filaments. We have therefore used different acquisition setups to detect and analyse the RF emissions from the filament. We were able to not only detect RF signals but also enhance it by varying some input laser parameters. As the process of filamentation creates widely varying dynamics in the plasma formation, the emissions although transient can be enhanced and modulated using the input pulse. We address this transient pulse in the frequency range of Radio waves and terahertz waves as an electromagnetic pulse. The effect of focusing conditions on the RF emission was first studied. Under these conditions the input polarization was also tuned to detect the enhancement. It was then shown that asymmetry in the pulse wavefront using lens tilt drastically increases the RF signal. These studies can be used to remotely generate an electromagnetic pulse using a properly tailored femtosecond pulse.

6.2 Experiment and analysis details

As the filament has a highly transient nature, the RF emitted from the filament is also equally transient, making RF acquisition a challenge because of which we have used a combination of a near field dipole antenna with an oscilloscope.

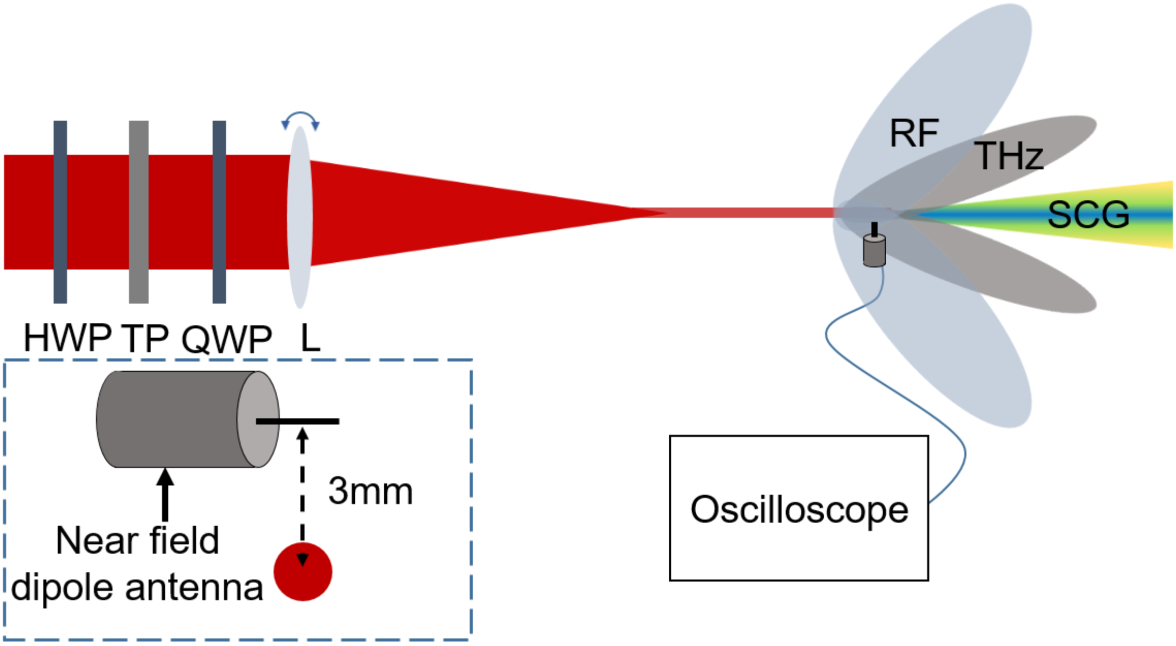

Figure 6.1: Experimental schematic. HWP- Half wave plate; QWP- Quarter wave plate, TP- Thin film polarizer; L-lens

On using the combination of a near field dipole antenna and an oscilloscope for the RF detection and characterization of filaments, we can get a direct RF signal only limited by the bandwidth of the antenna and the oscilloscope. The length of the antenna is 8mm and radius is 2mm, giving us a resonant frequency f ~4GHz. The antenna is therefore most sensitive in this region of the frequency range. The antenna has an input impedance of 50Ω. The oscilloscope has a sampling rate of 5GSa/s which gives us a maximum frequency acceptance of 2GHz. The schematic of the experiment is shown in the figure 6.1.

The RF signal acquired from a filament generated using a 150mm lens is shown in the figure 6.2. It can be seen that the oscillations can be resolved with the available antenna bandwidth and sampling rate of the oscilloscope. Signals from varying filaments can be easily distinguished using this acquisition setup.

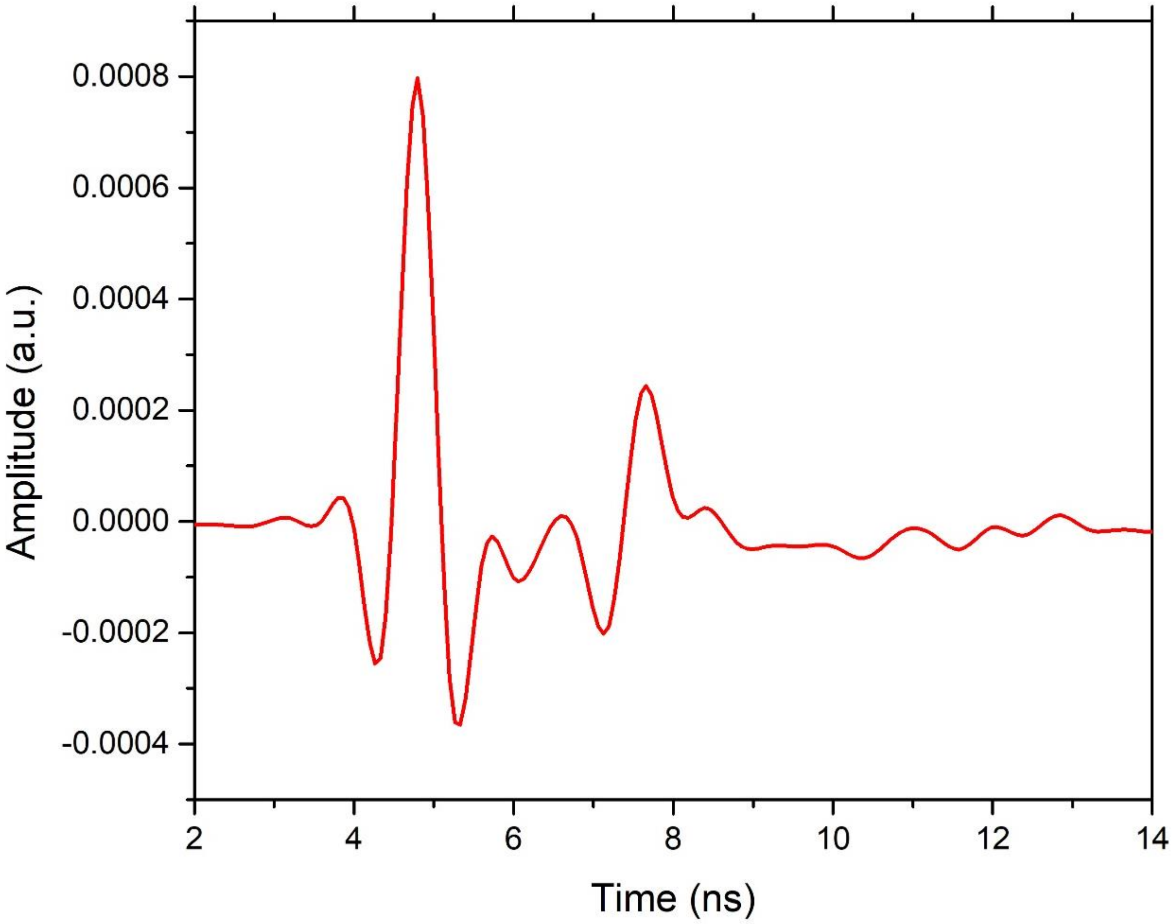

Figure 6.2: RF signal from a filament generated from a 150mm lens at a pulse energy of 2mJ using linearly polarized pulses.

The time domain signal can be better analysed by applying the Fourier transform which gives us the spectral content of the pulse. Figure 6.3 shows the frequency distribution of the acquired signal. The frequency distribution helps resolve frequency components arising due to discrete oscillating moments, which cannot be resolved from the time domain signal alone.

Figure 6.1 clearly shows the various optical elements used to modify the input pulse characteristics and the detection geometry used to collect emitted RF. The polarization of the input pulse was modified using a quarter wave plate. The combination of a half wave plate and polarizer help us vary the input pulse energy. The focusing conditions were chosen to generate filaments in the loose and tight focusing conditions, we have therefore used the lens with focal lengths 500mm and 150mm respectively. The lens were mounted on a rotational stage to induce lens tilt in the focusing conditions.

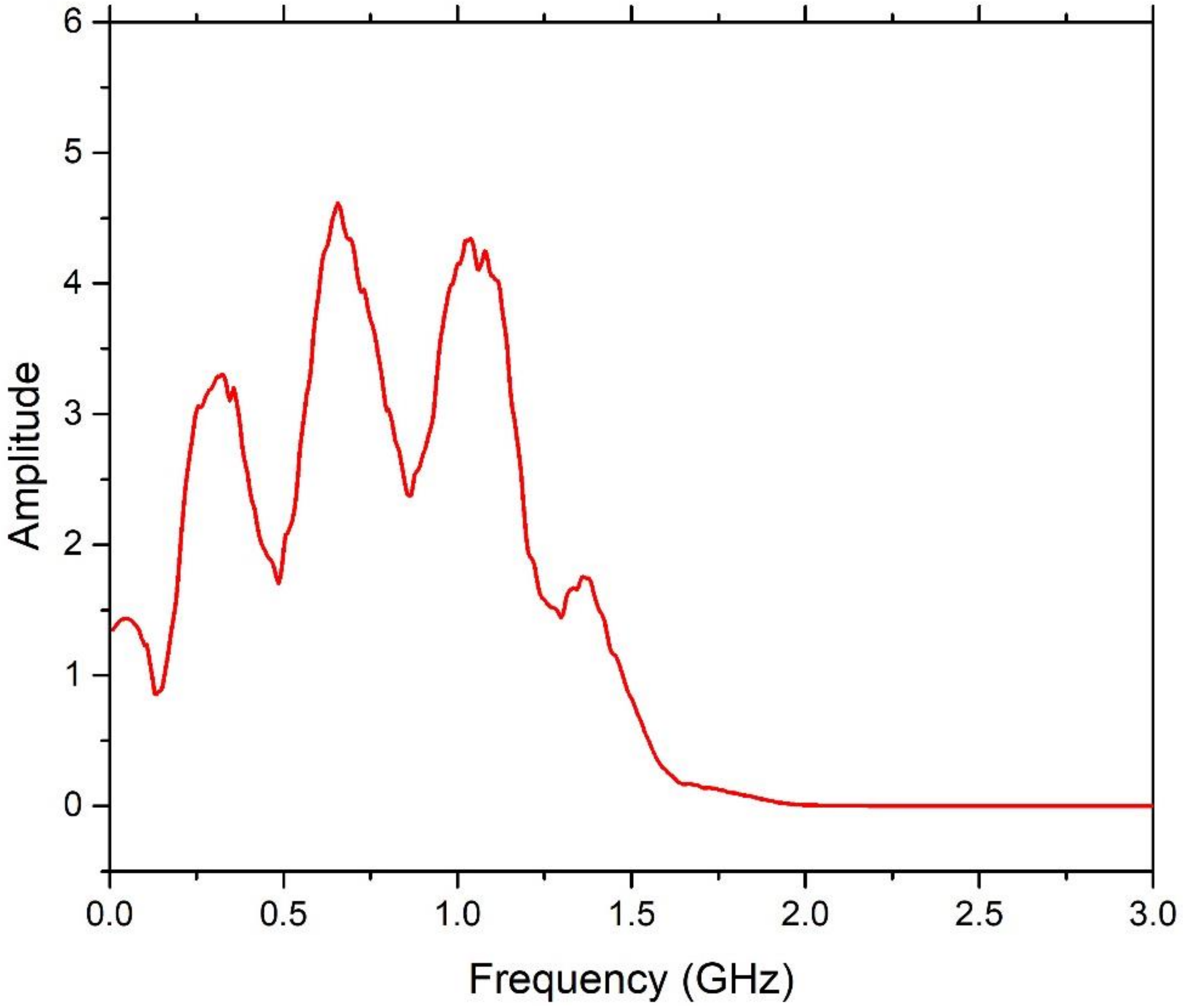

Figure 6.3: Frequency distribution of the RF signal from a filament generated from a 150mm lens at a pulse energy of 2mJ using linearly polarized pulses..

6.3 Role of focusing geometry

The variation in filamentation dynamics arising due to focusing conditions was discussed in the earlier chapters. The lenses used for focusing the light pulses were the 150mm and 500mm lens to generate tight and loose focusing conditions respectively. It was shown in the earlier chapters that the plasma density is more for tight focused filaments compared loose focused filaments. The spatial extent of the filament on the other hand increases by an order for loosely focused filaments as intensity clamping is easily achieved and the pulse front has minimal curvature before the onset of filamentation [11, 12]. The RF signal was observed using a band width limited near field dipole antenna coupled to an oscilloscope which has an acquisition rate of 5 GSa/s. The oscilloscope was triggered using the signal from a photodiode placed before the focusing lens. Light pulses used for this study were linearly polarized. The antenna was translated along the filament and the position where we obtained maximum amplitude was chosen to acquire the signal. Since the RF emissions occur as a conical emission, this position was found to be at a distance of 3mm above the filament and ~ 3 mm from the center of the filament in either direction. It should be noted that this position of the antenna is beyond the spatial extent of the filament for both the loose and tight focused filaments. This is because the emission is conical in nature similar to the emission nature of supercontinuum and terahertz radiation from the filament, indicating a coherent directional radiation. The RF signal can be seen to be a highly transient signal which lasts for <10ns (limited by the detection bandwidth). As will be shown these emissions have therefore a pulsed profile which can be modulated. These transient emissions hence observed are filament induced electromagnetic pulses.

Figure 6.4 shows the RF signals in the time domain from filaments generated from 150mm and 500mm lens. The RF emission in the case of the filament from the 150mm lens has twice the temporal width compared to that of the RF signal observed from the filament from 500mm lens. The amplitude of the signal also is twice for the filament from 150mm lens, especially for linearly polarised light. It can be seen that the amplitude of the trough of the RF pulse is not the equal to the crest of the RF pulse from filament generated using the 150mm lens, whereas they stay the almost same for the filament from the 500mm lens. Observation of the profile of the signal in time domain shows a simple pulse profile for the filament generated from the 500mm lens, but the oscillations observed from the filament generated from the 150mm filament can be seen to have irregularities along with increased temporal duration.

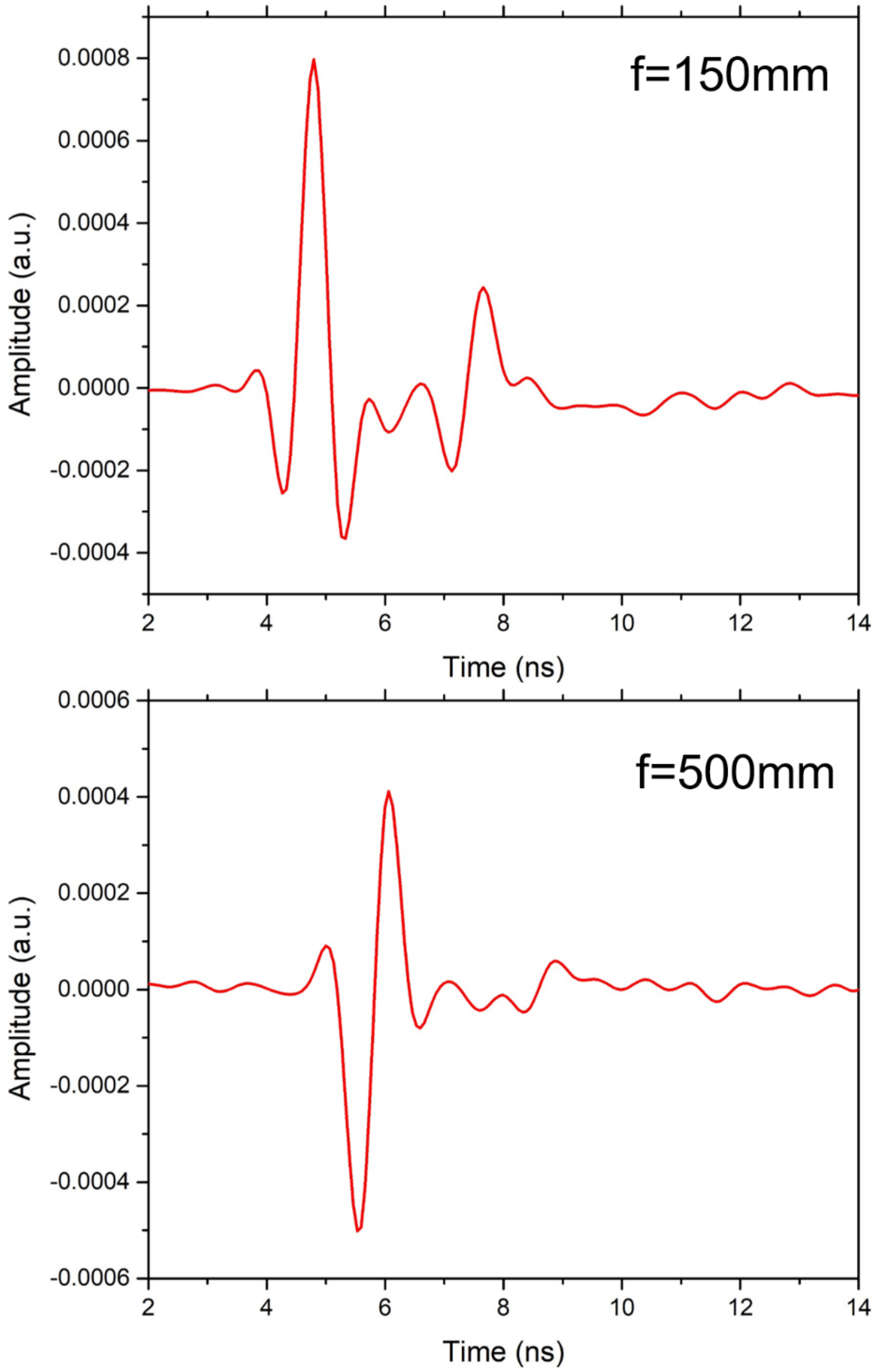

Figure 6.4: Time domain RF signals from filaments generated from lens with focal lengths of 150mm and 500mm using linearly polarized femtosecond pulse with pulse energy of 2mJ.

Figure 6.5 shows the frequency distribution of the RF pulses from 150mm and 500mm lens for linearly polarized light. The distribution in the frequency domain shows a broad distribution with a maximum at 0.8GHz as should be expected from simple transient pulses from the filament generated from the 500mm lens, but the spectral distribution of the signal from the filament from the 150mm lens shows multiple maximums. This study shows that loosely focused filaments have lower amplitude and pulse duration especially for linearly polarized light, but have a uniform pulse profile and frequency distribution when compared to tightly focused filaments.

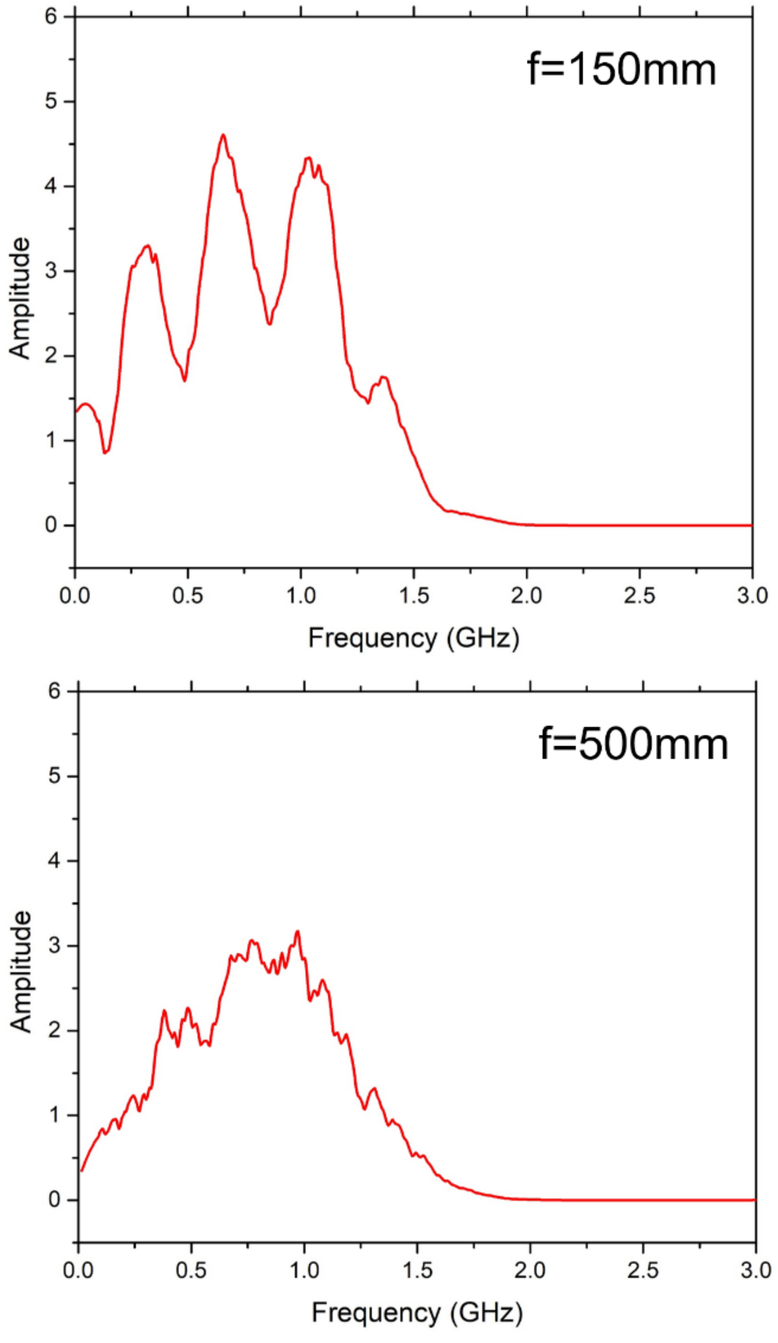

Figure 6.5: Frequency distribution by Fourier transform of the RF signals from filaments generated from lens with focal lengths of 150mm and 500mm

6.4 Role of polarization

We have shown in earlier chapters the effect of polarization on the 3rd order processes during filamentation such as third harmonic generation and self-phase modulation leading to UV and Supercontinuum respectively. Although efficiency of both processes reduces at circular polarization compared to linearly polarized input pulses, enhancement can be seen at an intermediate elliptical polarization. It was suggested that this was due to the occurrence of filamentation induced birefringence which induces optimal refractive index modulations for better third order processes. Change in polarization of the input pulses reduces the intensity of the filament as the critical power increases for circularly polarized light for all focusing geometries, this was shown in the chapter 3. In this study, polarization of the input pulse was varied using a quarter wave plate and the RF signal was collected at the location where maximum amplitude was observed at linear polarization. The signal was taken at three different polarizations, linear, elliptical and circular polarization according to the angle of rotation of the quarter wave plate at 0^0, 22^0, and 45^0 respectively with respect to the optic axis.

Variation of RF emissions from filaments with change in polarization as shown in the figure 6.6 show completely contrasting features when compared to other filament characteristics such as electron density, intensity and filament induced third order processes. We firstly find that amplitude of the signal increases for both focusing conditions with change in polarization from linear to circular. Closer observation shows drastic enhancement in amplitude by ~8 times for circularly polarized input pulses under loose focusing conditions, as compared to an increase by only ~0.4 times for tightly focused filaments. The amplitude of the signal for loosely focused filament at linearly polarized light was half of that observed for tightly focused filaments, but transition of polarization from linear to circular polarization causes RF from loosely focused filaments to surpass that from circularly polarized filaments and is now 3 times the RF observed from tightly focused filaments. It can also be seen from the inset in the figure that irregularities which exist in the RF signal in the time domain disappear for circularly polarized pulses while still having remnants at the intermediate elliptical polarization. The pulse oscillation profile for RF emission signal from loosely focused filament stays constant and uniform for all the varying polarizations, with a drastic increase in amplitude.

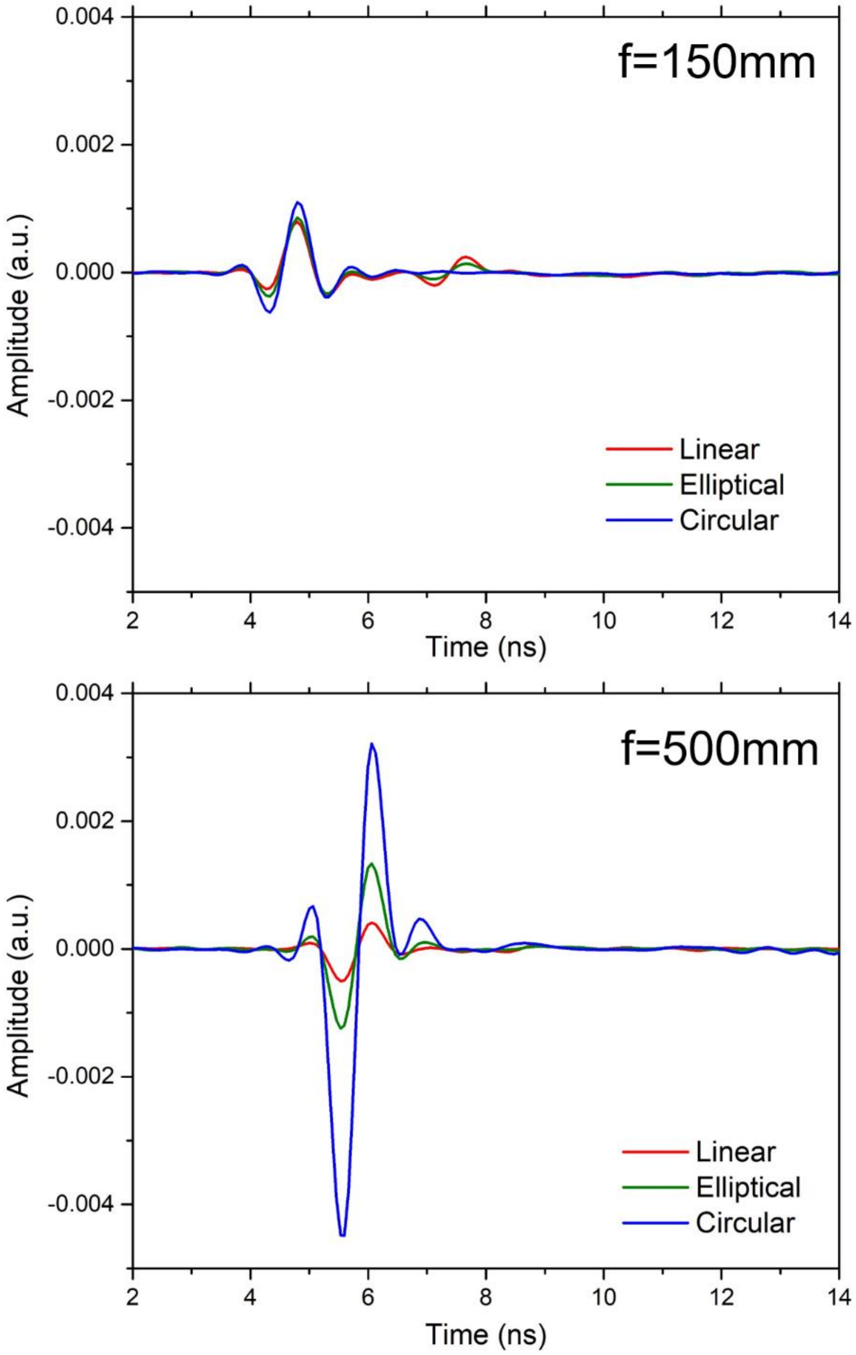

Figure 6.6: Time domain RF signals from filaments generated from lens with focal lengths of 150mm and 500mm at three different polarizations namely linear elliptical and circular polarization. Inset on the plots shows magnified signal to better illustrate signal profile.

The RF signal was transformed to the frequency domain and shown in the figure 6.7. It can be seen as expected that the amplitude of the peak from RF from tightly focused filaments does not show increase in amplitude but it can be seen that the multiple frequencies that exist for linearly and elliptically polarized pulses disappear for circularly polarized pulses which agrees with the loss of irregularities observed in the signal of the time domain. The frequency distribution of the RF from loosely focused pulses carries the similar frequency distribution with common central frequency for all the input polarization with an increase in amplitude as polarization changes from linear to circular as can be expected from observation of the uniform RF pulse profile observed from the time domain signal. Ion plasma (ω_i) frequencies and electron plasma (ω_e) frequency for the plasma number density estimated give frequencies of the order of 10^{10} Hz and 10^{12} Hz [25]. These frequencies are higher than the frequencies observed here indicating the presence of dipole oscillations in the filament.

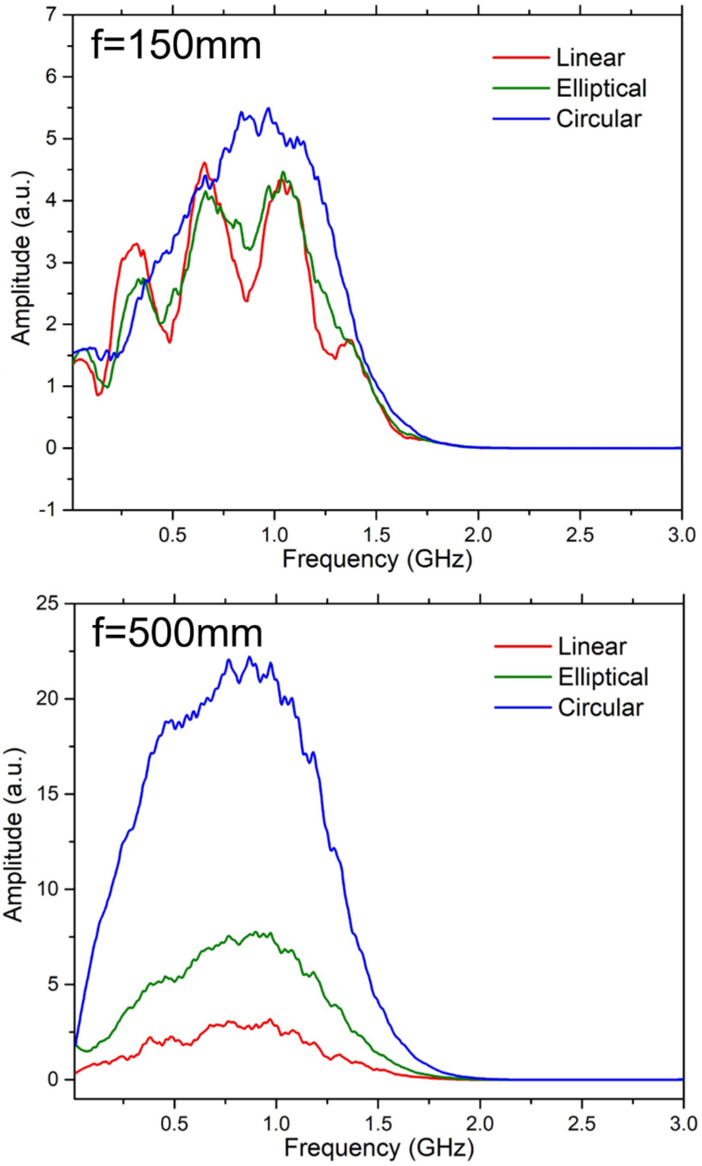

Figure 6.7: Frequency distribution by Fourier transform of the RF signals from filaments generated from lens with focal lengths of 150mm and 500mm at three different polarizations. (Notice change in y-axis scale between the plots for better illustration)

6.5 Role of lens tilt

The 3rd chapter of this thesis discusses the effect of lens tilt on input pulse and subsequent filament propagation. We have suggested that lens tilt induces a certain amount of tilt in the wavefront and causes an elongation of the focal region because of comatic aberration according to the angle of lens tilt [26-28]. Tilting of the lens can therefore have many effects on the propagation of filamentation. In the earlier works we have used lens tilt to increase the spatial extent of the filament and also suppress the supercontinuum. The introduction of spatial asymmetry into the pulse propagation causes the elongation of the filament leading to the formation of resolvable collinear and non-collinear filaments especially at tight focusing conditions in which regime we observe plasma-plasma interactions leading to increase in third harmonic generation and also supercontinuum generation at distinct tilt angles. We also observe variations in RF generation from the filament as well. RF emission being an outcome of charge movement and bulk oscillations, can be enhanced by the plasma and propagattion dynamics brought about by lens tilt in filamentation.

This study was done using the 150mm lens which is in the tight focusing geometry. It was not possible to conduct the study under loose focusing conditions because of the dramatic variation of filament structure with lens tilt demanding a complete characterization of the emission profile. The change in filament structure, intensity and supercontinuum with lens tilt is shown in the 3rd chapter (figure 3.15-3.18). Although the RF signal decreases with lens tilt, it increases dramatically at a lens tile angle of 6^0. Here, we show the signal that was obtained at a lens tilt of 6^0, this is the regime where we observe an increase in SCG with elongated filament. The filament intensity here is half of filament intensity at zero tilt at 80 TW/cm^2. On observing the RF signal from this filament and comparison to filament with zero tilt, we find that the observed signal has a uniform profile without irregularities as can be seen from the filament generated from zero tilt along with an increase in amplitude as shown in the figure 6.8. It is interesting to note that introduction of aberrations provides a much more uniform and enhanced signal compared to the filament without aberration.

We can further see from figure 6.9 that the frequency distribution has a single maximum when Fourier transform is taken. When the pulse was circularly polarized, the enhancement is 5 times more when compared to a filament with zero tilt where we observe only a 30% increase in amplitude. It can also be seen that in the frequency domain the frequency at the maximum of the frequency distribution shift towards higher frequencies with

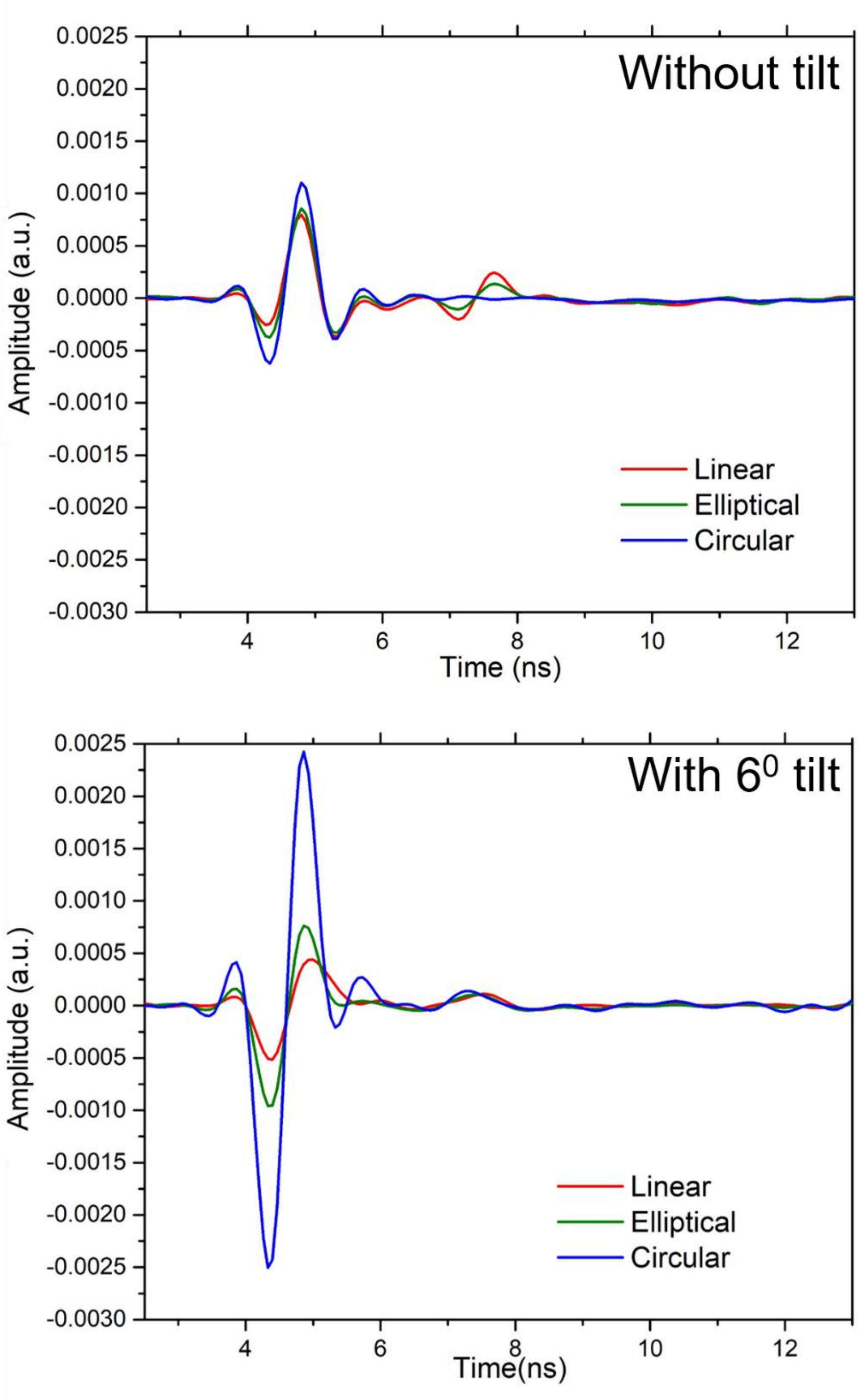

Figure 6.8: RF signals without lens tilt (top) and with lens tilt (bottom) at three different polarizations.

change in polarization from linear to circular. The behaviour of the filament under this lens tilt angle is very similar to a loosely focused filament except for shift in frequency at maximum towards higher frequency. Further exploration of the plasma dynamics of filamentation and characterization can shine light on the underlying reason for these mechanisms.

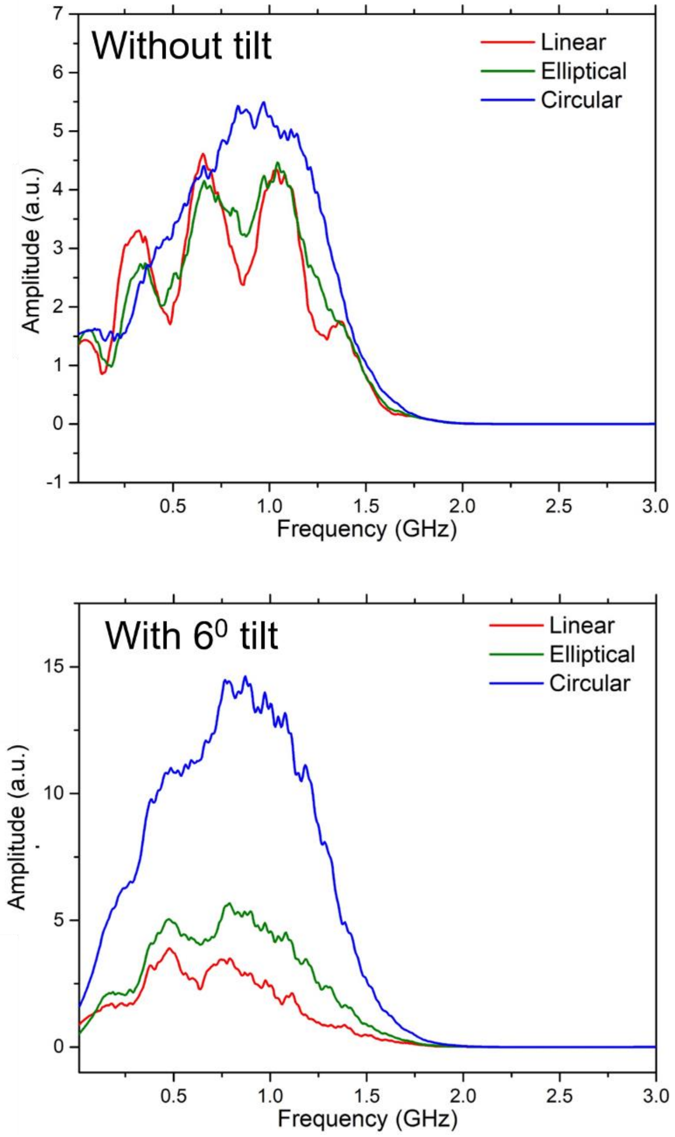

Figure 6.9: Frequency distribution of the RF signal from filament without lens tilt (top) and with lens tilt (right) of 6^0 at three different polarizations

6.6 Summary

We have observed RF from filaments generated from femtosecond pulses where the highly transient nature of femtosecond pulses ionizes the medium by multiphoton ionization alone where bulk charge oscillations are not significant. The role of input focusing conditions on the RF generated was shown and we can see from the RF pulse profile that loosely focused filaments have lesser amplitude but have a uniform pulse profile for linearly polarized pulses, whereas tightly focused filaments have larger amplitude but the pulse profile has many irregularities. These irregularities get more prominent when a Fourier transform is taken, we observe multiple maxima in the frequency domain for the RF generated from tightly focused filaments which can be due to the presence of multiple filaments. The study was extended to find the influence of input polarization on the RF emission, which showed drastic changes in the RF observed. We firstly find enhancement with filaments from both loose and tight focusing conditions when polarization changes from linear to circular. Closer observation shows that RF signal from loosely focused filament are enhanced much more than tightly focused filaments at circular polarization. Multiple maximums observed in the frequency domain from the filament generated from the 150mm lens disappear at circular polarization and we observe a single maximum with a broad distribution. Knowing that tilting lens introduces different plasma dynamics in the filament because of the asymmetry that gets induced in the pulse wavefront, we have studied RF from filaments generated under lens tilt. Significant enhancement was observed from at certain angle of lens tilt, where we have seen that not only signal gets amplified but we also see a disappearance of the irregularities in the pulse profile observed for filament under zero tilt, which can be seen in the smooth frequency distribution observed in the frequency domain. The effect of change in polarization shows drastic enhancement. The combination of lens tilt and circularly polarized light gave enhanced RF signal with a uniform pulse profile. The frequency at maximum amplitude was also seen to shift to higher frequencies with change in input polarization from linear to circular. The large dynamic variation of RF emission from filament with change in input pulse conditions shows that we can control the RF generated from a filament that is generated remotely, providing a highly promising tool for remote detection and probing.

References

1. S. L. Chin, *Femtosecond laser filamentation*, Elsevier (2009).
2. A. Proulx, A. Talebpour, S. Petit and S. L. Chin, *Fast pulsed electric field created from the self-generated filament of a femtosecond Ti: Sapphire laser pulse in air*, Opt. Commun. **174(1-4)**, 305-309 (2000).
3. P. Sprangle, J. R. Penano, B. Hafizi and C. A. Kapetanakos, *Ultrashort laser pulses and electromagnetic pulse generation in air and on dielectric surfaces*, Phys. Rev. E, **69(6)**, 066415 (2004).
4. M. Richardson, M. Baudelet and Tamar Seiderman. *Fundamentals of Filament Interaction*, University of Central Florida Orlando United States, (2017).
5. N. Barbieri, *Engineering and Application of Ultrafast Laser Pulses and Filamentation in Air*, (2013).
6. J. Yu, D. Mondelain, J. Kasparian, E. Salmon, S. Geffroy, C. Favre, V. Boutou, and J.–P. Wolf, *Sonographic probing of laser filaments in air*, Appl. Opt. 42, 7117-7120 (2003).
7. J. A. Bittencourt, *Fundamentals of Plasma Physics*, Springer (2004)
8. A. Couairon and A. Mysrowicz*, Femtosecond filamentation in transparent media*, Phys. Rep. 441, 47–189 (2007).

9. C. D'Amico, A. Houard, M. Franco, B. Prade, A. Mysyrowicz, A. Couairon and V. T. Tikhonchuk, *Conical Forward THz Emission from Femtosecond-Laser-Beam Filamentation in Air*, Phys. Rev. Lett. 98, 235002 (2007).
10. Y. S. You, T. I. Oh and K. Y. Kim, *Off-axis phase-matched terahertz emission from two-color laser-induced plasma filaments*, Phys. Rev. Lett. **109(18)**, 183902 (2012).
11. D. J. Cook and R. M. Hochstrasser, *Intense terahertz pulses by four-wave rectification in air*, Opt. Lett. **25**, 1210-1212 (2000).
12. B. A. Tozer, *Theory of the ionization of gases by laser beams*, Physical Review, **137(6A)**, A1665 (1965).
13. S. L. Chin, *Multiphoton Ionization of Gases*, Elsevier (2012).
14. S. Tzortzakis, G. Méchain, G. Patalano, Y.-B. André, B. Prade, M. Franco, A. Mysyrowicz, J.-M. Munier, M. Gheudin, G. Beaudin and P. Encrenaz, *Coherent subterahertz radiation from femtosecond infrared filaments in air*, Opt. Lett. **27**, 1944-1946 (2002)
15. J. A. Aspiotis, N. Barbieri, R. Bernath, C. G. Brown, M. Richardson and B. Y. Cooper, *Detection and analysis of RF emission generated by laser-matter interactions*, Enabling Technologies and Design of Nonlethal Weapons (International Society for Optics and Photonics), **6219**, 621908 (2006).
16. B. Clough, and X-C. Zhang, *Toward remote sensing with broadband terahertz waves*, Frontiers of Optoelectronics, **7(2)**, 199-219 (2014).
17. Y. Brelet, A. Houard, G. Point, B. Prade, L. Arantchouk, J. Carbonnel, Y-B. André, M. Pellet and A. Mysyrowicz, *Radiofrequency plasma antenna generated by femtosecond laser filaments in air*, App. Phys. Lett. **101(26)** 264106 (2012).
18. J. S. Pearlman and G. H. Dahlbacka, *Emission of rf radiation from laser-produced plasmas*, J. Appl. Phys. **49**, 457 (1978).
19. B. Forestier, A. Houard, M. Durand, Y-B. André, B. Prade, J-Y. Dauvignac, F. Perret, Ch Pichot, M. Pellet and A. Mysyrowicz, *Radiofrequency conical emission from femtosecond filaments in air*, App. Phys. Lett. **96(14)**, 141111 (2010).
20. C. D'Amico, A. Houard, M. Franco, B. Prade and A. Mysyrowicz, *Coherent and incoherent radial THz radiation emission from femtosecond filaments in air*, Opt. Express, **15**, 15274-15279 (2007).
21. Harry M. Jol, (ed.) *Ground penetrating radar theory and applications*, Elsevier (2008).
22. H. Nakajima, Y. Shimada, T. Somekawa, M. Fujita and K. A. Tanaka, *Nondestructive Sensor Using Microwaves From Laser Plasma by Subnanosecond Laser Pulses*, IEEE Geoscience and Remote Sensing Letters, **6(4)**, 718-722 (2009).
23. G. C. Franssen, Henricus Maria Antonius Schleijpen, J. C. Van den Heuvel, H. Buersing, B. Eberle and D. Walter, *Femtosecond lasers for countermeasure applications*, Technologies for Optical Countermeasures VI (International Society for Optics and Photonics), **7483**, 748309 (2009).
24. S. Varma, J. Spicer, B. Brawley and J. A. Miragliotta, *Plasma enhancement of femtosecond laser-induced electromagnetic pulses at metal and dielectric surfaces*, Optical Engineering, **53(5)**, 051515 (2014).
25. L. V. Kumar, E. Manikanta, Ch. Leela, and P. Prem Kiran, *Effect of laser intensity on radio frequency emissions from laser induced breakdown of atmospheric air*, J. Appl. Phys, **119**, 214904 (2016).
26. Y. Kamali, Q. Sun, J-F. Daigle, A. Azarm, J. Bernhardt and S. L. Chin, *Lens tilting effect on filamentation and filament-induced fluorescence*, Opt. Commun. **282(5)**, 950-954 (2009).
27. A. A. Dergachev, A. A. Ionin, V. P. Kandidov, D. V. Mokrousova, L. V. Seleznev, D. V. Sinitsyn, E. S. Sunchugasheva, S. A. Shlenov, and A. P. Shustikova, *Plasma channels during filamentation of a femtosecond laser pulse with wavefront astigmatism in air*, Quantum Electronics **44(12)**, 1085 (2014).
28. S. Zafar, D. Li, Z. Hao, and J. Lin, *Influences of astigmatic focusing geometry on femtosecond filamentation and supercontinuum generation in fused silica*, Optik **130**, 765-768 (2017).

This page was intentionally left blank

CHAPTER 7: Application of fs filaments

Abstract:

A large part of the work done in this thesis was to expand the applicability of femtosecond filamentation due to the dramatic nature of the multiple characteristics of filamentation. The work henceforth was largely directed towards exploring the viability and feasibility of filamentation assisted remote sensing. Along with the variety of emissions which were characterized and studied in the earlier chapters we have done preliminary studies to test the ability of femtosecond filament propagation to sense and characterize. FIBS studies of aerosols of different solvents was collected and the spectrum could resolve the spectral components which are characteristic to the solvents. The remnant pump light in the background reservoir and post filamentation was used to detect Riboflavin using 2-photon fluorescence. Moving forward, interaction of filament with solid elements such as copper and aluminium was also done and the subsequent breakdown via FIBS was analysed. Surface reflectivity of a composite material was used to study the damage incurred by the composite by filament interaction. It can be seen that the filament although highly susceptible to input laser characteristics is highly repeatable, reproducible and robust.

7.1 Introduction

Filamentation being a highly dynamic regime which sustains high intensities existing for short time scales over long distances can be applied to a range of applications [1-3]. Filamentation has opened doors towards many new research avenues which were not accessible or thought of before [4-12]. We have mostly focused our work on the applicability of filamentation towards remote sensing. Remote sensing and characterization of aerosols and atmospheric components using LIDAR has reached a stand still because of the requirement of multiple coherent laser sources to achieve resonant excitation of the target aerosol. LIDAR also demands propagation stability over long ranges and discrete spectral characterization. Filamentation was described earlier in terms of its characteristics such as intensity and electron density, which were correlated to the numerous emissions that come about due to the highly dynamic regime of its propagation. The ability to create filaments using highly intense infrared femtosecond pulses gives us a powerful tool to remotely generate filaments, which can overcome the above mentioned challenges for remote sensing. We are now able to generate pulses with much higher intensity than that used in our experiment, using setups which can also be made mobile [12]. Such mobile laser systems can be used to holistically characterize atmospheric regions over varied landscapes and environments, due to the plethora of emissions which can also be modulated. The first such mobile laser system to be built was the teramobile which produces 100fs pulses at a repetition rate of 10Hz, with a pulse energy of 350mJ thereby having a peak power of ~5TW [13]. From our studies we have shown the generation and modulation of the third harmonic UV, broadband supercontinuum, acoustic and radio frequency emissions which can be exploited towards building a hyperspectral remote sensing system, where along with identification of the composition, we can also find the particle size and concentration [9-17]. We have therefore conducted some exploratory proof of concept experiments to probe and collect characteristic spectra from aerosols during interaction with femtosecond filamentation and demonstrate its applicability towards sensing. We have also done a LIBS characterization of different materials as the LIBS from femtosecond filamentation (FIBS) is different from ns and ps LIBS [18-21]. Femtosecond LIBS has minimal thermal damage and heating of the surrounding region. Femtosecond LIBS also provides high spatial resolution. The reduced continuum in the case of femtosecond LIBS also increases the signal to noise ratio during acquisition. Filaments generated from femtosecond pulses enable remote interaction with materials and regions due to large transfer of energy over long distances. Filament interaction with different solid samples was done and the variation of the LIBS was studied to estimate the electron density and plasma temperature. Along with remote sensing studies we also performed damage dynamics of filament interaction with metals like aluminium was done to identify drilling time and damage spot sizes with different filaments. This study was extrapolated to study composite materials whose damage was dynamically studied using reflection analysis of a CW laser from the composite material. We have also performed a proof of concept study of FIAS (Filament Induced Acoustic Spectroscopy) is performed to explore the ability to use acoustic emissions from filament interaction with aerosols, and then use this acoustic signature to identify the constituent of the molecular aerosol. We performed this study using different concentrations of Tryptophan aerosol clouds. The temporal profile and frequency distribution of the acoustic pulse was studied to identify significant variation with change in concentration of tryptophan particles in aerosol which could aid in its detection. This variation was observed even in the presence of highly turbulent and inhomogeneous aerosol dissipated from the nebulizer, which makes it very promising for a sensing application. Further studies in this respect could help estimate particle sizes as well are discussed in the future scope of the thesis.

7.2 Detection of aerosol clouds of common solvents

Most warfare agents require dissolution in commonly used solvents, these warfare agents include high energy materials (HEMs) and chemical warfare agents (CWAs). Therefore the first step towards detection of harmful agents was to identify and characterize these solvents using the interaction of their aerosols with the filament and its emissions. This exploration towards sensing of ambient atmosphere and aerosols was done by conducting a FIBS (filament induced breakdown spectroscopy) study of methanol and acetone [22]. It can be seen clearly from figure 7.1 the drastic change in brightness of the scattered light when the aerosol is introduced into the filament. The sudden increase in brightness is because of the increased FIBS emissions in the visible region and some SCG generation from the aerosols.

Figure 7.1: Filament aerosol interaction without (Top) and with aerosol (Bottom).

We have first collected the scattered light from filament interaction with aerosols of methanol and acetone using a Maya 2000 spectrometer. As the collection optics connected to the spectrometer is placed 15cm from the aerosol region we are able to observe clear FIBS from the aerosols. The figure shows the FIBS spectra acquired from methanol and acetone compare to the FIBS of air. We can clearly identify from figure 7.2 the different lines associated with the atomic and break down constituents of the solvents which could be used to identify and classify them using PCA [19, 20].

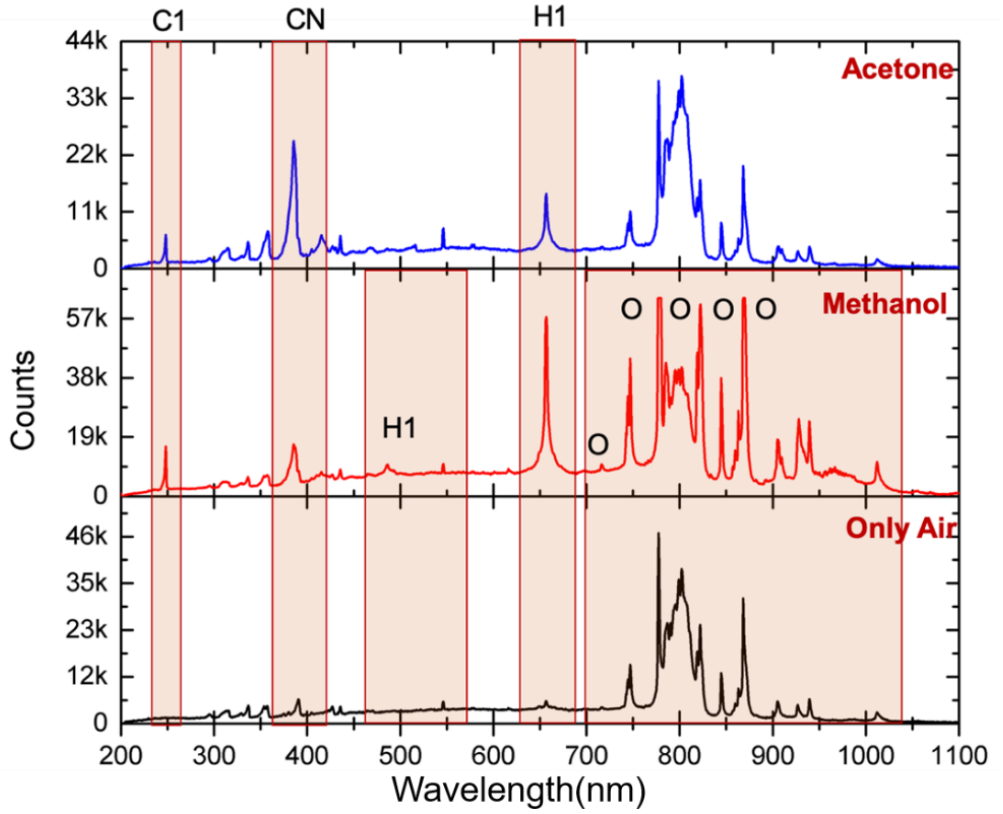

Figure 7.2: FIBS from Acetone and methanol aerosol compared to FIBS from air.

The requirement to probe multiple samples with varying compositions in varying phases demands the use of a spectrograph which has a broad dynamic range with high resolution. Filamentation creates emissions in a broad range of frequencies which get further enhanced depending on the interactions. We have used different liquids to make the aerosols and observed the emissions using the Kymera 328i spectrograph whose grating and acquisition can be varied according to the required wavelength range. LIBS signal was isolated using a gated acquisition offered by the iSCMOS sensor in the Kymera 328i. The spectrograph was coupled with the imaging lens which was placed at a distance of 1m from the filament aerosol interaction region as seen in the figure 7.3. The increase in the brightness of the filamentation region as seen in the figure with the aerosol shows the extent of interaction of filament and aerosol. As the iSCMOS sensor has a 2D output, the lines are better resolved when the filament is appropriately imaged onto the slit of the spectrograph. On doing so we can create a complete spatial wavelength distribution of the emissions from filament aerosol interactions.

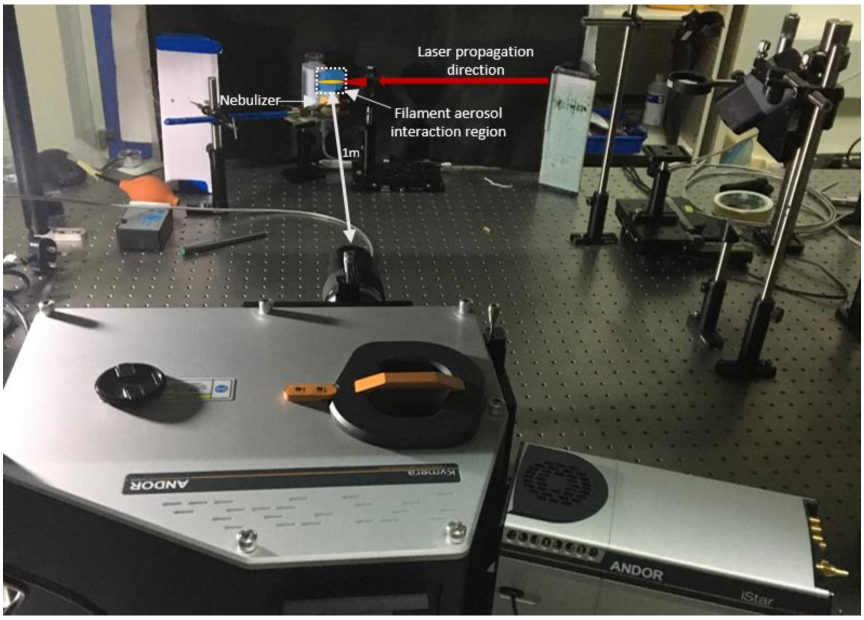

Figure 7.3: Experiment schematic with Kymera 328i.

The liquids used were Oil of wintergreen (methyl salicylate), Dimethyl sulphur dioxide (DMSO), methyl cyanide (CH3CN), dimethyl formamide (DMF) and water [24-26]. The spectra obtained are shown in the figure 7.4. All the solvents show similar spectra except for relative variation of the peaks. We also observe an emission band peaking at 520 nm which is prominent for aerosol from wintergreen oil but does not exist in water (shown as shaded region in the plots). As the interaction zone is low we do not identify characteristic distributions other than plasma continuum. Inclusion of various techniques such as reduction of broadband SCG using aberrations and increasing the interaction region will help better identification and characterization. We see that FIBS will only give elemental analysis. Although elemental analysis can provide only atomic data, we see that it can still distinguish between the various solvents from the ratios of the different peaks seen in Figure 7.2. Therefore we desire to move towards more definitive analysis where the molecular spectral signature can be obtained. This was done in the next section where we acquire fluorescence of riboflavin due to 2 photon excitation of riboflavin aerosol with filament.

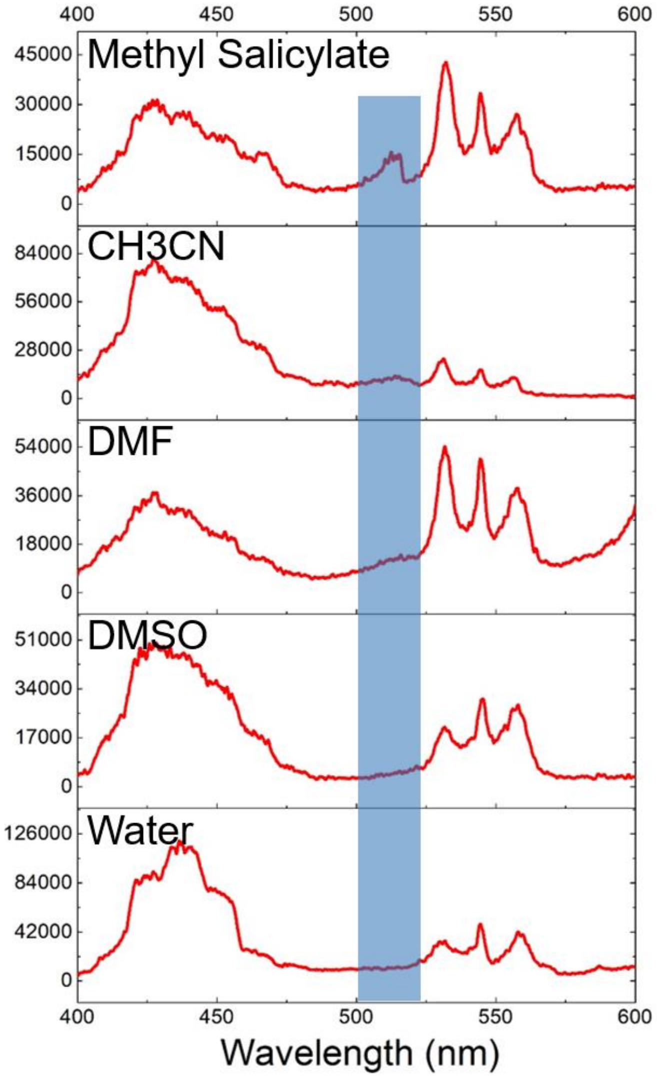

Figure 7.4: Spectra obtained from filament interaction with aerosols made from different solvents. Shaded region shows emission band at 520nm not observed for water.

7.3 2-photon fluorescence using filamentation

Along with the generation of SCG, filamentation also generates coherent UV light by third harmonic generation all of which can be used for exciting fluorescence in molecules. Fluorescence spectra provide the molecular composition of the material or medium as compared to the FIBS which gives the elemental composition. We can therefore have two characterization techniques which complement each other using one laser. To test detection using fluorescence we have used riboflavin which absorbs at 400nm, which can be excited by 2 photon excitiation using the residual pump wavelength (800nm) of the femtosecond laser filament. Aerosols were generated using a nebulizer using a solution of riboflavin dissolved in water. Riboflavin was chosen for this study because it has a characteristic fluorescence signature at 540nm with a broad absorption centred at 400nm. Riboflavin was also chosen because it is in many cases a component of multiple organic suspended particles which are bio agents (like bacteria) typically 1 μm in size [27]. They contain amino acids (e.g. tryptophan), nicotine amides (NADH), and flavins (e.g. riboflavin), which can be used as characteristic tracers of their biological nature. Figure 7.5 shows the absorption and fluorescence spectra of Riboflavin [27].

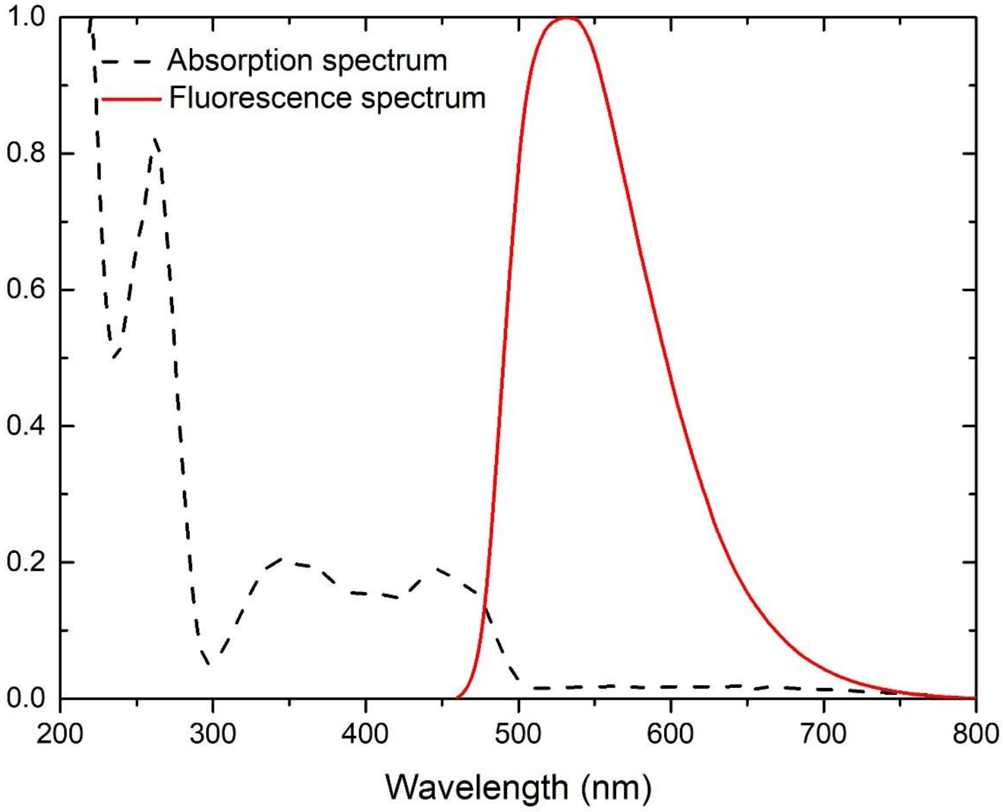

Figure 7.5: Absorption and fluorescence of Riboflavin.

The aerosol generated was confined using a lab made cardboard tube to get better interaction with the filament. When the filament is propagated in the tube with the aerosol the strong confinement of power causes localization of target region, because of which we can probe specific regions of interests. As the fs laser being used is centred at 800nm and the intensity is high enough, we can perform a 2 photon excitation of the Riboflavin molecule to induce fluorescence. With the laser being used we achieve intensities few orders higher than that required intensity for 2 photon fluorescence. The femtosecond laser pulse undergoes many dynamics during filamentation propagation because of which the spectral distribution of the pulse evolves to have multiple components such as the broadband supercontinuum and third harmonic UV. The usage of gated acquistions using the iCCD or iCMOS sensors helps us isolate the fluorescence signal from the other instantaneous emissions such as the broadband SCG and UV. The spectrum was acquired using a collection optics (Andor ME OPT-007) coupled to an optical fibre which is then coupled to the spectrometer which collected the scattered light from the aerosol from a distance of ~15cm. The femtosecond pulse can travel long distances and carry enough energy after propagation to ionize the medium through multiphoton ionization even at long distances. This energy is much higher than that required for 2 photon fluorescence.

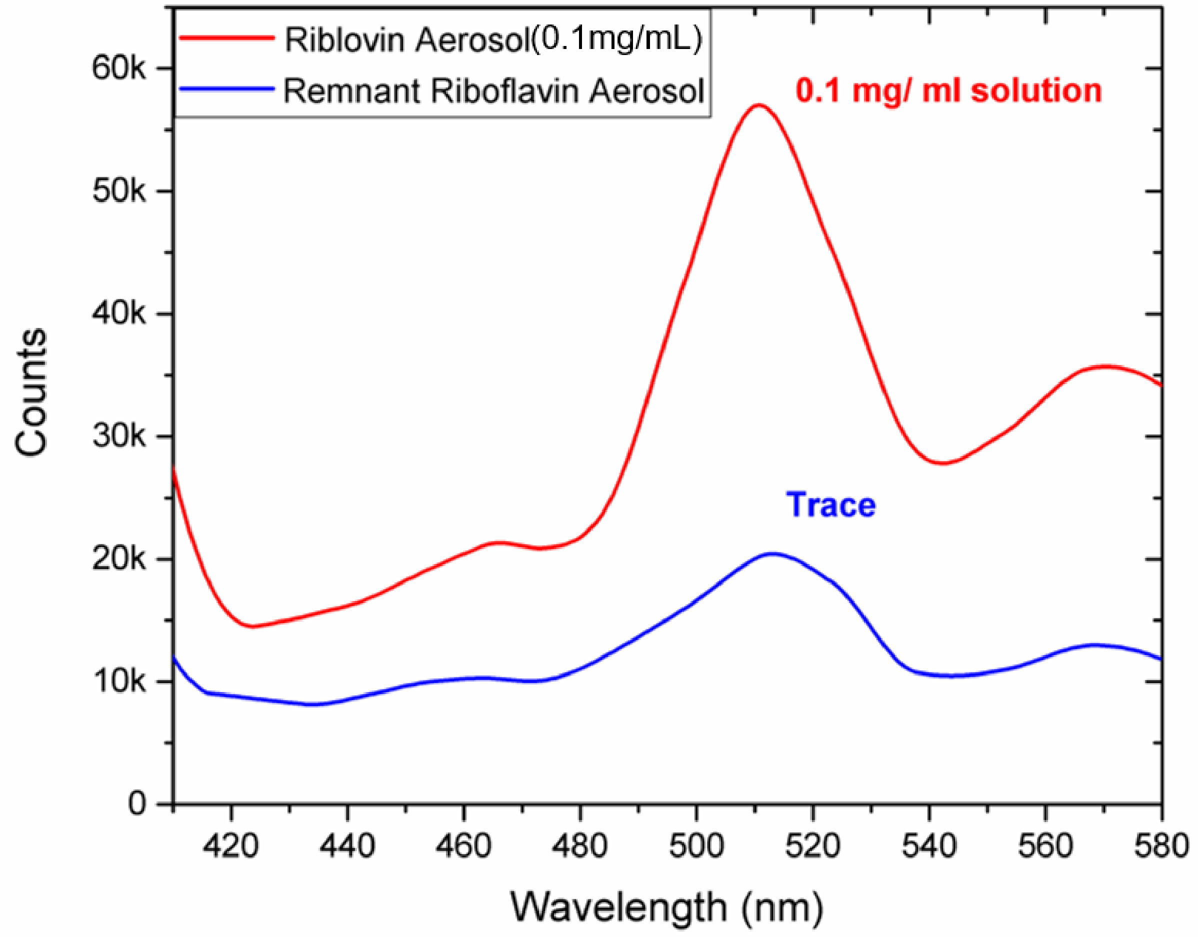

Figure 7.6: Observed 2-photon fluorescence with riboflavin. Spectrum obtained with 0.1mg/mL of riboflavin (red) and spectrum obtained from aerosol generated using same nebulizer containing water after clearing out the riboflavin solution showing the sensitivity.

Figure 7.6 shows the fluorescence emission of the Riboflavin aerosol at 520 nm, indicative of the two-photon absorption induced in Riboflavin. The signal was collected with good SNR although the interaction volume (diameter~100µm, filament length ~4mm) of the filament with the aerosol plume (made from a 0.1mg/mL concentration solution ~100ppm) was small (few mm^3), moreover we have further reduced the volume that is being observed by adjusting the focusing optics to have a range of ~3mm along the filament. In order to verify the sensitivity, the nebuliser was rinsed to remove traces of Riboflavin. Then the nebuliser was filled with just water and the experiment was repeated. We detected a fluorescence peak of Riboflavin from the trace amount still present in the nebuliser, even after rinsing the nebulizer which demonstrated the sensitivity of the excitation. This serves to show the sensitivity for measuring even trace amount of riboflavin (10 ppm) using filamentation and through efficient confinement and localization of the energy that is possible using filaments.

7.4 Filament electric field interaction with Condensed matter

Filamentation provides a unique tool to transport energy over long distance while having a high spatial resolution. In this respect filamentation can be used to identify unknown materials in far off regions. It can also be used to damage and destroy hostile entities from long distances. We have therefore done a LIBS study of various solid samples. Material breakdown caused by filamentation was also studied using aluminium plates and foils because aluminium is an element which has been extensively characterized and is also present in most alloys. These studies were done to explore femtosecond filament induced breakdown in solid materials and to test the viability as well as feasibility of solid material characterization using filamentation. Material damage caused due to filamentation on an unknown composite material was studied to demonstrate the ability of the femtosecond laser for remote threat neutralization.

7.4.1 LIBS of solid samples

LIBS accompanied with terahertz, photoacoustic and Raman characterization were found to be very efficient tools to identify and characterize High Energy Materials (HEMs) [16,17]. FIBS studies on solid targets with femtosecond filaments has not been well explored, although nanosecond and picosecond pulse interaction has been well explored [18- 23]. We have collected the FIBS from filament interaction with solid metallic samples such as Brass, Stainless steel, aluminium and a dielectric like teflon. A Mechelle spectrometer coupled with the ICCD was used to acquire this data because of the availability of gating and broad spectral range in a single shot. The experimental schematic is shown in the figure 7.7.

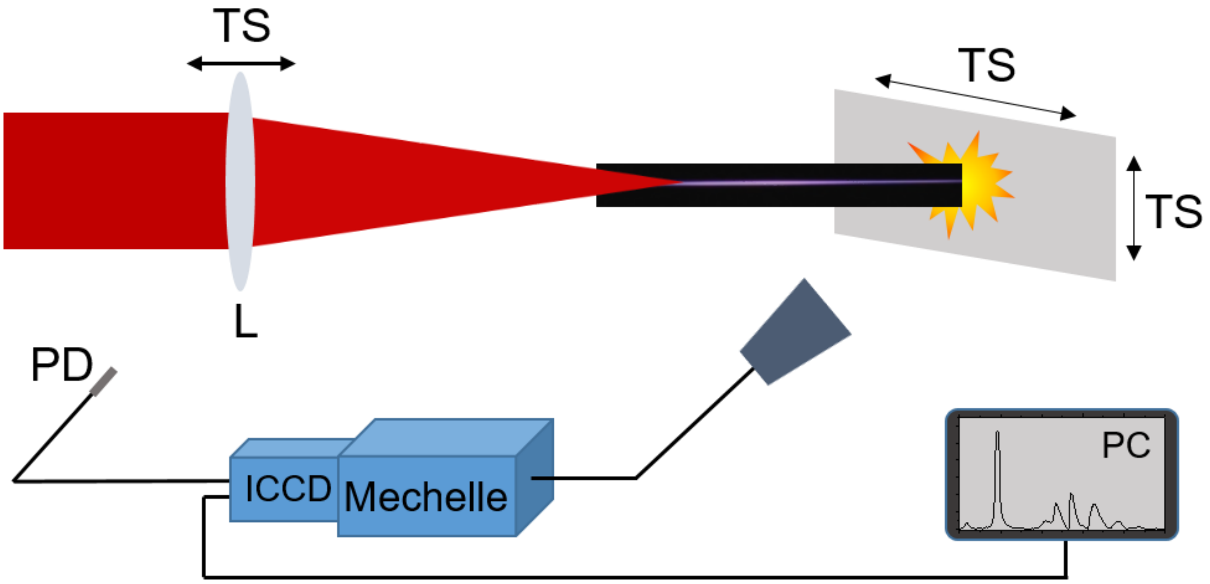

Figure 7.7: FIBS Experimental schematic

High spatial resolution, low ablation threshold and ability to do rapid analysis are some of the advantages of FIBS from femtosecond pulses. Filamentation provides a way to efficiently transport the laser energy to long distances to do remote excitation of FIBS of molecules of interest and increase SNR. The samples were mounted on a translational stage (TS) which can translate along two axes which are perpendicular to the direction of propagation. This was done to raster scan along the sample so that the femtosecond filament interacts with fresh sample surface for every pulse. The ICCD was triggered using the Pockels cell signal in the amplifier of the laser cavity and repeatability was checked using a photodiode (PD) placed near the lens [8]. Figure 7.8 shows some of FIBS spectra obtained from the samples. Although optical collection optimization along with large data acquisition and analysis can improve the characterization ability of the FIBS technique, we are mostly able to identify the composition of the various samples. It's easy to do this identification here because the samples used here are mostly pure metals and alloys. FIBS of organic and inorganic compounds sometimes yield identical spectra which needs additional classification like PCA – Principle component analysis [19]. So it is essential to identify a complimentary spectroscopic technique which along with FIBS aids in sensing with absolute specificity.

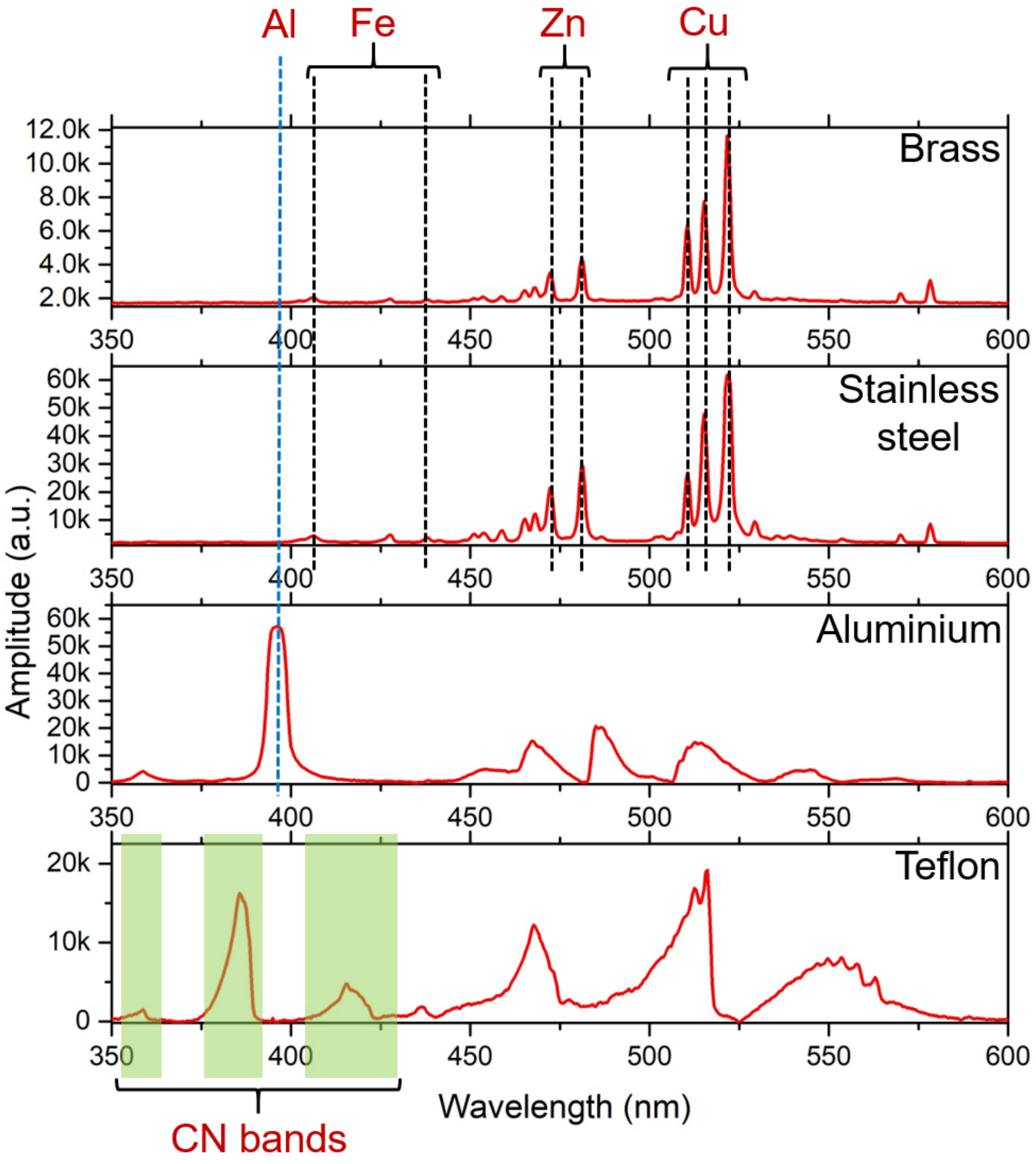

Figure 7.8: FIB Spectra observed from the solid samples interaction with filament.

7.4.2 Damage and spot analysis using Aluminium

We have first exposed Aluminum plates of defined thickness (~1.5mm- 1.8mm) to the filament generated by a 1000mm lens at different positions along the filament. According to the classification made in the earlier chapters this focusing condition is in the loose focusing regime. The damage was analysed at two different kinds of exposure to the filament, 5 second exposure to complete drilling of the Aluminium plate. Figure 7.9 shows the damage thus made.

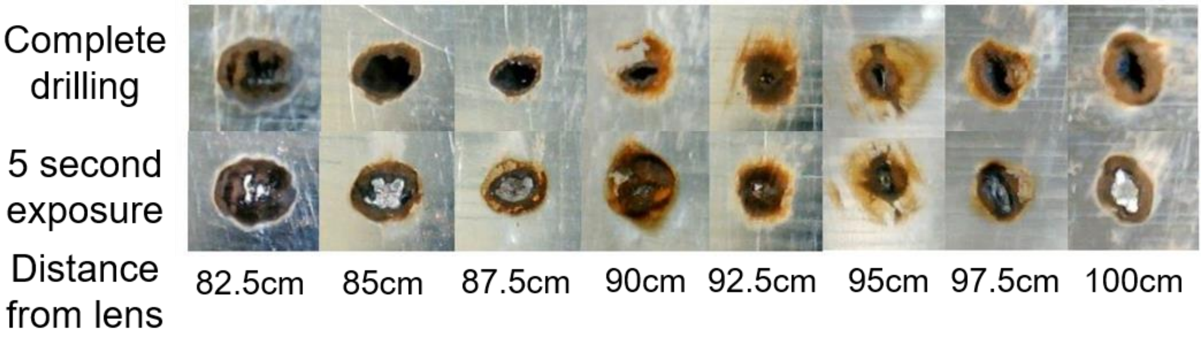

Figure 7.9: Breakdown caused by filament Aluminium interaction at different positions along the filament generated using a 1000m lens. 1st row: Images after complete drilling; 2nd row: Images after 5 second exposure (dwell time).

One can see difference in the spot size before and after the minimum spot observed indicating filament formation which keeps the intensity clamped. The spot dimensions were measured and plotted and we can see the asymmetry across the minimum spot size. The plots are shown in the figure 7.10. We can also see non-uniform distribution of the electric field when observing the spot shape which is not circular which shows in the plot showing the transverse and longitudinal spot dimensions. The difference between the transverse and longitudinal dimensions of the spot indicate astigmatism that arise in due to the lens being used. Although this non-uniformity exists we find that it is reproduced from shot to shot as the damaged spot shape does not differ from short term exposure to long term exposure. The Aluminium plate was also exposed to the filament for increasing exposure time in steps of 2 seconds and it can be seen the spot dimension increases initially for the first 10second exposure as seen in the figure. Intensity of the filament can also be estimated from the spot dimensions and it was found to be ~10TW/cm^2 which is what is estimated from spectroscopic studies.

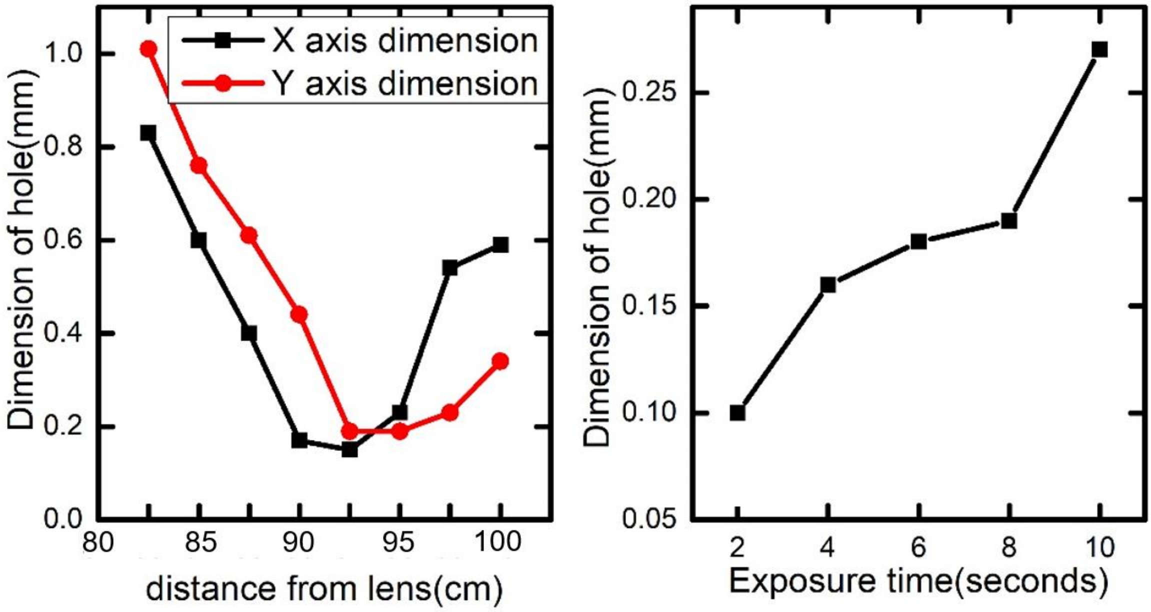

Figure 7.10: (left) Transverse dimensions of the damaged spot; (right) Dimensions of spot with increase in exposure time in steps of 2 seconds.

We have also taken an Aluminium foil of 11micron thickness and exposed to the filament at 3 different positions along the filament generated using a 1000mm lens. Photodiodes placed before and after the aluminium foil collect the scattered light from interaction of filament with Aluminium and the observed signal was plotted in the figure 7.11.

Using this setup we were able to measure the number of pulses required to drill through the Aluminium foil. Exposure 5cm before the onset of filament shows requirement of large number of pulses before the signal is detected from behind the foil, which amounts to ~600 pulses (~0.6s). At the centre of the filament 50 pulses (50ms) are enough to drill the foil. Post filament 100 pulses (100ms) are enough to drill the hole, which shows the effectiveness of the intensity clamping that occurs during and post filamentation.

Along with the studies done with filament interaction with the aluminium plate we find that the damage caused by femtosecond filaments is highly repeatable. Moreover the ability of fs filaments to transport energy over long ranges helps induce damage using fs filaments even in remote regions (>1km).

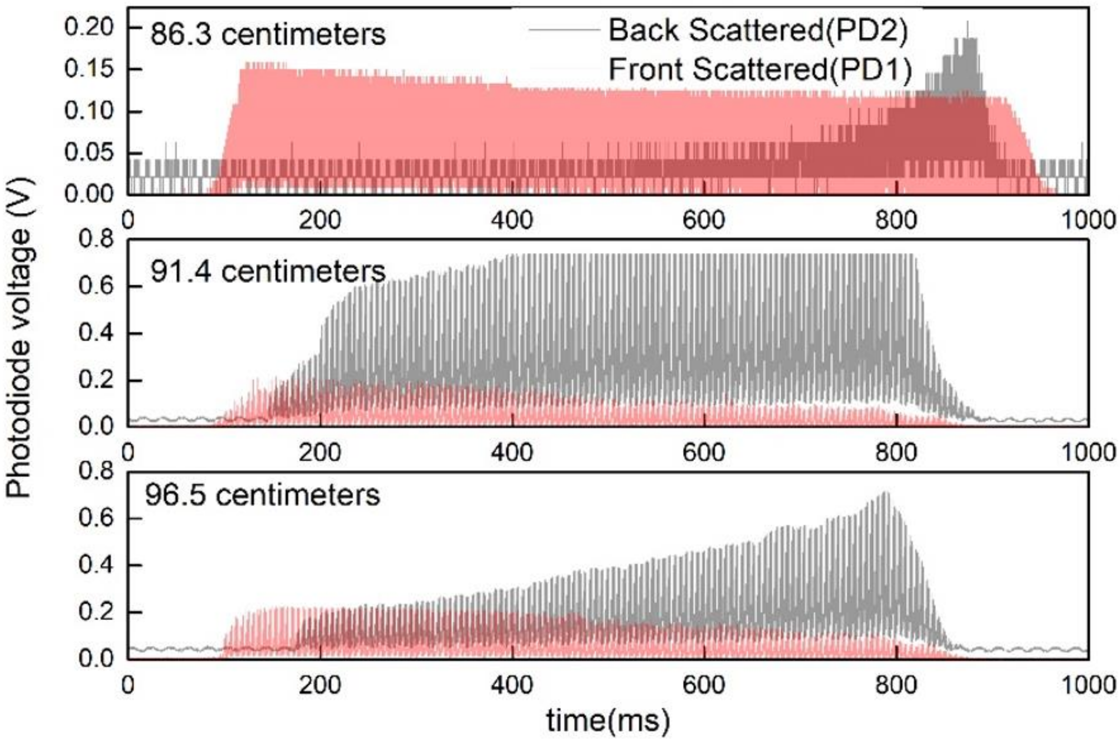

Figure 7.11: Shows the back and front scattered signals from the two photodiodes at 3 different positions along the filament.

7.4.3 Filament field interaction with composite material

Filament interaction studies done with Aluminum were extended to study an unknown composite material with surface irregularities. The study was first done to check if damage and spot created done by the filament is repeatable. The damage done by the filament was continuously noted by radiating the interaction spot with a CW Helium-Neon laser, and collecting the reflected light onto a photodiode. We find that the variation of the photodiode signal gives a definitive quantisation of the damage done as can be seen. Different focusing conditions were created by using lens of focal lengths 1000mm, 2000mm and 5000mm primarily in the loose focusing regime. The composite material was put at different points along the filament and exposed to the filament for different exposure times, which we have called dwell time of the filament on the composite. We have therefore measured the reflected signal with respect to varying dwell times, position and focusing conditions of the filament. The experimental schematic is shown in the figure 7.12. In addition the interaction region is imaged using an optical microscope.

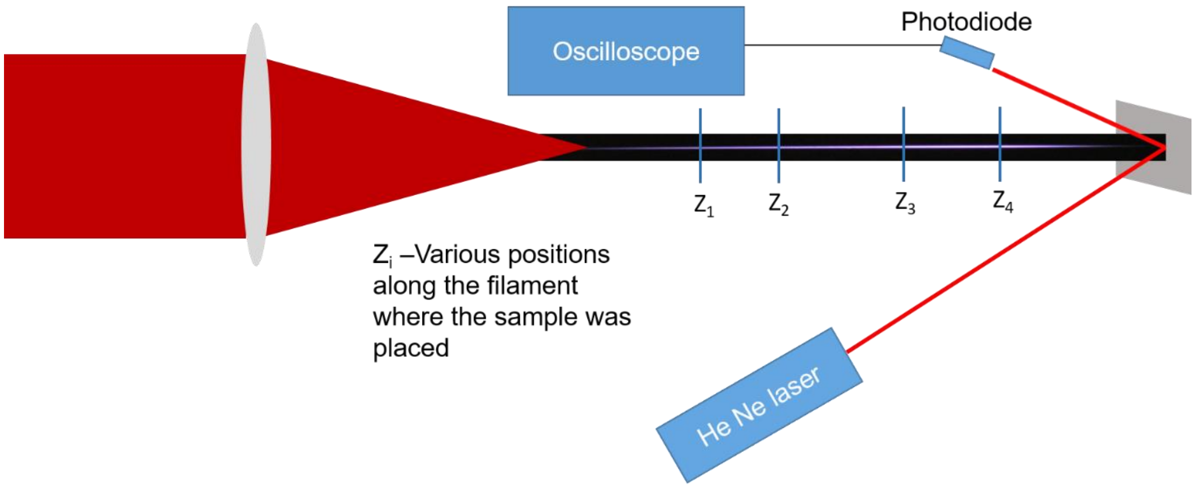

Figure 7.12: Schematic for reflectance measurement.

Table 7.1 shows the input power of used for the different filaments and the filament lengths observed. The next column shows the different positions at which the composite was tested.

Table 7.1: Different positions along the filament where the sample was exposed to the filament.

Focal length of the lens (mm)	Laser power (W)	Length of the total filament (mm)	Position of composite irradiation from the lens **Z_i** (mm)
1000	1.3	180	620, 680, 740, 800
2000	1.3	500	1020, 1120, 1200, 1280, 1360, 1440, 1520
5000	2.4	800	2900, 3100, 3300, 3500, 3700

As can be seen in the figure the reflectivity measurements of the filament irradiated spots of the composite at varying positions along the filament are plotted as a function of dwell time in Figure 7.13. Figure shows the damage from the filament generated using the 5000mm lens which generates a filament whose visible spatial extent is ~1m. We can divide the filament into three regions. Onset of the filament which is shown by Z_1 represents region 1. Z_2 and Z_3 as shown in our studies represent the central part which is the most intense part of the filament. The third region is beyond the intense central region of the filament given by Z_4, Z_5, Z_6.

Reflectivity which is normalized with reflectivity at no exposure, for region 1 was observed to change from 80 – 65 % with increase in dwell time. Although the reflectivity from the filament irradiated composite surface from the central region was observed to be around 65± 5 % for the maximum dwell times studied, it can be seen that the reflectivity falls close to this value much before maximum dwell time is reached. At the position Z_4 it can be seen that reflectivity does not fall drastically like the case of the central region but does not have the reflectivity of 90 – 75 % at the maximum dwell time, but displays the least reflectivity at maximum dwell time.

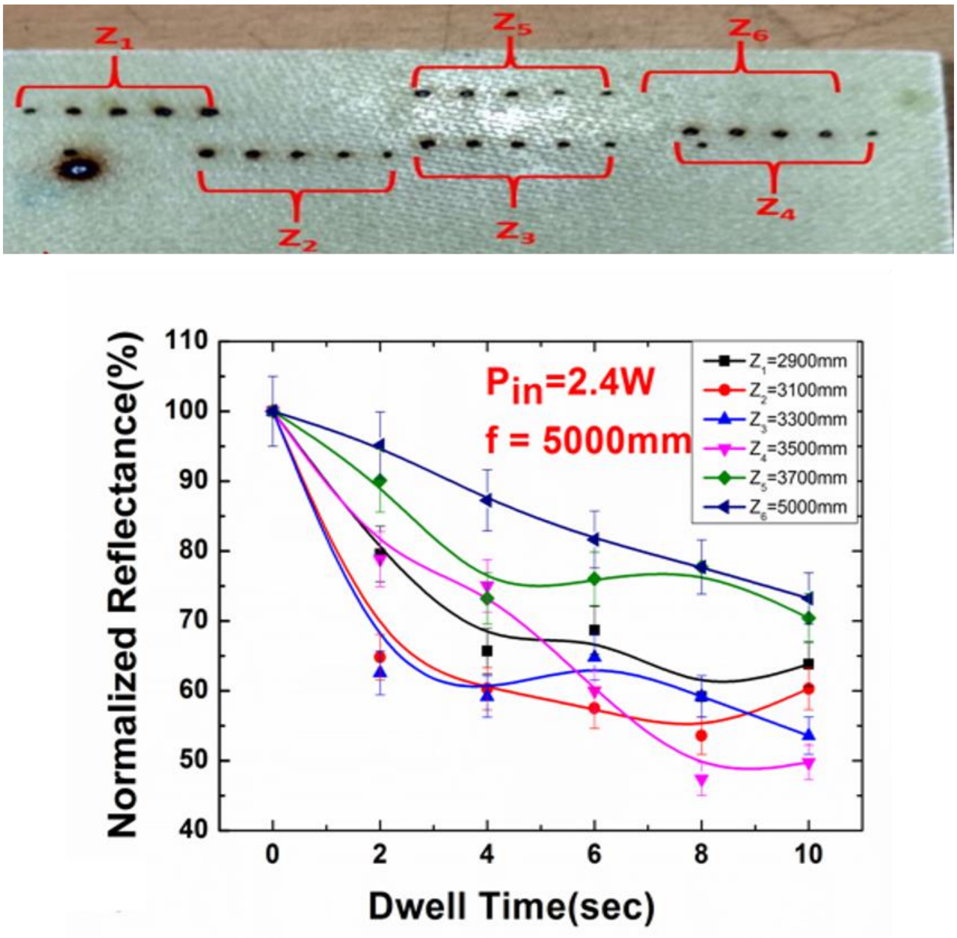

Figure 7.13: (Top) Filament induced spots on composite materials; (bottom) Normalized reflectance measured w.r.t dwell time of the filament at different positions along the propagation.

The composite material reflectance that was measured clearly shows a fall in the reflection with increase in dwell time, indicating that the reflectance reduced with the increased damage. We can therefore see that the damage done by a filament can be characterized in much more detail compared to damages by longer pulses which breakdown the material by not only ionization but also heating [28].

7.5 Proof of concept towards FIAS- Acoustic characterization of molecular aerosol

We have shown in chapter 5 acoustic profiling of femtosecond filaments. We attempt to extend this technique to probe aerosols and identify the composition using the acoustic signals generated from filament interactions. Hyun Jin et. Al. have used the acoustic signals from laser plasma interaction to estimate the particle size and concentration in the interaction region [14]. Molecular aerosols of tryptophan was generated using a nebuliser using solutions of different concentration. The acoustic signal from just the water aerosol was collected as reference and then aerosols of varying concentrations used and acoustic signals from their respective aerosols were studied. The filament was generated using a 150mm lens so that spatial extent of the filament interaction remains small. The filament structure is further suitable for this study as it completely overlaps the outlet of the nebulizer which is 1cm in diameter. FIBS Spectra obtained of this interaction contains a large amount of noise due to turbulence caused by the aerosol from due to the nebulizer. But on the other hand we observed that the acoustic signal had a stable pulse profile despite there being considerable turbulence. The image of the experimental schematic is shown in the figure 7.14.

Tryptophan was dissolved in water and the aerosol produced was exposed to the filament. Figure 7.15 shows the spectral comparison from acoustic emissions from air, water and tryptophan aerosols. The figure indicates the existence of multiple peaks within the spectrum for the aerosol of tryptophan in comparison to the smooth profile from that of water and air.

The aerosols were produced using 4 different concentrations of tryptophan in water. The acoustic signals were taken without change in experimental setup between concentration changes and the observed signals are shown in the figure 7.16. Observation of the time domain signals from each concentration shows increase in peak to peak overpressures with increase in concentration of tryptophan.

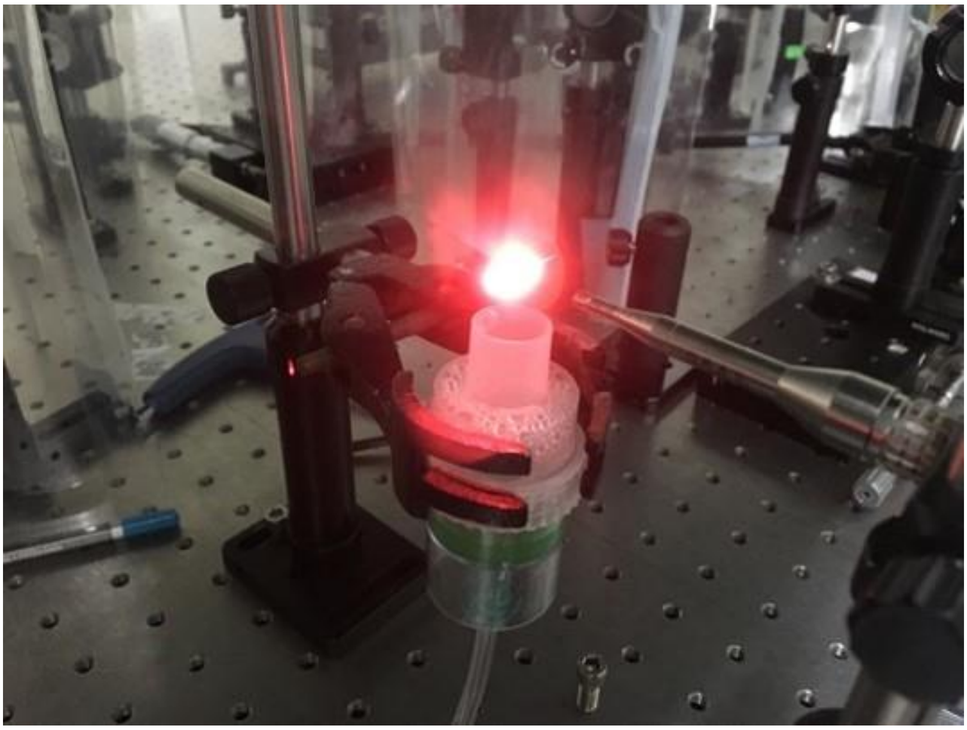

Figure 7.14: Image of the interaction zone and microphone arrangement.

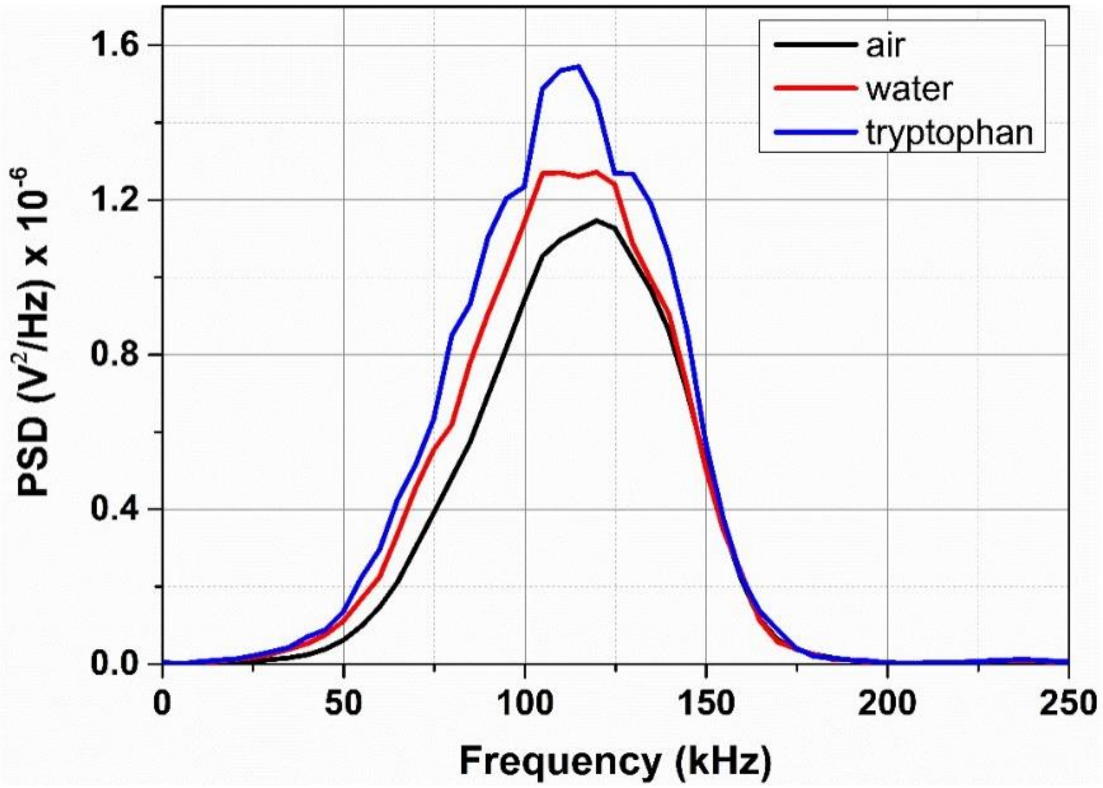

Figure 7.15: Typical acoustic spectra obtained from filament interaction with air, water and a tryptophan solution.

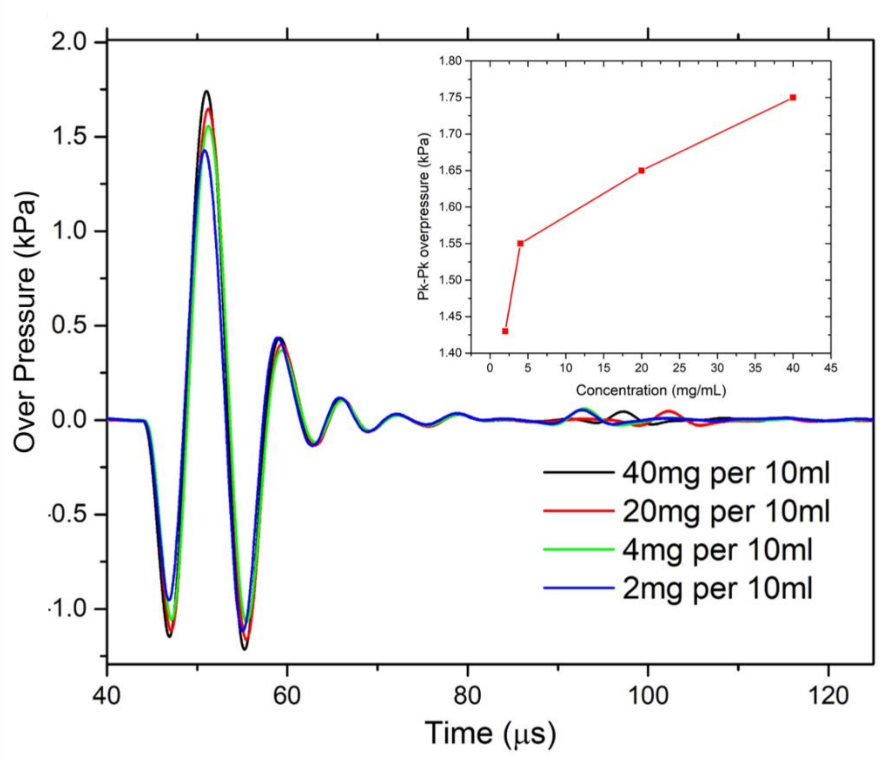

Figure 7.16: Acoustic pulse from the filament interaction with tryptophan aerosol of various concentrations.

The frequency distribution of the raw signals was taken and plotted in figure 7.17. The frequency distribution shows an even more emphasized difference in the peak power spectral density of the acoustic signals which varies with concentration. The profile of the frequency distribution also changes indicating existence of frequency peaks other than that observed from acoustic signals in air which are centred around 110 kHz. Although we can observe clear distinction between the frequency distribution from the acoustic signals obtained during filament interaction with different aerosols, the prominent frequency components cannot be resolved. To better resolve the peaks the time domain signal was zero padded to obtain higher resolution in the frequency domain. The spectrum of zero padding is shown in figure 7.18 for the different concentrations.

The amplitude in both the time and frequency domain shows a direct relation of the concentration to the amplitude especially in frequency domain as the amplitude increases with concentration. This being highly repeatable even under turbulent conditions indicates that this technique could be a good complimentary tool for optical methods for aerosol characterization and sensing. Further analysis of the frequency distribution of FIAS from aerosols indicates

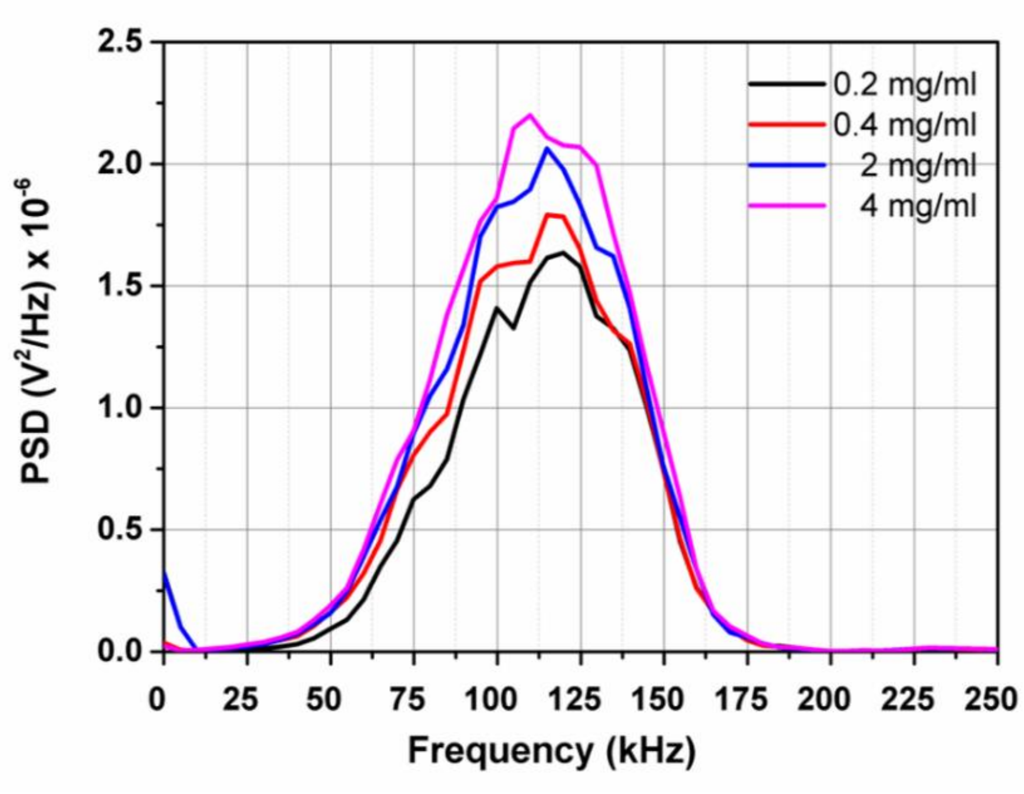

Figure 7.17: Acoustic signal frequency distribution obtained from filament interaction with aerosols having varying concentrations of tryptophan.

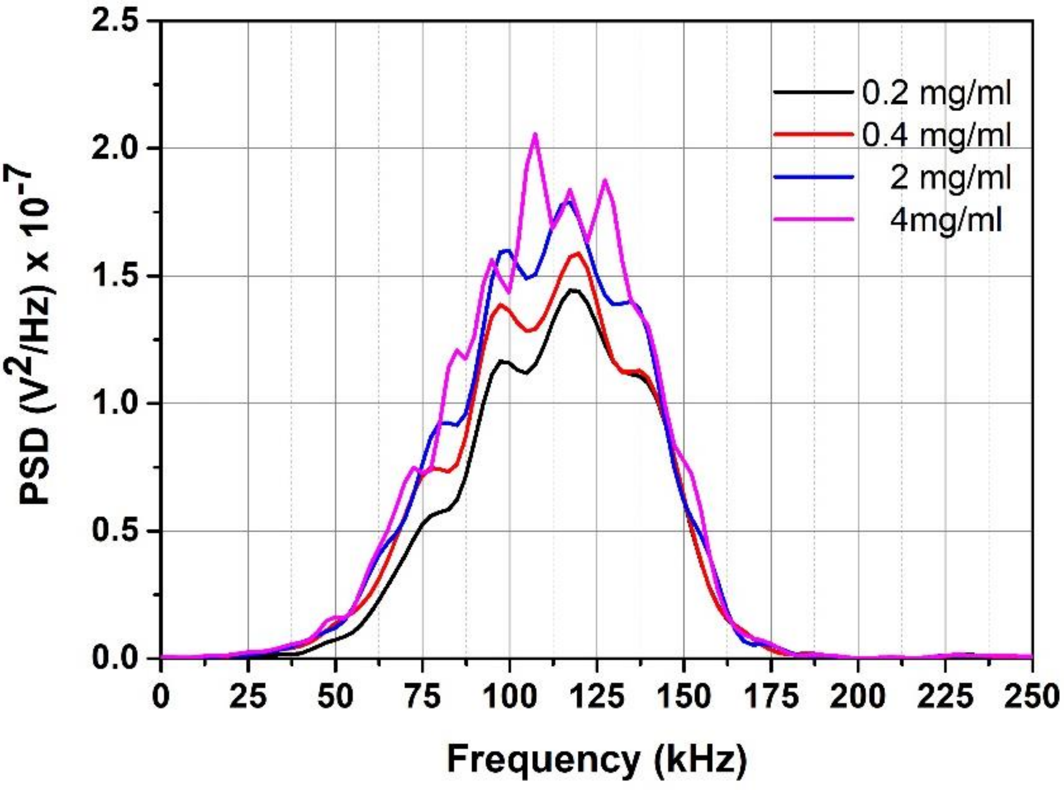

Figure 7.18: Acoustic signal frequency distribution obtained from filament interaction with aerosols having varying concentrations of tryptophan after zero padding

superposition of other peaks when compared to the frequency distribution from only air. The amplitude in both the time and frequency domain shows a direct relation of the concentration to the amplitude especially in frequency domain as the amplitude increases with concentration. This being highly repeatable even under turbulent conditions indicates that this technique could be a good complimentary tool for optical methods for aerosol characterization and sensing. Further analysis of the frequency distribution of FIAS from aerosols indicates superposition of other peaks when compared to the frequency distribution from only air, where the frequency is a broad and smooth distribution. The distribution was therefore analysed so as to separate the peaks that are being superimposed, we find that there are two main peaks with two side peaks. The main peaks exist around 90kHz and 110kHz. Frequency spectrum of the acoustic signal in air shows that the central peak frequency is at 110kHz, while the peak at 90kHz does not exist. The second peak at 90kHz which arises in the case of aerosol filament interaction can be a due to interaction of the tryptophan aerosol with filament. The peaks were therefore fit to multiple peaks and the fitting is shown for one concentration of tryptophan in figure 7.19.

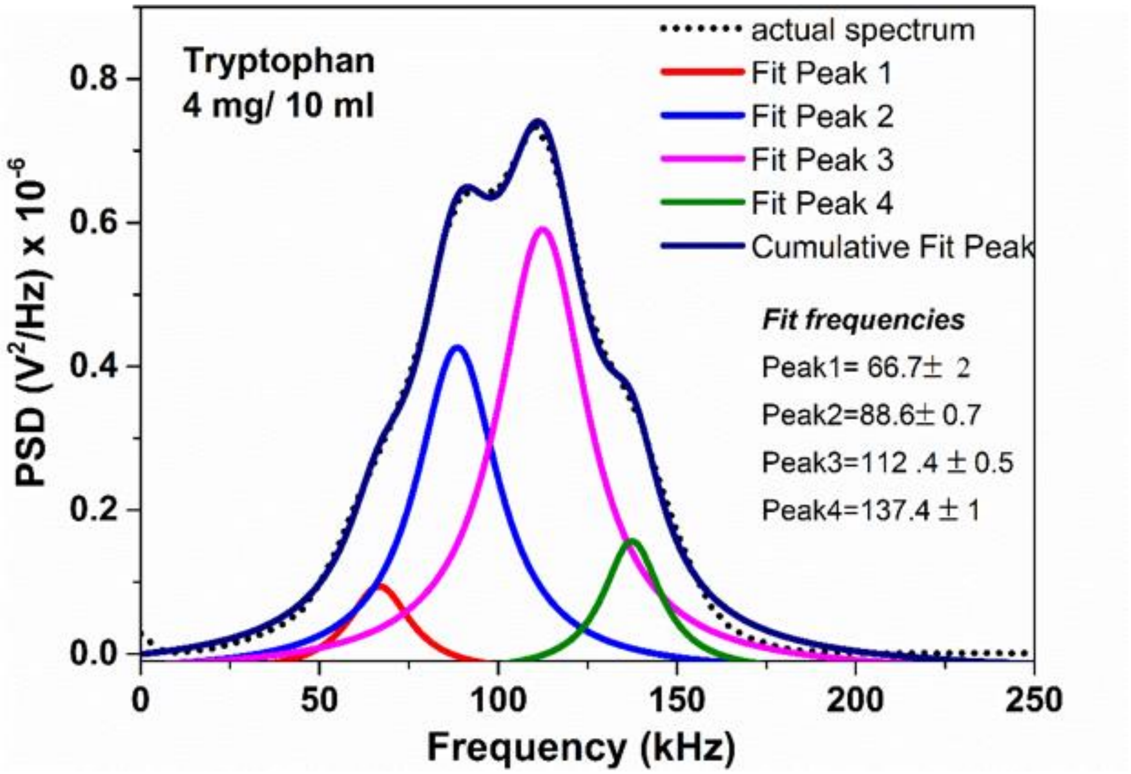

Figure 7.19: Figure showing the peak fits for acoustic frequency distribution obtained from tryptophan aerosol interaction with filament.

When this analysis is compared between different aerosols with variation of concentration it can be seen that the peak at 95kHz increases with concentration of tryptophan without increase in the peak at 110kHz. Further characterization of aerosol filament interaction needs to be done by varying the intensity and focal geometry of filament generation to establish the viability of FIAS characterization of aerosols or gases.

7.6 Summary

As filamentation has shown the ability to generate and modulate a variety of emissions arising from long range intense propagation of laser pulses, we have performed studies to explore the feasibility and prospect of application. We have first studied the FIBS of air and compared it to the FIBS of commonly used solvents like methanol and acetone. The breakdown spectrum can clearly distinguish the solvents when using a simple acquisition setup. The Filament was sent through aerosols made from other liquids as well and the transverse emitted spectrum which was collected from a distance of 1m using a Kymera 328i spectrometer coupled to an imaging lens can be used to moderately distinguish the liquids. As fluorescence spectrum is an indication of the molecular composition of any material, the pump wavelength in the filament was employed to detect Two-photon fluorescence from riboflavin aerosol clouds. We have clearly observed fluorescence from riboflavin aerosol produced from a solution of a concentration of 0.1mg/ml corresponding to 100 ppm.

Filament induced breakdown of solid materials was also done. This was done to test the viability of filamentation as a remote sensing tool and as a remote neutralizing agent against hostile entities. FIBS of different solid samples was done and one can easily extract the elemental composition of the different samples. Aluminum was used as the primary characterization element to test the material damage induced by filamentation. An Aluminium plate was placed at different positions of the filament over different exposure times and the dimensions of the holes caused due to damage were plotted at different positions on the filament. The spot dimensions show a variation in the tangential and sagittal focal plane of the focusing conditions. The number of pulses that drill an Aluminium foil were found at different point in the filament. The foil placed at different positions of the filament shows faster drilling time after filament onset as compared to before onset indicating the clamping of high intensity over long propagation ranges. The solid material characterization that was done was extended to study damage done to a composite material with surface irregularities. Reflectance of damaged spot can be distinguished between various filaments and filament positions, showing the characteristic reproducibility of filament induced damage that can be modulated. The work described in this chapter are preliminary studies to establish the ground for viable applications that filamentation can provide.

References

1. A. Braun, *Self-channelling of high-peak-power femtosecond laser pulses in air*, Opt. Letters **20**, 73-75 (1995).
2. A. L. Gaeta, *Collapsing Light Really Shines*, Science **301**, 54 (2003).
3. A. Couairon and A. Mysrowicz, *Femtosecond filamentation in transparent media*, Phys. Rep. **441**, 47–189 (2007).
4. L Chin and H. Xu, *Tunnel ionization, population trapping, filamentation and applications*, J. Phys. B:At. Mol. Opt. Phys. 49, 222003, (2016).
5. P. Rohwetter, J. Kasparian, Stelmaszczyk, Z. Hao, S. Henin, N. Lascoux, W. M. Nakaema, Y. Petit, M. Queißer, R. Salamé, E. Salmon, L. Wöste and K. J– P. Wolf, *Laser-induced water condensation in air*, Nature Photon, 4, 451–456 (2010).
6. N. Khan, N. Mariun, I. Aris and J Yeak, *Laser-triggered lightning discharge*, New J. Phys., 4 61 (2002)
7. P. M. Paul, E. S. Toma, P. Breger, G. Mullot, F. Augé, P. Balcou, H. G. Muller and P. Agostini, *Observation of a train of attosecond pulses from high harmonic generation*, Science, 292, 1689 (2001)
8. R. Junjuri, S. A. Nalam, E. Manikanta, S. Sree Harsha, P. Prem Kiran, and Manoj Kumar Gundawar, *Spatio-temporal characterization of ablative Cu plasma produced by femtosecond filaments*, Opt. Express 29, 10395-10405 (2021).
9. R. Berera, R. Van Grondelle, and J. T. M. Kennis*, Ultrafast transient absorption spectroscopy: principles and application to photosynthetic systems*, Photosynth Res, 101, 105–118 (2009).
10. L. Vinoth Kumar, E. Manikanta, Ch. Leela, and P. Prem Kiran, *Effect of laser intensity on radio frequency emissions from laser induced breakdown of atmospheric air*, J. Appl. Phys, 119, 214904 (2016).
11. M. Richardson, M. Baudelet and T. Seiderman, *Fundamentals of filament interaction*, AFOSR/JTO MRI Annual Report (2016).
12. G..Méjean, J. Kasparian, J. Yu, S. Frey, E. Salmon and J-P. Wolf, *Remote detection and identification of biological aerosols using a femtosecond terawatt lidar system*, Applied Physics B, **78(5)**, 535-537 (2004).
13. H. Wille, M. Rodríguez, J. Kasparian, D. Mondelain, J. Yu, A. Mysyrowicz, R. Sauerbrey, J. Wolf, and L. Woeste, *Teramobile: a mobile femtosecond-terawatt laser and detection system*, The European Physical Journal Applied Physics, **20(3),** 183-190 (2002).
14. J. Yu, D. Mondelain, J. Kasparian, E. Salmon, S. Geffroy, C. Favre, V. Boutou and J. Wolf, *Sonographic probing of laser filaments in air*, Appl. Opt. **42**, 7117-7120 (2003).
15. H. Jin, J-W. Kim, J-A. Son and J-G. Choi, *An acoustic based, laser induced breakdown method for determining the sizes and concentrations of nanoparticles*, Physical Chemistry Chemical Physics, **12(20)**, 5199-5202 (2010).
16. S. Caygill, F. Davis and S. P. J. Higson, *Current trends in explosive detection techniques*, Talanta, **88**, 14–29 (2012).
17. M. Baudelet, *Laser Spectroscopy for Sensing: Fundamentals, Techniques and Applications*, Elsevier (2014).
18. S. S. Harilal, J. R. Freeman, P. Diwakar and A. Hassanein, *Comparison of nanosecond and femtosecond LIBS*, CLEO: 2013, OSA Technical Digest (online) (Optical Society of America, 2013), paper CTu2H.8 (2013).

19. M. K. Gundawar, R. Junjuri, and A. K. Myakalwar, *Standoff detection of explosives at 1 m using laser induced breakdown spectroscopy*, Defence science journal, **67(6)**, 623 (2017).
20. R. Junjuri, C. Zhang, I. Barman, and M. K. Gundawar, *Identification of post-consumer plastics using laser-induced breakdown spectroscopy*, Polymer Testing **76**, 101-108 (2019):.
21. T. A. Labutin, Vasily N. Lednev, Alexey A. Ilyin, and Andrey M. Popov, *Femtosecond laser-induced breakdown spectroscopy*, Journal of Analytical Atomic Spectrometry, **31(1)**, 90-118 (2016).
22. Y. Xie, W. Cheng, B. Jin, C. Liang, Y. Ding and W. Zhang, *Solvent directed selective and sensitive fluorescence detection of target ions using a coumarin–pyridine probe*, Analyst, **143(22)**, 5583-5588 (2018).
23. Á. Fernández-Bravo, T. Delgado, P. Lucena and J. J. Laserna, *Vibrational emission analysis of the CN molecules in laser-induced breakdown spectroscopy of organic compounds*, Spectrochimica Acta Part B: Atomic Spectroscopy, **89**, 77-83 (2013).
24. F. A. Kiliçarslan, A. Erdoğmuş, N. Y. Coşkun, S. M. Yalçın and A. Gül, *Synthesis, spectral and photophysical investigation of porphyrazines with eight 3-quinolinecarboxy esters*, Journal of Coordination Chemistry, **66(24)**, 4316-4329 (2013).
25. Ricardo Lopez-Delgado and Sylvain Lazare. *Fluorescence properties of methyl salicylate in vapor, liquid, and solution*, The Journal of Physical Chemistry, **85(7)**, 763-768 (1981).
26. B. Zhao, Y. Yang, Y. Wu, B. Yang, J. Chai, X. Hu and B. Liu, *To re-evaluate the emission mechanism, AIE activity of 5-azidofluorescein and its reaction with H2S and NO*, Sensors and Actuators B: Chemical, **256**, 79-88 (2018).
27. Y. Bi, Z. Huang, B. Liu, Q. Zou, J. Yu, Y. Zhao and Q. Luo, *Two-photon-excited fluorescence and two-photon spectrofluoroelectrochemistry of riboflavin*, Electrochemistry Communications, **8(4)**, 595-599 (2006).
28. N. Kumar, S. A. Nalam, G. M. Kumar, and P. P.Kiran, *Filament Induced Surface Modification of Composite Material*, In 2017 IEEE Workshop on Recent Advances in Photonics (WRAP), pp. 1-2. IEEE, 2017.

This page was intentionally left blank

CHAPTER 8: Summary and Future scope

Abstract:

Femtosecond filamentation has shown to display numerous phenomenon which can be applied to complement a broad range of applications and explorations. In this chapter we have detailed work that can be done to further extend our understanding of filamentation dynamics such as Shadowgraphy and spectral interferometry. The large broadband with a high temporal resolution that is emitted from a filament can be used to probe ultrafast events. The requirement and prospects of scaling up to larger laser systems with better acquisition setups to increase the ability to probe remote regions are also discussed.

This chapter summarizes the highlights of the work presented in the thesis and indicates the roadmap on taking the lab results to the field. The FIBS, 2-photon fluorescence and UV excitation of aerosols can be taken to stand-off distances of > 100 mtrs to few kms by scaling up the input laser power using a multi-pass amplifier giving pulse energies of the order of 80 – 250 mJ as well as the collection optics and diagnostics. This also can be used for filamentation LIDAR. Our demonstration of a remotely generated UV source from the third harmonic emission also can be tested on the field to detect organic species.

The SCE from filaments is an excellent source for probing and imaging the spatio-temporal evolution of organic molecules, by enabling us temporal resolutions of a few fs over a large range of frequencies. Femtosecond pulses are highly beneficial for probing fast processes which cannot be resolved using electronic instrumentation, increasing the resolution by at least 3 orders. One such future scope that is being worked on is Spectral Interferometry using SCE such that we can study the Spatio-Temporal Evolution of Wavepackets (STEW) of organic molecules excited by short pulses[1, 2]. By observing the interferogram on a spectrograph in which two pulses, a reference pulse and a probe pulse with a defined time delay interfere, we can provide a complete picture of the dispersion induced in the probe pulse. This gives temporally resolved information of the plasma dynamics and the pulse induced refractive index changes in the object being observed, which in our case is a filament generated under different conditions of the medium .

Transient event imaging of many underlying principles in materials science, chemistry, and biology can greatly aid our understanding of nature. These events require ultra-high temporal resolutions while doing real-time imaging. Pump-probe ultrafast imaging techniques require the scene to be repeatable. Therefore single-shot ultrafast imaging techniques have been developed to image non-repeatable transient events. From the time of its demonstration in 2014, compressed ultrafast photography (CUP) has found many applications in a number of avenues such as time-of-flight 3D profilometry, secured image communication, and wide-field photo-luminescent lifetime mapping to name a few [3]. Fundamental light phenomena like the temporal focusing of a femtosecond laser pulse and the refraction of a picosecond laser pulse have been observed with frame rates of up to 70 trillion frames per second. Ultrafast imaging by CUP Captures instantaneous light patterns and goes to show that ultrafast imaging is indispensable in revealing spatio-temporal details. The Supercontinuum broadband generation from the filament can be used to illuminate and capture far off events at high frame rates by using an imaging system that creates an image by coupling a spectrograph and a CMOS camera.

Filamentation is finding applications in multiple fields and the study of filamentation dynamics further provides us with a clear understanding of intense femtosecond pulse propagation and medium interaction. This thesis aims to create a holistic understanding of filament behaviour and the corresponding emissions to establish the foundation to further apply and control femtosecond filamentation.

References

1. D. Patel, D. Jang, S. W. Hancock, H. M. Milchberg, and K-Y. Kim, *Simplified single-shot supercontinuum spectral interferometry*, Opt. Express **28**, 11023-11032 (2020).
2. L. Lepetit, G. Chériaux, and M. Joffre, *Linear techniques of phase measurement by femtosecond spectral interferometry for applications in spectroscopy*, J. Opt. Soc. Am. B 12, 2467-2474 (1995).
3. L. Gao, J. Liang, C. Li, and L. V. Wang, *Single-shot compressed ultrafast photography at one hundred billion frames per second*, Nature, **516(7529)** 74-77 (2014).

Outcome of the thesis:

Patents Applied:

- A method for tailoring of ultrashort infrared laser pulses for precise generation and control of an ultraviolet source for spectroscopic sensing Submitted On 15 Dec 2020 To Drdo Hqrs (Results from chapter # 4)

Patent application under preparation:

- Pulsed laser driven Filament induced eLectro Magnetic (FIeLM) pulses (Results from chapter # 6)

Peer Reviewed Publications:

- S. A. Nalam, S. S. Harsha and P. P. Kiran, Effect of Focusing element induced aberrations on filamentation and supercontinuum emission in ambient air, Opt. Express 29, 14668-14681 (2021). (Results from Chapter #3).
- **Samuel Anurag Nalam**, Manikanta Elle, S. Sree Harsha and P. Prem Kiran, *Acoustic measurements on femtosecond laser induced filaments*, In: Singh K., Gupta A.K., Khare S., Dixit N., Pant K. (eds) ICOL-2019. Springer Proceedings in Physics, vol 258. Springer, Singapore. https://doi.org/10.1007/978-981-15-9259-1_93. (Results from Chapter #5).
- Naveen. K. P., **S. A. Nalam**, G. M. Kumar and P. P. Kiran, *Filament Induced Surface Modification of Composite Material*, 2017 IEEE Workshop on Recent Advances in Photonics (WRAP), Hyderabad, India, (2017) (Results from chapter # 7)
- M. M. Neethish, V. V. Ravi Kanth Kumar, **Samuel Anurag Nalam**, S. Sree Harsha, and P. Prem Kiran, *Supercontinuum generation from zinc borate glasses: bandgap versus rare-earth doping*, Opt. Lett. 46, 1201-1204 (2021).
- Rajendar Junjuri, **Samuel Anurag Nalam**, S. Sree Harsha, P. Prem Kiran and G. Manoj Kumar, *Spatio temporal characterization of Cu plasma produced by femtosecond filaments*, Optics Express (2021). (Results from Chapter 7)

Manuscripts under Review/Preparation:

- **Samuel Anurag Nalam**, E. Manikanta, S. Sree Harsha and P. Prem Kiran, Filament Induced Acoustic Spectroscopy of aerosol clouds from Tryptophan, (Manuscript under preparation to be submitted to JAP/JOSAB) (Results from chapter # 5)
- **S. A. Nalam**, Naveen. K. P., G. M. Kumar and P. P. Kiran, Filament irradiation of metal and composite materials (to be submitted to EPJ Special Issue) (Results from Chapter #7)

Schools/Workshop attended:

- **GIAN workshop** on *Attosecond photonics*, IIT Madras, Chennai, 4th-8th November, (2016)
- **SERC School** *for Lasers and Nonlinear Optics***,** Pondicherry University, Pondicherry, India, 22nd March - 11th April (2016)

Conference Presentations/Proceedings:

- Samuel Anurag Nalam, C. Raghavendar, J. Yelliah, P. Naveen, Nagaraju Guthikonda, V. Rakesh Kumar, G. Manoj Kumar and P. Prem Kiran, *Spectral characterization of intensity of femtosecond filament in atmosphere*, National Laser Symposium-25, December 20th-23rd, KIIT, Bhubaneswar (2016). (POSTER)
- Samuel Anurag Nalam, Naveen kumar P, G. Manoj Kumar, P. Prem Kiran, *Filament Induced surface modification of Al sheet*, Ultrafast Science, November 2nd-4th, ACRHEM, University of Hyderabad (2017). (POSTER)
- Naveen kumar P, Samuel Anurag Nalam, G. Manoj Kumar, P. Prem Kiran, *Filament Induced surface modification of composite material*, IEEE Workshop on Recent Advances in Photonics, December 18th-19th, Mahindra école Centrale, Hyderabad, (2017). (POSTER)
- Samuel Anurag, S. Sree Harsha and P. Prem Kiran, *Ultrafast Filamentation in Air: Application towards long distance remote sensing*, National Laser Symposium-27, December 3rd-6th, RRCAT, Indore, (2018). (POSTER)
- Samuel Anurag Nalam, S. Sree Harsha, P. Prem Kiran, *Spectral characterization of intense Femtosecond pulse propagation*, Ultrafast Science, October 22nd-24th, RRCAT, Indore (2018). (POSTER)
- Samuel Anurag Nalam, S. Sree Harsha and P. Prem Kiran, *Femtosecond Filamentation for the detection of biological warfare agents (Riboflavin)*, 12th International High Energy Materials Conference & Exhibit, December 16th-18th, IITM Chennai, (2019). (POSTER)
- MM Neethish, Samuel Anurag Nalam, S Sree Harsha, VV Ravi Kanth Kumar and P Prem Kiran, *Tailoring glasses for Supercontinuum generation*, International Conference on optics and Electro optics, October 19th-22nd, Instruments Research and Development Establishment, Dehradun, India. (2019).(POSTER)
- Samuel Anurag Nalam, Manikanta Elle, S. Sree Harsha and P. Prem Kiran, *Acoustic measurements on femtosecond laser induced filaments*, International Conference on optics and Electro optics, October 19th-22nd, Instruments Research and Development Establishment, Dehradun, India (2019). (POSTER)
- Samuel Anurag Nalam, Sree Harsha Srikantaiah and Prem Kiran Pathuri, *Role of Focusing geometry on intense femtosecond filament generation*, International Conference on optics and Electro optics, October 19th-22nd, Instruments Research and Development Establishment, Dehradun, India (2019). (POSTER)
- Samuel Anurag Nalam, S. Sree Harsha and P. Prem Kiran, *Structural and spectral dynamics of intense femtosecond filament generation with transmitting and reflecting optics,* National laser symposium-28, January 8th-11th, VIT,Chennai (2020). (POSTER)
- Samuel Anurag Nalam, ,Manikanta Elle,S. SreeHarsha and P. Prem Kiran, *Effect of external focusing geometry on the acoustic and optical emissions from femtosecond laser filaments*, OSA Frontiers in optics+Laser Science, September 14th–17th, (2020). (POSTER)
- Samuel Anurag Nalam, S. Sree Harsha and P. Prem Kiran, *Influence of chirp and polarization on the third harmonic and supercontinuum generation dynamics during fs filamentationin air*, OSA Laser Congress, October 13th–16th, (2020). (POSTER)
- S. Sree Harsha, Samuel Anurag Nalam , and P. Prem Kiran*, Effect of Aberrations in focusing elements on femtosecond filaments*, IEEE International Conference on Plasma physics (ICOPS), December 6th–10th, (2020). (POSTER)

Femtosecond pulse propagation in air towards Filamentation Nonlinear Optics

by Samuel Anurag Nalam

Submission date: 12-Aug-2021 04:03PM (UTC+0530)
Submission ID: 1630581868
File name: Samuel_PhD_Thesis_Without_references_Final.pdf (38.06M)
Word count: 43375
Character count: 232274

P. Prem Kiran

Dr. P. Prem Kiran
Associate Professor
School of Physics
University of Hyderabad
Hyderabad-500 046. (TS) INDIA

Femtosecond pulse propagation in air towards Filamentation Nonlinear Optics

ORIGINALITY REPORT

8%	1%	8%	0%
SIMILARITY INDEX	INTERNET SOURCES	PUBLICATIONS	STUDENT PAPERS

PRIMARY SOURCES

1	Samuel Anurag Nalam, S. Sree Harsha, P. Prem Kiran. "Effect of focusing element-induced aberrations on filamentation and supercontinuum emission in ambient air", Optics Express, 2021 Publication	5%
2	Samuel Anurag Nalam, S. Sree Harsha, P. Prem Kiran. "Influence of chirp and polarization on the third harmonic and supercontinuum generation dynamics during fs filamentation in air", Laser Congress 2020 (ASSL, LAC), 2020 Publication	1%
3	Naveen Kumar P., Samuel Anurag Nalam, G. Manoj Kumar, P. Prem Kiran. "Filament Induced Surface Modification of Composite Material", 2017 IEEE Workshop on Recent Advances in Photonics (WRAP), 2017 Publication	<1%

P. Prem Kiran

Dr. P. Prem Kiran
Associate Professor
School of Physics
University of Hyderabad
Hyderabad-500 046. (TS) INDIA